Dissertations, Master's Theses and Master's Reports

2016

DYNAMIC ATOMISTIC STUDY OF TUNNEL FUNCTIONS IN NANOSTRUCTURED TRANSITIONAL METAL OXIDES

Yifei Yuan
Michigan Technological University, yifeiyua@mtu.edu

DYNAMIC ATOMISTIC STUDY OF TUNNEL FUNCTIONS IN
NANOSTRUCTURED TRANSITIONAL METAL OXIDES

By

Yifei Yuan

A DISSERTATION

Submitted in partial fulfillment of the requirements for the degree of

DOCTOR OF PHILOSOPHY

In Materials Science and Engineering

MICHIGAN TECHNOLOGICAL UNIVERSITY

2016

This dissertation has been approved in partial fulfillment of the requirements for the Degree of DOCTOR OF PHILOSOPHY in Materials Science and Engineering.

Department of Materials Science and Engineering

Dissertation Co-Advisor: *Reza Shahbazian Yassar*

Dissertation Co-Adviser: *Jun Lu*

Committee Member: *Stephen Hackney*

Committee Member: *Gregory Odegard*

Department Chair: *Stephen Kampe*

Table of Content

Preface

The contents in this publication covers five PhD projects I have done during my PhD period from 2012 Fall to 2016 Summer. The projects focus on atomistic exploration of tunnel functions, particularly, energy storage, in tunneled α-MnO$_2$ nanostructures using in (ex) situ STEM technique.

Chapter 3 covers the first project reviewing the application of *in situ* TEM technique in solving rechargeable battery problems. Mr. Yifei Yuan summarized and categorized the most recently updated literature in this area and wrote the review under direction of Dr. Jun Lu (Argonne National Laboratory) and Dr. Reza Yassar (University of Illinois at Chicago).

Chapter 4 covers the second project utilizing *in situ* (S)TEM to study the dynamic lithiation and Li$^+$-tunnel interaction in single α-MnO$_2$ nanowire. Experiments were designed, conducted and analyzed by Mr. Yifei Yuan under direction of Dr. Reza Yassar. Dr. Anmin Nie (University of Illinois at Chicago), Dr. Christopher Johnson and Dr. Jun Lu helped the experimental aspect, while Dr. Gregory Odegard and Dr. Dennis Meng (Department of Mechanical Engineering, MTU) contributed for the simulation work of Li$^+$-tunnel interaction and the material synthesis, respectively.

Chapter 5 covers the 3rd project applying *in situ* TEM to study the reversible (de)sodiation and Na$^+$-tunnel interaction in α-MnO$_2$ nanowire and compare the sodiation with lithiation process. Mr. Yifei Yuan designed and carried out this project under direction of Dr. Jun Lu and Dr. Reza Yassar. Miss Lu Ma and Dr. Tanpin Wu (Argonne National Laboratory) collaborated for the cell level *in situ* synchrotron X-ray scattering characterization of α-MnO$_2$ cathode. Mr. Wentao Yao (Department of Mechanical Engineering, MTU) contributed for the synthesis of α-MnO$_2$ nanowires.

Chapter 6 systematically discusses the effect of large cations (K$^+$ in this work) inside 2×2 tunnels on the electrochemical performance of α-MnO$_2$ as lithium ion battery

cathode. Mr. Yifei Yuan designed and conducted this work under direction of Dr. Jun Lu and Dr. Reza Yassar. Dr. Chun Zhan (Argonne National Laboratory) and Miss Kun He (University of Illinois at Chicago) collaborated to help the experiments. Dr. Saiful Islam contributed for the DFT calculation of α-MnO$_2$ electronic structure. Mr. Wentao Yao contributed for the synthesis of α-MnO$_2$ nanowires.

Chapter 7 explores the oriented attachment (OA) growth mechanism of α-MnO$_2$ nanowires during the hydrothermal synthesis process. Mr. Yifei Yuan designed and carried out this project under direction of Dr. Anmin Nie, Dr. Jun Lu and Dr. Reza Yassar. Mr. Wentao Yao contributed for the controlled synthesis of all the α-MnO$_2$ nanowires. Dr. Saiful Islam helped to conduct the DFT calculation of the energies of various α-MnO$_2$ facets.

Acknowledgements

am and whenever I have troubles. Their ever lasting support and encouragement have never changed since my childhood.

Yifei Yuan,
Michigan Technological University, July, 2016.

Abstract

Alpha (α-) MnO_2 is a well know transitional metal oxide possessing one dimensional 2×2 (4.6 × 4.6 $Å^2$) tunnels for accommodation of various ions. Such a characteristic tunneled structure has enabled the wide applications of α-MnO_2 in the fields of ion exchange, molecular sieves, biosensor, catalysis and energy storage. This PhD dissertation focuses on the dynamic study of ion transport functionality of α-MnO_2 at atomic level using an aberration corrected scanning transmission electron microscopy equipped with a special holder with a scanning tunneling microscopy probe.

The wide application of *in situ* TEM studying the dynamic behaviors/reactions in rechargeable lithium ion battery is first reviewed. Li^+-tunnel interaction during lithiation of a single α-MnO_2 nanowire was then systematically studied *in situ* at sub-Å resolution. An asynchronous tunnel expansion was for the first time captured with an ordered Jahn-Teller distortion theory proposed and confirmed further by DFT. Reversible Na^+ insertion in the 2×2 tunnels of α-MnO_2 is also explored and the tunneled structure is found to be less stable during sodiation than lithiation, which is explained by the larger Na^+ ionic size and thus stronger Na^+-tunnel interaction. The effect of large cations (K^+) occupying the center of 2×2 tunnels on the electrochemical performance of α-MnO_2 as a LIB cathode is systematically studied by controlling K^+ concentration. It is found that the presence of K^+ improves both the electronic conductivity and Li^+ diffusivity of α-MnO_2 nanowires, leading to superior discharge rate performance compared to the ones without K^+ presence. The last project explores the oriented attachment (OA) growth mechanism of α-MnO_2 in aqueous solution. The atomistic formation mechanism of the OA interface is demonstrated based on sub-Å analysis of the edge structures of related planes of α-MnO_2. The tunnel-based nature of OA interface is evidenced by direct atomic imaging. The role of surface atomic arrangement at single-tunnel level in directing the self assembly of α-MnO_2 nanowires is clearly illustrated with strong DFT theory support.

Chapter 1. Introduction

1.1. MnO₂ polymorphs, structure, synthesis and application

Manganese oxide (MnO_2) has been used as an important mineral for tens of centuries in human history due to the abundance of Mn and O in soils and deep sea sediments and the ubiquitous existence of MnO_2.[1] The polymorphic property of MnO_2 enables the wide applications ranging from pigment,[2] catalysis,[3] molecular sieve[4] and battery electrode[5]. These polymorphs are built based on the [MnO_6] octahedral units, as shown in Figure 1.1a. There are various ways by which these units are interconnected by sharing their edges and corners, leading to the formation of various MnO_2 phases. These polymorphs include layered phase (δ-MnO_2) and A×B tunneled phase, where A and B stand for the number of [MnO_6] units constructing the tunnel wall. The size variation among the tunnels further divides them into 3×3 tunnels (todorokite), 2×2 tunnels (α-MnO_2), 1×1 tunnel (β-MnO_2) and 1×2 tunnels (γ-MnO_2). Figure 1.1 illustrates several common MnO_2 polymorphs and their mineral names.[6]
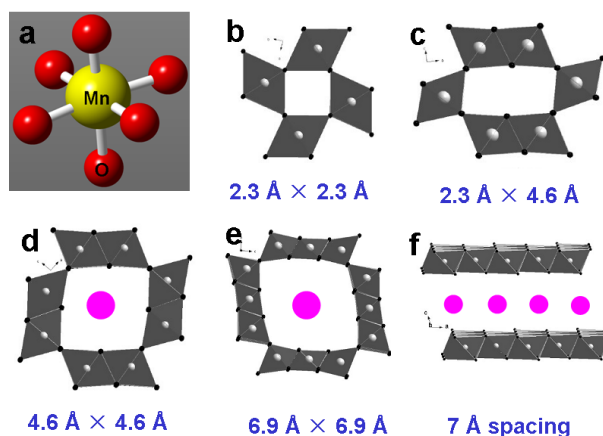
Figure 1.1. Crystallographic structures of MnO_2: the atomic model for [MnO_6] structural unit (a), β-MnO_2 (1×1 tunnel, pyrolusite) (b), γ-MnO_2 (1×2 tunnel, ramsdellite) (c), α-MnO_2 (2×2 tunnel, cryptomelane or hollandite) (d), 3×3 tunneled todorokite (e), δ-MnO_2 (layered, birnessite) (f). The tunnel size for each phase is shown under the image. The pink spheres indicate the presence of cations inside the tunnels and between layers.[6]

Among all the polymorphs, α-MnO$_2$ featuring 2×2 tunnels (4.6 Å × 4.6 Å) is mostly studied due to its proper tunnel size to accommodate different ions, such as Ag$^+$, Ba^{2+}, Cu^{2+}, K$^+$, Rb^{2+}.[7] Smaller cations such as Li$^+$, Na$^+$, Mg^{2+} can also be reversibly inserted into and extracted out of the 2×2 tunnels,[8,9] making α-MnO$_2$ a good candidate for rechargeable supercapacitor and battery electrode when its particle size goes to nanoscale. α-MnO$_2$ nanostructures are dominantly synthesized using the hydrothermal method in an aqueous solution environment, where MnO$_4^-$ and Mn^{2+} redox couples are mixed and heated to 120-180 °C in a sealed autoclave.[10] The formation of 2×2 tunnels in solution requires the presence of big cations such as Ba^{2+}, K$^+$ and Ag$^+$, which support the 2×2 tunnels and prevent them from collapse during synthesis. These cations will then stay in the as-formed tunnels and can thus affect the property and performance of MnO$_2$ as battery electrode by modifying its electronic structure, crystallographic structure and morphology. Based on the cation species in the tunnels, α-MnO$_2$ mineral is further named as cryptomelane (α-K$_x$MnO$_2$) and hollandite (α-Ba$_x$MnO$_2$).

In spite of the clear definition of different MnO$_2$ structures, the practically synthesized MnO$_2$ does not always exist in a pure phase state. 3×3, 2×7, 2×4, 2×3, 2×2 tunnels were reported to coexist inside one sample by the usage of high resolution transmission electron microscopy.[11,12] As a results, lots of structural distortion and crystalline defects have been observed but received no clear explanation due to the limited characterization methods to determine the highly localized signatures.[13,14,15] The generally existing large tunnel cations with varying concentrations further make the clarification of tunneled structure difficult. It is apparent that such structural features should be clearly identified and quantified before the tunnel growth mechanism can be well understood to further achieve size control of targeted tunneled phase for specific applications.

1.2. Primary battery cells using MnO$_2$

As early as 1860s, MnO_2 was used as the electrode in Leclanche wet cell and it has been widely commercialized as a cathode material in primary alkaline batteries for one and half centuries due to its low cost and abundance.[5],[16] The typical commercialized alkaline battery is zinc-manganese system (1.5 V) consisting of electrolytic MnO_2 cathode, aqueous electrolyte (KOH), and Zn powder anode, as shown in Figure 1.2a and b.[17] Such a primary battery type offers an energy density as high as 150 Wh/kg,[18] and has dominated the primary battery market over one century. Till now, however, the detailed working mechanism for this primary battery is not clear. While the typical Zn^{2+} intercalation mechanism has been reported in this system,[19],[20] a competing conversion reaction accompanied with phase transition is also demonstrated.[21],[16] Due to the light weight of Li metal and its strong negative potential, primary 3 V Li-MnO_2 batteries have also been commercialized since 1970s to meet various applications demanding high energy density over 220 Wh/kg. A nonaqueous electrolyte (lithium salts dissolved in organic solutions) is thus required to work safely with the metallic Li anode. In addition, the MnO_2 cathode must go through high temperature pretreatment to remove any residual water before the battery reaction happens.[22] A typical commercialized Li/MnO_2 coin cell is shown in Figure 1.2c with the discharge reactions shown in Figure 1.2d, where Li^+ intercalation into tunneled MnO_2 is believed to be the dominant mechanism. Figure 1.2e compares the development of various primary batteries over the past century, where Zn-MnO_2 and Li-MnO_2 systems are listed.[18] Figure 1.2 f and g compares the first discharge curves for Zn-MnO_2 (f) and Li-MnO_2 (g) among various MnO_2 polymorphs, where Zn-MnO_2 system shows an averaged discharge voltage around 1.3 V and Li-MnO_2 system exhibits a much higher value about 3 V.[23]
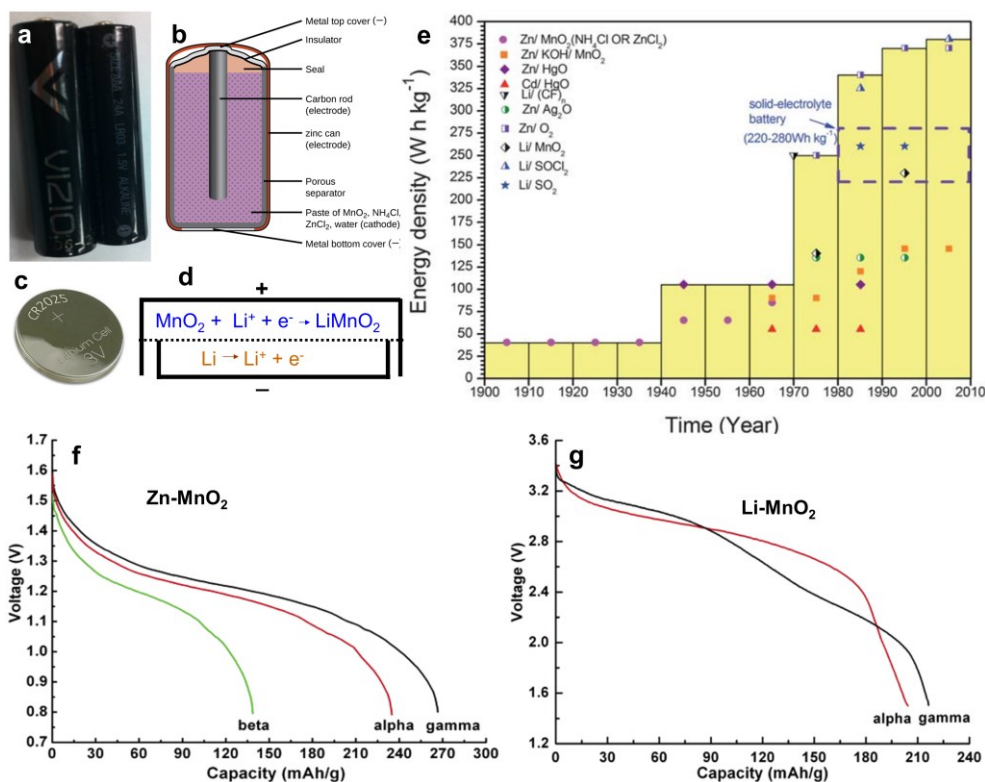
Figure 1.2. (a, b) Picture and schematic showing a commercialized 1.5 V Zn-MnO₂ alkaline battery and the inside components.[17] (c, d) Picture and schematic showing a commercialized 3 V Li/MnO₂ primary battery and inside components. (e) History of development of primary batteries in view of energy density.[18] (f, g) Comparison of the first discharge curves for Zn-MnO₂ (f) and Li-MnO₂ (g) among various MnO₂ polymorphs.[23]

1.3. Rechargeable lithium ion batteries using α-MnO₂ electrode

The fast development of rechargeable lithium ion battery (LIB) and its wide application in portable electronic devices, electric vehicles and electrical grids demand a cost-effective mass production starting form the raw materials supply. Current commercialized LIB mostly uses layered $LiCoO_2$ (or olivine $LiFePO_4$) as the cathode and graphite as the anode, and the working mechanism is shown in Figure 1.3 with the corresponding reactions expressed in Equation (1.1-1.3):[24]

14

(1.1) $Li_{1-x}CoO_2 + xLi^+ + xe^- = LiCoO_2$, for cathode reaction

(1.2) $LiC_6 = Li_{1-x}C_6 + xLi^+ + xe^-$, for anode reaction

(1.3) $LiC_6 + Li_{1-x}CoO_2 = Li_{1-x}C_6 + LiCoO_2$, for the full cell reaction
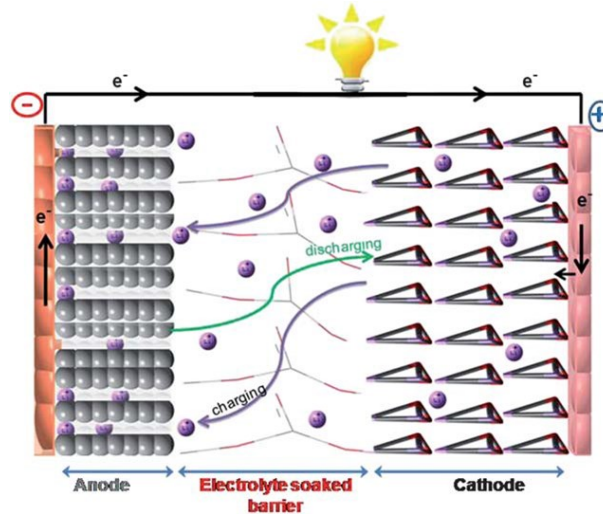
Figure 1.3. Schematic showing how a lithium ion battery is charged and discharged. During charge, Li^+ form the cathode side are extracted out and transported into the layered anode through the electrolyte. In discharge, Li^+ stored inside the anode are released and transported into the cathode side, and the electrons are conducted from the out side circuit to power devices.[24]

α-MnO_2, with the characteristic 2×2 tunnels suitable for reversible Li^+ intercalation, has been the research focus in the battery community for two decades. Research towards its application as a rechargeable lithium ion battery electrode was initiated in 1990s, when Rossouw and Thackeray demonstrated the reversible Li^+ insertion in α-MnO_2 with a discharge capacity higher than 180 mAh/g.[25] This value is much better than commercialized olivine $LiFePO_4$ (160 mAh/g), $LiCoO_2$ (160 mAh/g), and the widely studied spinel $LiMn_2O_4$ (120 mAh/g).[25,18,26] Table 1.1 and Figure 1.4 give the comparison among Li_xCoO_2, Li_xFePO_4, α-Li_xMnO_2 and spinel (s-) $Li_xMn_2O_4$ as rechargeable lithium ion battery cathodes.[5] It shows that the 3 V α-MnO_2 cathode, although possessing a lower potential *vs* Li, offers both highest theoretical and practical capacities. The theoretical energy density of α-Li_xMnO_2 is also much higher than the values of Li_xFePO_4 and spinel $Li_xMn_2O_4$, and comparable to that of $LiCoO_2$.

15

However, Co has very limited abundance in earth crust (0.001% wt), while the source for Mn is rich (0.1% wt). The real time price (on June 1st 2016) for 1 kg Mn metal is about 2.00 USD, while it is 23.7 USD for 1 kg Co of the same purity.[27] It has been estimated that the raw material cost to synthesize MnO_2 is about 1% the cost of Co raw materials.[5] In addition, Co-based cathode materials offer poor over charge stability and environmental compatibility, whereas Mn-based oxide are stable upon charge and are also environmentally friendly.[5] As such, there has been a long lasting driving force to explore the practical application of MnO_2 in rechargeable lithium ion batteries.

Table 1.1. Comparison among Li_xCoO_2, Li_xFePO_4, α-Li_xMnO_2 and spinel s-$Li_xMn_2O_4$ as rechargeable lithium ion battery cathodes. The definition of electrode utilization is to describe how much percentage of the theoretical capacity is achieved practically during battery cycling.

Intercalation electrode	Calculated discharge voltage (V)	X range	Theoretical capacity (mAh/g)	Theoretical Energy density (Wh/kg)	Practical capacity (mAh/g)	Electrode utilization %
Li_xCoO_2	3.70	$0 \leqq x \geqq 1$	274	1013	140-160	58
Li_xFePO_4	3.45	$0 \leqq x \geqq 1$	170	586	110-160	94
s-$Li_xMn_2O_4$	4.00	$0 \leqq x \geqq 1$	148	592	110-120	81
α-Li_xMnO_2	3.40	$0 \leqq x \geqq 1$	308	970	160-180	58

One can also note from Table 1.1 and Figure 1.4 that α-MnO_2 exhibits low electrode utilization upon cycling, which is less than 60% of the theoretical capacity and decays much faster with the increase of cycling numbers.[5] It is generally believed that, as an intercalation electrode, the electrode utilization of α-MnO_2 highly depends on the interaction between inserted Li^+ and the 2×2 tunnels to host Li^+, and that it is the tunnel instability that results in the low electrode utilization. Extensive studies have focused on characterization of Li-tunnel interaction using variety of methods, such as XRD,[31],[32] neutron scattering,[33] TEM,[34] and DFT simulation[8]. It gradually turns out that the Li^+ insertion in tunneled a α-MnO_2 is not a simple one-step intercalation, but a complicated multistep Li-tunnel interaction, as evidenced in Figure 1.5 showing the potential profile, CV scan as well as *in situ* XRD analysis for the first

discharge/charge cycle.[25],[32] It can be seen form Figure 1.5a and b that Li^+ insertion/extraction into 2×2 tunnels is featured by two-stage reactions rather than a simple single-stage insertion/extraction.[25] The *in situ* XRD analysis even observed excessive line broadening and a diffuse splitting of the diffraction peaks ((110) and (200)), which were attributed to a Jahn-Teller-induced phase change that was unknown by then.[32]
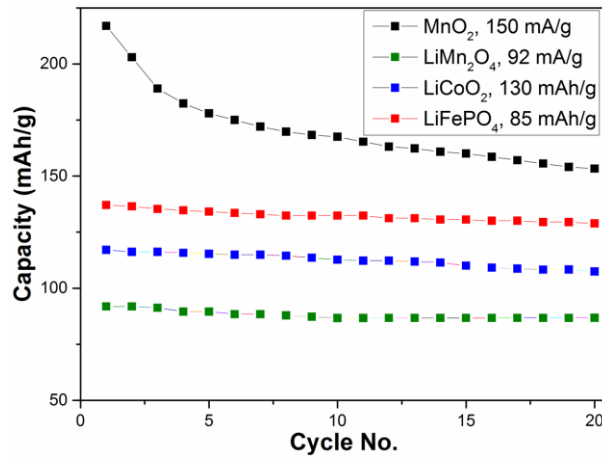
Figure 1.4. Comparison of cycling performance of various cathode materials for rechargeable lithium ion battery. Commercialized $LiCoO_2$[28] and $LeFePO_4$,[29] and widely studied olivine $LiMn_2O_4$[30] are compared to the targeted MnO_2 cathode.[23]
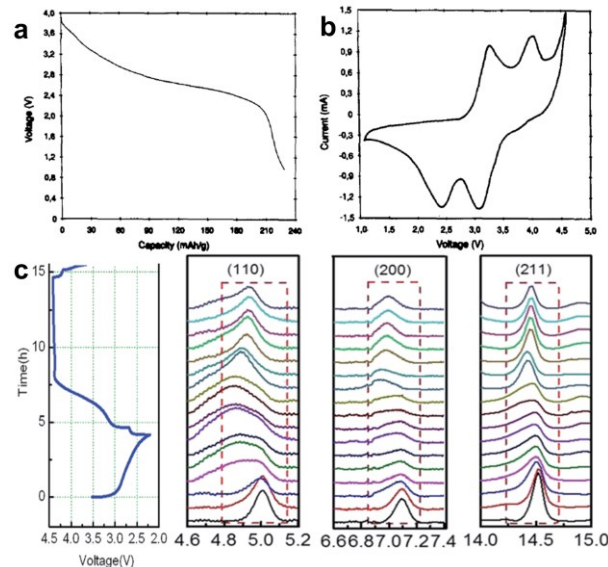
Figure 1.5. (a) CV scanning curve of a Li/ α-MnO_2 cell (scan rate = 1 mV/s). (b) The initial discharge curve of a Li/α-MnO_2 cell at a current rate of 0.2 mA/cm^2.[25] (c) In

17

situ XRD patterns of a Li/ α-MnO$_2$ cell during the first discharge/charge. The time resolved data show evolution of α-MnO$_2$-(110), (200) and (211) peaks during cycling. A reversible (110)- and (200)-peak splitting behavior during discharge/charge is observed, indicting the existence of reversible phase transitions.

Currently, it is accepted that the Jahn-Teller distortion of [MnO$_6$] octahedral during the reduction of Mn^{4+} to Mn^{3+} is the main reason for the resulted tunnel instability upon Li$^+$ insertion.[35] Figure 1.6 clearly illustrates Jahn-Teller distortion when [Mn^{4+}O$_6$] is reduced to [Mn^{3+}O$_6$].[36] Yet, details are still missing such as how does Jahn-Teller distortion proceed during Li$^+$ insertion? Also, how does the tunnel lattice respond at the unit cell level? And how does the macroscopic structural distortion happen during Li$^+$ intercalation.
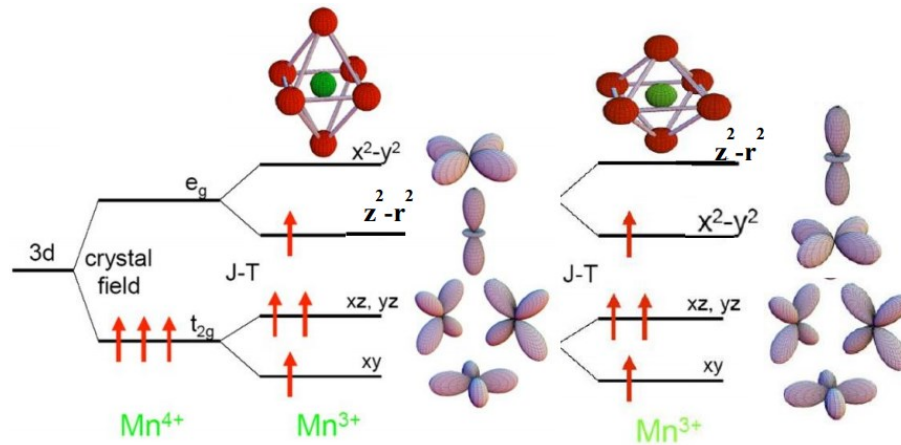
Figure 1.6. Schematic showing the electron distribution on [Mn^{4+}O$_6$] and [Mn^{3+}O$_6$]. Mn^{4+} has 3 electrons on the 3d level, which are evenly distributed to the three t$_{2g}$ orbits possessing lower energy, so there is no orbit degeneracy and thus no Jahn-Teller distortion. For Mn^{3+} with 4 electrons on the 3d level, the forth electron has to occupy e$_g$ orbit, where the orbit degeneracy happens and splits into z^2 orbit and x^2-y^2 orbit. [Mn^{3+}O$_6$] will then be stretched or compressed based on whether the forth electron occupies the z^2 orbit ((t$_{2g}$)3(dz^2)1) or x^2-y^2 orbit ((t$_{2g}$)3(dx^2-y^2)1).[36]

1.4. The order of chapters

18

This dissertation is organized in a way that our findings spanning the growth mechanism of MnO_2 nanostructures and their electrochemical behavior are explained in details. Chapter 2 discusses the key experimental methods for this PhD project. Specifically, the details of hydrothermal synthesis of α-MnO_2 nanostructures are provided together with the necessary morphology and phase analysis techniques such as X-ray diffraction (XRD) and scanning electron microscopy (SEM). *Ex situ* analytical (scanning) transmission electron microscopy (S)TEM for the atomic resolution analysis of the tunneled structure is also introduced together with the (S)TEM sample preparation methods. The *in situ* TEM setup to obtain the battery cycling process of a single MnO_2 nanowire is also explained in details. The coin cell level battery testing of MnO_2 cathode is described in terms of the lamination operation, coin cell assembly, galvanostatic (potentiostatic) (dis)charge and *in situ* synchrotron XRD and X-ray absorption near edge spectroscopy (XANES) procedures.

Chapter 3 provides a critical review on the application of *in situ* TEM technique in solving rechargeable battery problems. Real time observation of material behaviors using *in situ* TEM has been developed for decades, while its application exploring rechargeable lithium ion battery is relative new. Still, there have been more than 100 *in situ* TEM articles reporting interesting findings regarding the working process of rechargeable LIBs. As such, our fundamental understanding of (dis)charge mechanisms is greatly deepened.

Chapter 4 covers *in situ* (S)TEM to study the dynamic lithiation process in single α-MnO_2 nanowire. The aberration corrected (S)TEM enables us to observe the tunnel evolution during Li^+ insertion at atomic resolution, and to establish the relationships among the tunnel dimension, the compositional change and the electronic structure evolution. An ordered Jahn-Teller distortion of [MnO_6] octahedral is confirmed for the first time by both experiments and simulations. The resulted asynchronous unit cell expansion well explains the commonly observed low electrode utilization of α-

MnO$_2$ as LIB cathode, casting light on rational design of the electrode structures to improve the battery performance.

Chapter 5 describes our study on the reversible (de)sodiation process in single MnO$_2$ nanowire and compare the sodiation with lithiation in the same nanostructured MnO$_2$. Due to the difference in ionic diameters and electronegativities, Na$^+$ insertion in the tunnels exhibits sharply difference against Li$^+$ insertion in terms of Na$^+$ (Li$^+$)-K$^+$ interaction, tunnel stability and phase transition. An efficient discharge voltage control was shown to well maintain the tunneled structure during reversible Na$^+$ insertion. This work could guide future work focusing on improving the cycling performance of tunneled MnO$_2$ as sodium on battery cathode.

Chapter 6 systematically discusses the effect of K$^+$ concentrations inside 2×2 tunnels on the electrochemical performance of α-MnO$_2$ as LIB cathode. The concentration of K$^+$ in the tunnels is quantitatively controlled, and the resulted Li$^+$ diffusivity, electronic conductivity and the rate performance of Li/MnO$_2$ coin cells are compared at each K$^+$ concentration. This work comes to the conclusion that the presence of K$^+$ is favorable for both Li$^+$ and e$^-$ conductivity in the tunnels, and it also leads to improved battery performance compared to the ones without K$^+$ in the tunnels.

Chapter 7 explores the oriented attachment (OA) growth mechanism of α-MnO$_2$ nanowires during the hydrothermal synthesis process. The as-formed OA interfaces are further studied focusing on illustrating the interface atomic structure and the formation process of such interface. The atomic nature of the OA interface is clearly demonstrated with the detailed formation mechanism well understood at single tunnel level. This work is hoped to direct future synthesis work capable of controlled nanostructure engineering, especially for the synthesis of tunnel-based nanomaterials.

1.5. References

1. Post JE. Manganese oxide minerals: Crystal structures and economic and environmental significance. *Proceedings of the National Academy of Sciences* **96**, 3447-3454 (1999).

2. Beck L*, et al.* First use of portable system coupling X-ray diffraction and X-ray fluorescence for in-situ analysis of prehistoric rock art. *Talanta* **129**, 459-464 (2014).

3. Gorlin Y*, et al.* In situ X-ray absorption spectroscopy investigation of a bifunctional manganese oxide catalyst with high activity for electrochemical water oxidation and oxygen reduction. *Journal of the American Chemical Society* **135**, 8525-8534 (2013).

4. Yamaguchi K, Kobayashi H, Wang Y, Oishi T, Ogasawara Y, Mizuno N. Green oxidative synthesis of primary amides from primary alcohols or aldehydes catalyzed by a cryptomelane-type manganese oxide-based octahedral molecular sieve, OMS-2. *Catalysis Science & Technology* **3**, 318-327 (2013).

5. Johnson CS. Development and utility of manganese oxides as cathodes in lithium batteries. *Journal of Power Sources* **165**, 559-565 (2007).

6. Ghodbane O, Pascal J-L, Favier F. Microstructural effects on charge-storage properties in MnO2-based electrochemical supercapacitors. *ACS applied materials & interfaces* **1**, 1130-1139 (2009).

7. Ching S, Roark JL, Duan N, Suib SL. Sol-gel route to the tunneled manganese oxide cryptomelane. *Chemistry of Materials* **9**, 750-754 (1997).

8. Tompsett DA, Islam MS. Electrochemistry of hollandite α-MnO2: Li-ion and Na-ion insertion and Li2O incorporation. *Chemistry of Materials* **25**, 2515-2526 (2013).

9. Arthur TS*, et al.* Understanding the Electrochemical Mechanism of K-αMnO2 for Magnesium Battery Cathodes. *ACS applied materials & interfaces* **6**, 7004-7008 (2014).

10. Sui N, Duan Y, Jiao X, Chen D. Large-scale preparation and catalytic properties of one-dimensional α/β-MnO2 nanostructures. *The Journal of Physical Chemistry C* **113**, 8560-8565 (2009).

11. Turner S, Buseck PR. Manganese oxide tunnel structures and their intergrowths. *Science* **203**, 456-458 (1979).

12. Duncan M, Leroux F, Corbett J, Nazar L. Todorokite as a Li Insertion Cathode Comparison of a Large Tunnel Framework "" Structure with Its Related Layered Structures. *Journal of the Electrochemical Society* **145**, 3746-3757 (1998).

13. Shen XF, *et al.* Control of Nanometer‐Scale Tunnel Sizes of Porous Manganese Oxide Octahedral Molecular Sieve Nanomaterials. *Advanced Materials* **17**, 805-809 (2005).

14. Liu J, Makwana V, Cai J, Suib SL, Aindow M. Effects of alkali metal and ammonium cation templates on nanofibrous cryptomelane-type manganese oxide octahedral molecular sieves (OMS-2). *The Journal of Physical Chemistry B* **107**, 9185-9194 (2003).

15. Portehault D, Cassaignon S, Baudrin E, Jolivet J-P. Morphology control of cryptomelane type MnO2 nanowires by soft chemistry. Growth mechanisms in aqueous medium. *Chemistry of Materials* **19**, 5410-5417 (2007).

16. Lee B, Yoon CS, Lee HR, Chung KY, Cho BW, Oh SH. Electrochemically-induced reversible transition from the tunneled to layered polymorphs of manganese dioxide. *Scientific reports* **4**, (2014).

17. Davis. PDLaU. http://chemwiki.ucdavis.edu/ Textbook_Maps/General_ Chemistry_Textbook_Maps/Map%3A_Chemistry_(OpenSTAX)/17%3A_ Electrochemistry/17.5%3A_Batteries_and_Fuel_Cells. (This image is licensed under a Creative Commons Attribution-Noncommercial-Share Alike 3.0 United States License.).

18. Zu C-X, Li H. Thermodynamic analysis on energy densities of batteries. *Energy & Environmental Science* **4**, 2614-2624 (2011).

19. Alfaruqi MH, *et al.* Enhanced reversible divalent zinc storage in a structurally stable α-MnO 2 nanorod electrode. *Journal of Power Sources* **288**, 320-327 (2015).

20. Lee J, Ju JB, Cho WI, Cho BW, Oh SH. Todorokite-type MnO 2 as a zinc-ion intercalating material. *Electrochimica Acta* **112**, 138-143 (2013).

21. Pan H, *et al.* Reversible aqueous zinc/manganese oxide energy storage from conversion reactions. *Nature Energy* **1**, 16039 (2016).

22. Winter M, Brodd RJ. What Are Batteries, Fuel Cells, and Supercapacitors? *Chemical Reviews* **104**, 4245-4270 (2004).

23. Cheng F*, et al.* Facile controlled synthesis of MnO2 nanostructures of novel shapes and their application in batteries. *Inorganic chemistry* **45**, 2038-2044 (2006).

24. Pitchai R, Thavasi V, Mhaisalkar SG, Ramakrishna S. Nanostructured cathode materials: a key for better performance in Li-ion batteries. *Journal of Materials Chemistry* **21**, 11040-11051 (2011).

25. Rossouw M, Liles D, Thackeray M, David W, Hull S. Alpha manganese dioxide for lithium batteries: A structural and electrochemical study. *Materials research bulletin* **27**, 221-230 (1992).

26. Dai X*, et al.* Extending the High-Voltage Capacity of LiCoO2 Cathode by Direct Coating of the Composite Electrode with Li2CO3 via Magnetron Sputtering. *The Journal of Physical Chemistry C*, (2015).

27. http://www.infomine.com/investment/metal-prices/.

28. Ludwig B, Zheng Z, Shou W, Wang Y, Pan H. Solvent-Free Manufacturing of Electrodes for Lithium-ion Batteries. *Scientific reports* **6**, (2016).

29. Chang C-C, Chen T-K, Her L-J, Fey GT-K. Tris (pentafluorophenyl) borane as an electrolyte additive to improve the high temperature cycling performance of LiFePO4 cathode. *Journal of the Electrochemical Society* **156**, A828-A832 (2009).

30. Liu Y, Tan L, Li L. Ion exchange membranes as electrolyte to improve high temperature capacity retention of LiMn 2 O 4 cathode lithium-ion batteries. *Chemical Communications* **48**, 9858-9860 (2012).

31. Pang WK, Peterson VK, Sharma N, Zhang C, Guo Z. Evidence of solid-solution reaction upon lithium insertion into cryptomelane K0. 25Mn2O4 material. *The Journal of Physical Chemistry C* **118**, 3976-3983 (2014).

32. Yang Z*, et al.* In situ high-energy synchrotron X-ray diffraction studies and first principles modeling of α-MnO 2 electrodes in Li–O 2 and Li-ion coin cells. *Journal of Materials Chemistry A* **3**, 7389-7398 (2015).

33. Kijima N, Ikeda T, Oikawa K, Izumi F, Yoshimura Y. Crystal structure of an open-tunnel oxide α-MnO 2 analyzed by Rietveld refinements and MEM-based pattern fitting. *Journal of Solid State Chemistry* **177**, 1258-1267 (2004).

34. Yuan Y*, et al.* Asynchronous Crystal Cell Expansion during Lithiation of K+-Stabilized α-MnO2. *Nano letters* **15**, 2998-3007 (2015).

35. Ling C, Mizuno F. Capture lithium in αMnO2: insights from first principles. *Chemistry of Materials* **24**, 3943-3951 (2012).

36. Tsai T. Magnetotransport properties in magnetic layer coated charge ordering manganites. *A Master Thesis, Department of Electrophysics, College of Science, National Chiao Tung University*, (2012).

Chapter 2. Experimental Methods

The experimental details are provided here for the synthesis of α-MnO$_2$ nanowires used for all the projects, the working mechanism for the ACSTEM towards atomic level analysis of the tunneled MnO$_2$ structure, and the in situ TEM and in situ synchrotron X-ray scattering techniques for real time study at single-particle level and bulk level, respectively.

2.1. MnO$_2$ nanowires synthesis

α-MnO$_2$ nanowires were synthesized hydrothermally using KMnO$_4$ and MnSO$_4$ as reactants in aqueous solution.[1] Specifically, 0.9878 g of KMnO$_4$ and 0.4226 g of MnSO$_4$•H$_2$O were dispersed in 80 mL of deionized (DI) water under constant stir for 30 min to form a purple solution. The obtained slurry was then transferred to a 100 mL Teflon-lined stainless steel autoclave, sealed and heated at 160 ºC for 12 h. The synthesized nanowires were first separated from the solution by centrifugation, then washed with deionized (DI) water and ethyl alcohol, and finally dried in air at 60 ºC for 12 h. During the synthesis process, K$^+$ doped the initially formed 2×2 tunnels and remained trapped inside the tunneled structure.

2.2. *Ex situ* structural and compositional analyses

The *ex situ* atomic resolution imaging of the tunneled was done in an aberration corrected scanning transmission electron microscopy (ACSTEM), JEOL JEM-ARM200CF, equipped with a 200 KV cold emission source. The images are formed by scanning the ultra small electron probe across the sample surface and collecting the elastically scattered signal below the sample using a high angle annular dark field (HAADF) detector. The HAADF contrast is sensitive to the atomic number (Z) of the detected elements and the heavier the atom is, the more the electrons will be scattered toward high angles. Atomic images were mostly acquired using a 22 mrad probe convergence angle and a 90 mrad inner-detector angle. This process is illustrated in

Figure 2.1. The elemental information and electronic structure of α-MnO$_2$ nanowires were recorded on an Oxford X-max 80 SDD windowless X-ray detector and a postcolumn Gatan Enfina EELS spectrometer with a 45 mrad collection angle.

For the direct imaging of the tunneled structure of α-MnO$_2$ nanowires, ultramicrotome was utilized to cut the nanowires into slices within electron-transparent thickness. For the cross section slices preparation, the nanowires are first fixed using Epofix embedding resin and Epofix hardener mixture; the sample is then placed under an Edge Craft^{TM} diamond knife mounted in Ultramicrotome (Leica UCT) and is cut to slices, as shown in Figure 2.2. The slices are directly moved to copper grid and dried at 50 ºC for 24 hours before TEM characterization.
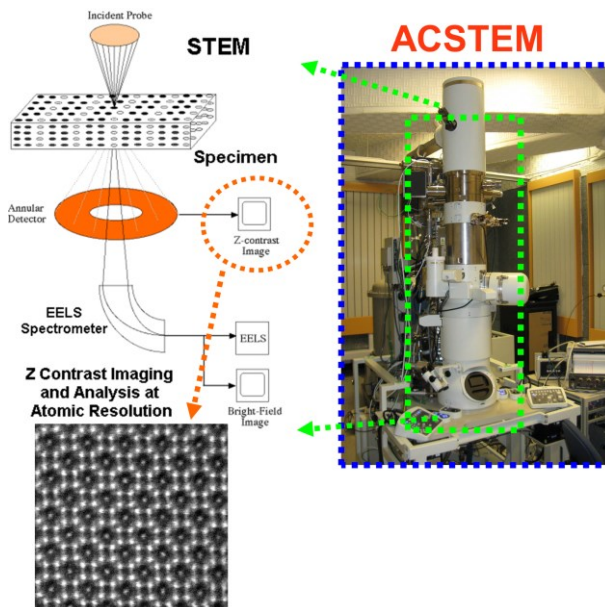
Figure 2.1. Schematic (left) showing the working mechanism of STEM with HAADF detector forming the Z-contrast images of α-MnO$_2$ tunneled structure using the elastically scattered electrons below the sample. The directly transmitted beam can be further deflected by a curved electron energy loss spectrometer (EELS) and reach the detector recording the inelastic energy loss of the electrons. The right picture shows a JEOL JEM-ARM200CF.
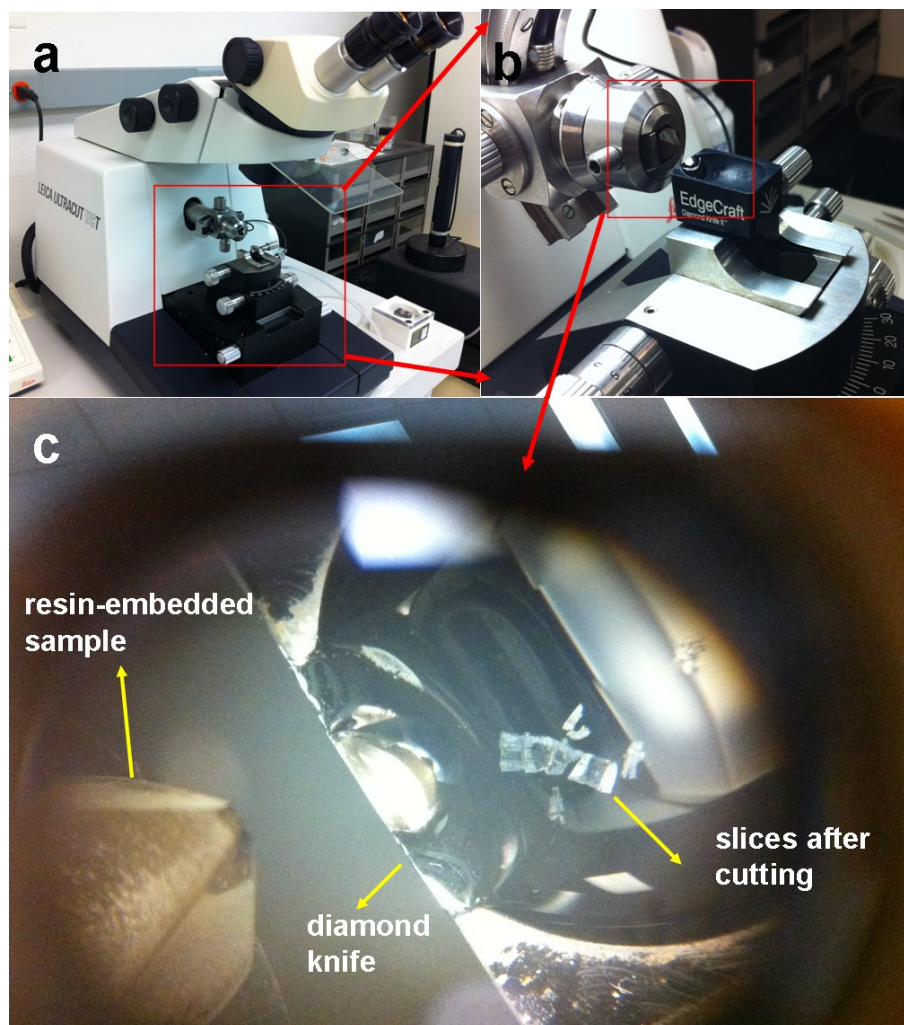
Figure 2.2. (a-b) Pictures showing the ultramicrotome setups for cutting α-MnO$_2$ nanowires into slices. (c) Enlarged optical picture showing the sample being cut into slices.

2.3. *In situ* techniques (TEM, XRD, XANES) for MnO$_2$-based battery

To construct a working lithium ion battery inside TEM chamber, a specially designed TEM holder capable of biasing was applied for the in situ lithiation and sodiation study in single α-MnO$_2$ nanowire. This "open cell" design is explained in Figure 2.3. The holder has two separated metallic rods near the sample imaging area with one rod fixed and the other movable. To build the battery, single α-MnO$_2$ nanowire is first

attached by conductive epoxy to the fixed rod tip to be the working electrode, and Li (Na) metal is attached to the other rod tip and functions as the counter electrode. This step is finished inside a glove box filled with Ar. Transportation of the holder from glove box to TEM will result in a naturally grown Li_2O (Na_2O) layer on the surface of Li (Na) metal, and this layer can function as a solid-state electrolyte to facilitate the diffusion of Li^+ and prevent e^- conduction. Inside the TEM chamber, the movable rod with Li/Li_2O (Na/Na_2O) in its tip is piezoelectric controlled to connect to the working electrode (the nanowire). After the connection, the reversible ion insertion/extraction is achieved *via* a alternating the applied bias between -3 to 3 V. The evolution of nanowire morphology, phase and electronic structure during ion insertion/extraction is dynamically recorded.
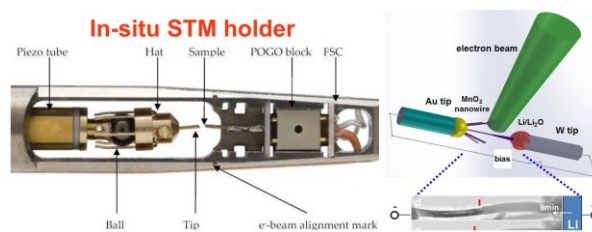
Figure 2.3. (Left): Picture of the in situ STM holder. (Right): Schematic showing the configuration of an "open cell" based on single α-MnO_2 nanowire inside TEM chamber, where the bottom TEM images shows the nanowire being partially lithiated from the right side to the left side.

To compensate for the single nanowire-level in situ TEM characterization, coin cell level battery in situ testing was also done using synchrotron X-ray scattering. The coin cell assembly and in situ testing setup are shown in Figure 2.4.[2] In-situ Synchrotron XRD (λ=0.118 Å) was performed at Beamline 11-ID-C located in Advanced Photon Sources of Argonne National Laboratory. The tested coin cell was assembled using pre-punctured spacer and electrode caps for better X-ray penetration.
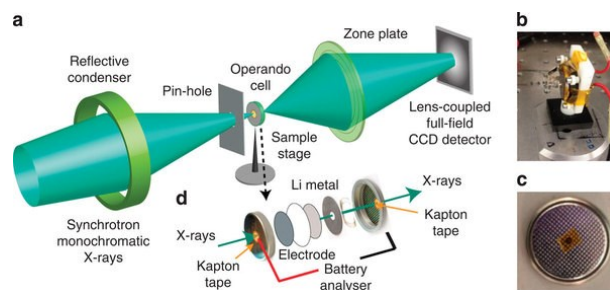
Figure 2.4. (a) Schematic showing the experimental setup for in situ synchrotron XRD of w working coin cell made of Li/α-MnO$_2$ electrodes. (b) The specially designed cell holder and (c) a perforated coin cell for sufficient X-ray transmission. (d) Schematic showing the components of a realistic battery.[2]

2.4. References

1. Santhanagopalan S, Balram A, Meng DD. Scalable High-Power Redox Capacitors with Aligned Nanoforests of Crystalline MnO2 Nanorods by High Voltage Electrophoretic Deposition. *ACS nano* **7**, 2114-2125 (2013).
2. Li L, *et al.* Visualization of electrochemically driven solid-state phase transformations using operando hard X-ray spectro-imaging. *Nature communications* **6**, (2015).

Chapter 3. Understanding Materials Challenges for Rechargeable ion Batteries and new Chemistries using *in situ* TEM: A Review[①]

3.1. Introduction and background

Current rechargeable ion batteries face various problems that prevent them from extensive and intensive applications in both industry and our daily life. These problems exist in battery electrodes, electrolytes, and solid electrolyte interfaces (SEI), and can not be easily detected due to the required sealed working environment. Real-time high resolution transmission electron microscopy techniques are emerging as powerful tool in revealing the underlying mechanisms responsible for the failure of rechargeable ion batteries such as gradual capacity fading during cycling, poor power supply at low temperatures, thermal runaway and overcharge instability.[1] Figure 3.1 illustrates a working rechargeable ion battery (centered schematic) where the most significant issues/problems existing in the anode, the cathode and the electrolyte are indicated. For each specific problem/issue, a proper TEM technique has been developed for real time study, as shown in each branched schematic in Figure 3.1.

Table 3.1 summarizes battery materials/behaviors that have been analyzed using in situ TEM. We have divided these materials based on the related discoveries in terms of new electrode designs, electrolyte issues, and new battery chemistries. Finally, we will discuss the side effect of electron beam on the observed electrochemistry results, and to which extent the nanoscale discoveries by *in situ* TEM can be applied to real battery electrochemistry at bulk level. A contrast between this review and the previous reviews on *in situ* TEM[2,3,4] is that the focus here is on the critical problems/issues in modern lithium ion batteries. The *in situ* TEM work on

---

[①] The material contained in this chapter is in preparation for submission to *Nature Communications*.

rechargeable batteries beyond lithium ions is also reviewed and compared with that of lithium ion batteries.
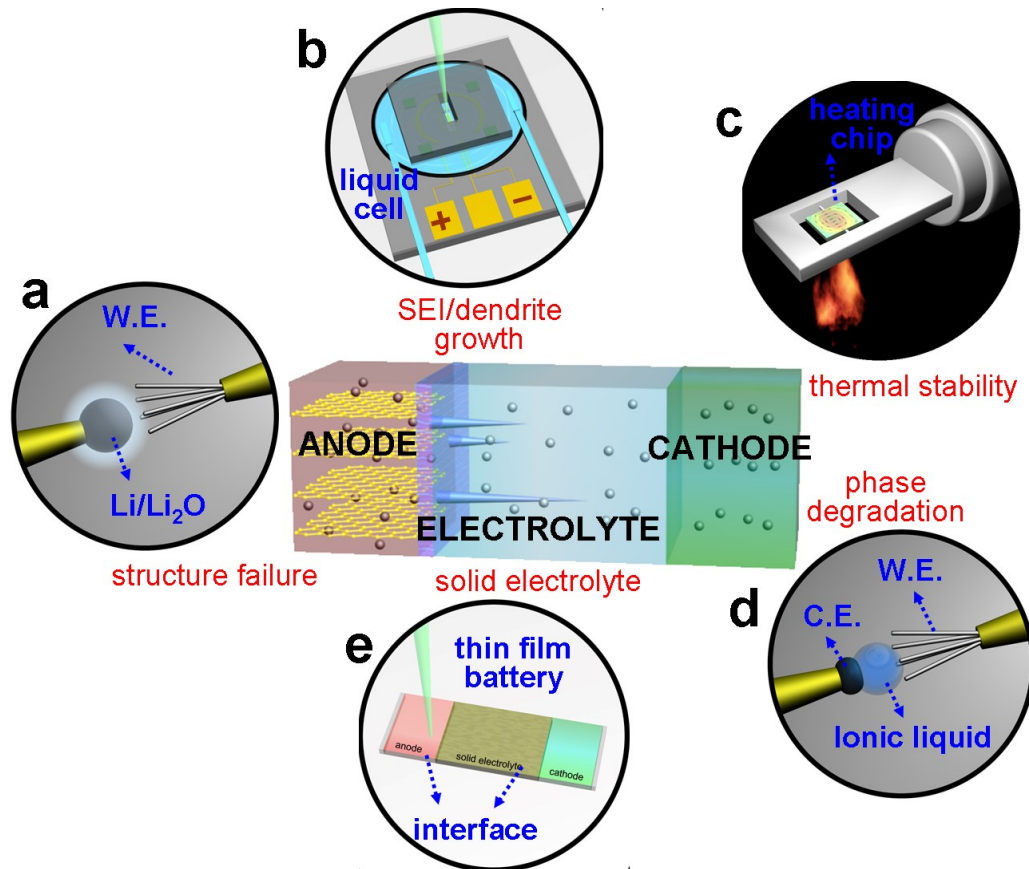
Figure 3.1 Schematic of the existing critical problems/issues in a lithium ion battery and the corresponding in situ TEM technique to study each problem/issue. (a) Solid state open cell design in vacuum for dynamic study of the structure failure in a working electrode with high spatial resolution. This design utilizes a STM TEM holder capable of biasing. Li metal (counter electrode) covered by a thin Li_2O layer (solid electrolyte) is attached to one circuit terminate, while the target material (working electrode) is attached to the other terminate. By piezoelectric manipulation in nanoscale, the target electrode is connected to Li/Li_2O, and the (de)lithiation process can then be controlled by alternating the bias. (b) Sealed electrochemical liquid cell design for dynamic TEM study of SEI formation and Li (de)plating in a real liquid electrolyte environment. Such a cell is fabricated based on two Si chips with an O-ring for the sealing. The liquid thickness is controlled by the spacer size,

which is usually in tens of nanometers to several microns. Each electrode is built on the surface of the bottom chip with its working area emmersed in the liquid chamber. SixNy windows are used near the working area to ensure good electron transparence. (c) In situ heating stage inside TEM chamber for study of thermal stability of Mn-, Co-, Ni-based cathode materials. The Joule heating circuit is built around the sample area to heat the sample to set temperature. (d) Open cell design based on ionic liquid which possesses extremely low vapor pressure[5] and good fluidity ensuring the interface wetting between the electrode and the liquid electrolyte. Compared to the solid state open cell in (a), this design enables the achievement of a full battery setup instead of a half cell inside the TEM chamber, while the spatial resolution is comparable to that of the design in (a). (e) The open cell design for the dynamic study of the interfaces in a solid state battery. The battery is thinned down (typically by FIB) to tens of nanometers for good electron transmission. To cycle the battery in TEM, the thin film device is welded to one circuit terminate of a biasing holder from either the cathode or anode side, and the other side can be connected to the circuit by piezoelectric control.

Table 3.1. Categorized problems/issues associated with lithium ion batteries that have been studied by in situ TEM

In situ TEM of rechargeable ion batteries								
Lithium Ion Battery								Beyond Li$^+$
Electrode						Electrolyte		
Thermal Stability	Charge Storage Mechanism			Structural Engineering		Liquid	Solid	Li-O$_2$[6,7]
	Intercalate	Alloy	Conversion	A+B				Li-S[8,9]
NCA[24]	α-MnO$_2$[37]	Si[47-56]	MnO$_2$[37,46] RuO$_2$[63]	Si-C[76-79]		SEI[27-30]	LATSPO[34]	Na/FeF$_2$[10]
NMC[25]			CuO[64]				LiPON[35,36]	Na/MnO$_2$[11]
LFP[26]	LFP[38-40]	Sn[57]	Fe$_2$O$_3$[65]	Si-ZnO[80]		Li Plating[2,7,30-33]		Na/CuO[12]
			SnO$_2$[66,67]					Na/NiO[13]
	LiMn$_2$O$_4$[41,42]	Ge[58,59]	FeF$_2$[68]	CoS$_2$-C[71]				Na/SnO$_2$[14]
		Al[60]	MoS$_2$[69] ZnO[61]		Defects[6,7,83]			Na/Zn$_4$Sb$_3$[15]
	Carbon[43,44]	Zn[61]	Co$_3$O$_4$[70] CoS$_2$[71]	NiO-C[75]				Na/Co$_9$S$_8$[16]
	TiO$_2$[45,46]	Ga[62]	MnFe$_2$O$_4$[72]					Na/Sn[17]
			Fe$_3$O$_4$[73]	Si-Sn[81]				Na/CNF[18]
			CeO$_2$[74]					Na/P[19,20]
			WO$_3$[22]	Ge-Si[82]				Na/Sb[21]
			NiO[13,75]					Na/WO$_3$[22]
								Ca/WO$_3$[22]
								Mg/Co$_3$O$_4$[23]

Note of Table 3.1. NCA stands for Li$_x$Ni$_{0.8}$Co$_{0.15}$Al$_{0.05}$O$_2$ cathode, NMC for Li$_x$Ni$_y$Mn$_z$Co$_{1-y-z}$O$_2$ cathode, LFP for LiFePO$_4$ cathode, LATSPO for slid state electrolyte based on Li-Al-Ti-Si-P-O. In the A+B composite expression, A stands for the core component and B stands for the shell or substrate component. CNF represents for carbon nanofibers.

3.2. Summary: research on rechargeable ion batteries using *in situ* TEM

3.2.1. Electrode

Developing advanced electrode materials such as Mn-rich cathodes and Si anodes is facing critical problems that demand in depth understanding of the electrode behavior

and effective solutions. Electrode-related scientific challenges include, but are not limited to: how cathodes experience thermal degradation and compromise battery safety; what is the charge storage mechanism for different materials; how Li dendrites nucleate and grow; how repetitive cycling leads to gradual capacity fading. *In situ* TEM work has been shown to be quite powerful in exploring the mechanisms addressing these questions.

3.2.1. 1. Thermal stability analysis

With the increasing demand for densely packed lithium ion batteries for high energy density applications, especially in EV and EG, thermal safety is most challenging because thermal failure in one battery unit will likely result in a chain reaction for large scale thermal release and even explosion.[84] Particularly, Co (Ni, Mn)-based transitional metal oxides, when at their charged states, are subject to O release into the electrolyte containing flammable organics,[85] resulting in exothermal electrolyte oxidation and even explosion. Real-time understanding of the thermal decomposition is thus the prerequisite toward the effective improvement of battery safety.

Incorporating an in situ heating stage into TEM, Hwang *et al.*[24] studied the thermal decomposition of $Li_xNi_{0.8}Co_{0.15}Al_{0.05}O_2$ (NCA) cathode material up to 450 ºC in vacuum, where a layered to rock-salt phase transition (Figure 3.2a and b) and the evolution of surface porosity associated with O release are dynamically recorded. The finding that some charged particles undergo morphological and structural change even below 100 ºC suggests the importance of thermal inhomogeneity causing the failure of cathode materials at normal operating temperatures. Using EELS to explore the surface electronic structures of $Li_xNi_yMn_zCo_{1-y-z}O_2$ (NMC) cathode upon heating, the reduction of unstable Ni^{4+} is confirmed to be the driven force for the lattice O instability, as shown in Figure 3.2c-i.[25] This indicates that although the incorporation of Ni increases the energy density,[86] it also introduces thermal instability into the cathode. By varying the x, y, z values in NMC after fully charged, the authors

optimized the composition giving the best combination of high capacity and reasonable thermal stability.
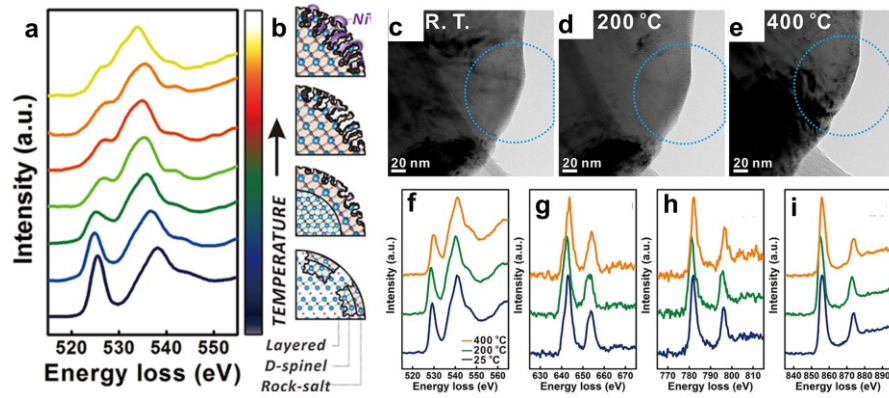
Figure 3.2. (a): Temperature dependence of oxygen K-edge EELS of one NCA particle showing the pre-edge peak of the O K-edge to move to the main peak with increasing temperature. (b): the ordered phase transitions first from layer to disordered spinel, and finally to rock-salt structures at high temperature.[24] (c, d, e) BF images from pristine NMC811 at room temperature, 200 °C, and 400 °C, respectively. (f, g, h, i) EELS of oxygen K-edge, and the Mn, Co, Ni $L_{2,3}$- edges at different temperatures. EELS and SAED patterns were acquired from the areas indicated in the TEM images.[25]

3.2.1.2. Charge storage mechanisms/kinetics/failure mechanism analysis

Li^+ (de)intercalation, Li^+ (de)alloying with single element, and conversion reaction have been widely recognized as three dominant mechanisms for energy storage in electrodes.[87] The typical intercalation electrodes possess intrinsic structures with one-, two- or three dimensional openings to facilitate Li^+ transport without any significant structural change ($LiCoO_2$ and graphite). The alloying mechanism proceeds by direct bonding between inserted Li^+ and the host element A (A for Si, Ge, Sn, *etc*.) with the formation of Li-A alloys. The conversion reaction happens when Li^+ insert into nanosized binary compounds as denoted by MX (M for Fe, Co, Cu, etc. and X for O, S, F, *etc*.), resulting in reduction of M cations to M^0 and formation of LiX. In general, the three mechanisms direct charge storage behaviors of electrode materials so differently that the resulted electrode capacity, morphology, volume and structure are

sharply distinct. *In situ* TEM technique has been extensively applied to clarify these charge storage mechanisms that determine distinct electrochemical performance of individual electrode material in terms of morphological, volumetric and structural evolution.

a. Intercalation Electrode: Phase Degradation

Ideally, an intercalation-based electrode should be structurally stable without any obvious phase transition during repetitive ion insertion. In practice, however, many reports have pointed out phase instability of these materials, especially in the cathode side, which leads to fast capacity decay with battery cycling. So it is important to understand the structural evolution during charge/discharge in real time and explore any inhomogeneous phase transition thermodynamics and kinetics. In situ TEM has been reported to track the dynamic response of various intercalation-based materials such as one dimensional α-MnO$_2$ and LiFePO$_4$ (LFP), three dimensional spinel LiMn$_2$O$_4$ and two dimensional graphite.

In the case of MnO$_2$ cathode featuring one dimensional tunneled structure, Yuan et al.[37] confirmed an asynchronous tunnel expansion across *a-b* plane that is driven by sequential Jahn-Teller distortion of [MnO$_6$] octahedral, as shown in Figure 3.3a. This asynchronous expansion damages the initial tetragonal symmetry of MnO$_2$ and the tunnel stability, intensively explaining the origins for low practical capacity of rechargeable Li/MnO$_2$ batteries. Lee *et al.*[42,41] studied the dynamic (dis)charge in single LiMn$_2$O$_4$ nanowire using the ionic liquid-based open cell design, where a cubic-tetragonal transition "fringe" region was clearly captured (Figure 3.3b). Unexpectedly, no fracture or crack is found in nanosized LiMn$_2$O$_4$, suggesting that the physical fracture and capacity fading of spinel materials caused by the notorious cubic-tetragonal transition[88] could be greatly modified *via* nanoscale engineering. Holtz *et al.*[40] studied the dynamic (de)lithiation of LFP nanoparticles in a sealed liquid cell containing aqueous electrolyte, which recovered the native working environment inside a real battery. The LFP particles immersed in liquid electrolyte

are found to experience inhomogeneous (de)lithiation based on their dynamic observation *via* a novel energy-filtered TEM technique (Figure 3.3c). This finding from real liquid electrolyte environment greatly compensates other in situ TEM reports showing either a solid solution zone (Figure 3.3d)[39] or a LFP-FP phase boundary (Figure 3.3e)[38] in partially (de)lithiated LFP. These kinetic features could reasonably account for the poor cycling performance of LFP-based cathodes during ex situ battery testing.
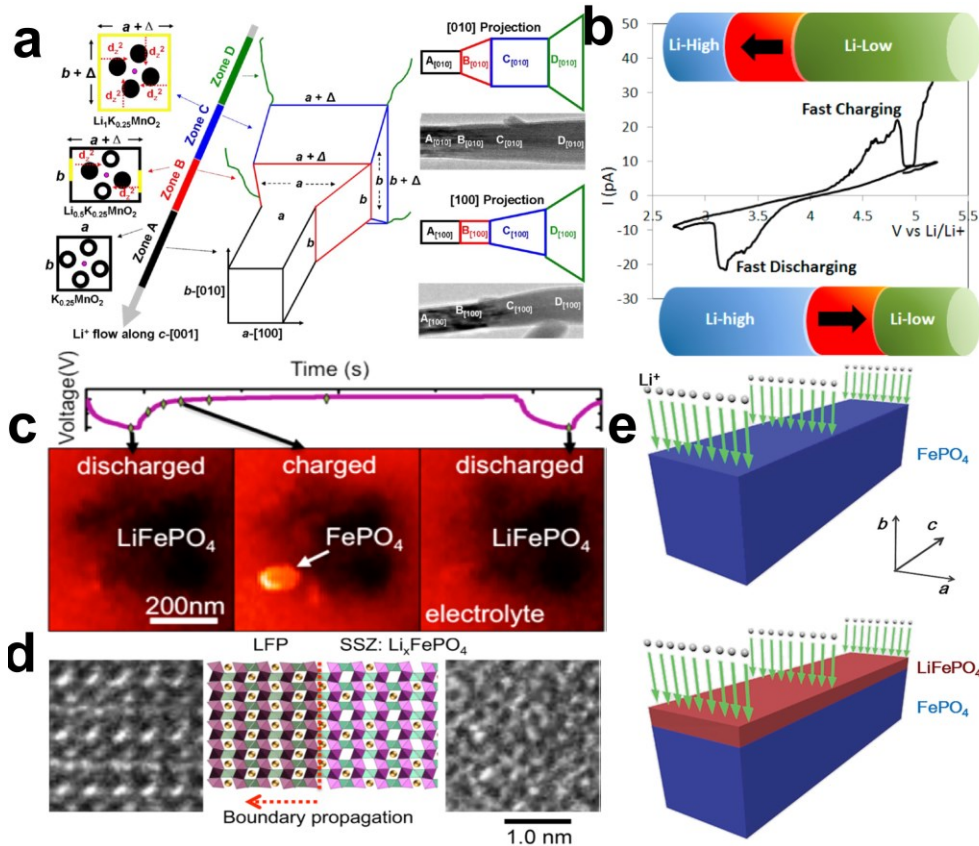
Figure 3.3 (a) Schematic showing how the microscopic asynchronous unit cell expansion (left) during lithiation leads to macroscopic morphology change of α-MnO_2 nanowire based on both theoretical prediction (middle) and experimental observation (right).[37] (b) Schematic showing the reversible movement of a phase transition region (red) between Li-rich and Li-poor phases during cyclic voltammogram testing of the open cell with a single $LiMn_2O_4$ nanowire-based electrode.[41] (c) The time-sequential energy-filtered TEM images of a $LiFePO_4/FePO_4$ cluster during one charge/discharge cycle. The brighter region indicates Li-poor

FePO$_4$ phase featuring a characteristic electron energy loss peak around 5 eV, based on which the contrast is formed.[40] (d) Schematic model and corresponding TEM images of the phase transition during delithiation process of a LFP crystal, where the solid solution zone and the boundary migration are dynamically recorded.[39] (e) Schematic of the migration direction of the LFP/FP phase boundary, where the lithium ion diffusion direction ([010]) is confirmed to be the same as the phase boundary migration direction. The green arrows mark the lithium ion insertion direction.[38]

b. Alloying electrodes—Volume change and capacity fading

Among all the alloying-based electrodes, Si is of great interest not only due to its abundance in nature, but also because of the extremely high theoretical capacity of 2200 mAh/g *via* the following reaction: $Li^+ + e^- + Si = Li_{4.4}Si$. However, Si anodes usually undergo serious capacity fading due to the large volume change during repetitive cycling, preventing its further commercialization in the market. As such, intensive *in situ* TEM work has been done to explore the capacity fading mechanisms during Li-Si alloying process, which is summarized in Figure 3.4. Some important kinetic discoveries during (de)lithiation of Si include two-phase alloying mechanism,[49,48,50] size-dependent fracturing[47,51] and lithiation anisotropy (<110> preferred).[56,55,52,54,53] In addition to Si, some other elemental materials such as Sn,[57] Ge,[59,58] and Ga[62] have also been explored by *in situ* TEM, where distinct (de)alloying behaviors are discovered compared to Si electrode. These *in situ* TEM studies have led to insightful understanding of the alloying mechanisms and the origins for poor cycling performance of alloying electrodes. Future battery work could greatly benefit from these in situ findings by focusing on size engineering, surface modification and growth control to improve the cycling stability and capacity of these alloying-based electrodes.
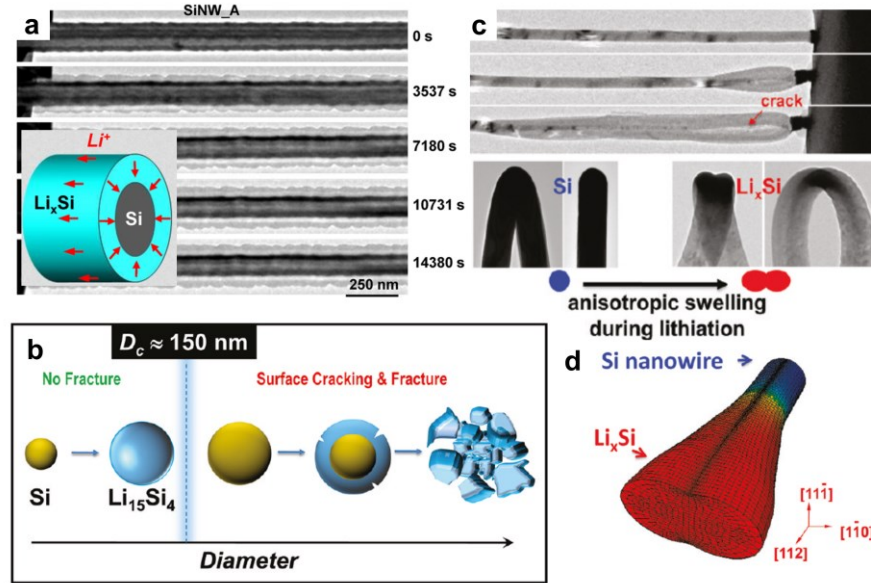
Figure 3.4. In situ TEM findings during (de)lithiation of Si anode. (a) Evolution of the morphology and two-phase microstructure (Si-Li$_x$Si core-shell) in one Si nanowire during lithiation.[50] (b) Schematic showing the 150 nm critical size for lithiation of c-Si below which the particle can be smoothly lithiatied and above which fractures are initiate from the surface.[47] (c) Crack formation during c-Si nanowire lithiation and tilted series images showing the dumbbell shape of the lithiated c-Si nanowire.[56] (d) 3D simulation of a partially lithiated Si nanowire showing the formation of a dumbbell-shaped cross section along the axis direction.[56]

c. Conversion Reaction Mechanism—Low coulombic efficiency and capacity fading

Transitional metal oxides, sulfides and fluorides show reversible Li$^+$ storage through conversion reaction when falls into nanosize.[89] The critical step during this conversion reaction is the formation of extremely small M nanoparticles with high specific surface area, which act as catalysts to improve the kinetics of the LiX-related reactions. Despite the decent capacity of these materials, several prominent problems exist, such as the low coulombic efficiency during the charge/discharge, the large overpotential and fast capacity fading.[89] The conversion reversibility involving Li$_2$O formation/decomposition is also unclear without the real time dynamic observation.

39

The fast capacity fading with cycles is largely attributed to the violent volume change during the repetitive (de)lithiation, which has been sufficiently proofed by open cell design exploring the (dis)charge of various materials such as RuO_2[63], CuO,[64] Fe_2O_3,[65] SnO_2,[66,67] FeF_2,[68] MoS_2,[69] ZnO,[61] and MnO_2[37]. Figure 5a illustrates the volumetric evolution of a single RuO_2 nanowire being partially lithiated, where the radial expansion is clearly shown.[63] Some conversion electrodes such as SnO_2 and ZnO also experience Li-Sn and Li-Zn alloying process after conversion, which thus results in more serious volume change. Another significant contribution of *in situ* TEM is the understanding of origins for improved activity of Li_2O-related reactions in conversion reactions, where Li_2O is electrochemically inactive in theory. High-mag *in situ* TEM has captured the formation of extremely small metallic nanograins (2-3 nm) during the lithiation-induced reduction of transitional metal oxides, such as Co_3O_4,[70] CoS_2[71], Fe_2O_3[65], RuO_2[63], MnO_2[37], FeF_2[68], CuO[64], and $MnFe_2O_4$[72]. Interestingly, these reduced metallic particles are found to be structurally interconnected with each other inside the Li_2O matrix, as exampled in Figure 3.5a-c demonstrating the Ru/Li_2O network after the in situ conversion reaction. The high surface area of the metallic nanograins and their network for fast electron conduction are critical for the improvement of the Li_2O reversibility. Coulombic efficiency (CE) is an important parameter when one electrode material is evaluated. It reflects the reversibility of the electrode materials and the capacity retention upon cycling. The first cycle CE is generally low in conversion-based TMOs electrodes (75% for TMOs compared with 90% in graphite).[90,91] In addition to the formation of thin SEI layers, the dominant origin for the low CE in TMOs is proposed to be related to the conversion reaction itself, which has been further confirmed by *in situ* TEM. For example, while the lithiation of CuO results in formation of superfine Cu nanograins, the delithiation proceeds in a different way that Cu_2O appears to be the final product instead of CuO. The following cycles are thus based on reversible conversion of Cu/Cu^{1+} (375 mAh/g) instead of Cu/Cu^{2+} (670 mAh/g), where the reversible capacity is greatly reduced compared to

the first cycle, as shown in Figure 3.5d and e.[64] Such a conversion feature is also reported in other TMOs such as Fe_2O_3,[65] Fe_3O_4,[73] and Co_3O_4 nanoparticles[70].
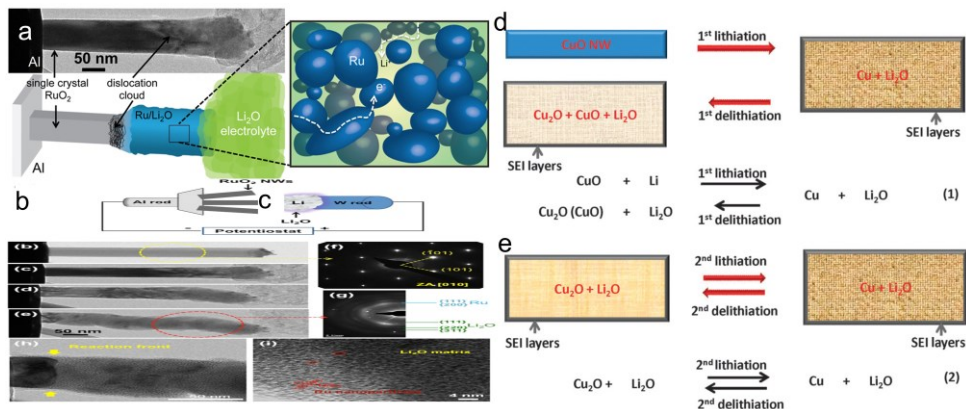
Figure 3.5. (a) In situ TEM setup showing RuO_2 nanowires attached to an Al rod and Li/Li_2O electrode/electrolyte. The fully converted/expanded area is analyzed to be Ru/Li_2O network, which is confirmed by HRTEM in (b,c).[63] (d-e) Schematic showing Li-insertion and Li-extraction, and corresponding phase transitions at different stages in CuO NWs: (d) 1st cycle, (e) 2nd cycle. The low coulombic efficiency is caused by the irreversible conversion reaction between Cu^0 and Cu^{2+}.[64]

The highly localized structural and morphological features in nanoscale during the conversion reaction requires the application of *in situ* TEM rather than any other collective in situ techniques such XRD, Raman and XPS. These *in situ* TEM findings strongly suggest the necessity of applying structural engineering and surface modification to improve the cycling stability of the TMO-based electrodes.

3.2.1.3. Compositional/structural engineering

It is common to improve energy storage performance of materials using either structural or compositional methods such as designing NiO-carbon[75] and Si-carbon composition[92] and doping targeted electrode with trace of functional elements[93]. Although these methods indeed improve the battery performance of various materials, the detailed mechanisms are not clear and need to be studied in real time.

The importance of the spatial correlation between Si and carbon matrix and how various Si-C geometries affect the (de)lithiation behavior of the composite electrode are well explored, as shown in Figure 3.6a.[79] The synergic interaction in other Si-C configurations such as Si-carbon nanofibers,[77] Si-graphene[54,76] and Si-C yolk-shell composites[78] are also well understood. Generally, two mechanisms have been proposed to explain the improved performance of these composites based on *in situ* TEM studies. First, carbon matrix functions as a strong and flexible buffer for the huge Si volume change during (dis)charge; second, the carbon shells covering Si particles prevent the repetitive SEI formation/decomposition on Si surface, maintaining most of the active Si materials. These two mechanisms are illustrated in Figure 3.6b and c using the Si@void@C particles with a york-shell design.[78]
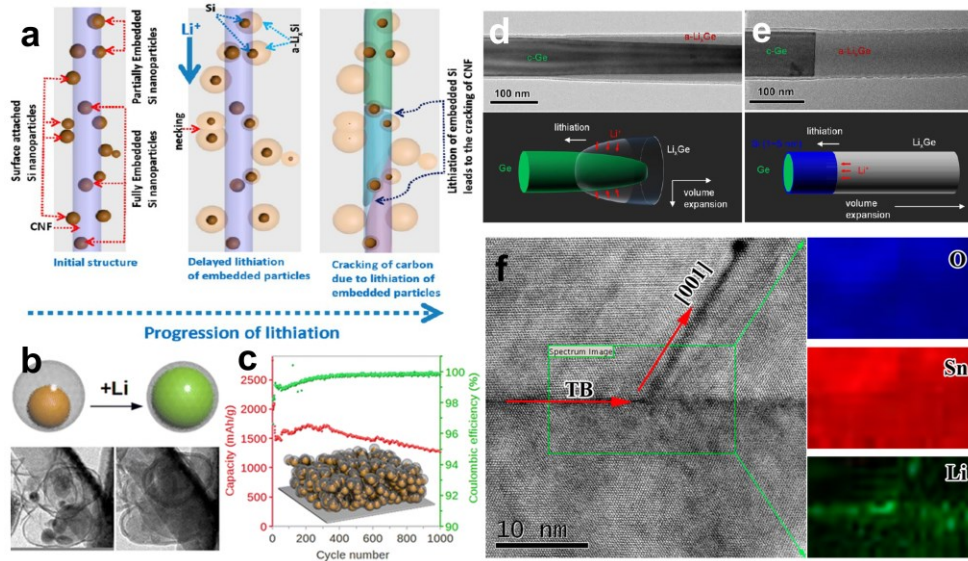
Figure 3.6. (a) Schematic drawing showing the lithiation characteristics of the particles attached to and embedded in CNF. (left) Original structure. (middle) Lithiation of the particles embedded in CNF is delayed when compared to the particles attached to the CNF surface. The necking of the particles confined by the CNF is clearly shown. (right) Lithiation of the particles embedded in the CNF leads to the cracking of the CNF.[79] (b) The schematic and *in situ* TEM images showing the free expansion of a core Si particle where carbon coating and the SEI layer on the outer surface are well maintained. (c) The superior cycling performance and the coulombic efficiency of the Si@void@C electrode.[78] (d,e) Core−shell *vs* axial

42

lithiation of Ge one nanowire with and without a thin Si coating. The pure Ge nanowire experiences a core−shell lithiation mechanism and shows the tapered shape phase boundary, while the Ge/Si core/shell nanowire experiences an axial lithiation mechanism behavior in sharp contrast with that of pure Ge.[82] (f) A HAADF image showing a lithiated SnO_2 nanowire with twin boundaries and the corresponding EELS maps of O, Li and Sn taken from the rectangular area. Li^+ diffuse form left to right. The twin boundaries and the dark strip along the [001] direction show stronger Li signals along the directions indicated by red arrows, whereas Sn signals are slightly weaker.[83]

The sensitivity of *in situ* TEM to spatially localized reaction has enabled the dynamic exploration of the mechanisms regarding the modification of battery kinetics through composite engineering. Graphene additives change the lithiation kinetics of CoS_2 particles from a side-to-side mode to a core-shell conversion with homogeneous expansion and delayed fracturing, which is ascribed to the increased Li^+ and e^- conductivity by graphene.[71] Similar kinetics modification has also been reported in other composites such as NiO-graphene[75], Si-Sn[81] and Ge-Si[82]. Figures 3.6d and e illustrate the efficient modification of lithiation kinetics by nanoscale interface and bandgap engineering *via* coating Si on single Ge nanowire surface.[82]

Inspired by the idea that ion transport could be accelerated along dislocation cores in crystals,[94] some in situ TEM reports have demonstrated the important role of structure defects in the (de)lithiation of crystalline electrodes. One material being intensively studied is SnO_2 nanowires, whose lithiation features stress-driven dislocation plasticity[67] and twin boundary-assisted Li^+ transport (Figure 3.6f)[83]. These findings disclose the positive roles of crystalline defects in improving the lithiation kinetics of nanostructured electrodes. As the material technology is being developed towards the controlled introduction of crystalline defects (dislocation, twin boundary, stacking faults), we could foresee the next generation rechargeable batteries with superior rate performance to greatly benefit from these fundamental studies.

3.2.2. Electrochemistry interface

3.2.2.1. Solid electrolyte interface (SEI) and Li dendrite growth

One fundamental challenge in battery characterization is the direct observation of SEI formation/decomposition and Li dendrite growth so as to understand and modify their behaviors correspondingly.[95] Current post-mortem studies inevitably cast doubt on the authenticity to reflect the original working status of SEI formation and Li plating due to the demanded battery disassembly exposing the air-sensitive components to air and causing damage. *In situ* TEM has been proved to be a good method for this study.

Cui's group have demonstrated the selective deposition and stable encapsulation of lithium *via* heterogeneous metallic seeded growth (Figure 3.7),[31] and the application of interfacial nanoscale engineering to guide Li plating and stabilize SEI[32]. The proposed substrate-dependent Li nucleation and the effectiveness of interfacial engineering could further guide the design of hollow nanocapsules with selective metallic substrates for Li anode and even inspire research of Li-O$_2$ and Li-S batteries, where the stability of metallic Li anode is critical.
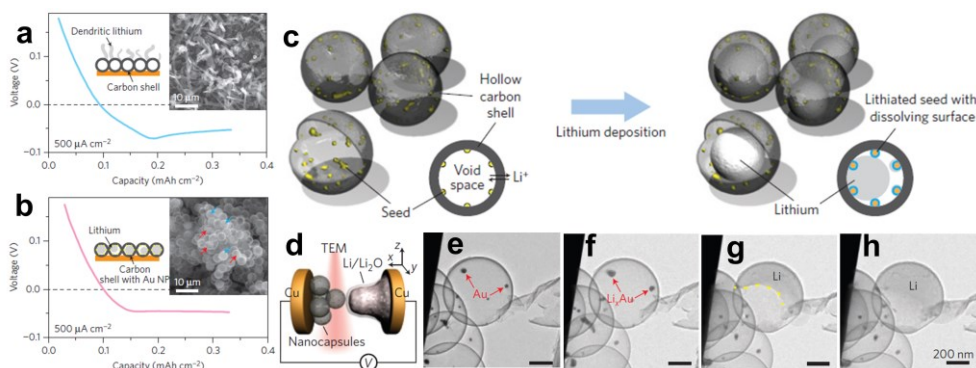
Figure 3.7. (a,b) Voltage profile during Li deposition on hollow carbon shells without (a) and with (b) Au nanoparticles. The inset shows the SEM image after deposition as well as the corresponding schematic. Fully filled and partially filled carbon spheres are marked by blue and red arrows, respectively. (c) Schematic of Li metal nanocapsules design. Au are loaded inside hollow carbon spheres, where a large void space is reserved for Li metal. Li is expected to nucleate from the Au seed. Carbon

shells provide both confinement and protection of the Li metal, as well as conduction channels for both electrons and Li metal. (d) Schematic of open cell for *in situ* Li deposition study with TEM. (e-h) TEM snapshots of the Li deposition process inside carbon shells with Au during *in situ* Li metal plating.[31]

Since SEI formation and Li plating typically happen in the real battery environment of aqueous and nonaqueous organic electrolytes, *in situ* liquid cell TEM has been increasingly used to study the evolution SEI and Li plating behaviors in liquid electrolyte.[40,96,30] Zeng *et al.*[27,28] studied the Li^+ dendrite growth and SEI formation/decomposition dynamically using $LiPF_6$/EC/DEC as the electrolyte and Au as the electrodes, as shown in Figure 3.8a and b, where Li dendrite grows fast starting from Li-Au alloying. The deplating process is inhomogeneous and initiated from the tip part immersed in the electrolyte, leading to "dead" Li metal that is disconnected form the circuit, which is also reported by Leenheer *et al.*[30] The SEI formation is initially fast and accompanied with gaseous products formation, while its growth stops later and indicates the electron-transport limited growth property. Similar behaviors were also reported by Mehdi *et al.*[33], as shown in Figure 3.8 (c-e). Changing the liquid electrolyte to $LiPF_6$/EC/DMC, Sacci *et al.*[29] found that the SEI formation on the Au electrode is not uniform but in the shape of "dendrites" that are similar to Li dendrites. Further more, the SEI dendrite grows prior to the following Li deposition, implying the critical effect of electrolyte composition and its electrode decomposition on Li plating. These *in situ* observations could help to understand the kinetics of Li deposition and SEI growth and further to circumvent the related problems and battery failure.
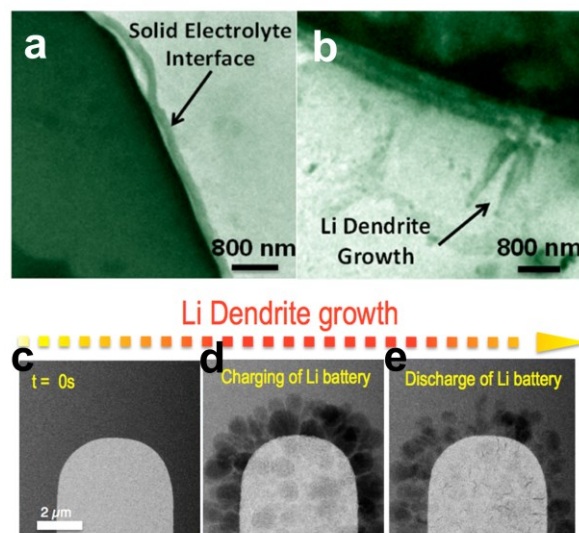
Figure 3.8. (a) *In situ* observed growth of the SEI film with a gas bubble emerged between the Au electrode and the SEI film. b: *In situ* observed growth of Li dendrites from the counter electrode (Au).[27] (c-e) HAADF images of Li deposition (d) and dissolution (e) at the interface between the Pt working electrode and the $LiPF_6/PC$ electrolyte. Note that while Li dendrite exhibits darker contrast than the surrounding liquid organic electrolyte does in the bright-field TEM in (b), it indeed shows a darker contrast in the dark-field STEM images in (c-e).[33]

As one can see, the spatial resolution of the liquid cell falls far behind that of the open cell design where no thick liquid species are present, not to mention the elemental and electronic structure sensitivity. Some reports have demonstrated the possibility of extracting crystalline structure and electronic structure information of targeted materials immersed in aqueous solution[97] and even organic electrolyte solvent.[98] Still, future work should aim to increase the spatial resolution and the analytical ability of the liquid TEM technique by reducing the liquid thickness along electron path, replacing the electrodes (Au) with lighter/inert elements (carbon/graphene, etc.), shortening the path of characteristic X-ray to the detector and using target materials with larger electron scattering cross section.

3.2.2.2. Solid State Electrolyte (SEI resistance, thickness effect, thermal, *etc*.)

46

Conventional lithium ion batteries with flammable and combustible liquid electrolyte generally have safety problems that limit their scalability and compatibility with metallic Li anode.[84] Solid state electrolyte (SSE), on the other hand, is composed of safe and nonflammable materials and is compatible with metallic Li.[99] In addition, the absence of liquid leakage in SSE allows more flexible configurations such as thin film and miniature batteries.[100] Currently, however, there are several critical issues not well understood, such as electric potential distribution across the SSE/electrode interface, nanoscale (miniature battery) electrochemistry, complicated interfacial elemental interdiffusion and its effect on Li (de)plating, effect of temperature on Li^+ diffusion and interface migration. To answer these questions clearly, *in situ* TEM coupled with localized elemental/valence detecting capability is intensively applied to dynamically track Li^+ diffusion kinetics and SSE/electrode interface migration, providing insightful understanding of the ionic transport mechanisms.
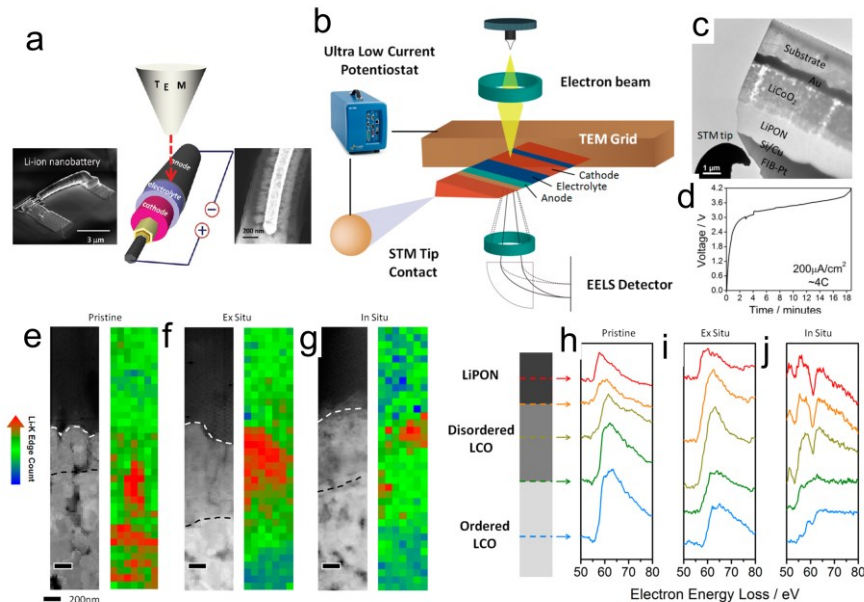
Figure 3.9. (a) The SEM (left), schematic (middle) and HAADF (right) images showing a Si-nanowire based lithium ion battery (NWLIB). These NWLIBs, with the electrolyte layer as thin as <200 nm, are further cycled inside TEM, with the structure evolution at the electrode/SSE interface dynamically recorded. (b) Schematic of the thin film nanobattery mounted on a TEM grid via focus ion beam operation. The

47

cathode is electrically connected to the grid and a piezo-controlled STM tip makes contact with the anode current collector. (c) TEM of STM tip connecting a thin film nanobattery. (d) Electrochemical profile of the in situ cell galvanostatically charged in the TEM. (e−g) HAADF images of the nanobattery stack along with Li K-edge concentration mapping of (e) pristine, (f) *ex situ*, and (g) *in situ* samples with scale bar representing 200 nm. (h−j) Li K-edge spectra from various parts of the layers displayed for (h) pristine, (i) *ex situ*, and (j) *in situ* samples.[101]

Currently, two representative designs for the miniature solid state batteries are proposed for *in situ* study, i.e. the single nanowire-based battery and the thin film battery, as shown in Figure 3.9. Using the nanowire-based design, the rapid battery self-discharge phenomenon is found when the SSE layer is thinner than certain critical value (180 nm in case of $LiCoO_2$/LIPON/Si).[35] It is proposed that the space-charge limited electronic conduction could shorten the anode and cathode directly through the electrolyte and lead to rapid self-discharge with void formation at the interface. Considering the rising demand for miniature 3D lithium ion batteries to power the microsystems operating without power hardwires or communications, this work provides useful metric guidelines for the future battery design. Wang *et al*.[101] carried out nanoscale spectroscopic characterization of a $LiCoO_2$/LiPON/Si thin film battery across the $LiCoO_2$/LiPON interface during charge, as shown in Figure 3.9b-i. A structurally disordered layer was for the first time captured and featured obvious chemical change with Co oxidation and Li oxide formation during charge, which accounts for the commonly observed interfacial impedance in solid state batteries. Applying *in situ* holography to the similar thin film design, Yamamoto *et al*.[34] quantified the dynamic 2D potential distribution caused by movement of lithium ions near the $LiCoO_2$ cathode/Li-Al-Ti-Si-P-O electrolyte interface.

With increasing research interest in all-solid-state batteries, the powerfulness of *in situ* TEM in detecting localized phase, composition, and electronic structure across interface regions will provide deep understanding of the (dis)charge reactions as well

as the failure mechanisms. As interfacial Li^+ distribution has been detected directly by EELS in either STEM or EFTEM mode,[102] it is hoped that the Li^+ diffusion kinetics will be soon to be explored dynamically with more details unveiled. Another promising direction is about the dynamic study of the thermal response of the miniature solid state batteries and the Li^+ diffusion across the electrode/SSE interface at different temperatures. With the fast development of lab-on-chip technology and the multifunctional TEM holders capable of biasing and heating simultaneously, the thermal-related *in situ* TEM study of SSE is expected to come out soon.

3.2.3. Beyond lithium ion battery (Na^+, Mg^{2+}, Ca^{2+}, Al^{3+}, *etc.*)

3.2.3.1. Rechargeable batteries with metallic lithium anodes

Current lithium ion batteries, although being suitable for small-scale devices, can not reach the high energy density or longevity requirement to power electric vehicles with comparable performance to that of internal combustion vehicles. Researchers are thus turning to new electrochemical couples such as $Li-O_2$ or Li-S providing at least 5 times the practical energy density of current lithium ion batteries.[103] Up to now, however, neither of them is commercialized due to some significant hurdles that have not been well understood and overcome. In $Li-O_2$ battery, the well known problems include formation of insulating Li_2O_2 during discharge, gradual passivation of electrode surface, and large charge overpotential.[104] Li-S couple also suffers from insulating Li_2S and S phases, large volume expansion as well as dissolvable intermediate polysulfides shuttling between anode and cathode.[105],[106] There are a few *in situ* studies, although not many, focusing on the dynamic study of Li-S and $Li-O_2$ electrochemistry.

Zhong *et al.*[6] explored the origin for large charge overpotential in $Li-O_2$ battery with the *in situ* design and observation shown in Figure 3.10 (a-c).The finding that the decomposition of Li_2O_2 always starts near the e^- sink (carbon nanotubes) rather than the Li^+ sink (Si) suggests the charge/oxidation kinetics to be limited by e^- transport

49

rather than Li$^+$ transport. Kushima *et al*. dynamically studied both the formation and decomposition of Li$_2$O$_2$ (Figure 3.10 (d-f)).[7] While similar e$^-$ transport-limited charge reaction is observed, the discharge process surprisingly features Li$_2$O$_2$ accumulation near the interface between the electrolyte and the reaction product. This is a strong indication that although the charge process is limited by e$^-$ conductivity, the discharge is limited by Li$^+$ diffusion, resulting in large overpotentials during charge and discharge, respectively. The idea of directly using gas-rich solution in this liquid cell experiment can be potentially used in other *in situ* studies involving gas/liquid/solid electrochemical reactions, where the introduction of gas into the TEM chamber has always been a challenge. Although these two *in situ* reports utilized either solid state open cell or sealed liquid cell design, their findings regarding the charge kinetics agree well with each other. This further demonstrates the importance of designing conductive porous cathode materials with ability to confine the dissolution of Li$_2$O$_2$ into the electrolytes.
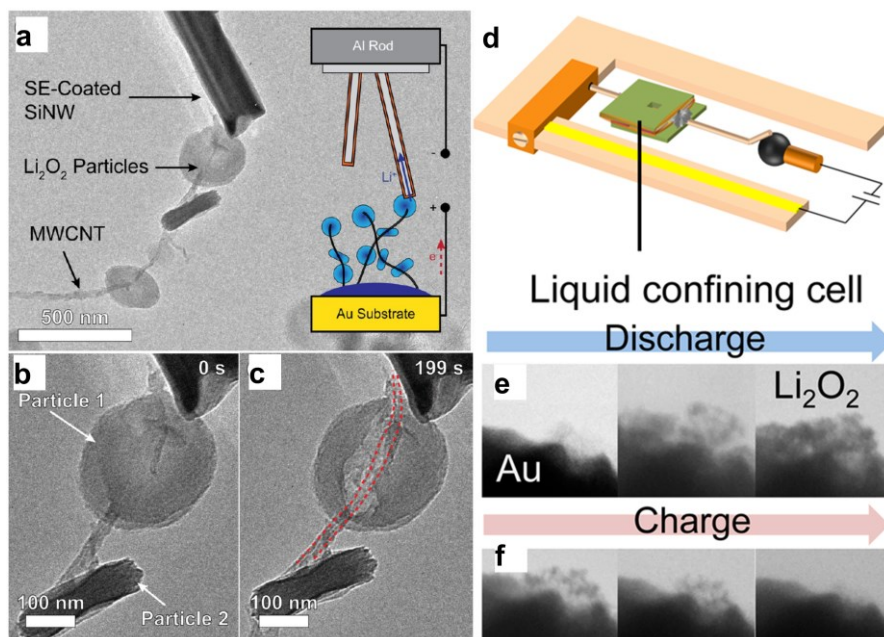
Figure 3.10. (a) Schematic of an *in situ* TEM microbattery based on a LiAlSiO$_x$-coated Si NW contacting a single Li$_2$O$_2$ particle. (b) High-magnification TEM image of the Li$_2$O$_2$ particle in (a) showing a MWCNT contacting the particle. (c) Oxidation of Li$_2$O$_2$ during application of a 10 V potential to the MWCNT/ Li$_2$O$_2$ positive

electrode against the Si NW negative electrode. The Li_2O_2 particle near the MWCNT bundle in Particle 1 is rapidly oxidized.[6] (d) A sealed liquid cell mounted onto a Nanofactory STM holder capable of applying biasing. The cell is glued to two Au wires with conductive epoxy. (e-f) The formation and decomposition of Li_2O_2 on Au electrode surface during discharge (e) and charge (f).[7]

For Li-S electrochemistry, a S_8/Li_2S interface during discharge was captured in real time by Xu *et al.*[8], as shown in Figure 3.11 (a-c). The authors believe such an interface could prevent further Li^+ diffusion into the bulk S due to the insulating character of Li_2S, leading to the incomplete sulfur reduction during high-rate discharge. Kim *et al.*,[9] on the other hand, proposed an opposite theory that the Li_2S/S interface is electrically conductive (Figure 3.11 (d-i)), which is deduced based on the observation of a sharp and flat Li_2S/S_8 lithiation interface in sulfur nanowire covered by CNT. This discovery regarding the novel property of Li_2S/S_8 interface could guide further work on the modification/engineering of electrochemistry interfaces for improved battery performance. The application of protective layers (CNT) on sulpur also demonstrated an efficient method to study electron beam-sensitive materials for future *in situ* TEM study.
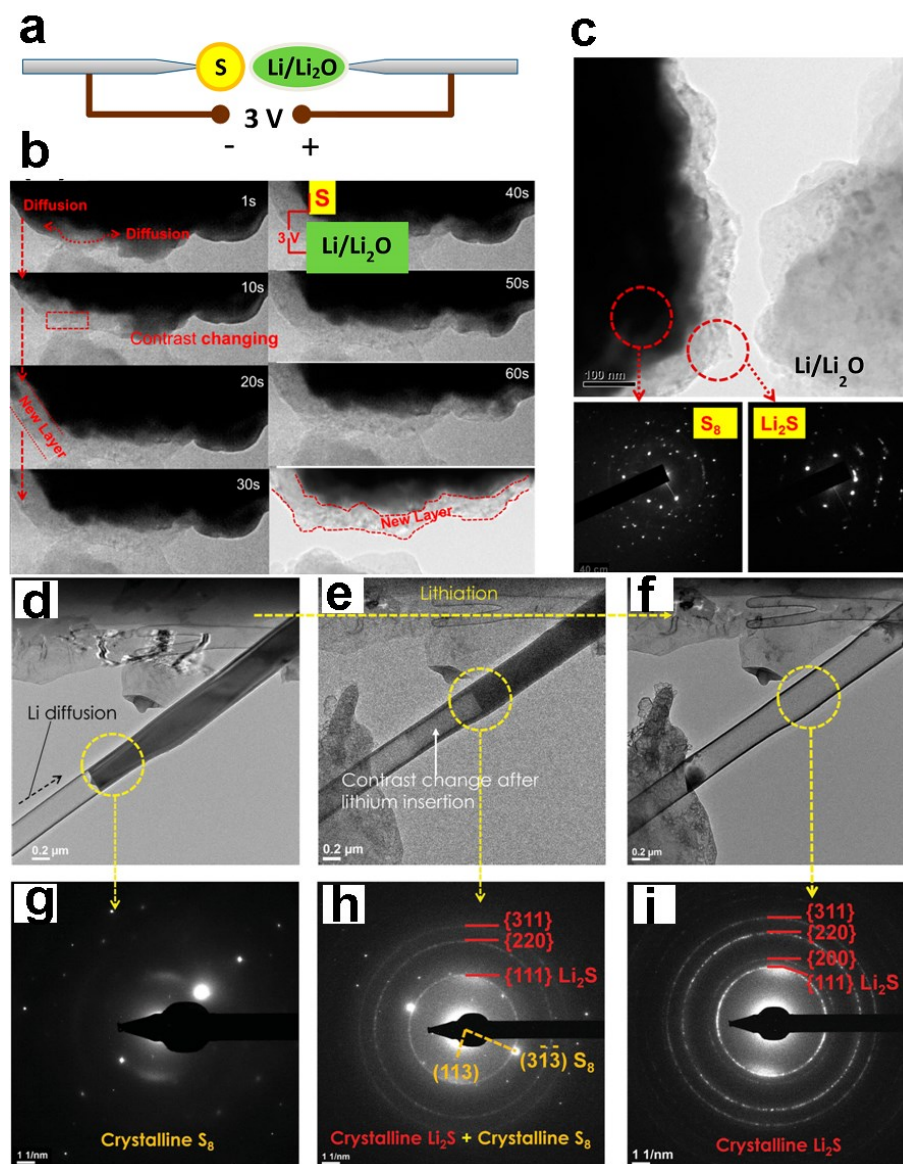
Figure 3.11. (a) Schematic showing the Li−S cell setup for *in situ* TEM investigation, (b) TEM images of the Li−S cell for its discharge process (1−60 s), (c) SAED patterns of sulfur and the formed new layer.[8] (d–f) TEM images captured during lithiation of S confined in a carbon nanotube and (g–i) their corresponding diffraction patterns.[9]

3.2.3.2. Rechargeable batteries with non-Li candidates.

Li has limited abundance in earth crust, which can hardly meet the explosively growing demand for rechargeable batteries. People are thus seeking alternative charge

carriers for extensive energy storage applications. Beyond Li^+, Na^+ is a very promising candidate due to its rich storage in earth as well as the relatively light atomic weight.[107] Some multivalent ions such as Mg^{2+}, Ca^{2+} and Al^{3+} are also studied as promising candidates to replace Li^+ due to their high energy density.[108,109] However, due to the variation in electronegativities and ionic sizes, the dynamic (dis)charge process is expected to exhibit distinct features compared to that in lithium ion batteries. The dynamic study in this area is still at the preliminary stage and current findings are frequently compared to that from the intensively studied Li^+-based electrochemistry.

      a. *Rechargeable Sodium Ion Battery*

          Phase transition difference:

To understand how ionic size and electronic structure of different ionic species affect the electrochemical performance and result in various failure mechanisms, many *in situ* TEM reports focus on the comparison of the phase transition in sodiation and lithiation of various electrode materials. Materials being compared include FeF_2, MnO_2 and CuO, where distinct (de)sodiation mechanisms are discovered. The sodiation of FeF_2 nanoparticles is a multistep reaction involving regular conversion on the particle surface and a disproportionation reaction in the core, while the lithiation process is a direct one-step conversion reaction to Fe and LiF.[10] Due to the different diffusion paths of Li^+ and Na^+ inside the tunnels,[110,111] tunneled α-K_xMnO_2 maintains its stability during lithiation up to Li_1MnO_2,[37] while it degrades much faster during sodiation before it reaches $Na_{0.5}MnO_2$,[11] as shown in Figure 3.12 (a-c). The (de)sodiation of CuO anode is totally reversible between CuO and Cu with Cu_2O as the intermediate phase,[12] whereas the previous (de)lithiation work of CuO[64] only demonstrates partial reversibility with Cu_2O as the final product. The physical properties of Li_2O/Cu_2O and Na_2O/Cu_2O interfaces should be responsible for the difference in reaction activity, which apparently requires more fundamental study.
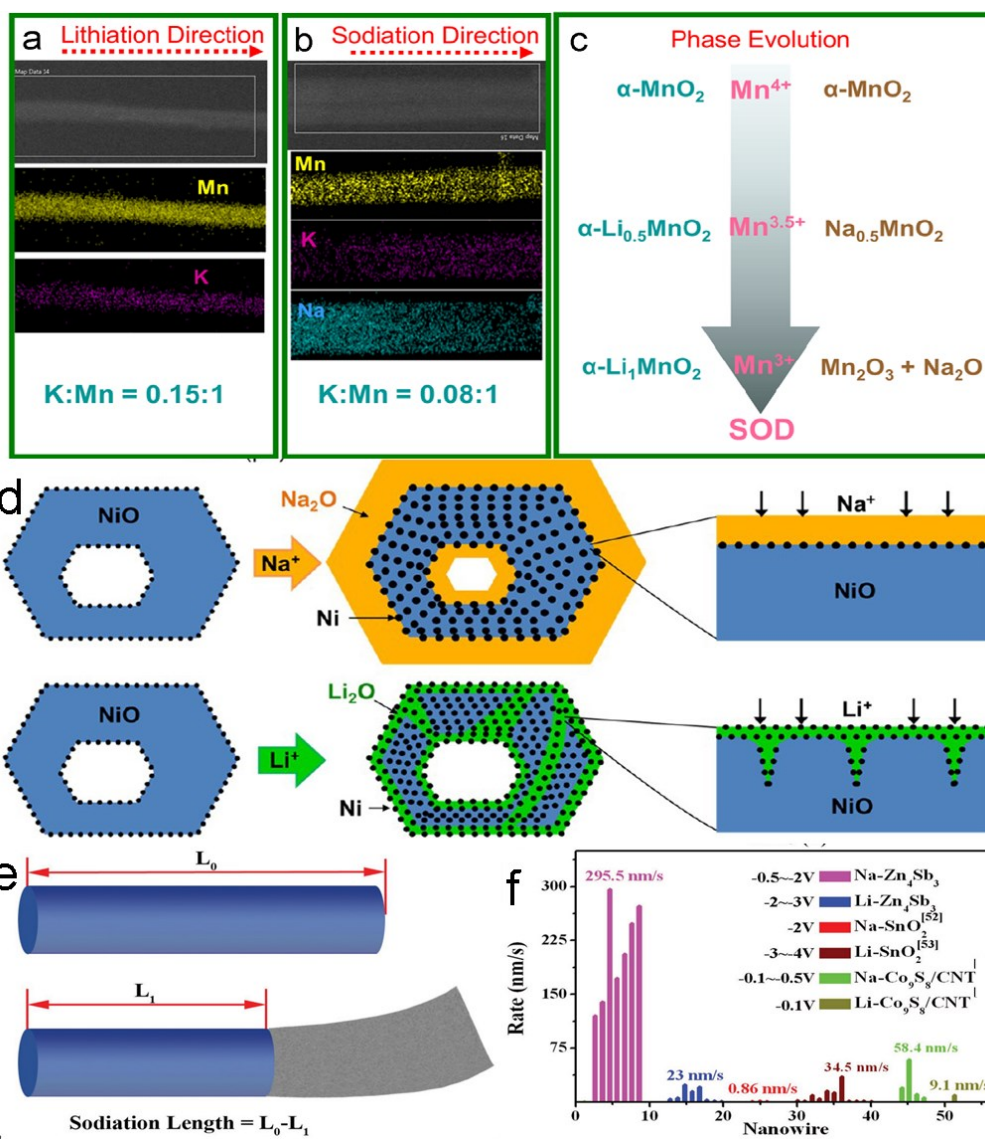
Figure 3.12. (a-c) Comparison of lithiation and sodiation in K$^+$-stabilized α-MnO$_2$ nanowires in terms of the stability of K$^+$ in the tunnel and the phase evolution.[11] (d) Schematic cartoons showing different reaction modes between sodiation and lithiation of NiO. The sodiation process exhibits a "shrinking-core" mode that thickens the Na2O surface layer and thus impedes further Na+ insertion, while the lithiation features finger-like heterogeneous reaction fronts enabling continuous lithiation.[13] (e,f) Schematic showing how to define the sodiation length, and the comparison of sodiation *vs* lithiation front propagation speeds of Zn$_4$Sb$_3$, SnO$_2$, and Co$_9$S$_8$/CNT nanowires.[15]

In addition to the phase transition variation, the reaction kinetics of sodiation and lithiation should also exhibit certain difference considering the distinct sizes of Na^+ (1.02 Å) and Li^+ (0.76 Å).[111] Compared to the lithiation of NiO featuring a "finger-like" heterogeneous reaction front, its sodiation is much delayed due to the "shrinking-core" mode that thickens the Na_2O surface layer and thus impedes further Na^+ insertion, as shown in Figure 3.12d.[13] In terms of diffusion rate, Na^+ diffusion was found to proceed 30 times slower than Li^+ in SnO_2 nanowire due to the larger size of Na^+, the resulted higher Na^+ diffusion barrier and the disconnected Sn network providing poor electron paths.[14,67] Contrary to SnO_2 electrochemistry, the counterintuitive influences are reported for the sodiation and lithiation processes in Zn_4Sb_3 nanowires[15,112] and carbon nanofiber-confined Co_9S_8,[16,113] where sodiation proceeds faster than lithiation over one order of magnitude. Figures 3.12e and f summarize the reaction front kinetics of several electrodes focusing on the comparison of their lithiation and sodiation processes. It is predicted that the improved reaction kinetics in sodiation of these materials might be ascribed to the high electrical conductivity of various phases involved[15].

Multivalent rechargeable batteries:

Although many *ex situ* battery experiments have demonstrated the promising future for multivalent batteries, there are few *in situ* TEM reports exploring the dynamic cation (de)insertion mechanisms. Bivalent Ca^{2+} was first reported to be electrochemically inserted into single crystalline WO_3 films using the open cell design in TEM, where an intercalation step (Ca_xWO_3) prior to conversion of WO_3 into W and CaO is explicitly revealed at atomic scale.[22] Luo *et al.*[23] compared the Co_3O_4 nanocubes anode regarding the lithiation, Mg^{2+} insertion and Al^{3+} insertion. The experiments applied the same solid state open cell design with Li, Mg and Al as the counter electrodes, respectively. In contrast to the fast conversion kinetics for the lithiation, the insertion of Mg^{2+} shows no sign of conversion reaction of Co_3O_4 other than Mg plating on the surface in the form of Mg nanoparticles. Al^{3+} insertion is even more sluggish with no obvious reaction. Such a reaction sluggish is largely

determined by the inactive solid state oxide layers (MgO and Al_2O_3) covering the surface of metallic anodes, as well as the large repulsive forces encountered by the inserted multivalent cations. The achievement of multivalent cation insertion for *in situ* TEM study largely depends on the choice of a proper electrolyte with low cation diffusion barrier, and the counter electrode with large openings and little repulsive forces against continuous insertion.

3.2.4. How electron beam affects the real electrochemistry in TEM

Compared to other characterization techniques such as Raman, XRD and optical microscopy, electron microscopy provides information by direct particle-particle interaction, which results in easier sample damage and acquisition of fake information. For battery research, since the reaction essentially involves electron transfer, the effect from electron beam is thus more obvious with the possibility of changing the environment of the very original reactions. Li, being the lightest solid element in the current periodic table, is hard to detect by TEM due to its weak scattering cross section and vulnerability to beam radiation. As such, when the battery electrochemistry is studied dynamically using *in situ* TEM, extra care should be taken to consider the side effect induced by high energy electron beam, especially when the sample contains electron-sensitive liquid electrolyte. These side reactions include atomic knockout damage, radiolysis of liquid, bubble formation, surface contamination and particle precipitation.[114]

Typical side effects for an open cell design include electron heating, material ionization, and atomic knock-on damage. Solid Li_2O is not always stable under high energy electron beam, and its instability can affect the observed electrochemical behaviors.[115] It has been reported that the electron beam can either slow down the lithiation process in Si nanowires[2] or initiate the chemical lithiation of SnO_2 nanowires by decomposing the Li_2O electrolyte into elemental Li and gas[4], as shown in Figure 3.13 (a-f). In spite of these observed differences, the *in situ* electrochemistry

generally agrees with ex-situ real battery electrochemistry in terms of reaction kinetics and structural evolution. For example, Liu *et al.*[56] reported the anisotropic lithiation of Si nanowires based on *in situ* TEM, while similar anisotropic Si expansion was also reported from *ex situ* coin cell-level testing.[116] The reversible (de)lithiation of Ge nanowires and formation of nanopores are also confirmed by both *in situ* and ex-situ TEM recently.[59,117] In fact, by taking sequential intermittent images (with limited exposure time) instead of continuous video recording, the effect from electron beam can be minimized.[71]
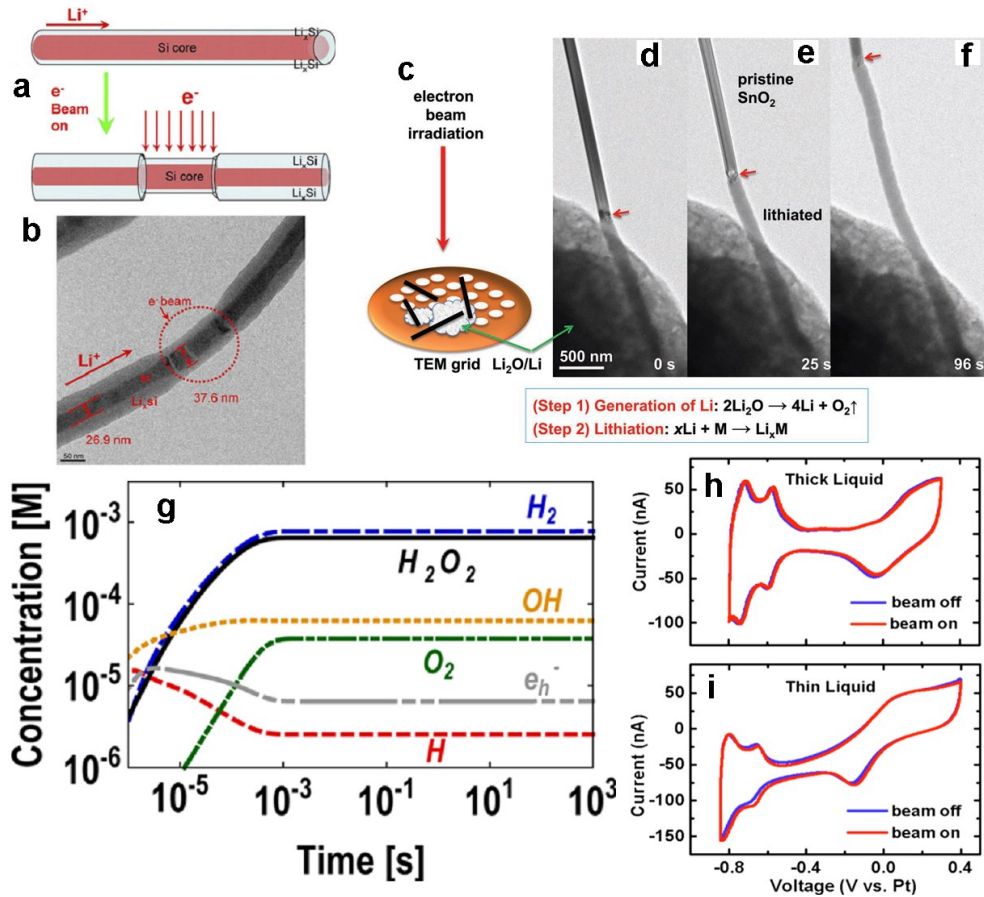
Figure 3.13. (a, b) Schematic drawing (a) and TEM imaging (b) showing the retardation of the lithiation of Si nanowire by the imaging electron.[2] (c) Schematic illustration of the *in situ* chemical lithiation design using a conventional TEM holder, where SnO₂ nanowires are mixed with Li metal coated with native Li₂O. (d-f) Lithiation of a SnO₂ nanowire driven by the electron beam. Note that the nanowire showed the same microstructural evolution as reported in the *in situ* electrochemical

lithiation experiment.[4] (g) Calculated concentrations of e_h^-, $H^\bullet$, H_2, H_2O_2, $OH^\bullet$ and O_2 in water as functions of exposure time under electron beam.118 (h,i) Pt cyclic voltammetry in (h) for thick liquid and (i) for thin liquid environments in sealed liquid TEM cells. The blue curve is obtained with electron beam off while the red one is when beam is on. The *in situ* liquid TEM chips exhibited electrochemical activities qualitatively similar to that of *ex situ* microelectrodes. For extremely thin liquid layer of about 150 nm, the voltammetric profile exhibits a significant Ohmic drop in (i).[40]

For sealed liquid cell TEM, Holtz *et al*.[40] have demonstrated the accuracy of *in situ* liquid TEM in measuring the real battery electrochemistry by performing cyclic voltammetry of one Pt film, as shown in Figure 3.13h and i. The *in situ* C-V response agrees with the characteristic voltammetry of a polycrystalline Pt electrode at an appropriate current range regardless of the electron beam. This is an indication that liquid cell electrochemistry can replicate the situations of a conventional electrochemical battery, although the liquid thickness has been shown to affect the Ohmic resistance. It is also notable that electrolyte instability and even decomposition were also reported for liquid electrolyte in sealed liquid cell containing a range of aqueous/inorganic/salt complexes associated with state-of-the-art Li-ion battery systems[118,119]. Figure 13g shows the possible species generated by electron beam inside an aqueous solution, where various gases (bubbles) and free radicals could potentially affect the battery electrochemistry as well. Figure 3.14 shows how the SEI nucleates and grows on Li deposit when the liquid electrolyte ($LiPF_6$/EC/DMC) is exposed to electron beam and decomposed.[30] It is apparent that these side products by radiolysis should be carefully addressed before the observed behaviors using *in situ* TEM can be confidently applied to real battery environment.
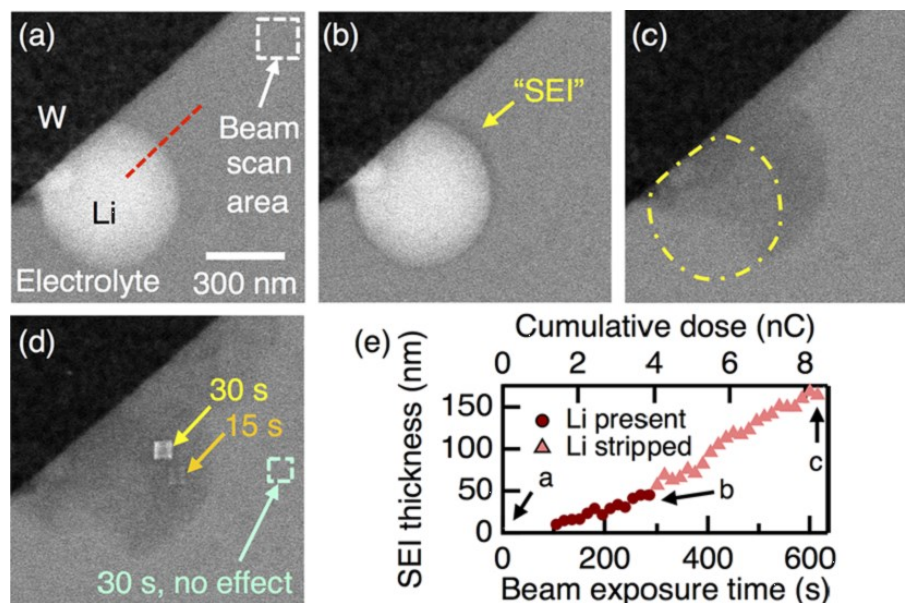
Figure 3.14. Beam-induced SEI growth. (a) BF STEM image of a Li grain during deposition and nearby 150 nm box for beam scanning in the electrolyte; (b) image after 5 min beam exposure. On the side of the Li grain closer to the beam exposure, a dark SEI deposit formed and grew; (c) image after 12 min beam exposure, where the location of the electrochemically stripped Li grain is indicated by a dotted yellow line; (d) image after scanning the beam in 75 nm boxes inside and outside the beam-induced SEI; (e) approximate thickness of the SEI measured along the red dotted line in (a).[30]

3.3. Conclusions

We have categorized and summarized the current critical problems in rechargeable batteries (lithium ion, Li-O$_2$, Li-S and sodium ion batteries) that have been explored by *in situ* (S)TEM in real time. Compared to other *in situ* techniques, (S)TEM enables the direct visualization of the electrochemical process in terms of the phase evolution and reaction kinetics. The sensitivity of (S)TEM in capturing localized information and inhomogeneity also compensate with other in situ methods such as XRD and Raman that are good at obtaining collective information. These *in situ* techniques have contributed significantly to the fundamental understanding of the operation of rechargeable batteries.

It is apparent that there are still many challenges during this early development stage of *in situ* TEM for battery study and worth of future research exploration. The decrease of spatial resolution by introduction of various electrochemical stimuli should be minimized. The artifacts not related to real battery electrochemistry should also be carefully interpreted with consideration of the actual TEM working environment and the high-energy electron beam effect. As batteries can work in various conditions, such as high temperature, compressive forces, intense light and ion radiation, it is also worth studying these effects dynamically by bringing as many stimuli into TEM chamber as possible. This goal could be probably achieved in the near future by delicate design of different TEM holder, chips and reaction chambers with the abilities of heating, lighting and compressing in addition to biasing. It could be foreseen that in situ TEM will be more extensively and intensively applied into the study of battery reactions in the future, together with the fast development of lab-on-a-chip microprocessing technology.

3.4. References

1. Erickson EM, Ghanty C, Aurbach D. New horizons for conventional lithium ion battery technology. *The journal of physical chemistry letters* **5**, 3313-3324 (2014).

2. Wang C-M. In situ transmission electron microscopy and spectroscopy studies of rechargeable batteries under dynamic operating conditions: A retrospective and perspective view. *Journal of Materials Research* **30**, 326-339 (2015).

3. Gu M, He Y, Zheng J, Wang C. Nanoscale silicon as anode for Li-ion batteries: The fundamentals, promises, and challenges. *Nano Energy* **17**, 366-383 (2015).

4. Liu XH*, et al.* In situ TEM experiments of electrochemical lithiation and delithiation of individual nanostructures. *Advanced Energy Materials* **2**, 722-741 (2012).

5. Armand M, Endres F, MacFarlane DR, Ohno H, Scrosati B. Ionic-liquid materials for the electrochemical challenges of the future. *Nature materials* **8**, 621-629 (2009).

6. Zhong L, *et al.* In situ transmission electron microscopy observations of electrochemical oxidation of Li2O2. *Nano Letters* **13**, 2209-2214 (2013).

7. Kushima A, Koido T, Fujiwara Y, Kuriyama N, Kusumi N, Li J. Charging/Discharging Nanomorphology Asymmetry and Rate-Dependent Capacity Degradation in Li–Oxygen Battery. *Nano Letters* **15**, 8260-8265 (2015).

8. Xu R, *et al.* Insight into Sulfur Reactions in Li–S Batteries. *ACS Applied Materials & Interfaces* **6**, 21938-21945 (2014).

9. Kim H, Lee JT, Magasinski A, Zhao K, Liu Y, Yushin G. In Situ TEM Observation of Electrochemical Lithiation of Sulfur Confined within Inner Cylindrical Pores of Carbon Nanotubes. *Advanced Energy Materials* **5**, (2015).

10. He K, *et al.* Sodiation via Heterogeneous Disproportionation in FeF2 Electrodes for Sodium-Ion Batteries. *ACS nano* **8**, 7251-7259 (2014).

11. Yuan Y, *et al.* Dynamic study of (De)sodiation in alpha-MnO2 nanowires. *Nano Energy* **19**, 382-390 (2016).

12. Zhang L, *et al.* In situ Transmission Electron Microscopy Study of the Electrochemical Sodiation Process for a Single CuO Nanowire Electrode. *RSC Advances*, (2016).

13. He K, *et al.* Sodiation kinetics of metal oxide conversion electrodes: A comparative study with lithiation. *Nano Letters* **15**, 5755-5763 (2015).

14. Gu M, *et al.* Probing the failure mechanism of SnO2 nanowires for sodium-ion batteries. *Nano Letters* **13**, 5203-5211 (2013).

15. Nie A, *et al.* Ultrafast and Highly Reversible Sodium Storage in Zinc‐Antimony Intermetallic Nanomaterials. *Advanced Functional Materials*, (2015).

16. Su Q, *et al.* In Situ Transmission Electron Microscopy Observation of Electrochemical Sodiation of Individual Co9S8-Filled Carbon Nanotubes. *ACS nano* **8**, 3620-3627 (2014).

17. Wang JW, Liu XH, Mao SX, Huang JY. Microstructural Evolution of Tin Nanoparticles during In Situ Sodium Insertion and Extraction. *Nano Letters* **12**, 5897-5902 (2012).

18. Liu Y, *et al.* In situ transmission electron microscopy study of electrochemical sodiation and potassiation of carbon nanofibers. *Nano Letters* **14**, 3445-3452 (2014).

19. Sun J, *et al.* A phosphorene–graphene hybrid material as a high-capacity anode for sodium-ion batteries. *Nature nanotechnology* **10**, 980-985 (2015).

20. Nie A, *et al.* Selective Ionic Transport Pathways in Phosphorene. *Nano Letters*, (2016).

21. Li Z, *et al.* Coupling In situ TEM and ex situ analysis to understand heterogeneous sodiation of antimony. *Nano Letters* **15**, 6339-6348 (2015).

22. He Y, *et al.* Atomistic Conversion Reaction Mechanism of WO3 in Secondary Ion Batteries of Li, Na, and Ca. *Angewandte Chemie International Edition*, (2016).

23. Luo L, *et al.* Reactions of graphene supported Co3O4 nanocubes with lithium and magnesium studied by in situ transmission electron microscopy. *Nanotechnology* **27**, 085402 (2016).

24. Hwang S, *et al.* Investigating Local Degradation and Thermal Stability of Charged Nickel-Based Cathode Materials through Real-Time Electron Microscopy. *ACS Applied Materials & Interfaces* **6**, 15140-15147 (2014).

25. Hwang S, *et al.* Using Real-Time Electron Microscopy To Explore the Effects of Transition-Metal Composition on the Local Thermal Stability in Charged LixNiyMnzCo1–y–zO2 Cathode Materials. *Chemistry of Materials* **27**, 3927-3935 (2015).

26. Trudeau M, *et al.* In situ high-resolution transmission electron microscopy synthesis observation of nanostructured carbon coated LiFePO 4. *Journal of Power Sources* **196**, 7383-7394 (2011).

27. Zeng Z, Liang W-I, Liao H-G, Xin HL, Chu Y-H, Zheng H. Visualization of electrode–electrolyte interfaces in LiPF6/EC/DEC electrolyte for lithium ion batteries via in situ TEM. *Nano Letters* **14**, 1745-1750 (2014).

28. Zeng Z, *et al.* In Situ Study of Lithiation and Delithiation of MoS2 Nanosheets Using Electrochemical Liquid Cell Transmission Electron Microscopy. *Nano Letters* **15**, 5214-5220 (2015).

29. Sacci RL*, et al.* Direct visualization of initial SEI morphology and growth kinetics during lithium deposition by in situ electrochemical transmission electron microscopy. *Chemical Communications* **50**, 2104-2107 (2014).

30. Leenheer AJ, Jungjohann KL, Zavadil KR, Sullivan JP, Harris CT. Lithium electrodeposition dynamics in aprotic electrolyte observed in situ via transmission electron microscopy. *ACS nano* **9**, 4379-4389 (2015).

31. Yan K*, et al.* Selective deposition and stable encapsulation of lithium through heterogeneous seeded growth. *Nature Energy* **1**, 16010 (2016).

32. Zheng G*, et al.* Interconnected hollow carbon nanospheres for stable lithium metal anodes. *Nature nanotechnology* **9**, 618-623 (2014).

33. Mehdi BL*, et al.* Observation and Quantification of Nanoscale Processes in Lithium Batteries by Operando Electrochemical (S)TEM. *Nano Letters* **15**, 2168-2173 (2015).

34. Yamamoto K*, et al.* Dynamic Visualization of the Electric Potential in an All‐Solid‐State Rechargeable Lithium Battery. *Angewandte Chemie International Edition* **49**, 4414-4417 (2010).

35. Ruzmetov D*, et al.* Electrolyte stability determines scaling limits for solid-state 3D Li ion batteries. *Nano Letters* **12**, 505-511 (2011).

36. Wang Z*, et al.* In situ STEM/EELS Observation of Nanoscale Interfacial Phenomena in All-Solid-State Batteries. *Nano Letters*, (2016).

37. Yuan Y*, et al.* Asynchronous Crystal Cell Expansion during Lithiation of K+-Stabilized α-MnO2. *Nano Letters* **15**, 2998-3007 (2015).

38. Zhu Y*, et al.* In Situ Atomic-Scale Imaging of Phase Boundary Migration in FePO4 Microparticles During Electrochemical Lithiation. *Advanced Materials* **25**, 5461-5466 (2013).

39. Niu J*, et al.* In situ observation of random solid solution zone in LiFePO4 electrode. *Nano Letters* **14**, 4005-4010 (2014).

40. Holtz ME*, et al.* Nanoscale imaging of lithium ion distribution during in situ operation of battery electrode and electrolyte. *Nano Letters* **14**, 1453-1459 (2014).

41. Lee S*, et al.* In situ TEM observation of local phase transformation in a rechargeable LiMn2O4 nanowire battery. *The Journal of Physical Chemistry C* **117**, 24236-24241 (2013).

42. Lee S*, et al.* Phase Transitions in a LiMn2O4 Nanowire Battery Observed by Operando Electron Microscopy. *ACS nano* **9**, 626-632 (2014).

43. Liu Y*, et al.* Lithiation-Induced Embrittlement of Multiwalled Carbon Nanotubes. *ACS nano* **5**, 7245-7253 (2011).

44. Liu XH*, et al.* In situ transmission electron microscopy of electrochemical lithiation, delithiation and deformation of individual graphene nanoribbons. *Carbon* **50**, 3836-3844 (2012).

45. Gao Q*, et al.* Direct evidence of lithium-induced atomic ordering in amorphous TiO2 nanotubes. *Chemistry of Materials* **26**, 1660-1669 (2014).

46. Cao K, Kuang M, Zhang Y, Liu J, Wang H, Meng L. In-situ TEM on the coalescence of birnessite manganese dioxides nanosheets during lithiation process. *Materials Research Bulletin* **79**, 36-40 (2016).

47. Liu XH, Zhong L, Huang S, Mao SX, Zhu T, Huang JY. Size-dependent fracture of silicon nanoparticles during lithiation. *ACS nano* **6**, 1522-1531 (2012).

48. McDowell MT*, et al.* In situ TEM of two-phase lithiation of amorphous silicon nanospheres. *Nano Letters* **13**, 758-764 (2013).

49. McDowell MT, Lee SW, Wang C, Nix WD, Cui Y. Studying the kinetics of crystalline silicon nanoparticle lithiation with in situ transmission electron microscopy. *Advanced Materials* **24**, 6034-6041 (2012).

50. Liu XH, Fan F, Yang H, Zhang S, Huang JY, Zhu T. Self-limiting lithiation in silicon nanowires. *ACS nano* **7**, 1495-1503 (2013).

51. Ghassemi H, Au M, Chen N, Heiden PA, Yassar RS. In situ electrochemical lithiation/delithiation observation of individual amorphous Si nanorods. *ACS nano* **5**, 7805-7811 (2011).

52. Leblanc D, Wang C, He Y, Bélanger D, Zaghib K. In situ transmission electron microscopy observations of lithiation of spherical silicon nanopowder produced by induced plasma atomization. *Journal of Power Sources* **279**, 522-527 (2015).

53.Yuk JM, Seo HK, Choi JW, Lee JY. Anisotropic lithiation onset in silicon nanoparticle anode revealed by in situ graphene liquid cell electron microscopy. *ACS nano* **8**, 7478-7485 (2014).

54. Luo L, Wu J, Luo J, Huang J, Dravid VP. Dynamics of electrochemical lithiation/delithiation of graphene-encapsulated silicon nanoparticles studied by in-situ TEM. *Scientific reports* **4**, (2014).

55. Liu XH*, et al.* In situ atomic-scale imaging of electrochemical lithiation in silicon. *Nature nanotechnology* **7**, 749-756 (2012).

56. Liu XH*, et al.* Anisotropic swelling and fracture of silicon nanowires during lithiation. *Nano Letters* **11**, 3312-3318 (2011).

57. Janish MT, Mackay DT, Liu Y, Jungjohann KL, Carter CB, Norton MG. TEM in situ lithiation of tin nanoneedles for battery applications. *Journal of Materials Science* **51**, 589-602 (2016).

58. Liang W*, et al.* Tough germanium nanoparticles under electrochemical cycling. *ACS nano* **7**, 3427-3433 (2013).

59. Liu XH, Huang S, Picraux ST, Li J, Zhu T, Huang JY. Reversible nanopore formation in Ge nanowires during lithiation–delithiation cycling: An in situ transmission electron microscopy study. *Nano Letters* **11**, 3991-3997 (2011).

60. Liu Y, Hudak NS, Huber DL, Limmer SJ, Sullivan JP, Huang JY. In situ transmission electron microscopy observation of pulverization of aluminum nanowires and evolution of the thin surface Al2O3 layers during lithiation–delithiation cycles. *Nano Letters* **11**, 4188-4194 (2011).

61. Su Q, Dong Z, Zhang J, Du G, Xu B. Visualizing the electrochemical reaction of ZnO nanoparticles with lithium by in situ TEM: two reaction modes are revealed. *Nanotechnology* **24**, 255705 (2013).

62. Liang W*, et al.* Nanovoid Formation and Annihilation in Gallium Nanodroplets under Lithiation–Delithiation Cycling. *Nano Letters* **13**, 5212-5217 (2013).

63. Gregorczyk KE, Liu Y, Sullivan JP, Rubloff GW. In situ transmission electron microscopy study of electrochemical lithiation and delithiation cycling of the conversion anode RuO2. *ACS nano* **7**, 6354-6360 (2013).

64. Wang X, *et al.* Revealing the conversion mechanism of CuO nanowires during lithiation–delithiation by in situ transmission electron microscopy. *Chemical Communications* **48**, 4812-4814 (2012).

65. Su Q, Xie D, Zhang J, Du G, Xu B. In situ transmission electron microscopy observation of the conversion mechanism of Fe2O3/graphene anode during lithiation–delithiation processes. *ACS nano* **7**, 9115-9121 (2013).

66. Nie A, *et al.* Atomic-Scale Observation of Lithiation Reaction Front in Nanoscale SnO2 Materials. *ACS nano* **7**, 6203-6211 (2013).

67. Huang JY, *et al.* In situ observation of the electrochemical lithiation of a single SnO2 nanowire electrode. *Science* **330**, 1515-1520 (2010).

68. Wang F, *et al.* Tracking lithium transport and electrochemical reactions in nanoparticles. *Nature communications* **3**, 1201 (2012).

69. Cheng Y, Nie A, Zhang Q, Gan L-Y, Shahbazian-Yassar R, Schwingenschlogl U. Origin of the Phase Transition in Lithiated Molybdenum Disulfide. *ACS nano* **8**, 11447-11453 (2014).

70. Luo L, Wu J, Xu J, Dravid VP. Atomic resolution study of reversible conversion reaction in metal oxide electrodes for lithium-ion battery. *ACS nano* **8**, 11560-11566 (2014).

71. Su Q, Xie J, Zhang J, Zhong Y, Du G, Xu B. In situ transmission electron microscopy observation of electrochemical behavior of CoS2 in lithium-ion battery. *ACS Applied Materials & Interfaces* **6**, 3016-3022 (2014).

72. Liu S, *et al.* Understanding Li-storage mechanism and performance of MnFe2O4 by in situ TEM observation on its electrochemical process in nano lithium battery. *Nano Energy* **8**, 84-94 (2014).

73. Xu Z-L, *et al.* In-situ TEM examination and exceptional long-term cyclic stability of ultrafine Fe 3 O 4 nanocrystal/carbon nanofiber composite electrodes. *Energy Storage Materials* **1**, 25-34 (2015).

74. Su Q, Chang L, Zhang J, Du G, Xu B. In situ TEM observation of the electrochemical process of individual CeO2/graphene anode for lithium ion battery. *The Journal of Physical Chemistry C* **117**, 4292-4298 (2013).

75. Shan X-Y, Zhou G, Yin L-C, Yu W-J, Li F, Cheng H-M. Visualizing the roles of graphene for excellent lithium storage. *Journal of Materials Chemistry A* **2**, 17808-17814 (2014).

76. Li Y, Yan K, Lee H-W, Lu Z, Liu N, Cui Y. Growth of conformal graphene cages on micrometre-sized silicon particles as stable battery anodes. *Nature Energy* **1**, 15029 (2016).

77. Wang C-M*, et al.* In situ TEM investigation of congruent phase transition and structural evolution of nanostructured silicon/carbon anode for lithium ion batteries. *Nano Letters* **12**, 1624-1632 (2012).

78. Liu N, Wu H, McDowell MT, Yao Y, Wang C, Cui Y. A yolk-shell design for stabilized and scalable Li-ion battery alloy anodes. *Nano Letters* **12**, 3315-3321 (2012).

79. Gu M*, et al.* In situ TEM study of lithiation behavior of silicon nanoparticles attached to and embedded in a carbon matrix. *ACS nano* **6**, 8439-8447 (2012).

80. Zhu B, Liu N, McDowell M, Jin Y, Cui Y, Zhu J. Interfacial stabilizing effect of ZnO on Si anodes for lithium ion battery. *Nano Energy* **13**, 620-625 (2015).

81. Lu X, Bogart TD, Gu M, Wang C, Korgel BA. In Situ TEM Observations of Sn-Containing Silicon Nanowires Undergoing Reversible Pore Formation Due to Fast Lithiation/Delithiation Kinetics. *The Journal of Physical Chemistry C* **119**, 21889-21895 (2015).

82. Liu Y*, et al.* Tailoring lithiation behavior by interface and bandgap engineering at the nanoscale. *Nano Letters* **13**, 4876-4883 (2013).

83. Nie A*, et al.* Twin Boundary-Assisted Lithium Ion Transport. *Nano Letters* **15**, 610-615 (2015).

84. Wang Q, Ping P, Zhao X, Chu G, Sun J, Chen C. Thermal runaway caused fire and explosion of lithium ion battery. *Journal of Power Sources* **208**, 210-224 (2012).

85. Johnson CS. Development and utility of manganese oxides as cathodes in lithium batteries. *Journal of Power Sources* **165**, 559-565 (2007).

86. Konishi H, Yuasa T, Yoshikawa M. Thermal stability of Li1−yNixMn(1−x)/2Co(1−x)/2O2 layer-structured cathode materials used in Li-Ion batteries. *Journal of Power Sources* **196**, 6884-6888 (2011).

87. Wu HB, Chen JS, Hng HH, Lou XWD. Nanostructured metal oxide-based materials as advanced anodes for lithium-ion batteries. *Nanoscale* **4**, 2526-2542 (2012).

88. Thackeray M. Structural considerations of layered and spinel lithiated oxides for lithium ion batteries. *Journal of the electrochemical society* **142**, 2558-2563 (1995).

89. Poizot P, Laruelle S, Grugeon S, Dupont L, Tarascon J. Nano-sized transition-metal oxides as negative-electrode materials for lithium-ion batteries. *Nature* **407**, 496-499 (2000).

90. Pralong V, Leriche J-B, Beaudoin B, Naudin E, Morcrette M, Tarascon J-M. Electrochemical study of nanometer Co 3 O 4, Co, CoSb 3 and Sb thin films toward lithium. *Solid State Ionics* **166**, 295-305 (2004).

91. Wu Z-S*, et al.* Graphene anchored with Co3O4 nanoparticles as anode of lithium ion batteries with enhanced reversible capacity and cyclic performance. *ACS nano* **4**, 3187-3194 (2010).

92. Wu H, Cui Y. Designing nanostructured Si anodes for high energy lithium ion batteries. *Nano Today* **7**, 414-429 (2012).

93. Li J*, et al.* Improve first-cycle efficiency and rate performance of layered-layered Li1. 2Mn0. 6Ni0. 2O2 using oxygen stabilizing dopant. *ACS Applied Materials & Interfaces* **7**, 16040-16045 (2015).

94. Legros M, Dehm G, Arzt E, Balk TJ. Observation of giant diffusivity along dislocation cores. *Science* **319**, 1646-1649 (2008).

95. Verma P, Maire P, Novák P. A review of the features and analyses of the solid electrolyte interphase in Li-ion batteries. *Electrochimica Acta* **55**, 6332-6341 (2010).

96. Gu M*, et al.* Demonstration of an electrochemical liquid cell for operando transmission electron microscopy observation of the lithiation/delithiation behavior of Si nanowire battery anodes. *Nano Letters* **13**, 6106-6112 (2013).

97. Li D, Nielsen MH, Lee JR, Frandsen C, Banfield JF, De Yoreo JJ. Direction-specific interactions control crystal growth by oriented attachment. *Science* **336**, 1014-1018 (2012).

98. Unocic RR*, et al.* Probing battery chemistry with liquid cell electron energy loss spectroscopy. *Chemical Communications* **51**, 16377-16380 (2015).

99. Wang Y*, et al.* Design principles for solid-state lithium superionic conductors. *Nature materials* **14**, 1206-1031 (2015).

100. Motavalli J. Technology: A solid future. *Nature* **526**, S96-S97 (2015).

101. Wang Z*, et al.* In Situ STEM-EELS Observation of Nanoscale Interfacial Phenomena in All-Solid-State Batteries. *Nano Letters* **16**, 3760-3767 (2016).

102. Santhanagopalan D*, et al.* Interface limited lithium transport in solid-state batteries. *The journal of physical chemistry letters* **5**, 298-303 (2013).

103. Thackeray MM, Wolverton C, Isaacs ED. Electrical energy storage for transportation—approaching the limits of, and going beyond, lithium-ion batteries. *Energy & Environmental Science* **5**, 7854-7863 (2012).

104. Bruce PG, Freunberger SA, Hardwick LJ, Tarascon J-M. Li-O2 and Li-S batteries with high energy storage. *Nature materials* **11**, 19-29 (2012).

105. Manthiram A, Fu Y, Chung S-H, Zu C, Su Y-S. Rechargeable lithium–sulfur batteries. *Chemical reviews* **114**, 11751-11787 (2014).

106. Luntz A. Beyond Lithium Ion Batteries. *The journal of physical chemistry letters* **6**, 300-301 (2015).

107. Yabuuchi N, Kubota K, Dahbi M, Komaba S. Research development on sodium-ion batteries. *Chemical reviews* **114**, 11636-11682 (2014).

108. Lin M-C*, et al.* An ultrafast rechargeable aluminium-ion battery. *Nature* **520**, 324-328 (2015).

109. Singh N, Arthur TS, Ling C, Matsui M, Mizuno F. A high energy-density tin anode for rechargeable magnesium-ion batteries. *Chemical Communications* **49**, 149-151 (2013).

110. Young MJ, Holder AM, George SM, Musgrave CB. Charge Storage in Cation Incorporated α-MnO2. *Chemistry of Materials* **27**, 1172-1180 (2015).

111. Tompsett DA, Islam MS. Electrochemistry of Hollandite α-MnO2: Li-Ion and Na-Ion Insertion and Li2O Incorporation. *Chemistry of Materials* **25**, 2515-2526 (2013).

112. Nie A*, et al.* Lithiation-Induced Shuffling of Atomic Stacks. *Nano Letters* **14**, 5301-5307 (2014).

113. Su Q*, et al.* In Situ Transmission Electron Microscopy Investigation of the Electrochemical Lithiation–Delithiation of Individual Co9S8/Co-Filled Carbon Nanotubes. *ACS nano* **7**, 11379-11387 (2013).

114. Woehl TJ, Jungjohann KL, Evans JE, Arslan I, Ristenpart WD, Browning ND. Experimental procedures to mitigate electron beam induced artifacts during in situ fluid imaging of nanomaterials. *Ultramicroscopy* **127**, 53-63 (2013).

115. Krexner G, Prem M, Beuneu F, Vajda P. Nanocluster Formation in Electron-Irradiated L i 2 O Crystals Observed by Elastic Diffuse Neutron Scattering. *Physical review letters* **91**, 135502 (2003).

116. Lee SW, McDowell MT, Choi JW, Cui Y. Anomalous shape changes of silicon nanopillars by electrochemical lithiation. *Nano Letters* **11**, 3034-3039 (2011).

117. Park MH, Cho Y, Kim K, Kim J, Liu M, Cho J. Germanium Nanotubes Prepared by Using the Kirkendall Effect as Anodes for High‐Rate Lithium Batteries. *Angewandte Chemie* **123**, 9821-9824 (2011).

118. Abellan P*, et al.* Probing the degradation mechanisms in electrolyte solutions for Li-ion batteries by in situ transmission electron microscopy. *Nano Letters* **14**, 1293-1299 (2014).

119. Schneider NM, Norton MM, Mendel BJ, Grogan JM, Ross FM, Bau HH. Electron–water interactions and implications for liquid cell electron microscopy. *The Journal of Physical Chemistry C* **118**, 22373-22382 (2014).

Chapter 4. Asynchronous Crystal Cell Expansion during Lithiation of K⁺-Stabilized α-MnO₂[②]

4.1. Introduction

Manganese dioxide (MnO_2) is well known as an important functional metal oxide being applied in the fields of biosensor, ion exchange, catalysis, molecular adsorption, and particularly, energy storage.[1-4] These various applications originate from the polymorphic property of MnO_2, which allows the existence of different structural forms (α-, β-, γ-, δ-types, etc.).[5-7] These forms differ in the way the structure units ([MnO_6] octahedra) are interlinked. As such, they possess interlayers or tunnels with gaps of different sizes in Å range.[8] Figure 4.1 illustrates crystal structures of tunnel-based MnO_2 polymorphs. Among them, hollandite α-MnO_2 is body-centered tetragonal with I4/m space group and has one dimensional 2×2 (4.6 Å × 4.6 Å) and 1×1 (1.9 Å × 1.9 Å) tunnels intergrowth along c axis,[8] as shown in Figures 4.1c and 4.1d. The 2×2 tunnels are generally stabilized by cations (NH_4^+, Ba^{2+}, Ag^+, K^+ etc.) introduced during synthesis process.[2,9]

Its low cost, natural abundance[10] and environmental friendliness[11] make α-MnO_2 one of the most important materials for electric energy storage in lithium ion battery, supercapacitor and Li-O_2 battery. For this application, the presence of tunnels plays a key role as the reversible capacity is largely determined by tunnel-driven (de)intercalation of Li^+.[12-14] α-MnO_2 is believed to show topotactic reduction of Mn (Li^+ solid solution) during lithiation. Specifically, partially lithiated α-MnO_2 was reported to show identical expansion tendency along a and b directions, and thus, the

---

tetragonal symmetry is maintained without any phase transition.[15-17] On the other hand, several groups pointed out that the first galvanostatic discharge curve of Li/α-MnO$_2$ battery was characterized by stepwise potential variation or obvious voltage multi-plateaus, indicating existence of phase transition.[18-20] Yet, none of them could provide direct structural evidence for these specific lithiation stages. In addition, it is still unclear what is the origin for the commonly observed low electrode utilization of α-MnO$_2$, where the discharge capacity is less than 60% of the theoretical value.[20]
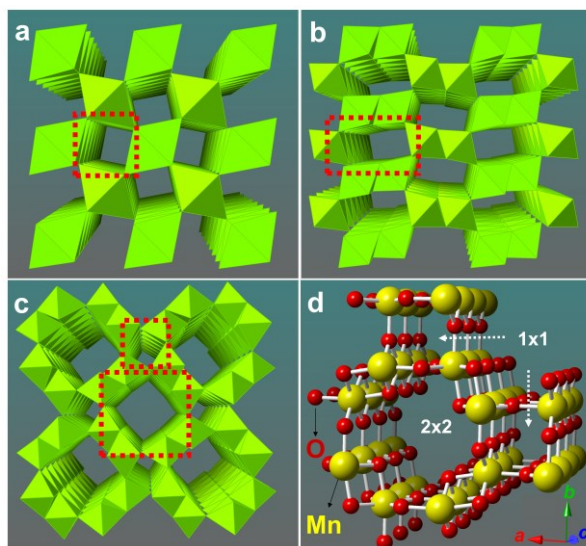
Figure 4.1 (a-c): Crystal structures of β- (1×1 tunnel), γ- (1×2 tunnel), and α-MnO$_2$ (1×1 and 2×2 tunnels) using [MnO$_6$] octahedra model demonstrating the tunnel structures by red dashed squares. (d): Atomic structure of one 2×2 tunnel and two adjacent 1×1 tunnels of α-MnO$_2$ growing along [001] (*c*-axis).

These uncertainties result mainly from two practical limitations: first, it is difficult to precisely characterize Å-sized tunnels in MnO$_2$ due to resolution limitations of the most characterization techniques. Second, under electrochemical cycling, it is difficult to acquire structural and compositional information with any conventional ex-situ electrochemistry methods. In-situ Transmission Electron Microscopy (TEM) nanoscale electrochemistry studies using an "open-cell" concept has recently been developed[21] and proved later by many experiments to be powerful in real-time study

of electrode materials such as graphene,[22] Si,[23-25] Ge,[26] CuO,[27] ZnO,[28] TiO$_2$,[29] SnO$_2$,[30] FeF$_2$,[31] LiFePO$_4$[32] and different nanocomposites[33-35] under electrochemical cycling.

In this paper, in-situ Scanning TEM (STEM) was used for the study of lithiation behavior in single crystalline α-MnO$_2$ nanowire. Local morphological changes including lattice expansion and Mn valence evolution of the nanowire during dynamic lithiation process are revealed. Our findings show that α-MnO$_2$ nanowire exhibits two types of tunnels: 1×1 and K$^+$-stabilized 2×2 tunnels. Lithiation of α-MnO$_2$ nanowires is characterized by asynchronous behavior of lattice parameters a and b, resulting in a Tetragonal-Orthorhombic-Tetragonal (TOT) symmetrical transition of lithiated α-MnO$_2$. This is contradicting to the widely accepted understanding that a and b lattice parameters expand synchronously when tetragonal α-MnO$_2$ is discharged. DFT calculation reveals that the asynchronous lattice expansion originates from Li$^+$ preferably occupying Wyckoff 8h sites inside 2×2 tunnels in a specific sequence. The symmetry transition of α-MnO$_2$ electrode during lithiation is expected to explain the appearance of stepwise potential variations during discharge and the commonly observed low electrode utilization in Li/MnO$_2$ batteries.[10,36,37]

4.2. Methods

The experimental details for the nanowire synthesis, TEM sample preparation, *ex situ* and *in situ* TEM operation and simulations are provided in Appendix A.

4.3. Results and discussion

Figure 4.2 shows the atomic structure of an α-MnO$_2$ nanowire prepared via hydrothermal method.[38] Figures 4.2a and b indicate that the nanowire is single crystalline α-MnO$_2$ phase with growth direction (*c*-axis) along [001]. HAADF image of the nanowire viewed along <010> is given in Figure 4.2c with the corresponding Inverse Fast Fourier Transform (IFFT) image and simulated crystal structure along

<010> direction given in Figures 4.2d and e, respectively. The Mn atomic columns, marked by yellow dots in IFFT, can be easily identified. The appearance of O atoms in every two Mn columns contributes to the alternative changes in the brightness of Mn columns as marked by the yellow dots in two different sizes (Figure 4.2d). Close examination of figures 4.2c and d indicates that there are extra atomic columns lining up between two Mn columns, as marked by the pink dots. Considering the hydrothermal synthesis where potassium (K^+) was present (see Supporting Information), these extra columns are indicative of K atoms acting as stabilizers inside 2×2 tunnels of α-MnO$_2$. This was subsequently confirmed by energy dispersive spectroscopy (EDS) as discussed in the following.
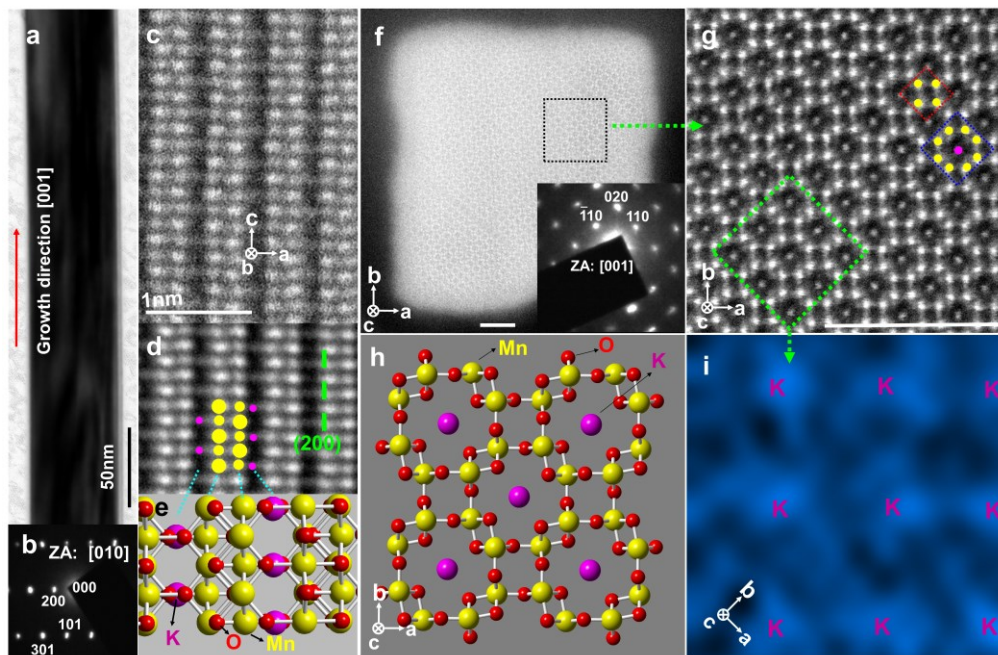
Figure 4.2 (a,b): TEM image of a single α-MnO$_2$ nanowire and its SAED along <010>; (c): HAADF image of the same α-MnO$_2$ nanowire along <010>; (d,e): IFFT of the original HAADF shown in (c) and the atomic model structure along <010> direction, respectively. Yellow spots indicate Mn atoms, while pink represents K and red indicates O atoms. (f): HAADF image of an α-MnO$_2$ nanowire cross section and the corresponding SAED along [001] direction; (g): Atomic resolution HAADF image of an area in f (black dotted box) showing Mn atomic column (yellow), K column (pink), 1×1 (red dotted square) and 2×2 (blue dotted square) tunnels. Scale

bars in f and g are both 3 nm; (h): The simulated image of K^+-occupied α-MnO$_2$ viewed along [001] direction; (i): EDS mapping of the green dotted box in g confirms the center atoms to be K (this figure is rotated 45° compared to g for viewer's convenience).

The HAADF image in Figure 4.2f shows the cross section of an α-MnO$_2$ nanowire viewed along [001] zone axis (inset). The sample preparation method is provided in the Supporting Information. The magnified HAADF image in Figure 4.2g clearly shows that the atomic structure consists of two types of tunnels: the small 1×1 tunnels and the large 2×2 tunnels as indicated by the red and blue dashed squares, respectively. This definition is based on the number of [MnO$_6$] octahedra in each side.[39] The 1×1 tunnels are expected to have limited contribution to the discharge capacity while 2×2 tunnels determine the overall discharge capacity in cathodic application of α-MnO$_2$ nanowires.[40]

The bright spots surrounding each tunnel refer to Mn ([MnO$_6$]) atomic columns (yellow dots) while the spots in the center of each 2×2 tunnel belongs to K ions (pink spots), as confirmed by EDS mapping of K signal in Figure 4.2i. To the authors' knowledge, this [001] zone axis image is the first atomistic observation of the tunneled structure in α-MnO$_2$ capturing the position of tunnel stabilizers. Considering figures 4.2d and g, the Wyckoff Position of K^+ in α-MnO$_2$ is determined to be 2a site (0, 0, 0), which is in excellent agreement with the theoretical K^+ position[41]. The composition of the nanowire is thus determined to be K$_{0.25}$MnO$_2$.

The *in situ* setup and time sequence TEM images of an α-MnO$_2$ nanowire during lithiation along [010] zone axis are shown in Figure A1 and Movie A1 in Appendix A. They show that the lithiation process is associated with two distinct expansion fronts. The first expansion front proceeds quickly (42 nm/min on average) along the nanowire and results in fast radial expansion. Subsequently, the second expansion happens with slower propagation speed (28 nm/min) than the first reaction front,

indicating lithiation retardation probably due to the electrochemical-induced stresses. The section squeezed by these two reaction fronts maintains a constant diameter. For another α-MnO$_2$ nanowire viewed along [100] zone axis, however, the lithiation process is sharply different as shown in Figure A2. In this nanowire, one cannot detect the two reaction front phenomena during lithiation, and instead, a gradual increase in diameter was observed. This is intriguing knowing that the [010] and [100] zone axes of α-MnO$_2$ should essentially exhibit similar lithiation behavior due to the tetragonal crystal symmetry. It is unlikely that such a deviation is due to any experimental error as this observation was repeatable for nanowires under [010] (figures A3, A4a) and [100] (Fig.A4b, Movie A2) zone axes. It is worth mentioning that some pristine nanowires show "bundling" phenomenon (figures 4.3a, 4.5a, A3 and A4b), which should be caused by lateral oriented attachment (OA) growth mechanism that is widely accepted for solution-grown α-MnO$_2$ nanowires[39,42,43]. This mechanism is also confirmed in Fig.A5 showing that one secondary nanowire branches at its end while still maintains single crystalline property. Considering the facts that the OA mechanism still results in single crystals and that the two-step expansion (or single expansion) situation appears in both bundled and non-bundled nanowires (see figures A1-4) with varying diameters, the size and morphology factors can be excluded.

Figure 4.3 shows the morphological analysis for the two nanowires viewed along [010] and [100] zone axes. Figure 4.3a shows the [010] projection of the partially lithiated nanowire where the two-reaction fronts feature is captured. The first reaction front (red dashed line) shows a conical shape visualized by contrast change indicating the existence of surface lithiation[44]. Since the conical angle (about 90º) here is much larger than the previously reported angle (15º-20º)[44] for other materials, longitudinal lithiation is believed to play a key role in the formation of the first reaction front. The second reaction front (blue dashed line) appears to be relatively flat and results in formation of numerous small nanoparticles (marked as black circles) embedded in the matrix. The section between the two reaction fronts has a constant diameter with

uniform image contrast implying good structural stability upon lithiation in this area. As such, four zones $A_{[010]}$, $B_{[010]}$, $C_{[010]}$ and $D_{[010]}$ with distinct features are defined in Figure 4.3a. The quantitative description of changes in the diameter of this nanowire is represented in this figure.
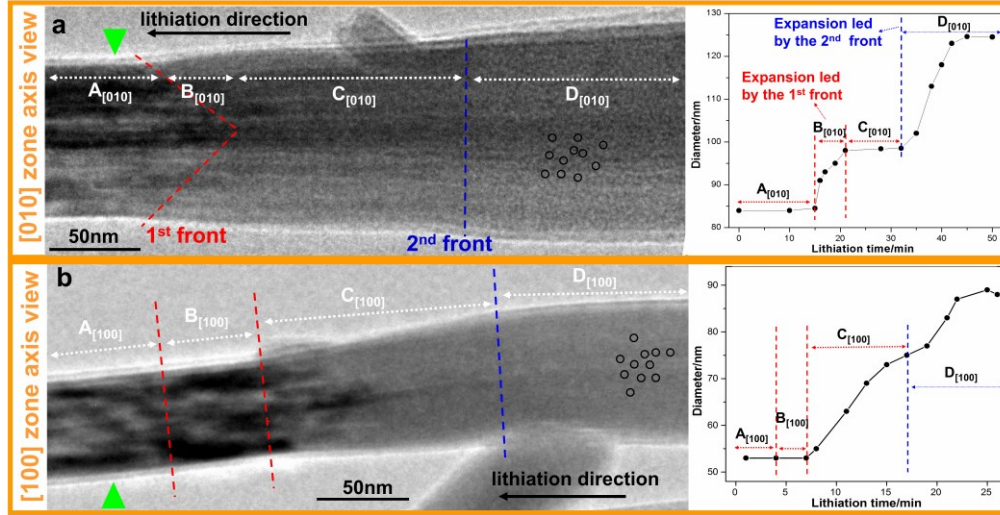
Figure 4.**3** (a): [010] TEM projection of a partially lithiated α-MnO$_2$ nanowire showing two lithiation reaction fronts. The red dashed line corresponds to the first reaction front and the blue dashed line relates to the second reaction front. Four zones with different characteristics are defined: Zone $A_{[010]}$ for unlithiated section of the nanowire, Zone $B_{[010]}$ for the expanded region associate with the first reaction front, Zone $C_{[010]}$ for the section with a constant diameter surrounded between two reaction fronts, and Zone $D_{[010]}$ for the fully expended region associated with the second reaction front and featured by numerous nanodomains (black circles). The right graph shows diameter evolution during lithiation. (b): [100] projection of the partially lithiated α-MnO$_2$ nanowire showing a gradually expanding zone. Similarly, four zones are defined: Zone $A_{[100]}$ for pristine nanowire, Zone $B_{[100]}$ for stressed (dark contrast) section without diameter expansion, Zone $C_{[100]}$ for gradually expanding section and Zone $D_{[100]}$ for the final lithiated state featured by numerous nanodomains (black circles). The right graph shows diameter evolution during lithiation. The green triangles in Figure 3a and 3b indicate the fixed positions on two nanowires for diameter measurement.

Figure 4.3b shows the [100] projection of the partially lithiated α-MnO$_2$ nanowire without observation of any two-reaction fronts feature. Instead, a gradually expanding Zone C$_{[100]}$ was observed as seen in the graph in Figure 4.3b. It is notable that although the two-reaction front feature is not detectable in this case, a highly stressed Zone B$_{[100]}$ appears just ahead of the gradually expanding Zone C$_{[100]}$. Zone B$_{[100]}$ is characterized by the obvious dark contrast, indicating possible existence of lithiation-induced strain in this area. Interestingly, Zone B$_{[100]}$ shows no sign of diameter change.

To better understand the underlying mechanisms responsible for the morphological evaluation of the nanowires viewed at [100] and [010] zone axes during lithiation, phase analysis is carried out. Figures 4.4a-d show SAED patterns for the four different zones (A$_{[010]}$-D$_{[010]}$) designated in Figure 4.3a for a partially lithiated nanowire viewed along [010] zone axis. In Zone A$_{[010]}$, the nanowire is still in pristine state (no lithiation). The (200) plane that is parallel to the growth direction [001] has a characteristic spacing of 4.9 Å, which equals to *a*/2 of α-MnO$_2$ unit cell and thus is used as a signature of α-MnO$_2$ tunneled structure. For Zone B$_{[010]}$, the diffraction pattern still belong to α-MnO$_2$ phase but it is blurred and stretched along [100] direction, indicating the existence of structural distortion due to lattice deflection induced by Li$^+$ intercalation. This can be attributed to Jahn−Teller distortion of [MnO$_6$] units when Mn is partially reduced from smaller Mn^{4+} ions to larger Mn^{3+} ions due to the insertion of Li$^+$.[45] From Zone A$_{[010]}$ to Zone B$_{[010]}$, the (200) spacing increases from 4.9 to 5.3 Å. No distortion is observed along the longitudinal direction [001] further conforming the anisotropic expansion behavior of α-MnO$_2$ as reported by others[15,46]. It is surprising to observe in Figure 4.4c that the tunneled structure inside Zone C$_{[010]}$ is well maintained with (200) lattice showing no obvious expansion throughout this zone, which is apparently squeezed by two swelling reaction fronts. The microscopically constant (200) spacing should account for the macroscopically observed constant diameter through Zone C$_{[010]}$ in Figure 4.3a. Figure 4.4d shows a completely different diffraction pattern for Zone D$_{[010]}$, where the bright and sharp

rings are indexed to be polycrystalline Li_2O indicating the formation of Li_2O following the second lithiation front. The diffused ring(s) relates to the formation of nanoparticles of Mn as shown in Zone $D_{[010]}$ by black circles in Figure 4.3a. The average diameter of Mn nanoparticles was measured to be 3 nm. HRTEM images in Figures 4.4e-h for the four zones clearly demonstrate the evolution of α-MnO_2 (200) lattice and agree well with corresponding SAED patterns.
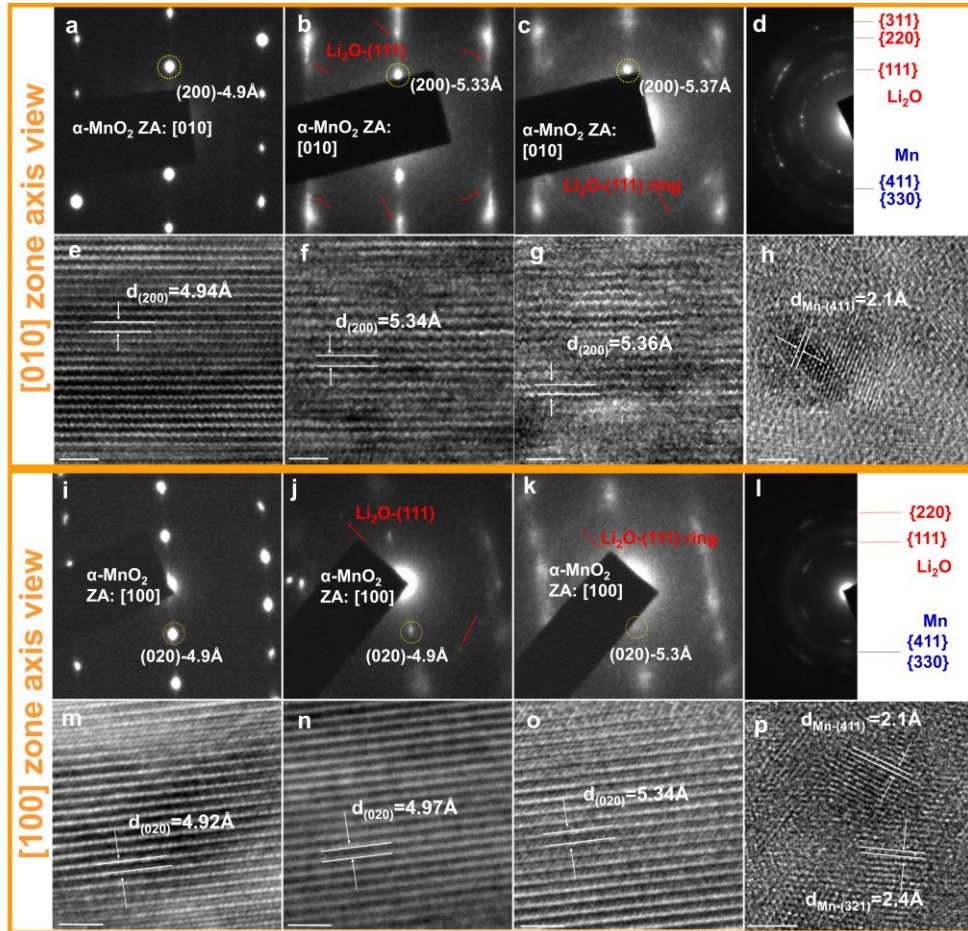
Figure 4.4 (a-d): The corresponding SAED patterns from the four zones shown in Figure 4.3a. SAD pattern shown in (a) is for Zone $A_{[010]}$, (b) from the right end of Zone $B_{[010]}$, (c) from the right end of Zone $C_{[010]}$ and (d) for Zone $D_{[010]}$. (e-h): The corresponding to the HRTEM images of zones $A_{[010]}$, $B_{[010]}$, $C_{[010]}$ and $D_{[010]}$. (i-l): The corresponding SAED patterns from the four lithiation zones shown in Figure 4.3b where (i) is for Zone $A_{[100]}$, (j) is from the right end of Zone $B_{[100]}$, (k) is from

the right end of Zone $C_{[100]}$, and (l) is for Zone $D_{[100]}$. (m-p): The corresponding HRTEM images for zones $A_{[100]}$, $B_{[100]}$, $C_{[100]}$ and $D_{[100]}$. The scale bar is 2 nm.

Figures 4.4i-l show SAED patterns for the four lithiation zones marked as $A_{[100]}$-$D_{[100]}$ in Figure 4.3b. Figure 4.4i confirms the pristine nanowire to be single crystalline α-MnO_2 viewed along [100] zone axis with its (020) spacing of 4.9 Å. The α-MnO_2 diffraction pattern in Figure 4.4j is blurred, indicating lattice distortion possibly due to initial lithiation in Zone $B_{[100]}$. Overall, however, the (020) spacing is still maintained at 4.9 Å without obvious expansion. As evident from the diffraction pattern, small amount of Li_2O forms during this stage confirming the existence of initial lithiation. Figure 4.4k shows that α-MnO_2 pattern from Zone $C_{[100]}$ is further blurred but still maintains the tunneled structure as the (020) lattice is still clear and gradually expands from 4.9 to 5.3 Å. Figure 4.4l shows that the host in Zone $D_{[100]}$ is thoroughly reduced to Mn and Li_2O via conversion reaction. Figures 4.4m-p show HRTEM images of (020) lattice for the four zones and they match the corresponding SAED patterns very well.

The *d* spacing of 2.1 and 2.4 Å in figures 4.4h and p belong to the $(411)_{Mn}$ and $(321)_{Mn}$ planes, respectively. This confirms the formation of Mn nanoparticles in Zone $D_{[010]}$ and Zone $D_{[100]}$. See also Figure A6 for more evidence. As such, one can conclude that under both [010] and [100] projections, Zone D is the fully lithiated stage featured by conversion reaction usually found in deep discharged transitional metal oxides. In this paper, however, we will not focus on this conversion reaction as it has been discussed extensively by others [31,47,48].

For nanowires viewed along [100] and [010] zone axes, we focus on Zone $B_{[010]}$ and Zone $B_{[100]}$, Zone $C_{[010]}$ and Zone $C_{[100]}$, where the nanowires are partially lithiated and show interesting morphologies. Considering the facts that {020} spacing reflects the dimension of lattice parameters *a* and *b*, and that [010] TEM projection is sensitive to the evolution of lattice *a* but insensitive to that of *b* (vise versa for [100]

projection), we hypothesize that this morphological difference originates from asynchronous expansion of α-MnO$_2$ unit cell along [100] (*a* direction) and [010] (*b* direction). Specifically, in the initial Li$^+$ intercalation (zones B$_{[010]}$ and B$_{[100]}$), lattice parameter *a* is expected to expand with *b* keeping constant; in the following Li$^+$ intercalation stage (zones C$_{[010]}$ and C$_{[100]}$), it is likely that *a* remains constant while *b* expands gradually to catch up with *a*. During this process, *a/b* ratio reaches a maximum value around 1.1 at the end of zones B$_{[010]}$ and B$_{[100]}$ and then returns to 1 at the end of zones C$_{[010]}$ and C$_{[100]}$, resulting in a Tetragonal-Orthorhombic-Tetragonal (TOT) symmetry transition. It will be discussed below that the proposed asynchronous expansion is associated with sequential filling of tunnels in α-MnO$_2$ with lithium ions. As such, electron energy loss spectroscopy (EELS) was applied to quantify the lithiation degree in zones B and C under both [010] and [100] zone axes by analyzing the Mn valence evolution. Since the chemical signal is less dependent on crystallographic orientation, it is expected that Mn valence evolution under [010] and [100] projections should show similarity in zones B and C.

To study the oxidation state evolution of Mn during lithiation, EELS line scans were performed on partially lithiated α-MnO$_2$ nanowires viewed along [010] and [100] zone axes. Figures 4.5a-c depict the analysis for the partially lithiated nanowire under [010] projection, while figures 4.5d-f represent the nanowire under [100] projection. The EELS data were analyzed from three key locations 1, 2 and 3 indicated by yellow dots on both nanowires to conduct Mn valence analysis. Figures 4.5b and e show the constructed whole spectra where the prepeak (K$_\alpha$) of oxygen K edge and Mn L$_3$/L$_2$ white lines are indicated. The physical origins of these peaks and observed Mn peak shift are explained in the Supporting Information.
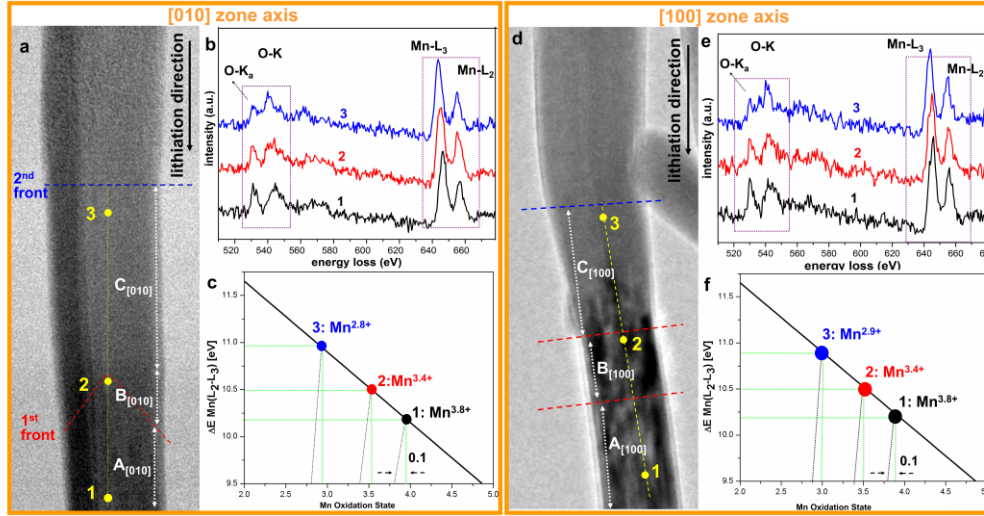
Figure 4.5 (a,d): [010] and [100] HAADF/TEM images of partially lithiated α-MnO$_2$ nanowires. The EELS data are extracted from three locations on the nanowire, i.e. 1 for Zone A$_{[010]}$ and Zone A$_{[100]}$, 2 around the end of Zone B$_{[010]}$ and Zone B$_{[100]}$, 3 around the end of Zone C$_{[010]}$ and Zone C$_{[100]}$. (b,e): The EELS spectra constructed from locations 1, 2 and 3 where the zero loss peak was calibrated as energy reference point. The purple-colored frames indicate O-K edge and Mn-L$_3$/L$_2$ edges. (c,f): Mn valence identification based on reference data using ΔE Mn(L$_2$-L$_3$) fingerprint; the black, red and blue dots correspond to locations 1, 2 and 3, respectively. Location 1 with known Mn$^{3.8+}$ valence is used to slightly offset the horizontal coordinate value for more precise valence identification of locations 2 and 3.

The EELS data for MnO$_2$ have several fingerprints that can be used to quantify Mn valence. The commonly used methods to analyze the valance change include the absolute energy shift of Mn white lines,[49] white-line intensity ratio L$_3$/L$_2$[50,51], oxygen K prepeak splitting,[52] branching energy difference ΔE(L$_2$-L$_3$)[53] and ΔE(L$_3$-O Kα)[54]. In our study, ΔE(L$_2$-L$_3$)[53] and ΔE(L$_3$-O Kα)[54] are independently used as the fingerprints to analyze Mn valence in different lithiation stages. Considering that K$^+$ presence could slightly alter the Fermi level of α-MnO$_2$, the known valence state of Mn$^{3.8+}$ (unlithiated composition is K$_{0.25}$MnO$_2$, which is rounded to be K$_{0.2}$MnO$_2$ for easier discussion) in Location 1 is used as an offset reference to the Mn valence study of locations 2 and 3. Since all the data points are obtained from the same line scan

across the same nanowire, these two ΔE methods are less likely to be affected by any instrumental variation.

To better determine the EELS peak positions, the fine structure of each peak is demonstrated in figures A7a, b, d and e. Figures 4.5c and f show the fitted linear curves for ΔE (L_2-L_3) vs Mn valence from a reference[53]. The symbolic points for locations 1, 2 and 3 are placed accordingly in the graph based on their specific ΔE values obtained from fine analysis in figures A7b and e. During this process, 0.1 offset value (for the Mn valence state) is calibrated and applied for valence quantification of locations 2 and 3. As such, the valence is determined to be $Mn^{3.4+}$ and $Mn^{2.8+}$ for locations 2 and 3 on [010] projected nanowire, and $Mn^{3.4+}$ and $Mn^{2.9+}$ for locations 2 and 3 on [100] projected nanowire. The alternative quantification method using $\Delta E(L_3$-O $K\alpha)$ fingerprint is demonstrated in figures A7c and f. The Mn valence is determined to be $Mn^{3.5+}$ and $Mn^{3.0+}$ for locations 2 and 3 on [010] projected nanowire, and $Mn^{3.5+}$ and $Mn^{3.0+}$ for locations 2 and 3 on [100] projected nanowire. It is evident that these two independent methods give similar Mn valence evolution in partially lithiated nanowires. For each method, Mn valence evolution from Zone $B_{[010]}$ to Zone $C_{[010]}$ and from Zone $B_{[100]}$ to Zone $C_{[100]}$ is also similar, confirming the proposed asynchronous expansion. By averaging these two methods, experimental Mn valence evolution is determined as following: $Mn^{(3.8+)}$ is reduced to $Mn^{(3.4+)}$ in Zone B; $Mn^{(3.4+)}$ is further reduced to $Mn^{(2.9+)}$ in Zone C; $Mn^{(2.9+)}$ is thoroughly reduced to $Mn^{(0)}$ in the following conversion reaction
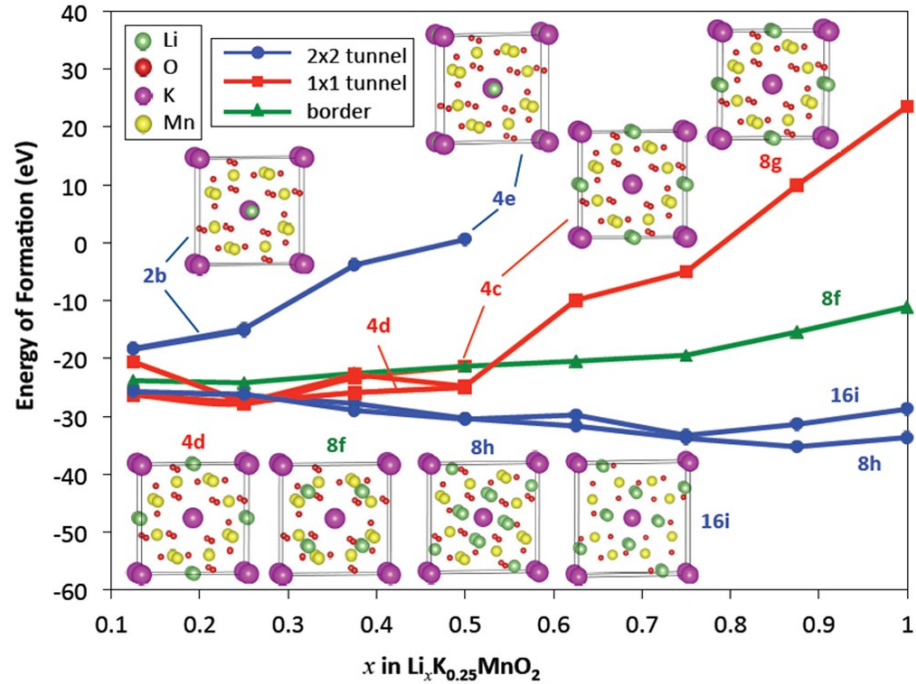
Figure 4.6 Demonstration of possible Li^+ insertion sites in α-MnO_2 as well as site occupancy energy calculation for possible Li^+ insertion sites. It can be seen that 4c, 4d and 8f sites are also initially preferred for Li^+ insertion, but their insertion energy increases very fast upon further lithiation. Thus the capacity contribution from 1×1 tunnels can be neglected here. 8h sites provide the lowest formation energy for Li^+ insertion up to $Li_1K_{0.25}MnO_2$.

It is known that Jahn-Teller distortion[55] occurs locally around certain [MnO_6] units that are close to the insertion sites for lithium.[45] According to our Density Functional Theory (DFT) simulation in Figure 4.6, there are different sites inside the 2×2 tunnels of K^+-stabilized α-MnO_2 that can accommodate Li^+. Interestingly, the center position (2b or 4e) in the tunnel is calculated to be unfavorable for initial lithium insertion, and instead, 8h sites near the tunnel walls provide the lowest binding energy for lithium accommodation up to Li_1MnO_2. The Li^+ occupancy at 8h sites of each 2×2 tunnel is not random but is predicted to exhibit a regular sequence. Figure 4.7a shows simulated Li^+ occupancy at 8h sites based on two adjacent 2×2 tunnels (there are two tunnels in the periodic unit cell) with K^+ placed at 2a sites.

84
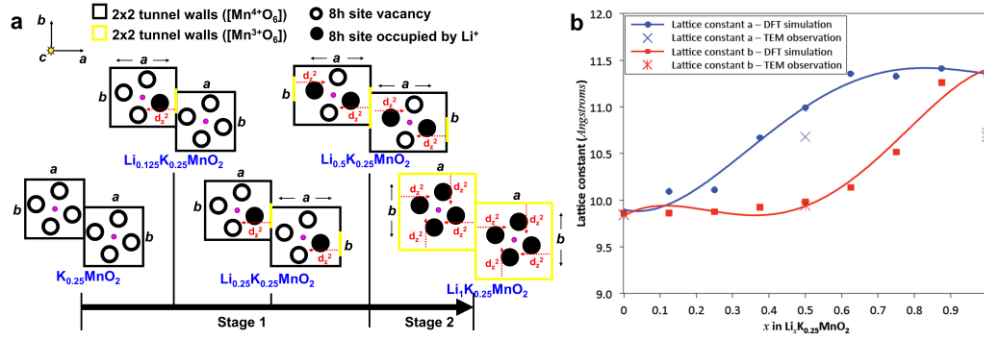
Figure 4.7 (a): Schematic of the occupancy of 8h sites in the ground state structures of α-$K_{0.25}Li_xMnO_2$ (pink dots: K^+ stabilizers at 2a sites; open circle: unoccupied 8h; solid circle: occupied 8h); d_z^2 is the orbital that distorts upon Mn reduction by Li^+ insertion. (b): Predicted behavior of lattice parameters *a* and *b* upon lithiation as well as their experimentally observed behavior during lithiation obtained from figures 4.4 and 4.5.

It can be seen that when the first lithium occupies the 8h site, the second Li^+ preferably fills the same site in the adjacent 2×2 tunnel (equivalent to $K_{0.25}Li_{0.25}MnO_2$). The third and fourth Li^+ fill the 8h sites that are the most remote from the first and second Li^+ in each 2×2 tunnel (equaling $K_{0.25}Li_{0.5}MnO_2$). This behavior is due to their mutual repulsive force resulting in a low energy configuration. The result is a cooperative Jahn-Teller expansion of the two opposite octahedral $[Mn^{(3+)}O_6]$ that strengthens each other to achieve unit cell expansion along [100] direction during lithiation Stage 1. Subsequently, inserted Li^+ ions occupy the remaining 8h sites during lithiation Stage 2. This process is accompanied by another Jahn-Teller expansion of the unit cell solely along [010] direction. The result of this sequential 8h site filling is asynchronous expansion across *a-b* plane, where the lattice parameter *a* first increases in Stage 1 while it remains constant in Stage 2. On the other hand, the lattice parameter *b* remains unchanged in Stage 1 and then increases in Stage 2. The simulated Li^+ occupancy sequence at 8h sites along [001] direction was also calculated based on a two-layer tunnel model with two Li^+ inserted. The result is shown in Fig.A8 demonstrating five Li^+ possible configurations. It can be seen that when *c*-axis lithiation is considered, the second Li^+ prefers to occupy either

two remote 8h sites in one 2×2 tunnel (Situation 5) or two 8h sites in two 2×2 tunnels aligning parallel to c axis (Situation 1). Both of these two situations, with successive lithiation occurring, can result in a strengthened Jahn-Teller distortion along one specific direction (a-[100]), while situations 2 (strengthened distortion), 3 and 4 (counterbalanced distortion) are less likely to appear thermodynamically.

Fig. 4.7b illustrates the theoretical DFT calculation of the evolution of lattice parameters a and b as well as the in-situ TEM experimental data based on figures 4.4 and 4.5. It can be seen that the trend in differential expansion of lattice parameters a and b is in agreement with TEM observation. However, it can also be seen that the magnitude in the predicted lattice parameters is larger for $x > 0.25$. This discrepancy in the magnitude is most likely caused by two reasons: first, DFT assumes tunnel stabilizer K^+ to be fixed in Wyckoff 2a site upon Li^+ insertion at 8h sites nearby, while partial removal of K atoms in the lithiated nanowire was experimentally observed (Figure A9); the second reason is the difficulty with DFT functionals accurately and simultaneously predicting a wide range of physical properties of materials containing transition metal elements, and the tendency of PBE functionals to overestimate lattice constants with transition metals[56]. It is speculated that the interconnected 2×2 tunnels affect Li^+ occupancy sequence in each other through a chain interaction. Such an interaction would result in a macroscopically uniform 8h site occupancy configuration. Thus the nanowire macroscopically experiences asynchronous expansion first along [100] in Zone B and then along [010] direction in Zone C. Fig. 4.8 summarizes the whole process starting from unit cell simulation to experimental TEM observation.

As such, the full discharge process in single α-$K_{0.2}Mn^{(3.8+)}O_2$ nanowire can be written as:

$[\alpha$-$K_{0.2}Mn^{(3.8+)}O_2]$ *tetragonal* $+ 0.5Li^+ + 0.5e^- = [\alpha$-$K_{0.1}Li_{0.5}Mn^{(3.4+)}O_2]$orthorhombic $+ 0.1[K]$

↑   Stage 1

$[\alpha\text{-}K_{0.1}Li_{0.5}Mn^{(3.4+)}O_2]_{orthorhombic}$ + $0.5Li^+$ + $0.5e^-$ = $[\alpha\text{-}K_{0.1}Li_1Mn^{(2.9+)}O_2]$ $_{tetragonal}$

Stage 2

$[\alpha\text{-}K_{0.1}Li_1Mn^{(2.9+)}O_2]$ $_{tetragonal}$ + $3Li^+$ + $3e^-$ = $Mn^{(0)}$ + $2Li_2O$ + $0.1[K]$

Conversion
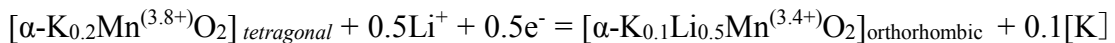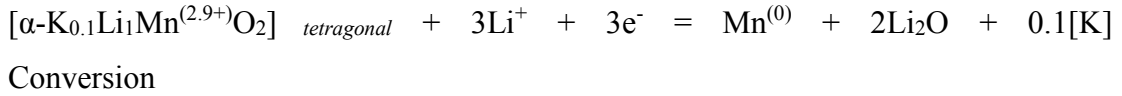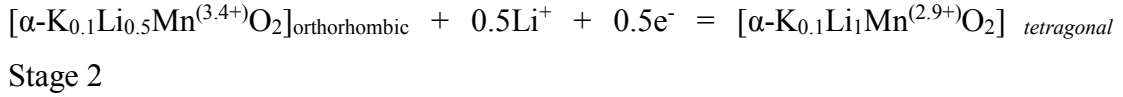
It is difficult to clearly distinguish and quantify the sole effect of K^+ in this process due to its low concentration, so half K atoms are roughly supposed to be removed upon initial lithiation. The release of K stabilizers during tunnel degradation was possibly due to the weakening of tunnel restriction and their volatilization in vacuum environment.[57]
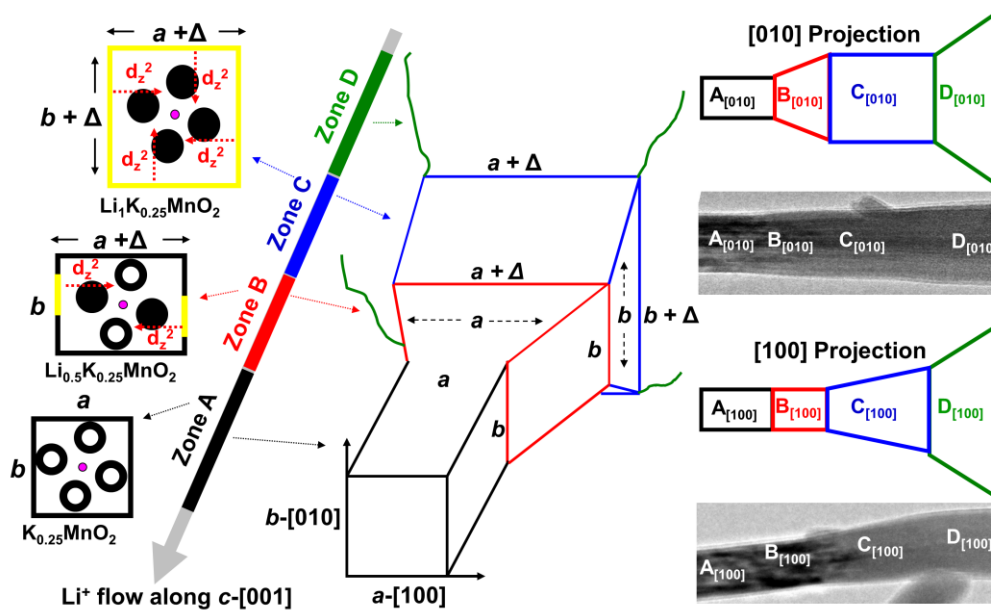
Figure 4.8 Left: Simulated Li^+ occupancy sequence at 8h sites in one 2×2 tunnel; Middle: 3D model showing the asynchronous expansion of single $\alpha\text{-}K_{0.25}Li_xMnO_2$ nanowire upon lithiation; Right: Predicted and observed morphology of one partially lithiated $\alpha\text{-}K_{0.25}Li_xMnO_2$ nanowire under [010] and [100] zone axes

Such a TOT symmetry transition involves Li^+ accommodation in 8h sites with different insertion energy and can thus potentially account for the appearance of double cathodic peaks in the 1st cycle cyclic voltammetry curve of $Li/\alpha\text{-}MnO_2$ batteries (Fig. A10). The reoccurrence of double peaks in the anodic scanning indicates that such a transition is reversible. To further demonstrate the symmetry

transition, the phase evolution during the first cycle of Li/α-MnO$_2$ battery is investigated using in-situ synchrotron XRD in Fig.A11. It shows that among all characteristic peaks of α-MnO$_2$, {200} and {600} show relatively apparent peak broadening upon lithiation. This is reasonable considering that they are directly related to the dimension of a (b). Besides the peak broadening, a weak shoulder peak ($\approx$5.2 Å) splits away from {200} main peak ($\approx$4.9 Å) during lithiation and stays until the cycle ends. The expanded 5.2 Å spacing is close to TEM observed value ($\approx$5.3 Å) for expanded {200}. This peak splitting could thus be ascribed to the asynchronous expansion between a and b, indicating the existence of TOT transition in the working Li/α-MnO$_2$ coin cell. Similar phenomenon was also reported in a recently published work using in-situ synchrotron XRD technique,[58] where "excessive line broadening" and "diffuse splitting of the peaks" were observed for a working Li/α-MnO$_2$ battery and an unknown phase transition was proposed. In this sense, the current work here explained the underlying phase transition very well. There are, however, many other factors that could potentially affect the peaks' behavior considering the complicated electrochemical environment inside a large-scale coin cell rather than in the single nanowire-based open cell design. The related discussion is given in Supporting Information.

4.4. Conclusion

In summary, tetragonal α-MnO$_2$ is featured by 1×1 and 2×2 tunnels. The 2×2 tunnels are supported by K$^+$ and 1×1 tunnel are unfilled. DFT calculations show that 1×1 tunnels have limited contribution to the discharge capacity of Li/α-MnO$_2$ batteries. On the other hand, the 8h sites inside 2×2 tunnels are the most favorable sites for lithiation and thus determine the overall discharge capacity for the application of α-MnO$_2$ as a cathode material. In-situ TEM study reveals asynchronous expansion of tetragonal unit cell in α-MnO$_2$ along a and b lattice directions upon lithiation. Specifically, in the first intercalation Stage 1, lattice parameter a expands while b keeps constant; in the following intercalation Stage 2, a remains constant while b expands gradually to catch up with a. Such an asynchronous expansion behavior is

well understood by our DFT calculation showing an energy-guided Li^+ occupancy sequence at 8h sites inside each 2×2 tunnel. This asynchronous behavior leads to a TOT symmetry transition in α-MnO_2 upon lithiation, which is believed to account for the appearance of multi lithiation stages when Li/α-MnO_2 battery is discharged. The degradation of initial tetragonal symmetry and resulted structural instability in α-MnO_2 host during lithiation are expected to explain the commonly observed low electrode utilization of α-MnO_2 in Li/α-MnO_2 batteries.

Our research provides fundamental understanding of lithiation property of α-MnO_2 and explores origins for its specific electrochemical behaviors, casting light on possible compositional modification and structural design to improve its energy storage performance in supercapacitor as well as Li/α-MnO_2 and Li-O_2 batteries. Such an asynchronous expansion behavior is expected to exist not only in Li^+ storage but also for Na^+ storage, as Na^+ and Li^+ both carry one charge and their ionic radii are both much smaller than the tunnel size in α-MnO_2.

4.5. References

1. Truong, T. T.; Liu Y.; Ren, Y.; Trahey, L.; Sun, Y. *ACS Nano* **2012,** 6, 8067-8077.

2. Boppana, V. B.; Jiao, F. *Chem. Commun. (Camb)* **2011,** 47, 8973-8975.

3. Débart, A.; Paterson, A. J.; Bao, J.; Bruce, P. G. *Angew. Chem.* **2008,** 120, 4597-4600.

4. Chen, S.; Zhu, J.; Wu, X.; Han, Q.; Wang, X. *ACS Nano* **2010,** 4, 2822-2810.

5. Cheng, F.; Zhao, J.; Song, W.; Li, C.; Ma, H.; Chen, J.; Shen, P. *Inorg. Chem.* **2006,** 45, 2038-2044.

6. Wang, X.; Li, Y.; *J. Am. Chem. Soc.* **2002,** 124, 2880-2881.

7. Chen, K.; Dong Noh, Y.; Li, K.; Komarneni, S.; Xue, D. *J. Phys. Chem. C* **2013,** 117, 10770-10779.

8. Devaraj, S.; Munichandraiah, N. *J. Phys. Chem. C* **2008,** 112, 4406-4417.

9. Li, L. ; King, D. L. *Chem. Mater.* **2005,** 17, 4335-4343.

10. Li, L.; Nan, C.; Lu, J.; Peng, Q.; Li, Y. *Chem Commun (Camb)* **2012**, 48, 6945-6947.

11. Yu, A.; Park, H. W.; Davies, A.; Higgins, D. C.; Chen, Z.; Xiao, X. *J. Phys. Chem. Lett.* **2011,** 2, 1855-1860.

12. Noailles, L. D.; Johnson, C. S.; Vaughey, J. T.; Thackeray, M. M. *J. Power Sources* **1999,** 81, 259-263.

13. Johnson, C. S.; Thackeray, M. M. *J. Power Sources* **2001,** 97, 437-442.

14. Luo, J.; Zhang, J.; Xia, Y. *Chem. Mater.* **2006,** 18, 5618-5623.

15. Kijima, N.; Takahashi, Y.; Akimoto, J.; Awaka, J. *J. Solid State Chem.* **2005,** 178, 2741-2750.

16. Ohzuku, T.; Kitagawa, M.; Sawai, K.; Hiroi, T. *J. Electrochem. Soc.* **1991,** 138, 360-365.

17. Pang, W. K.; Peterson, V. K.; Sharma, N.; Zhang, C.; Guo, Z. *J. Phys. Chem. C* **2014,** 118, 3976-3983.

18. Rossouw, M. H.; Liles, D. C.; Thackeray, M. M. *Mater. Res. Bull.* **1992,** 27, 221-230.

19. Kumagai, N.; Sasaki, T.; Oshitari, S.; Komaba, S. *J. New Mater. Electrochem. Syst.* **2006,** 9, 175-180.

20. Johnson, C. S. *J. Power Sources* **2007,** 165, 559-565.

21. Huang, J.; Zhong, L.; Wang, C.; Sullivan, J. P.; Xu, W.; Zhang, L.; Mao, S. X.; Hudak, N. S.; Liu, X.; Arunkumar Subramanian, Hongyou Fan,; Liang Qi, A. K., Ju Li. *Science* **2010,** 330, 1515-1520.

22. Liu, X.; Wang, J.; Liu, Y.; Zheng, H.; Kushima, A.; Huang, S.; Zhu, T.; Mao, S. X.; Li, J.; Zhang, S.; Lu, W.; Tour, J. M.; Huang, J. *Carbon* **2012,** 50, 3836-3844.

23. McDowell, M. T.; Lee, S. W.; Harris, J. T.; Korgel, B. A.; Wang, C.; Nix, W. D.; Cui, Y. *Nano Lett.* **2013,** 13, 758-764.

24. Ghassemi, H.; Au, M.; Chen, N.; Heiden, P. A.; Yassar, R. S. *ACS Nano* **2011,** 5, 7805-7811.

25. Ghassemi, H.; Au, M.; Chen, N.; Heiden, P. A.; Yassar, R. S. *Appl. Phys. Lett.* **2011,** 99, 1-3.

26. Liang, W.; Yang, H.; Fan, F.; Liu, Y.; Liu, X. H.; Huang, J. Y.; Zhu, T.; Zhang, S. *ACS Nano* **2013,** 7, 3427-3433.

27. Wang, X.; Tang, D.; Li, H.; Yi, W.; Zhai, T.; Bando, Y.; Golberg, D. *Chem. Commun.*, **2012**, 48, 4812–4814.

28. Su, Q.; Dong, Z.; Zhang, J.; Du G.; Xu, B. *Nanotechnology* **2013,** 24 255705.

29. Gao, Q.; Gu, M.; Nie, A.; Mashayek, F.; Wang, C.; Odegard, G. M.; Yassar, R. S. *Chem. Mater.* **2014,** 26, 1660-1669.

30. Nie, A.; Gan, L.; Cheng, Y.; Li, Q.; Yuan, Y.; Mashayek, F.; Wang, H.; Klie, R. F.; Schwingenschlogl U.; Yassar, R. R. *Nano Lett.* **2015,** 15, 610-615.

31. Wang, F.; Yu, H. C.; Chen, M. H.; Wu, L.; Pereira, N.; Thornton, K.; Van der Ven, A.; Zhu, Y.; Amatucci, G. G.; Graetz, J. *Nat. Commun.* **2012,** 3, 1201-1208.

32. Zhu, Y.; Wang, J. W.; Liu, Y.; Liu, X.; Kushima, A.; Xu, Y.; Mao, S. X.; Li, J.; Wang, C.; Huang, J. Y. *Adv. Mater.* **2013,** 25, 5461-5466.

33. McDowell, M. T.; Woo Lee, S.; Wang, C.; Cui, Y. *Nano Energy* **2012,** 1, 401-410.

34. Liu, Y.; Liu, X. H.; Nguyen, B. M.; Yoo, J.; Sullivan, J. P.; Picraux, S. T.; Huang, J. Y.; Dayeh, S. A. *Nano Lett.* **2013,** 13, 4876-4883.

35. Liu, N.; Wu, H.; McDowell, M. T.; Yao, Y.; Wang, C.; Cui, Y. *Nano Lett.* **2012,** 12, 3315-3321.

36. Wu, M.; Lee, J. Y.; Lin. J. C. *J. Phys. Chem. B* **2005,** 109, 23279-23284.

37. Desilvestro, J.; Haas, O. *J. Electrochem. Soc.* **1990,** 137, 17-21.

38. Santhanagopalan, S.; Balram, A.; Meng, D. D. *ACS Nano* **2013,** 7, 2114-2125.

39. Portehault, D.; Cassaignon, S.; Baudrin, E.; Jolivet, J. P. *Chem. Mater.* **2007,** 19, 5410-5417.

40. Kumar, V. G.; Gnanaraj, J. S.; Salitra, G.; Abramov, A.; Gedanken, A.; Aurbach, D.; Soupart, J. B.; Rousche, J. C. J. *Solid State Electrochem.* **2004,** 8, 957-967.

41. Post, J. E.; Von Dreele, R. B.; Buseck, P. R. *Acta Crystallogr.* **1982,** 38, 1056-1065.

42. Lan, B.; Yu, L.; Lin, T; Cheng, G.; Sun, M.; Ye, F.; Sun, Q.; He, J. ACS Appl. Mater. Interfaces 2013, 5, 7458−7464 .

43. Galindo, H.M.; Carvajal, Y.; Njagi, E.; Ristau, R.A.; Suib, S.L. Langmuir 2010, 26, 13677–13683.

44. Liu, X. H.; Zhang, L. Q.; Zhong, L.; Liu, Y.; Zheng, H.; Wang, J. W.; Cho, J. H.; Dayeh, S. A.; Picraux, S. T.; Sullivan, J. P.; Mao, S. X.; Ye, Z. Z.; Huang, J. Y. *Nano Lett.* **2011,** 11, 2251-2258.

45. Ling, C.; Mizuno, F. *Chem. Mater.* **2012,** 24, 3943-3951.

46. Johnson, C.S.; Dees, D. W.; Mansuetto, M.F.; Thackeray, M. M.; Vissers, D. R.; Argyriou，D.; Loong, C. K.; Christensen, L.. *J. Power Sources* **1997,** 68, 570-577.

47. Balaya, P.; Li, H.; Kienle, L.; Maier, J. *Adv. Funct. Mater.* **2003,** 13, 621-625.

48. Poizot, P.; Laruelle, S.; Grugeon, S. ;Dupont, L.; Tarascon, J. M. *Nature* **2000,** 407, 496-499.

49. Chen, C.; Ding, N.; Wang, L.; Yu, Y.; Lieberwirth, I. *J. Power Sources* **2009,** 189, 552-556.

50. Riedl, T.; Gemming, T.; Wetzig, K. *Ultramicroscopy* **2006,** 106, 284-291.

51. Wang, Z. L.; Yin, J. S.; Jiang, Y. D.; Zhang, J. *Appl. Phys. Lett.* **1997,** 70, 3362-3364.

52. Kurata, H.; Colliex, C. *Phys. Rev. B* **1993,** 48, 2102-2108.

53. Schmid, H. K.; Mader, W. *Micron* **2006,** 37, 426-432.

54. Zhang, S.; Livi, K. J. T.; Gaillot, A. C.; Stone, A. T.; Veblen, D. R. *Am. Mineral.* **2010,** 95, 1741-1746.

55. Jahn, H. A.; Teller, E. *Proc.-R. Soc. London, Sect. A: Math. Phys. Sci.* **1937**, 220-235.

56. Cramer, C. J.; Truhlar, D. G. *Phys. Chem. Chem. Phys.* **2009,** 11, 10757-816.

57. Vasconcelos, P.M.; Wenk, H. R.; Echer, C. *Am. Mineral.* **1994,** 79, 80-90.

58. Yang, Z.;Trahey, L.; Ren, Y.; Chan, M. K. Y.; Lin, C,; Okasinski, J.; Thackeray, M.M. *J. Mater. Chem.* **2015,**

Chapter 5. Dynamic Study of (De)sodiation in alpha-MnO$_2$ nanowires[③]

5.1. Introduction

Lithium ion batteries (LIB) have led the market of rechargeable energy storage devices for decades as a high-energy power source.[1] However, due to the limited storage of Li source in the Earth's crust and the wide-scale implementation of renewable energy in the fields of electric vehicles and portable devices, the world is now driven to explore new charge carriers as Li alternatives.[2] Compared with Li$^+$, Na$^+$ possesses the same amount of charge while its resources are much richer in the world, making sodium ion batteries (NaIB) the ideal alternative to LIB.[3] A substantial amount of research has been devoted to the development of electrode materials for NaIB, including nanostructured manganese oxides.[3,4,5]

Manganese oxides are well known for the various polymorphs possessing different open structures to facilitate the initial Na$^+$ insertion. Materials of this family include orthorhombic Na$_{0.44}$MnO$_2$,[6,7] Na$_{0.66}$MnO$_2$,[8] β-NaMnO$_2$,[9] and α-(β-, λ-)MnO$_2$[10,11,12,13], whose initial discharge capacity can be as high as 350 mAh/g. However, these materials always suffer from poor cycling performance with their capacity decaying very fast to even below 100 mAh/g before reaching 100 cycles.[8,11] Although it has been explained theoretically that the fast capacity decay is due to the relatively large size of Na$^+$ compared with Li$^+$ that strongly affects the host structure, no *in situ* work has been performed to identify the character of such interactions. Besides, the dynamic response of nanostructured manganese oxides during repetitive (de)sodiation

is currently not reported yet, leading to the lack of knowledge on the underlying electrochemical mechanisms.

In this report, α-MnO$_2$ nanowires featuring one dimensional tunneled structure (Supporting Information Figure B1) are studied by monitoring the morphology and phase evolution during electrochemical (de)sodiation using *in situ* transmission electron microscopy (TEM). It is found that the tunneled structure of α-MnO$_2$ maintains stable until Mn^{4+} is reduced to Mn$^{3.5+}$, and the following deep sodiation lead to formation of Mn$_2$O$_3$ with polycrystalline Na$_2$O. An intermediate phase Na$_{0.5}$MnO$_2$ is discovered during the first sodiation. This phase dominates the rest of (de)sodiation cycles through a reversible conversion reaction with Mn$_2$O$_3$ polycrystals. The Mn valence evolution during (dis)charge of α-MnO$_2$ at the coin cell level is also studied by *in situ* X-ray Absorption Spectroscopy (XAS) measurement, the result of which agrees well with the TEM observation. The sodiation of α-MnO$_2$ nanowires is further compared with our previous lithiation study of the same type of nanowires to understand the different electrochemical mechanisms of the cation-tunnel interactions. The initial sodiation and lithiation proceed by the same tunnel-driven intercalation mechanism until Mn^{4+} is reduced to Mn$^{3.5+}$. For the following deep cation insertion, the tunnels can survive up to LiMnO$_2$ (Mn^{3+}) during lithiation, while the sodiation process results in fast tunnel degradation and intermediate phase formation around Mn$^{3.5+}$, which is ascribed to the much stronger effect from inserted Na$^+$ than Li$^+$ on the host structure.

5.2. Methods

5.2.1. Material synthesis

The nanowires are synthesized by a hydrothermal method using KMnO$_4$ and MnSO$_4$ as the raw materials.[14] During the formation of the tunneled structure in solution, K$^+$ will be automatically trapped inside the tunnels.

5.2.2. Open cell design in TEM

The open cell is built using the *in situ* STM TEM holder equipped with two dangling gold tips being connected to the outside circuit. The nanowires are glued to one Au tip by conductive epoxy, and the metallic sodium is attached to the other Au tip by scratching the tip across the surface of a sodium foil in glovebox. During the holder transfer into the TEM chamber, sodium metal is partially oxidized to Na_2O, which functions as the solid electrolyte in the open cell design. The piezo-controlled movement is operated at single nanowire level to make it connected to the Na/Na_2O on the other side, and an appropriate bias is then applied to initiate the sodiation process. The desodiation process is started by reversing the bias.

Both *ex situ* and *in situ* TEM are performed inside the JEOL JEM-ARM200CF equipped with a 200 KV cold field emission electron source. The elemental information is obtained using an Oxford X-max 100TLE windowless SDD X-ray detector.

5.2.3. Coin cell making

The laminate contains α-MnO_2 nanowires, PVDF and black P with the weight ratio of 8:1:1. The coin cell was assembled using α-MnO_2 nanowires as the cathode, glass microfiber as the separator, $NaPF_6$ in EC/DEC as the electrolyte and metallic Na foil as the anode. Punched coin cell cases and spacers with Kapton window were used to guarantee X-ray transmission at Mn K-edge.

5.2.4 *In situ* X-ray Absorption Spectroscopy.

The XAS measurement for the Mn K-edge was performed at the Advanced Photon Source (APS) on the bending-magnet beamline 9-BM-B with electron energy of 7 GeV and average current of 100 mA. The radiation was monochromatized by a Si

(111) double-crystal monochromator. Harmomic rejection was accomplished with an Rh-coated mirror. All spectra were collected in transmission mode. For energy calibration, a Mn foil was measured simultaneously at the reference ionization chamber. The peak of the first derivative of Mn foil was adjusted to the tabulated value of 6539 eV. The coin cell was first discharged to 1 V and then charged back to 4 V at 0.1 C rate. X-ray absorption near edge spectra (XANES) data reduction and analysis were processed by Athena software.

5.3. Results and discussion

5.3.1. Basic structure characterization

The basic structural characterization of the nanowires from both the lateral and axial TEM imaging is given in Figure 5.1. Figures 5.1a and b show that the nanowire is monocrystalline with a uniform diameter of about 60 nm and a [001] growth direction. The [010] lateral HAADF imaging in Figure 5.1c illustrates the atomic structure of α-MnO_2. Referring to the model in Figure 5.1d, Mn (red dots) as the tunnel walls and K (green dots) in the tunnel center are clearly identified. The [001] axial TEM imaging in Figure 5.1e demonstrates a square-shaped cross section of the nanowire. The atomic structure of the white framed area is given in Figure 5.1f, where the tunneled structure is directly captured with one 2×2 tunnel highlighted, surrounded by the Mn atoms (red dots) and occupied by one K^+ atomic column (green dot). The accurate composition of the nanowire based on both the lateral and axial atomic imaging is thus determined to be $K_{0.25}MnO_2$. The inset of Figure 5.1f gives the atomic model, which agrees with the observation well.
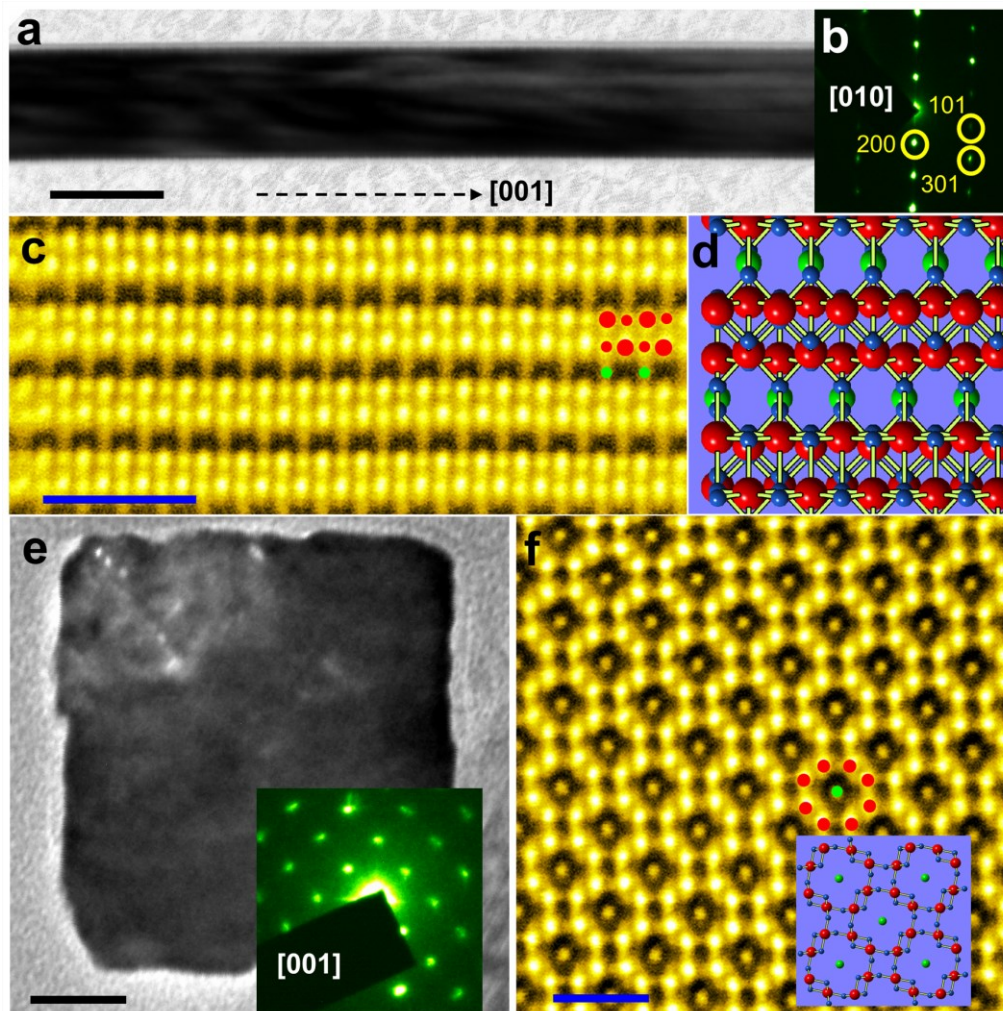
Figure 5.1. (a,b) [010] Bright field TEM image of one α-MnO₂ nanowire with its corresponding SAED; scale bar: 50 nm; (c,d) [010] HAADF STEM image of the α-MnO₂ nanowire with the atomic model given, where red is for Mn, blue for O and green for K; scale bar: 1 nm; (e) [001] TEM image of one cross sectioned α-MnO₂ slice with the SAED given in the inset; scale bar: 10 nm; (f) [001] HAADF STEM image showing the atomic tunneled structure. One 2×2 tunnel is highlighted by red dots standing for Mn atomic columns and the atomic model is given in the inset. Scale bar: 1 nm.

5.3.2. *In situ* TEM of the sodiation and resulted phase evolution

The sodiation of two α-MnO$_2$ nanowires is recorded in the Movie B1 and B2 in Appendix. It can be seen that the nanowires can be readily sodiated being evidenced by the obvious radial expansion. No apparent axial expansion is captured, indicating that the Na$^+$ insertion is not an isotropic process. Despite the anisotropy, the host structure maintains stable as there is not any fracture or crack formation. To further explore the sodiation kinetics, the reaction front position is measured versus the sodiation time and the results are given in Supporting Information Figure B2. Both two curves generally follow the parabolic shape, which is the typical feature of a diffusion-controlled process described earlier by other *in situ* literatures[15,16]. This indicates that the sodiation in α-MnO$_2$ nanowires is limited by Na$^+$ diffusion instead of interface reaction.

Figure 5.2 shows the analysis of the phase transition from one partially sodiated nanowire. Four sections are defined based on their sodiated morphologies, i.e. the pristine section before sodiation (b), the slightly sodiated section (c), the heavily sodiated section (d) and the fully sodiated section (e). The Selected Area Electron Diffraction (SAED) patterns from these four sections are provided in Figure 5.2b-e, respectively. As shown in Figure 5.2b, the pristine nanowire is viewed along [1 0 $\bar{1}$] zone axis with the (0 2 0) lattice diffraction (yellow ring) directly seen with a spacing of 4.95 Å. For section (c) that is slightly sodiated, the (0 2 0) spacing increases to 5.1 Å, which can be explained by the gradually enhanced Jahn-Teller distortion when more Mn^{4+} are reduced by the inserted Na$^+$. Although the host lattice is severely distorted, the parent α-MnO$_2$ phase is well maintained as evidenced by the remaining [1 0 $\bar{1}$] patterns, indicating that the 2×2 tunnels are still active for Na$^+$ insertion. However, several new ring-like diffractions (yellow arrows) are observed to coexist with the α-MnO$_2$ patterns in Figure 5.2c and they are indexed to be Na$_{0.5}$MnO$_2$ (SG: Pnma). In the heavily sodiated section (d), the tunneled structure is totally degraded and the sole phase is indexed to be Na$_{0.5}$MnO$_2$. Upon the full sodiation, the metastable Na$_{0.5}$MnO$_2$ is finally converted to the polycrystalline Mn$_2$O$_3$ (white arrows) and Na$_2$O (green arrow) as confirmed in Figure 5.2e.
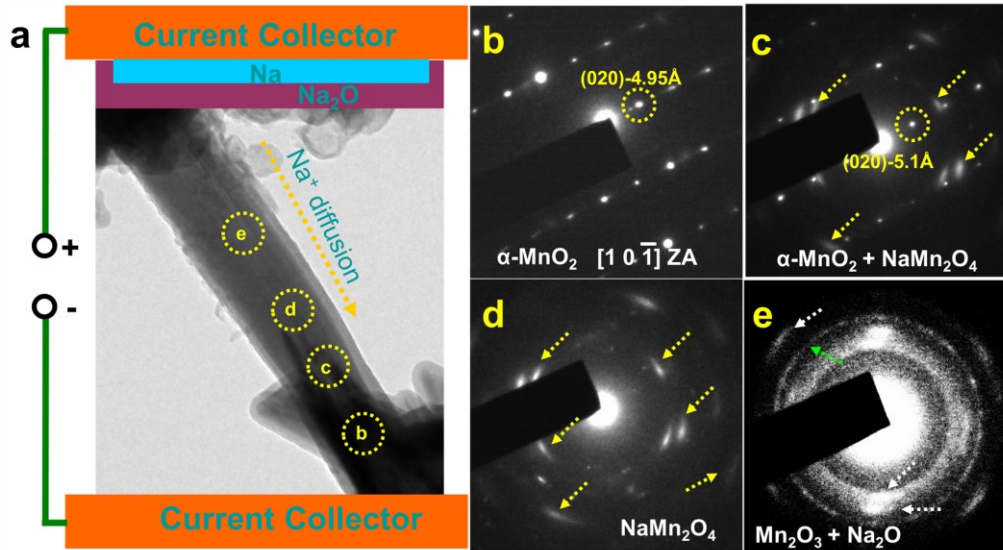
Figure 5.2. (a) The *in situ* open cell design inside TEM chamber showing one α-MnO$_2$ nanowire being sodiated; (b-e) The corresponding SAED patterns from the four predefined sections in (a).

As such, the tunneled structure of α-MnO$_2$ maintains its stability until 0.5 Na$^+$ are intercalated into the host with the subsequent formation of Na$_{0.5}$MnO$_2$ as an intermediate phase. The sodiation process can thus be written as a two-step based reaction:

$$MnO_2 + 0.5Na^+ + 0.5e^- = Na_{0.5}MnO_2 \qquad (5.1)$$

$$Na_{0.5}MnO_2 + 0.5Na^+ + 0.5e^- = 0.5Mn_2O_3 + 0.5Na_2O \qquad (5.2)$$
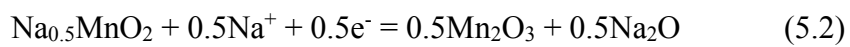
The presence of K$^+$ is not considered in this part of discussion due to the complexity of different cations' interaction, which, however, is further addressed in the last discussion part.

5.3.3. *In situ* TEM of the sodiation/desodiation cycling

The repetitive sodiation/desodiation of single nanowire is recorded in Movie B3 in Appendix B. It shows that the nanowire expands during sodiation and reversibly contracts during desodiation, and no fracture or crack is observed up to five cycles,

99

indicating the good reversibility of α-MnO$_2$ nanostructures. The diameter of the nanowire is measured versus the sodiation time, and the result is shown in Figure 5.3a. The first full sodiation results in about 50% radial expansion while the first desodiation only leads to 15% contraction. The expansion and contraction rates of the rest cycles are limited within 20%, indicating that the mechanism dominating the first sodiation of the nanowire must be different from the mechanism during the rest (de)sodiation cycles.
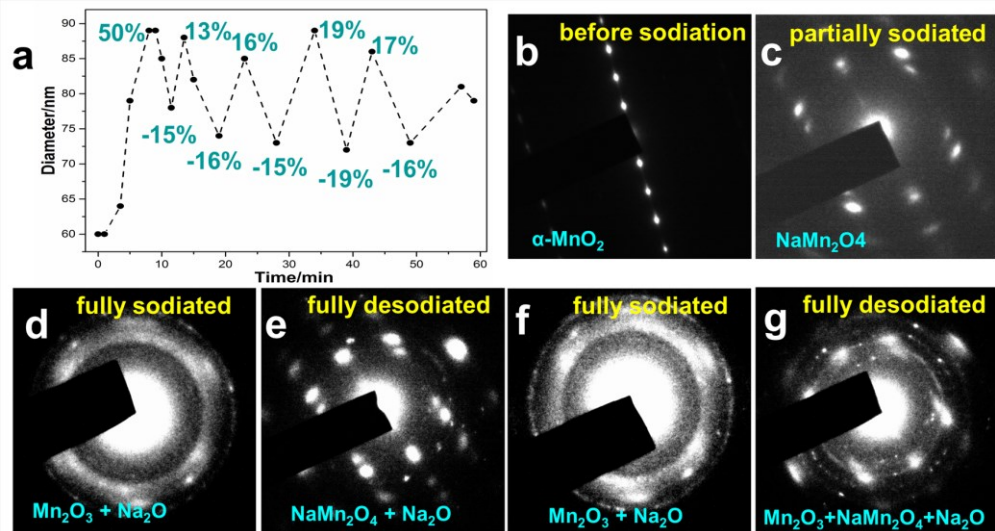
Figure 5.3. (a) The measured diameter versus sodiation time for one α-MnO$_2$ nanowire being repetitively cycled; the numeric percentages are for the diameter expansion (positive) and contraction (negative) during each event; (b-g) the corresponding SAED patterns of the same nanowire at different (de)sodiation states.

To clarify the different mechanisms, the phase evolution of the same nanowire is characterized for the first two cycles with the results illustrated in Figure 5.3b-g. The first full sodiation (Figure 5.3b-d) features the formation of an intermediate phase Na$_{0.5}$MnO$_2$ and the final conversion to Mn$_2$O$_3$ and Na$_2$O, which follows the similar two-step phase evolution as discussed in Figure 5.2. For the full desodiated phase, however, no crystalline α-MnO$_2$ is detected, and the reformation of Na$_{0.5}$MnO$_2$ dominates the reaction. Some residual Na$_2$O polycrystals are detected, which is probably due to their poor electron conductivity that makes part of them difficult to

decompose during desodiation. During the 2nd full sodiation, the $Na_{0.5}MnO_2$ is totally converted to Mn_2O_3 and Na_2O, while it appears again during the 2nd desodiation. So compared with the first sodiation process where α-MnO_2 is sodiated to $Na_{0.5}MnO_2$ and finally converted to Mn_2O_3 and Na_2O, the following cycles are characterized by the reversible conversion reaction between $Na_{0.5}MnO_2$ and Mn_2O_3. It is also notable in Figure 5.3g that in the fully desodiated state, Mn_2O_3 cannot be totally converted back to $Na_{0.5}MnO_2$, which can be explained by the gradual pulverization of Mn_2O_3 polycrystals during repetitive cycles that makes the electron path discontinuous inside Na_2O matrix. As such, it is expected that the following cycles should exhibit very quick capacity fading as more and more Na_2O accumulates in the electrode and thus gradually cuts off the electron conductive path. This capacity fading mechanism can also explain the reported fast capacity decay of NaIBs using manganese oxides as the electrode.[11] It is apparent that certain methods should be utilized to improve the conductivity of Mn-based oxides for reversible Na^+ storage, such as proper structure modification and surface coating of conductive materials.

5.3.4. Coin-cell level *in situ* XAS measurement for (de)sodiation

To study the mechanism of the (de)sodiation process of MnO_2 nanowires in bulk scale, the cycling stability, the voltage profile and *in situ* XAS data were collected during the battery cycling where α-MnO_2 nanowires were utilized as cathode and Na metal as anode. The cycling results are provided in Figure B3. It shows that the Na-MnO_2 battery initially shows a discharge capacity of 300 mAh/g while the capacity drops quickly with the cycles. After 50 cycles, both discharge and charge capacities are below 50 mAh/g, indicating the poor cycling stability of MnO_2 electrode. The voltage profile during the first discharge/charge cycle is shown in Figure B4, where the discharge process exhibits one slope region (2.5 V – 1.3 V) and one plateau region (1.3 V – 1 V). The slope region should be related with the initial intercalation of Na^+ into the tunneled structure and the plateau region should indicate the following conversion reaction to Mn_2O_3. It is notable that these two stages contribute almost

equal discharge capacity, agreeing well with the *in situ* TEM results, where 0.5 Na$^+$ first intercalate into tunneled MnO_2 (150 mAh/g in theory), and then extra 0.5 Na$^+$ insertion results in the conversion reaction (150 mAh/g in theory). During the charge process, only about 130 mAh/g capacity is reversible, which also agrees with the partially reversible conversion from Mn_2O_3 to $Na_{0.5}MnO_2$ as confirmed by *in situ* TEM. Both the poor cycling stability and the large voltage hysteresis between discharge and charge can be ascribed to the poor reaction kinetics that is limited by the gradual formation of electron-insulating Na_2O as well as the gradually isolated Mn-based redox centers.
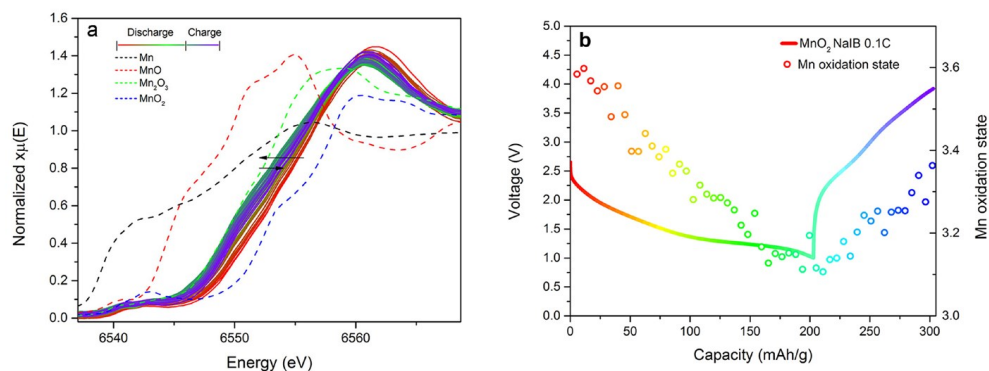
Figure 5.4. (a) Normalized XANES spectra of one NaIB with α-MnO_2 nanowire electrode and standard Mn, MnO, Mn_2O_3 and MnO_2; (b) Charge-discharge profile and the oxidation state of Mn during battery cycling.

In situ XANES spectra, which are used for identifying the oxidation state of Mn are shown in Figure 5.4a with the spectra of the standard Mn, MnO, Mn_2O_3 and MnO_2. The initial oxidation state of α-MnO_2 nanowires (red solid line) is slightly lower than 4$^+$, compared with the standard MnO_2 (blue dashed line). During the discharge process, the oxidation state of Mn continuously decreased and was close to 3$^+$ when fully discharged to 1V (green solid line). During the charge, the oxidation state of Mn increased obviously (from green to purple solid line) but it was not totally recovered to its pristine state even fully charged to 4 V. To quantitatively analyze the Mn oxidation state change, the liner combination fitting (LCF) of the *in situ* XAS spectra with standard Mn_2O_3 and MnO_2 was conducted. The LCF result with the battery

discharge-charge profile is shown in Figure 5.4b. The initial oxidation state of the α-MnO$_2$ nanowires was ~3.6$^+$, which roughly matches the initial composition of the nanowires (K$_{0.25}$MnO$_2$). Then, it decreased to ~3.1$^+$ at the end of discharge. During charge, the oxidation state of Mn increased to ~3.4$^+$, which is probably in accordance with the state of charge observed in TEM when intermediate Na$_{0.5}$MnO$_2$ is the dominant phase. The fact that Mn cannot recover its oxidation state during charge to its initial state before discharge indicates that the first cycle is not totally reversible, which could be explained by the residual Na$^+$ left in the α-MnO$_2$ nanowires that can not be totally extracted out. The *in situ* XAS results thus agree well with the *in situ* TEM observation in terms of the Mn valence evolution and the reversibility of the host structure.

5.3.5. Comparison between sodiation and lithiation in 2×2 tunnels

It has been predicted that due to the size difference, Na$^+$ is inserted into the 2×2 tunnels of α-MnO$_2$ *via* a distinct path compared with Li$^+$.[17] Specifically, many reports have pointed out that Li$^+$ prefers to diffuse along the Wyckoff 8h sites that are off-centered, while Na$^+$ thermodynamically occupies the near-centered position inside the 2×2 tunnels.[17,18] Practically, since most hydrothermally synthesized α-MnO$_2$ products inevitably have their 2×2 tunnels partially occupied by large cations (like K$^+$ in our case), the complicated reactions inside the host are more than just Li$^+$/Na$^+$-tunnel interaction. It is thus expected here that α-MnO$_2$ nanowire behaves distinctly during lithiation and sodiation in terms of tunnel stability, structure evolution, and phase transition.

To confirm this hypothesis, the *in situ* sodiation of the same α-MnO$_2$ nanowires is compared with our previous *in situ* lithiation work[18] with the results shown in Figure 5.5. Based on the EDS mappings of Mn, K and Na in Panel A and Panel B, it can be seen that both lithiation and sodiation can result in partial removal of K$^+$ from the inserted area while Mn atoms maintain stable. This should be ascribed to the

repulsive forces exerted to K^+ from inserted Li^+ and Na^+ possessing the same positive charge. It is worth noting that Na^+ insertion has a stronger interaction with K^+ than Li^+ insertion does, resulting in more K^+ being removed from the inserted tunnels as evidenced by the measured K/Mn atomic ratio. This finding confirms the previous prediction that Na^+, with a larger cation size (1.02 Å) than Li^+ (0.76 Å), diffuse through the host *via* a distinct path that is closer to the tunnel center.[17,18] It is this centered path that results in stronger Na^+ and K^+ interaction because the latter atoms also occupy the tunnel center (Wyckoff 2a sites). The fact that K^+ are easier to be removed upon sodiation indicates that the tunneled structure should be more vulnerable when it takes in Na^+ than Li^+, which is further confirmed in Panel C of Figure 5.5.

It can be seen from Panel C that the phase evolutions during lithiation and sodiation are sharply different. The 2×2 tunneled structure of α-MnO_2 is well maintained even one Li^+ are intercalated into the unit MnO_2 host.[18] The tunneled structure becomes vulnerable when Na^+ ions diffuse in, and is totally replaced by a new phase even before 0.5 Na^+ are inserted in. Since it has been shown in Section 3.3 that the tunneled structure of α-MnO_2 cannot be recovered once it is totally degraded, portion of the 1st discharge capacity contributed from the Na^+ intercalation is no longer counted in the following cycles. In the sense, this mechanism well explains the fast capacity fading of α-MnO_2 as a NaIB electrode immediately after its 1st cycle, as well as the fact that Li/MnO_2 batteries generally exhibit higher cycleable capacity than Na/MnO_2 batteries.[19,20,21]
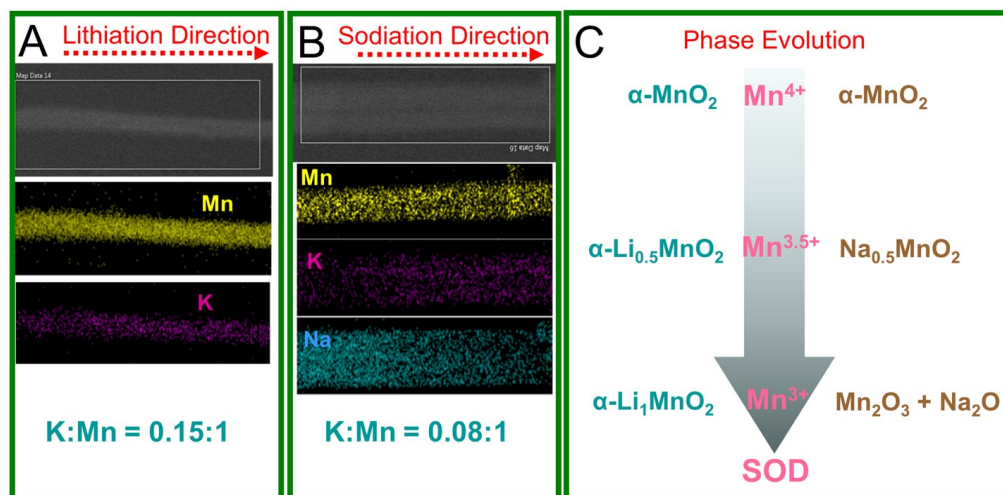
Figure 5.5. (Panel A) The EDS maps of Mn and K for a partially lithiated $K_{0.25}MnO_2$ nanowire; the atomic ratio of Mn and K from the fully inserted nanowire is given at the bottom; (Panel B) The EDS maps of Mn, K and Na for a partially sodiated $K_{0.25}MnO_2$ nanowire with the atomic ratio of K/Mn given at the bottom; (Panel C) The schematic showing the phase evolution of α-MnO_2 nanowire electrode at different states of discharge (SOD) during lithiation[18] and sodiation.

It has been reported that large cations such as K^+, Ba^{2+} and Ag^+ are required to stabilize the large 2×2 tunnel cavity of α-MnO_2 and the 2×2 tunneled phase is more likely to form when the concentration of the large cations is high.[22,23] Small cations such as H^+, Li^+ and Na^+ would not efficiently support the tunnels without the presence of large cations.[24] Based on this, it is understandable that the tunneled structure is more vulnerable during sodiation than it is during lithiation, knowing that inserted Na^+ result in the removal of more K^+ form the tunnels than Li^+ do. It is also worth mentioning that in the current experimental conditions, it is difficult to quantitatively study the K^+ effect since K ions are hard to be dynamically tracked and imaged during Na^+ (Li^+) insertion, and the underlying interactions are more complicated than being discovered here. But it is reasonably to expect that future work, inspired by our current fundamental findings, could clear this ambiguity, and the electrochemical performance of MnO_2-based electrodes could be efficiently improved by proper structural and compositional modifications.

5.4. Conclusion

We reported for the first time the dynamic study of (de)sodiation mechanism in single α-MnO$_2$ nanowire combining both *in situ* TEM and *in situ* synchrotron XAS. During first sodiation cycle, the tunneled structure of α-MnO$_2$ can survive Na$^+$ insertion when Mn^{4+} is gradually reduced to Mn$^{3.5+}$. It is then followed by fast tunnel degradation with formation of an intermediate phase, Na$_{0.5}$MnO$_2$, and the final conversion to Mn$_2$O$_3$ and Na$_2$O. The 1st desodiation process and the following cycles are dominated by the partially reversible conversion reaction between Na$_{0.5}$MnO$_2$ and Mn$_2$O$_3$. The comparison between lithiation and sodiation shows that the initial Na$^+$ and Li$^+$ insertion in α-MnO$_2$ proceed *via* the same tunnel-driven intercalation mechanism accompanied by tunnel expansion until Mn^{4+} is reduced to Mn$^{3.5+}$. For the subsequent deep insertion, the sodiation exerts a strong destructive effect on the tunneled structure of α-MnO$_2$ that leads to fast tunnel degradation and phase transition, while the lithiation causes little tunnel degradation up to Mn^{3+}. The difference in charge carrier (Na$^+$/Li$^+$) insertion mechanisms should be ascribed to Na$^+$'s bigger ionic size and the resulted stronger interaction with the host structure than that of Li$^+$.

This work clarifies the underlying charge storage mechanisms when manganese oxides (α-MnO$_2$) are utilized as NaIB electrodes. Although MnO$_2$-based electrode has not been reported to give the best performance among various reported electrode candidates, we believe that the interaction mechanisms between inserted Na$^+$ (Li$^+$) and the host structure discovered in this work can help to further improve the electrochemical performance of these materials by proper structure engineering and chemical modification.

5.5. References

1. M. Armand, J. M. Tarascon, Nature 451 (2008) 652-657.
2. S. Yuan, X. Huang, D. Ma, H. Wang, F. Meng, X. Zhang, Adv. Mater. 26 (2014) 2273-2279.

3. N. Yabuuchi, K. Kubota, M. Dahbi, S. Komaba, Chem. Rev. 114 (2014) 11636-11682.

4. M. Gu, A. Kushima, Y. Shao, J. G. Zhang, J. Liu, N. D. Browning, J. Li, C. Wang, Nano Lett. 13 (2013) 5203-5211.

5. L. Yu, L. Wang, S. Xi, P. Yang, Y. Du, M. Srinivasan, Z. Xu, Chem. Mater. 27 (2015) 5340-5348.

6. Y. Cao, L. Xiao, W. Wang, D. Choi, Z. Nie, J. Yu, L. V. Saraf, Z. Yang, J. Liu, Adv. Mater. 23 (2011) 3155-3160.

7. M. D. Slater, D. Kim, E. Lee, C. S. Johnson, Adv. Funct. Mater. 23 (2013) 947-958.

8. Y. Wang, L. Mu, J. Liu, Z. Yang, X. Yu, L. Gu, Y. Hu, H. Li, X. Yang, L. Chen, X. Huang, Adv. Energy Mater. 2015, just accepted, DOI: 10.1002/aenm.201501005.

9. J. Billaud, R. J. Clement, A. R. Armstrong, J. Canales-Vazquez, P. Rozier, C. P. Grey, P. G. Bruce, J. Am. Chem. Soc. 136 (2014) 17243-17248.

10. K. Chen, Y. D. Noh, K. Li, S. Komarneni, D. Xue, J. Phys. Chem. C 117 (2013) 10770-10779.

11. D. Su, H. J. Ahn, G. Wang, J. Mater. Chem. A 1 (2013) 4845-4850.

12. K. Chen, C. Sun, D. Xue, Phys. Chem. Chem. Phys. 17 (2015) 732-750.

13. C. Sun, Y. Zhang, S. Song, D. Xue, J. Appl. Cryst. 46 (2013) 1128-1135.

14. S. Santhanagopalan, A. Balram, and D. D. Meng. ACS Nano 7 (2013) 2114-2125.

15. J. Y. Huang, L. Zhong, C. M. Wang, J. P. Sullivan, W. Xu, L. Q. Zhang, S. X. Mao, N. S. Hudak, X. H. Liu, A. Subramanian, H. Fan, L. Qi, A. Kushima, J. Li, Science 330 (2010) 1515-1520.

16. Meng Gu, Y. Li, X. Li, S. Hu, X. Zhang, W. Xu, S. Thevuthasan,; D. R. Baer, J. G. Zhang, J. Liu, C. Wang. ACS Nano 6 (2012) 8439-8447.

17. M. J. Young, A. M. Holder, S. M. George, C. B. Musgrave, Chem. Mater. 27 (2015) 1172-1180.

18. Y. Yuan, A. Nie, G. M. Odegard, R. Xu, D. Zhou, S. Santhanagopalan, K. He, H. Asayesh-Ardakani, D. D. Meng, R. F. Klie, C. Johnson, J. Lu, R. Shahbazian-Yassar, Nano Lett. 15 (2015) 2998-3007.

19. C. S. Johnson, J. Power Sources 165 (2007) 559-565.

20. S. Wang, H. Zheng, Q. Zhang, L. Li, H. Wu, G. Li, C. Feng, J. Nanopart. Res. 16 (2014) 2231-2240.

21. C. S. Johnson, M. M. Thackeray, J. Power Sources 97-98 (2001) 437-442.

22. D. Portehault, S. Cassaignon, E. Baudrin, J. P. Jolivet, J. Mater. Chem. 19 (2009) 2407–2416.

23. X. Wang, Y. Li, Chem. Eur. J. 9 (2003) 300-306.

24. X. Shen, Y. Ding, J. Liu, J. Cai, K. Laubernds, R. P. Zerger, A. Vasiliev, M. Aindow, S. L. Suib, Adv. Mater, 17 (2005) 805-809.

Chapter 6. The Influence of Large Cations on the Electrochemical Properties of Tunnel-Structured Metal Oxides[④]

6.1. Introduction

Metal oxides with an internal tunnel structure such as α-MnO$_2$, TiO$_2$ and β-FeOOH are widely used for charge storage in rechargeable batteries and supercapacitors where charge carriers such as Li$^+$, Na$^+$ and Mg^{2+} can be reversibly inserted and extracted.[1-4] Of these oxides, α-MnO$_2$, which possesses the typical octahedral molecular sieve (OMS) structure, is characterized by well-ordered one dimensional 1×1 and 2×2 tunnels,[5] as illustrated in Figure C1. The 2×2 tunnel (4.6 Å $\times$ 4.6 Å) is large enough to accommodate charge carriers such as Li$^+$, Na$^+$ and Mg^{2+}, enabling fast ion diffusion inside the tunnel cavity.[6] In addition, Mn-based oxides are also low cost, environmentally friendly, and safer with respect to over-charge conditions compared to Co-based oxide electrodes.[7] Consequently, α-MnO$_2$ has been extensively studied as a promising cathode material for lithium (sodium and magnesium) ion batteries,[8-11] lithium air batteries,[12,13] and supercapacitors.[14-16]

Recent research shows that large cations such as K$^+$, Ba^{2+}, and NH$_4^+$ can be introduced during synthesis of α-MnO$_2$.[17,18] These cations, which partially occupy the tunnel cavities at certain stabilized lattice sites, are expected to interact with the charge carrier (Li$^+$, Na$^+$, Mg^{2+}) and thus affect the charge storage performance of α-MnO$_2$ where tunnel-driven (de)intercalation contributes to the overall capacity.[16,18-20] Despite considerable research devoted to improving the charge storage performance of α-MnO$_2$, the underlying mechanism by which tunnel cations affect the insertion/extraction of charge carriers is poorly understood.

[④]The material contained in this chapter has been submitted to *Nature Communications*.

In the case of Li$^+$ being the charge carrier, many researchers believe that the presence of large cations (K$^+$, Ba^{2+}) inside the 2×2 tunnels impedes the diffusion of Li$^+$ by physical blocking and repulsive electrostatic forces.[18,21-23] Others have pointed out that fast (de)intercalation of Li$^+$ requires a stable tunnel structure, and the existence of cations helps to prevent the collapse of the tunnels.[24,25] As yet, no conclusive evidence has been provided to clarify whether the tunnel cations promote or impede rapid migration of Li ions. An important factor that contributes to this ambiguity is the difficulty of visualizing these cations and determining their content and position, given the spatial resolution limits of most non-aberration corrected electron microscopes. It is apparent that there is a pressing need to understand the effect of tunnel cations on charge storage behavior of materials such as α-MnO$_2$ to allow the synthesis methods and properties of such tunnel-structured oxides to be optimized.

In this report, nanowires of K$^+$-doped α-MnO$_2$ were hydrothermally synthesized and the K$^+$ concentration was controlled and differentiated by acid solution treatment. The effect of varying K$^+$ concentration on the rate performance of a Li/α-MnO$_2$ battery was studied systematically by measuring the electronic conductivity and Li$^+$ diffusivity in the α-MnO$_2$ cathode. The underlying mechanism was revealed using a powerful combination of aberration-corrected scanning transmission electron microscopy (ACSTEM), transmission electron microscopy (TEM), electrical response measurements of single α-MnO$_2$ nanowires, electrochemical impedance spectroscopy (EIS), and density functional theory (DFT) simulations.

6.2. Methods

6.2.1. Materials synthesis and composition control

α-MnO$_2$ nanowires were synthesized hydrothermally using KMnO$_4$ and MnSO$_4$ as reactants in aqueous solution.[14] Specifically, 0.9878 g of KMnO$_4$ and 0.4226 g of

MnSO$_4$•H$_2$O were dispersed in 80 mL of deionized (DI) water under constant stir for 30 min to form a purple solution. The obtained slurry was then transferred to a 100 mL Teflon-lined stainless steel autoclave, sealed and heated at 160 °C for 12 h. The synthesized nanowires were first separated from the solution by centrifugation, then washed with deionized (DI) water and ethyl alcohol, and finally dried in air at 60 °C for 12 h. During the synthesis process, K$^+$ doped the initially formed 2×2 tunnels and remained trapped inside the tunneled structure.

The control of K$^+$ concentration inside the 2×2 tunnels was achieved by acid treatment using concentrated HNO$_3$. The as-synthesized nanowires were first soaked in HNO$_3$ solution accompanied by magnetic stirring (800 rpm at 60 °C) for 1 and 4 days. This procedure was followed by repeated washing of the nanowires with deionized water until the solution was neutralized (pH ≈ 7). These nanowires were finally heated at 280 °C in air. According to literature,[7] 280 °C dry heating is efficient in removal of any residual water in the tunnels.

6.2.2. Structure, composition and thermal stability characterization

Cross-sectional specimens were prepared using an ultramicrotome (Leica UCT). The nanowires were first mixed with cold-mounting epoxy resin (EPOFIX, Electron Microscopy Sciences) before subjecting them to 10 min supersonic vibrations. The hardener (EPOFIX, Triethylenetetramine, Electron Microscopy Sciences) was then added to speed up the solidification process in air at 60°C for 24 hours. After solidification, the sample was placed under an Edge CraftTM diamond knife mounted in an ultramicrotome (Leica UCT) to be cut into slices with a feeding step size of 500 nm.

(S)TEM characterization was performed using an aberration-corrected JEOL JEM-ARM 200CF STEM equipped with a 200 keV cold-field emission gun, a high angle annular dark field (HAADF) detector, and an Oxford X-max 80 SDD X-ray detector.

HAADF images were acquired using a 22 mrad probe convergence angle and a 90 mrad inner-detector angle. EELS data were captured in a postcolumn Gatan Enfina EELS spectrometer with a 45 mrad collection angle. The spectra were fitted using Gaussian function.

XPS was obtained from a Kratos AXIS-165 Surface Analysis System with the spectra collected with a monochromatic Al Ka source (1,486.7 eV). For survey spectra, the data were collected at a pass energy of 80 eV (fixed analyser transmission mode), a step size of 1 eV and a dwell time of 200 ms. High-resolution regional spectra were collected with a pass energy of 20 eV (fixed analyser transmission mode), a step size of 0.1 eV and a dwell time of 500 ms.

Gas adsorption analysis was performed using a micromeritics porosity analyzer (ASAP 2020), by subjecting solids to varying partial pressures of N_2 at 77 K in a liquid nitrogen bath. All MnO_2 samples were initially degassed on the instrument degassing station (180 $^{\circ}$C at 10×10^{-3} torr for 4h). The measurement consists of 30 points (15 adsorption and 15 desorption points). For consistent and reliable results, data in the linear range of P/P_o of 0.06-0.3 (R^2=0.9999) was used to calculate the BET surface area.

Thermogravimetric analysis was done with a SDT-Q600 TGA/ DSC instrument with 100 ng sensitivity under high purity nitrogen atmosphere. In this experiment, 2.1 mg of sample was poured in a clean aluminum pan, then the sample was kept at 40 $^{\circ}$C for 30 min to stabilize the system and then it was heated to 450 $^{\circ}$C with the rate of 10 $^{\circ}$C/min continuously.

In situ TEM heating was done inside a JEOL 3010 TEM. The nanowires were first dispersed onto a TEM grid and then mounted to an *in situ* heating holder. After loaded into TEM chamber, the nanowires were heated to 450 $^{\circ}$C with the rate of 10

ºC/min. Data were collected at 25, 200, 280, 350, 400 and 450 ºC after maintaining samples at each specific temperature for 5 min.

6.2.3. *In situ* TEM testing of the I-V response of single α-MnO$_2$ nanowire

The I-V response of a single α-MnO$_2$ nanowire was obtained using a Nanofactory scanning tunneling microscope (STM) holder inside a JEOL 3010 TEM operated at 300 KeV. An *in situ* STM holder was utilized to manipulate single α-MnO$_2$ nanowires into the desired position. All the tested nanowires have similar morphologies (50-60 nm in diameter and 500-700 nm in length). Each nanowire was first vertically attached to the tungsten (W) tip on one side of the circuit and moved toward the W tip on the other side using a piezoelectric control. To minimize contact effects, the W tips were electrochemically etched immediately before use. After a nanowire was connected to both W tips to form a complete circuit, a high voltage with a current of about 1 μA was applied to achieve a tight contact between the nanowire and the two tips.

6.2.4. *Ab initio* computer modeling

Calculations were performed based on density functional theory (DFT) with PAW potentials, as implemented in the VASP code. The HSE06 hybrid functional with 25% Hartree-Fock exchange was applied, which has been demonstrated by others to describe well d electron localization and therefore can reproduce correct mixed charge states of transition metal oxides.[16] For bulk calculations a planewave basis set cutoff energy of 500 eV and a minimum grid of 2×2×7 k-points were used in the Brillouin zone. The structure including lattice parameters and atomic positions were relaxed until the residue force on each atom is less than 0.03 eV/ Å. The calculated lattice parameters for K$_{0.25}$MnO$_2$ agree well with experiment, as shown in Table C3.

6.2.5. Electrochemical testing

The electrode slurry was made of 80 wt% α-MnO$_2$ nanowires, 10 wt% super P carbon and 10 wt% PVDF binder in N-methyl-pyrrolidinone (NMP). The mixture was then cast onto an Al foil to make the electrode. The electrode was dried at 75 °C for 4 hours, followed by thorough drying at 75 °C overnight under vacuum. Electrochemical measurement of the first discharge capacity was carried out using CR2032 coin cells with Li metal as the counter electrode, 1.2 M LiPF$_6$ in EC/EMC (3:7 by weight) as the electrolyte, and Celgard$^{®}$ 2325 membrane as the separator. Cells were cycled between 1.5 to 4 V at different rates calculated using 130 mAh/g as the practical capacity.

Electrochemical impedance data were collected with a Solartron 1470E and 1451A cell testing system, using a 5 mV AC perturbation with frequencies ranging from 100 KHz to 50 mHz. A three-electrode system was used so that the spectra obtained correspond to the impedance of the cathode side only. A Li metal wire was used as the reference electrode and a piece of Li foil was used as the counter-electrode. Spectra were fit according to the equivalent circuit in Figure 6.4a, where R_e is the electrolyte resistance, R_{ct} is the charge-transfer resistance, C_{dl} is the double layer capacitance that takes the roughness of the particle surface into account, and Z_W is the Warburg diffusive impedance.[23] The semicircle in the high frequency region of the impedance spectra can be assigned to the $R_{ct}C_{dl}$ elements, while the slope of curve in the low frequency region is governed by the Warburg diffusion of Li$^+$ into the bulk of cathode particles. Galvanostatic intermittent titration technique (GITT) measurements were carried out with a negative current pulse at C/20 for 30 seconds, followed by relaxations for 5 hours. This sequence of discharge pulse followed by a relaxation time was repeated until the potential reached 1.5 V.

6.3. Results and discussion

6.3.1. Structural characterization of α-K_xMnO$_2$ with different K$^+$ contents

Hydrothermally synthesized α-MnO$_2$ nanowires were characterized using ACSTEM, and the results are shown in Figure 6.1. It can be seen from figures 6.1a and b that the α-MnO$_2$ nanowire is monocrystalline, growing in the [001] direction with a uniform diameter. The [100] atomic resolution high angle annular dark field (HAADF) image in Figure 6.1c shows the 2×2 tunnels (dark stripes) surrounded by two Mn atomic columns (yellow spheres) corresponding to the tunnel walls on each side. It can also be seen that the 2×2 tunnels are decorated with ordered K atomic columns (pink spheres) around their center positions, based on which the [100] atomic model is provided in Figure 6.1d. K$^+$ ions are successfully introduced during synthesis because excess K$^+$ are present in solution to support the 2×2 tunnels during their initial formation. The down-tunnel image of one α-MnO$_2$ nanowire (Figure 6.1e) shows that the nanowire has a square shaped cross-section with four {100} lateral surfaces. The corresponding crystal structure is shown in Figure 6.1f, in which 1×1 and 2×2 tunnels are clearly observed. 1×1 tunnels are essentially empty while each 2×2 tunnel is found to contain one atomic column, in good agreement with the lateral HAADF image in Figure 6.1c. The energy dispersive spectroscopy (EDS) along the [110] direction shown in Figure 1f confirmed the tunnel walls to be Mn and the central atoms inside the 2×2 tunnels to be K$^+$ (Wyckoff 2a positions), from which the atomic model shown in the bottom inset of Figure 6.1f was constructed. From these observations, the K$^+$ concentration in as-synthesized α-MnO$_2$ was determined to be K$_{0.25}$MnO$_2$.
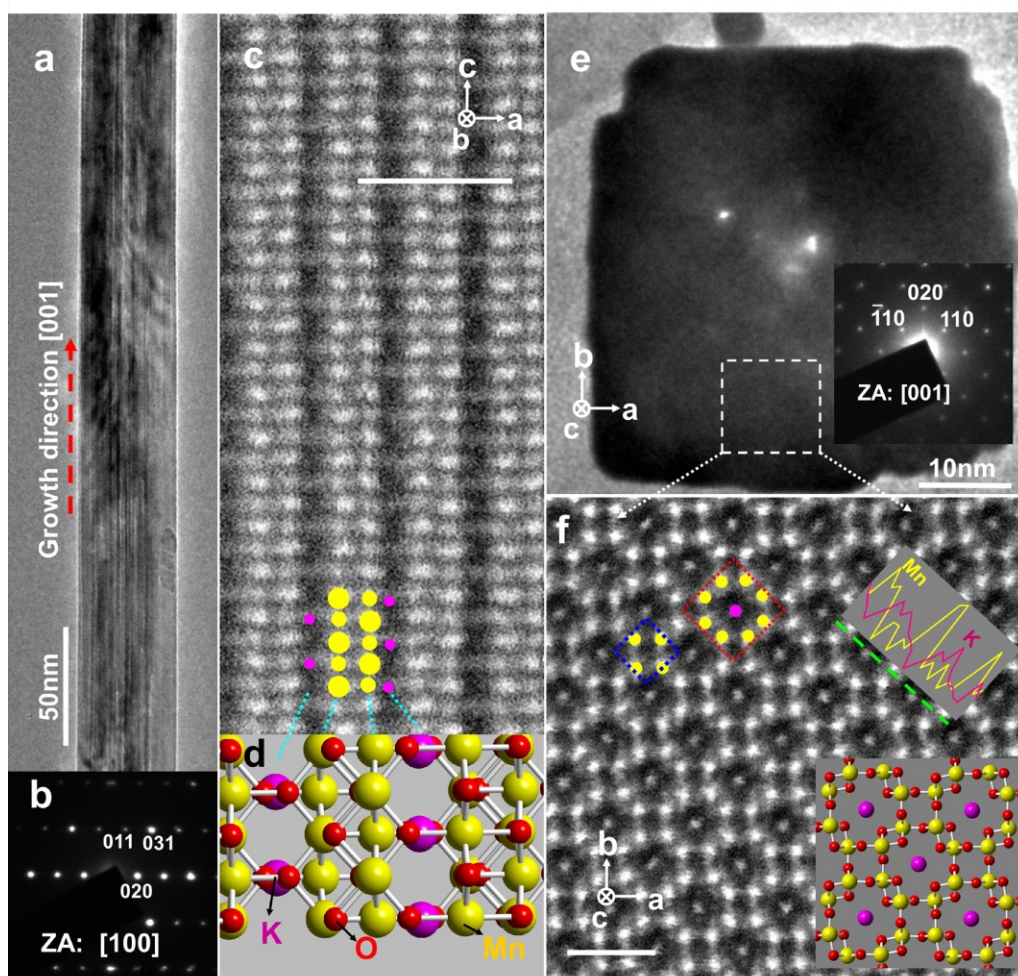
Figure 6.1. (a,b) A low-magnification TEM image of the as-synthesized α-MnO$_2$ nanowire and the corresponding [100] electron diffraction pattern; (c,d) The [100] HAADF image of the same nanowire with the representative atomic model. The yellow spheres indicate Mn atomic columns, while red and pink represent O and K$^+$ ions, respectively. (e) A low-magnification [001] TEM image showing one cross section of α-MnO$_2$ nanowire; (f) A [001] HAADF image revealing the atomic structure of tunneled α-MnO$_2$ with the red dotted square demarcating a 2×2 tunnel and the blue dotted square a 1×1 tunnel. The green line indicates the region along which EDS linear scanning was carried out. The bottom inset shows a model of the tunnel structure viewed down the tunnel axis. Scale bars in (c) and (f): 1 nm.

116

The structural and compositional analyses of the nanowires after HNO_3 treatment are carried out using X-ray powder diffraction (XRD) with Rietveld refinement and analytical STEM with EDS. The XRD results are shown in Figure 6.2. It can be seen that the α-MnO_2 phase is well maintained during the acid treatment as no extra peak generation or elimination is observed. However, with the increase of treatment time, all the peaks gradually shift toward higher angles, and this trend is more clearly demonstrated by the inset image showing the $(200)_{\alpha\text{-}MnO2}$ peak. The Rietveld refinement in the table quantifies the trend of tunnel contraction during acid treatment by deriving lattice parameters a, b and c, where the anisotropic tunnel expansion (mainly along a-b plane) is indicated. The estimated K^+ concentration further confirms that the tunnel contraction is essentially determined by the gradual removal of K^+ from the tunnels.

The atomic imaging of the tunnels with different K^+ concentrations in Figure 6.3 reveals that HNO_3 treatment was effective in removing K^+ from the 2×2 tunnels, and the K^+ concentration can be controlled by altering the treatment time. After 1-day treatment, K^+ has been partially removed from the nanowire, and the 2×2 tunnels are thus only partially filled. After 4-day treatment, α-MnO_2 is essentially free of any K^+ ions, as confirmed by both the HAADF image showing no K^+ contrast (Figure 6.3c) and the lack of any K^+ signal in the EDS spectra shown in the inset. The compositions of α-MnO_2 nanowires without treatment and after 1- and 4-day acid treatment were thus deduced to be $K_{0.25}MnO_2$, $K_{0.25\text{-}x}MnO_2$ and undoped MnO_2, respectively. It is also notable that the 2×2 tunnels slightly contract after K^+ removal, as indicated by the {020} spacing changing from 4.97 Å for the untreated nanowire to 4.84 Å for the 4-day treated nanowire. This tunnel contraction trend is clearly illustrated in figures 6.3d-f. Although the tunnel experiences significant volume change, the overall tunneled structure of α-MnO_2 is still maintained after K^+ removal, enabling all these three types of nanowires to function as an intercalation cathode in a lithium ion battery.

117
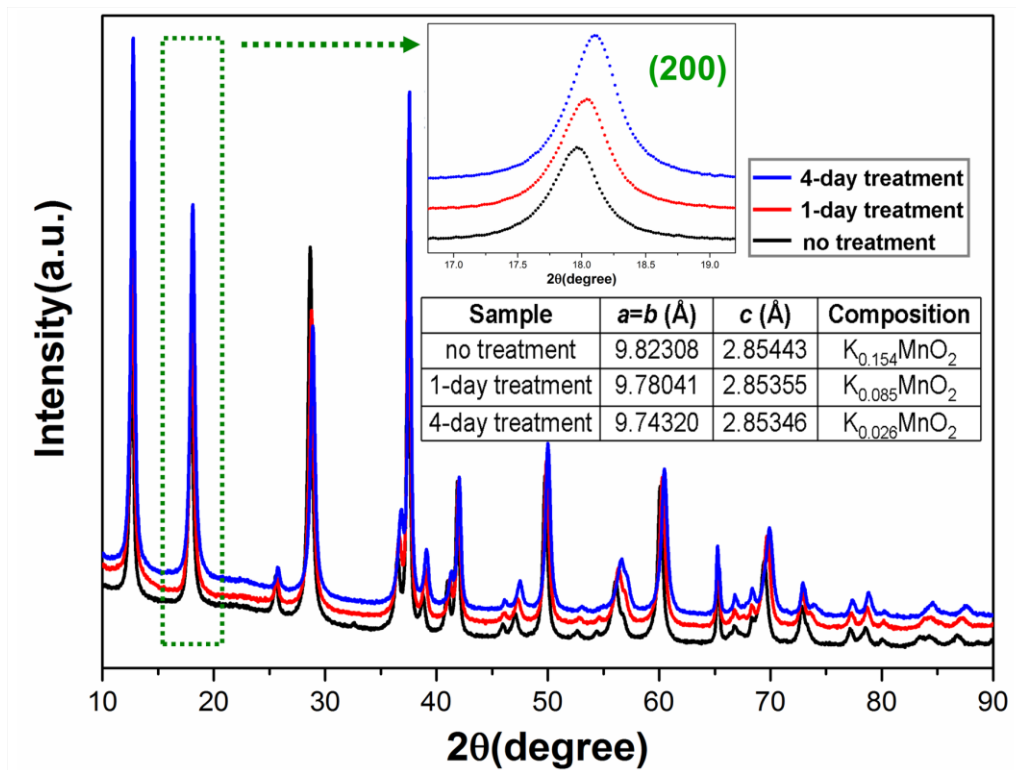
Figure 6.2. XRD results of the three groups of nanowires after acid treatment over different time scales. The inset image is the enlarged view of the α-MnO$_2$ (200) peak, where the gradual peak shift toward higher angle direction with increase of treatment time is observed. The table lists the calculated lattice parameters and compositions from the Rietveld refinement.

There is a slight variation between XRD and atomic STEM imaging in determining the K$^+$ concentration and lattice constants. This is understandable considering that STEM focuses on local atomic structure of a single nanowire, while XRD studies bulk information including the surface lattice and structural defects. In our case, since the composition of the nanowires without HNO$_3$ treatment is determined by counting the Mn and K atoms in the STEM image, which is mathematically more accurate than XRD, we have identified these nanowires as K$_{0.25}$MnO$_2$. This indicates that all 2a sites inside the 2×2 tunnels are occupied by K$^+$.[26] The composition for 4-day treated nanowires is determined to be nominally MnO$_2$ because both atomic STEM/EDS and

Rietveld refinement hardly show any signal for K^+. For 1-day treated nanowires, we express the composition using $K_{(0.25-x)}MnO_2$.
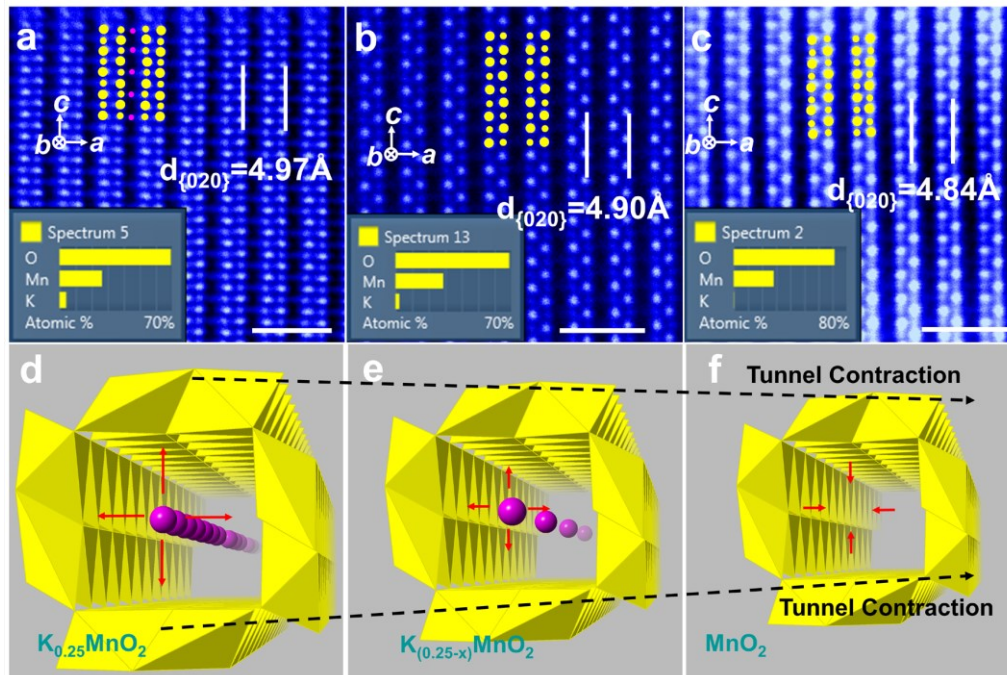
Figure 6.3. (a-c) False-colored [100] HAADF images of α-MnO_2 nanowires after (a) untreated, being treated with HNO_3 for (b) 1 day, and (c) 4 days. Yellow spheres indicate Mn and pink spheres represent K^+ inside 2×2 tunnels. The inset in each image shows the elemental concentrations of Mn, K and O based on EDS analysis of many nanowires. Scale bars: 1 nm. (d-f) The schematics of 2×2 tunnel cavity with different K^+ concentrations showing the tunnel contraction when K^+ ions are removed from the tunnel center. The pink spheres indicate K^+ on the centered 2a sites.

Previous studies suggest that the removal of K^+ from 2×2 tunnels in acid solutions is explained by either the K^+-H^+ exchange mechanism,[27,28] Mn oxidation mechanism,[23,29] or the existence of both[30]. The critical difference between them is whether the Mn valence is increased or not. In our study, the dominant mechanism is found to be Mn oxidation to Mn^{4+} rather than K^+-H^+ exchange. The detailed analysis using electron energy loss spectroscopy (EELS) and X-ray photoelectron spectroscopy (XPS) is provided in Supporting Information Figure C2 and Figure C3, respectively. Both EELS and XPS confirm the existence of Mn^{3+} in the nanowires before acid

treatment ($K_{0.25}MnO_2$), while a portion of Mn^{3+} gradually decreases with increase of treatment time. The average Mn valence gradually increases to Mn^{4+} as a result of K^+ removal. The exclusion of the K^+-H^+ exchange mechanism is not straightforward due to the difficulty in quantifying H concentration before and after acid treatment, which was done in a H_2O-based solution. In this work, since both XPS and EELS confirm K^+ removal to be accompanied by Mn oxidation rather than the K^+-H^+ exchange mechanism, the possibility of H^+ presence in the tunnels is minimized.

Prior to electrochemistry analysis, the surfaces and thermal stability of the nanowires were characterized to check whether the nanowires are affected by the acid treatment. The Brunauer–Emmett–Teller (BET) analysis in Supporting Information Table C1 (Appendix C) shows no significant change in the surfaces of nanowires. Thermogravimetric analysis (TGA) and *in situ* TEM heating techniques are used to test the thermal stability of the nanowires after K^+ removal from the tunnels, and the results and detailed analysis are shown in Supporting Information Figure C4 and Figure C5, respectively. The results confirm that the nanowires after K^+ removal from the tunnels are thermally stable without any phase transition or tunnel collapse up to 350 ºC.

6.3.2. Effect of K^+ on electronic and ionic conductivities of α-MnO$_2$ nanowires

Our previous simulation work[17] suggest that 2×2 tunnels are the preferred Li^+ transport channels in pure α-MnO$_2$. We have also reported previously that Li^+ ions thermodynamically occupy the off-centered Wyckoff 8h site inside each 2×2 tunnel rather than the tunnel center,[8,17] which is also demonstrated by other groups.[31] Therefore, with K^+ on the centered 2a sites and the tunnel expanded by K^+, it is reasonable to expect the K^+ concentration inside the 2×2 tunnels to affect both electronic and ionic transport and hence the electrochemical behavior of an α-MnO$_2$

cathode. To examine these effects, the electronic conductivity and Li$^+$ diffusivity of α-MnO$_2$ nanowires with different K$^+$ concentrations were characterized using *in situ* TEM and EIS methods.
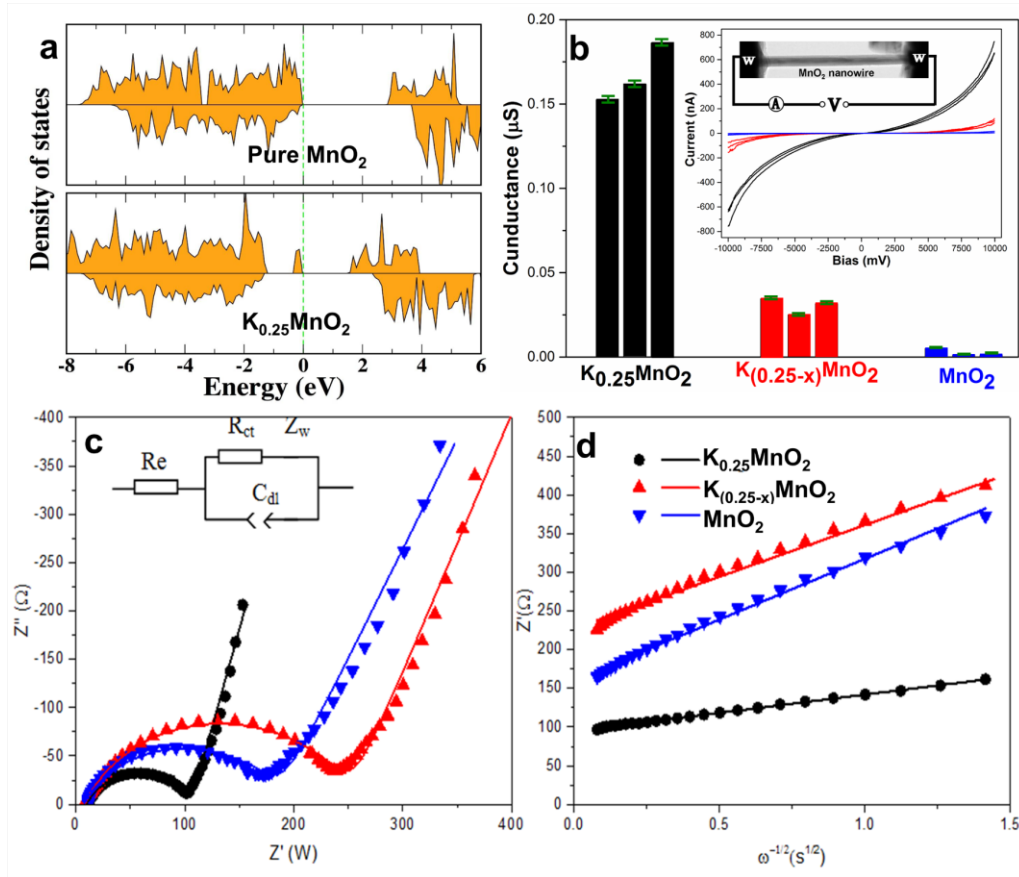
Figure 6.4. (a) Calculated electron density of states near the Fermi level region of K$_{0.25}$MnO$_2$ and pure MnO$_2$. (b) Conductance of α-MnO$_2$ nanowires with different K$^+$ concentrations. Three nanowires were tested for each K$^+$ concentration, as indicated by different colored bars. The inset shows the *in situ* TEM experimental setup and the I-V responses of the nine α-MnO$_2$ nanowires. (c) Impedance spectra (Nyquist plots) and (d) linear fitting to Z' vs. ω$^{-1/2}$ plots in the low frequency range (<25 Hz) of the electrodes with K$_{0.25}$MnO$_2$, K$_{0.25-x}$MnO$_2$ or undoped MnO$_2$ as the active material. The scatter points are the experimental data and the lines represent the simulation results using the equivalent circuit shown in (c).

The electronic structure was also examined by density functional theory (DFT) simulations and also by direct electrical probing within the microscope, the results of which are given in Figure 6.4a-b. This computational work complements and extends previous DFT studies[8,16] on interstitial cation incorporation in α-MnO$_2$. The simulated density of states (shown in Figure 6.4a) indicates that pure α-MnO$_2$ has a band gap of approximately 2.8 eV suggesting semiconductor behavior, and agrees well with the reported value of Young et al.[16] For K$_{0.25}$MnO$_2$, newly formed occupied states appear inside the original MnO$_2$ bandgap , indicating mixed Mn^{4+} and Mn^{3+} in K$_{0.25}$MnO$_2$, which is compatible with previous reports.[32] This indicates that the presence of K$^+$ inside the 2×2 tunnels can enhance the electronic conductivity of α-MnO$_2$ through electron hopping between Mn^{4+}/Mn^{3+}.

For each K$^+$ concentration, the conductivity of three nanowires was measured to test reproducibility. The I-V responses of all the nanowires with different K$^+$ concentrations measured *in situ* in the microscope (inset of Figure 6.4b) are nonlinear but symmetric in the low-bias regime. This can be ascribed to the Schottky barriers formed between the semiconducting nanowire and the metal (W) electrodes.[33] In the large-bias regime (8-10 V), the I–V curves exhibit a near-linear relationship, and the conductance (G) of the nanowires can be calculated according to G = dI/dV.[34] G was calculated to be 0.15~0.19 μS for K$_{0.25}$MnO$_2$, 0.025~0.034 μS for K$_{0.25-x}$MnO$_2$, and 0.0011~0.0050 μS for undoped MnO$_2$; the results are plotted in Figure 6.4b, and details of the data fitting are provided in Supporting Information Table C2. Because of the similar diameters and lengths of the selected nanowires used for testing, the conductivities of nanowires with different K$^+$ concentrations should exhibit similar trends as the conductance. It can be seen that K$_{0.25}$MnO$_2$ has a conductivity about 40 times higher than that of pure α-MnO$_2$, indicating the important role of tunnel cations in enhancing the electronic conductivity of α-MnO$_2$ nanowires. The origin of the improved electronic conductivity of α-MnO$_2$ containing K$^+$ can be attributed to the electron hopping between heterovalent Mn pairs (Mn^{3+}/Mn^{4+}) induced by K$^+$ doping.[35,36] Increasing the cation content will produce more regions inside the

nanowire with mixed Mn^{3+}/Mn^{4+} valence states, resulting in higher electronic conductivity.[37]

Li^+ diffusion in α-MnO$_2$ nanowires with different K^+ contents was characterized by EIS, and the results are shown in Figure 6.4c-d. Figure 6.4c shows the impedance spectra (Nyquist plots) of electrodes with $K_{0.25}MnO_2$, $K_{0.25-x}MnO_2$ or undoped MnO_2 as the active material. In the low frequency region the real part of the impedance (Z') is linear against the -1/2 power of the angular frequency ($\omega^{-1/2}$), and the slope is called the Warburg coefficient (σ). Linear fits to the Z' $vs.$ $\omega^{-1/2}$ plots for the untreated and treated α-MnO$_2$ electrodes are shown in Figure 4d, and the corresponding σ values are listed in Table 6.1. In addition, the equivalent circuit (inset of Figure 6.4c) was used to fit the spectra and the results are listed in Table 6.1. The charge transfer resistance (R_{ct}) increased after K^+ removal, indicating that doping with K^+ enhances lithium intercalation near the electrode/electrolyte interface.

The chemical diffusion coefficient of Li ions ($\tilde{D}_{Li}$) inside an electrode can be derived using the following equation,[38]

$$\tilde{D}_{Li} = \frac{1}{2}\left(\frac{V_m}{FS\sigma}\frac{dE}{dy}\right)^2 \qquad (1),$$

where V_m is the molar volume of the active material, F is the Faraday constant, S denotes the active surface area of the positive electrode, and dE/dy is the slope of the open circuit potential (OCP) vs. the Li^+ concentration y in $Li_yK_xMnO_2$. The value of dE/dy was obtained from galvanostatic intermittent titration technique (GITT) measurements. The specific surface areas were obtained from BET results (Supporting Information Table C1), with 28.2 m^2/g for $K_{0.25}MnO_2$, 26.8 m^2/g for $K_{0.25-x}MnO_2$ after 1-day acid treatment and 26.7 m^2/g for pure MnO_2 after 4-day treatment, respectively. The measured values agree well with reported specific surface areas for hydrothermally synthesized α-MnO$_2$ nanostructures which is in the range of 20-40 m^2/g.[12,39-41] The values of $\tilde{D}_{Li}$ are listed in Table 6.1 showing that the

chemical diffusion coefficient of Li$^+$ is reduced by removal of K$^+$. In addition, extending the time of acid treatment from 1 day to 4 days leads to a three-orders-of-magnitude decrease in the value of $\tilde{D}_{Li}$. These results directly confirm that K$^+$ in α-MnO$_2$ tunnels facilitates diffusion of Li$^+$. Although there are currently no measured diffusion data on Li/K-MnO$_2$ for direct comparison, the magnitudes of $\tilde{D}_{Li}$ are comparable to other electrode materials; for example, experimental diffusion coefficients of 10^{-8} to 10^{-12} cm$^2 \cdot$s^{-1} have been reported for Li$^+$ diffusion in layered oxide cathodes such as LiCoO$_2$ and Li(Ni,Mn,Co)O$_2$.[42,43,44] The increase of Li$^+$ diffusivity by the addition of K$^+$ can be attributed mainly to the expansion of the tunnel cavity by the large centered K$^+$ cation at 2a sites. The improved e$^-$ conductivity is also beneficial for Li$^+$ conductivity in the tunnels with K$^+$ presence.

Table 6.1 Transport properties derived from the impedance spectra (at T = 25 °C).

Samples	$R_e(\Omega)$	$R_{ct}(\Omega)$	σ ($\Omega \cdot$s$^{-1/2}$)	$\tilde{D}_{Li}$ (cm$^2 \cdot$s^{-1})
K$_{0.25}$MnO$_2$	9.916	97.26	47.10	1.91×10^{-12}
K$_{(0.25-x)}$MnO$_2$	8.198	246.3	133.5	7.16×10^{-13}
Pure MnO$_2$	7.261	182.2	160.5	2.82×10^{-15}

6.3.3. Rate performance of α-MnO$_2$ cathodes with different K$^+$ concentrations

Since the presence of tunnel cations improves both the electronic conductivity and Li$^+$ diffusivity of α-MnO$_2$, the rate performance of a Li/α-MnO$_2$ battery would be expected to be enhanced when K$^+$ occupy the tunnels. Before we examined the rate performance, the tunnel stability as well the stability of K$^+$ inside the tunnels during repetitive cycling is characterized. Figure C6a-c in the Supporting Information shows the morphology and phase analysis of three groups of nanowires (K$_{0.25}$MnO$_2$, K$_{0.25-}$

$_x$MnO$_2$, pure MnO$_2$) after 100 battery cycles (Li/α-K$_x$MnO$_2$ coin cells). Figure C6d shows the EDS quantification of K$^+$ concentrations inside the tunnels before and after battery cycles for the electrode initially composed of K$_{0.25}$MnO$_2$ nanowires. The K$^+$ concentration in the tunnels is slightly reduced after cycling (probably lost into the electrolyte), while the majority of K$^+$ remains inside the nanowires. All the nanowires, including those with K$^+$ (partially and totally) removed, retain their tunneled α-MnO$_2$ structure with no obvious morphology change during battery cycling. Therefore the good stability of K$^+$ ions in the tunnels can retain their effect on the battery performance upon continuous cycling.

To investigate the effect of K$^+$ concentration on the first cycle performance, the galvanostatic discharge/charge curves for three groups of nanowires are shown in Figure C7 (Supporting Information). While all exhibit a discharge reaction around 2.5 V *vs* Li/Li$^+$, the discharge capacity of the nanowires without acid treatment (143 mAh/g) is relatively lower than that of the treated nanowires (157 mAh/g and 170 mAh/g), which can be ascribed to the addition of inactive mass of K$^+$ into the electrode. Upon charge, however, the capacity of the treated nanowires is lower than the capacity of the nanowires with no treatment.

To study the rate performance, the first discharge capacity of a Li/α-MnO$_2$ battery under different current rates (0.1, 0.5, 1, 2 and 5 C) was measured for the three groups of nanowires. To make the comparison more straightforward, the discharge capacity at 0.1 C was normalized to 100%. From Figure 6.5a, it can be seen that the first discharge capacities of cathodes made of K$_{0.25}$MnO$_2$, K$_{0.25-x}$MnO$_2$ and undoped MnO$_2$ were all reduced when the C rate was increased from 0.1 to 5 C. The capacity retention behavior under high discharge currents, however, varied with different K$^+$ concentrations. Li/K$_{0.25}$MnO$_2$ exhibited 62% capacity retention at 5 C, while Li/K$_{0.25-x}$MnO$_2$ retained only 54% capacity and Li/MnO$_2$ showed capacity retention as low as 8% at 5 C. The cycling-rate performance of the three groups of nanowires is shown in Figure C8 (Supporting Information). While the capacity retention is similar for the

three groups at 1 C, it indeed shows better capacity retention at higher currents (2 C and 5 C) for the nanowires with the highest K^+ concentration. The mechanisms accounting for the rate performance variation (especially during the first cycle) of K^+-doped nanowires is illustrated in Figure 6.5b. As discussed earlier, the presence of K^+ in tunneled α-MnO_2 not only improves electronic conductivity by boosting e^- hopping *via* Mn^{3+}/Mn^{4+} couples, but also enhances Li^+ diffusivity.
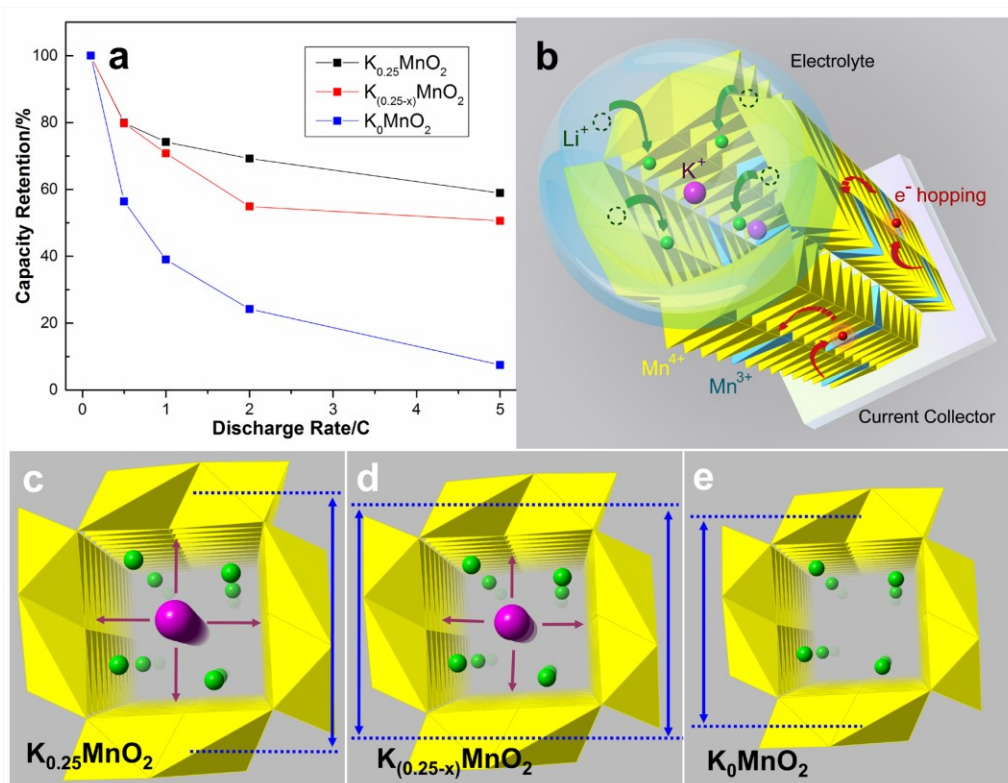
Figure 6.5. (a) Capacity measurements during the first discharge process of $Li/K_{0.25}MnO_2$, $Li/K_{0.25-x}MnO_2$ and Li/MnO_2 based batteries at discharge rates of 0.1, 0.5, 1, 2, and 5 C. The 0.1 C capacities were normalized to 100% for a straightforward comparison between different C rates. (b) 3D schematic showing how K^+ doping facilitates Li^+ accommodation by expanding the tunnel cavity and improves the electron conductivity by boosting the electron hopping mechanism during the electrochemical cycling inside a Li/α-MnO_2 battery. The pink spheres indicate K^+ occupying the centered 2a sites, green spheres indicate inserted Li^+ on the off-centered 8h sites. The yellow octahedra represent $[Mn^{4+}O_6]$ while the blue ones represent $[Mn^{3+}O_6]$. The red arrows indicate the electron hopping along Mn^{3+}/Mn^{4+}

paths. (c-e) The schematics of single 2×2 tunnel showing the atomic configuration of K^+ (pink) at centered 2a sites and Li^+ (green) at off-centered 8h sites. The trend of tunnel contraction when K^+ ions are removed from the tunnel center is also illustrated by the blue arrows. The atomic configuration of Li^+, K^+ and O^{2-} in one 2×2 tunnel is calculated and explained in Supporting Information.

Our investigation opens up further research opportunities in this area. For example, although not a trivial task, future atomistic simulations could be used to explore Li-ion diffusion in these nanowire structures with large cations inside. It would also be interesting to explore replacing K^+ with other cations such as Ag^+, Ba^{2+}, to examine models related to cation-tunnel interactions, such as charge-switching states proposed by Young *et al.*[16], and to study the effect of trace amounts of H^+ *via* sensitive techniques such as quasi-elastic neutron scattering. Currently, we have found no experimental evidence showing the direct capacity contribution from Li^+ intercalation at 1×1 tunnel. Still, future work could explore the possibility of Li^+ intercalation at 1×1 tunnels as a competing mechanism agaist its insertion at 2×2 tunnels where large cations reside.

6.4. Conclusions

In this study, the effect of tunnel cations (K^+) on the electrochemical performance of α-MnO_2 cathodes was examined using a powerful combination of analytical aberration-corrected STEM, *in situ* TEM, electrochemical testing and *ab initio* modeling. α-MnO_2 nanowires with different K^+ concentrations were prepared and imaged at sub-ångstrom resolution to determine the structure of tunnels as well as the location and content of K^+. It was found that the presence of K^+ inside the 2×2 tunnels of α-MnO_2 nanowires improves both their electronic conductivity and Li^+ diffusivity. These enhancements facilitate favorable electrode kinetics, and thus result in good rate performance of Li/α-MnO_2 based batteries.

The results of our systematic study provide a valuable framework for the rational selection of tunnel cations and their concentrations to improve the rate performance of tunnel-based intercalation electrodes. In addition, the positive effect of K^+ incorporation suggests that further exploration of tunnel-based cathodes with new battery chemistries based on Na^+, Mg^{2+}, and Al^{3+} ions is also warranted.

6.5. References

1. Wang, Y. & Cao, G. Developments in nanostructured cathode materials for high performance lithium-ion batteries. *Adv. Mater.* **20**, 2251-2269 (2008).

2. Islam, M. S. & Fisher, C. A. J. Lithium and sodium battery cathode materials: computational insights into voltage, diffusion and nanostructural properties. *Chem. Soc. Rev.* **43**, 185-204 (2014).

3. Zhang, K. *et al.* Nanostructured Mn-based oxides for electrochemical energy storage and conversion. *Chem. Soc. Rev.* **44**, 699-728 (2015).

4. Wang, Y. *et al.* Ti-substituted tunnel-type $Na_{0.44}MnO_2$ oxide as a negative electrode for aqueous sodium-ion Batteries. *Nat. Commun.* 6:6401 (2015).

5. Ren, Y. *et al.* A solid with a hierarchical tetramodal micro-meso-macro pore size distribution. *Nat. Commun.* 4:2015 (2013).

6. Ghodbane, O., Pascal, J. L. & Favier, F. Microstructural effects on charge-storage properties in MnO_2-based electrochemical supercapacitors. *ACS Appl. Mater. Interfaces* **1**, 1130-1139 (2009).

7. Johnson, C. S. Development and utility of manganese oxides as cathodes in lithium batteries. *J. Power Sources* **165**, 559-565 (2007).

8. Tompsett, D. A & Islam, M. S. Electrochemistry of hollandite α-MnO_2: Li-ion and Na-ion insertion and Li_2O incorporation. *Chem. Mater.* **25**, 2515-2526 (2013).

9. Arthur, T.S. *et al.* Understanding the electrochemical mechanism of K-alpha MnO_2 for magnesium battery cathodes. *ACS Appl. Mater. Interfaces* **6**, 7004-7008 (2014).

10. Su, D., Ahn, H. J. & Wang, G. Hydrothermal synthesis of α-MnO$_2$ and β-MnO$_2$ nanorods as high capacity cathode materials for sodium ion batteries. *J. Mater. Chem. A* **1**, 4845–4850 (2013).

11. Zhang, R. *et al.* α-MnO$_2$ as a cathode material for rechargeable Mg batteries. *Electrochem. Commun.* **23**, 110–113 (2012).

12. Trahey, L. *et al.* Synthesis, Characterization, and structural modeling of high-capacity, dual functioning MnO$_2$ electrode/electrocatalysts for Li-O$_2$ cells. *Adv. Energy Mater.* **3**, 75-84 (2013).

13. Yang, Z. *et al. In situ* high-energy synchrotron X-ray diffraction studies and first principles modeling of α-MnO$_2$ electrodes in Li–O$_2$ and Li-ion coin cells. *J. Mater. Chem. A* **3**, 7389–7398 (2015).

14. Santhanagopalan, S., Balram, A. & Meng, D. D. Scalable high-power redox capacitors with aligned nanoforests of crystalline MnO$_2$ nanorods by high voltage electrophoretic deposition. *ACS Nano* **7**, 2114–2125 (2013).

15. Simon, P., Gogotsi, Y. & Dunn, B. Where do batteries end and supercapacitors begin? *Science Magazine* **343**, 1210-1211 (2014).

16. Young, M.J. *et al.* Charge storage in cation incorporated α-MnO$_2$. *Chem. Mater.* **27**, 1172−1180 (2015).

17. Yuan, Y. *et al.* Asynchronous crystal cell expansion during lithiation of K$^+$-stabilized alpha-MnO$_2$. *Nano Lett.* **15**, 2998-3007 (2015).

18. Zhai, D. *et al.* A study on charge storage mechanism of α-MnO$_2$ by occupying tunnels with metal cations (Ba^{2+}, K$^+$). *J. Power Sources* **196**, 7860– 7867 (2011).

19. Wei, W. *et al.* Manganese oxide-based materials as electrochemical supercapacitor electrodes. *Chem. Soc. Rev.* **40**, 1697–1721 (2011).

20. Toupin, M. *et al.* Charge storage mechanism of MnO$_2$ electrode used in aqueous electrochemical capacitor . *Chem. Mater.* **16**, 3184-3190 (2004).

21. Hill, L. I., Verbaere, A. & Guyomard, D. MnO$_2$ (α-, β-, γ-) compounds prepared by hydrothermal-electrochemical synthesis: characterization, morphology, and lithium insertion behavior. *J. Power Sources* **119**, 226-231 (2003).

22. Wang, H. *et al.* Facile synthesis and electrochemical characterization of hierarchical α-MnO$_2$ spheres. *J. Alloys Compd.* **466**, 250-257 (2008).

23. Kijima, N. *et al.* Synthesis, crystal structure, and electrochemical properties of hollandite-type K$_x$Ti$_{1-y}$Mn$_y$O$_2$. *Solid State Ionics* **262**, 14-17 (2014).

24. Johnson, C. S. & Thackeray, M. M. Ammonia- and lithia-doped manganese dioxide for 3 V lithium batteries. *J. Power Sources* **97**, 437-442 (2001).

25. Wang, S. *et al.* Effects of polyaniline coating of cryptomelane-type KMn$_8$O$_{16}$ on electrochemical performance for lithium-ion batteries. *J. Nanopart. Res.* **16**, 2232 (2014).

26. Luo, J. *et al.* Tuning Magnetic Properties of r-MnO$_2$ Nanotubes by K$^+$ Doping. *J. Phys. Chem. C* **19**, 8782-8786 (2010).

27. Tanaka, Y. *et al.* ESCA and thermodynamic studies of alkali metal ion exchange reactions on an α-MnO$_2$ phase with the tunnel structure. *Phys. Chem. Chem. Phys.* **2**, 1473-1479 (2000).

28. Kijima, N. *et al.* Crystal structure of an open-tunnel oxide α-MnO$_2$ analyzed by Rietveld refinements and MEM-based pattern fitting. *J. Solid State Chem.* **177**, 1258-1267 (2004).

29. Feng, Q. *et al.* Alkali metal ions insertion/extraction reactions with hollandite-type manganese oxide in the aqueous phase. *Chem. Mater.* **7**, 148-153 (1995).

30. Feng, Q. Manganese oxide porous crystals. *J. Mater. Chem.* **9**, 319-333 (1999).

31. Ling, C. & Mizuno, F. Capture lithium in α-MnO$_2$: insights from first principles. *Chem. Mater.* **24**, 3943-3951 (2012).

32. Cockayne, E. & Li, Lan. First-principles DFT + U studies of the atomic, electronic, and magnetic structure of α-MnO$_2$ (cryptomelane). *Chem. Phys. Lett.* **544**, 53–58 (2012).

33. Zhang, Z. *et al.* Quantitative analysis of current–voltage characteristics of semiconducting nanowires: decoupling of contact effects. *Adv. Funct. Mater.* **17**, 2478-2489 (2007).

34. Asthana, A. *et al.* Deformation-driven electrical transport in amorphous TiO$_2$ nanotubes. *Appl. Phys. A* **109**, 127-132 (2012).

35. Subramanian, M. A., Ramirez, A. P., Kwei & G. H. Colossal magnetoresistance behavior in manganese oxides: pyrochlore versus perovskite. *Solid State Ionics* **108**, 185-191 (1998).

36. Umek, P. *et al.* Synthesis of 3D hierarchical self-assembled microstructures formed from α-MnO_2 nanotubes and their conducting and magnetic properties. *J. Phys. Chem. C* **113**, 14798–14803 (2009).

37. Noh, T. *et al.* Structural and impedance analysis of copper doped LSM cathode for IT-SOFCs. *J. Alloys Compd.* **557**, 196-201 (2013).

38. Arora, P., Popov, B. & White, R. E. Electrochemical investigations of cobalt‐doped $LiMn_2O_4$ as cathode material for lithium-ion batteries. *J. Electrochem. Soc.* **145**, 807-815 (1998).

39. Xiao, W., Wand, D. & Lou, X. Shape-controlled synthesis of MnO_2 nanostructures with enhanced electrocatalytic activity for oxygen reduction. *J. Phys. Chem. C* **114**, 1694–1700 (2010).

40. Boppana, V. B. & Jiao, F. Nanostructured MnO_2: an efficient and robust water oxidation catalyst. *Chem. Commun.* **47**, 8973-8975 (2011).

41. Liang, S. *et al.* Effect of phase structure of MnO_2 nanorod catalyst on the activity for CO oxidation. *J. Phys. Chem. C* **112**, 5307–5315 (2008).

42. Shaju, K. M. *et al.* Influence of Li-ion kinetics in the cathodic performance of layered $Li(Ni_{1/3}Co_{1/3}Mn_{1/3})O_2$. *J. Electrochem. Soc.* **151**, A1324-A1332 (2004).

43. Gozu, M. *et al.* Structural and transport properties of layered $Li_{1+x}(Mn_{1/3}Co_{1/3}Ni_{1/3})_{1-x}O_2$ oxides prepared by a soft chemistry method. *J. Power Sources* **194**, 38–44 (2009).

44. West, W.C. *et al.* Electrochemical behavior of layered solid solution Li_2MnO_3-$LiMO_2$ (M=Ni, Mn, Co) Li-ion cathodes with and without alumina coatings. *J. Electrochem. Soc.* **158**, A883-A889 (2011).

Chapter 7. Atomistic Insights Into the Oriented Attachment of Tunneled Oxide Nanostructures[⑤]

7.1. Introduction

Considerable attention has been devoted to the study of inorganic compounds with open tunnel structures. Materials in this category include, but are not limited to, zeolites,[1,2] titanium silicates,[3] TiO_2[4,5] and MnO_2-based molecular sieves.[6-10] The characteristic tunnel-based structure allows these materials to accommodate and transport charge carriers (also called tunnel stabilizers) with different sizes and charges, enabling their wide application in catalysis, ion exchange and energy storage.[11-14] Controlled synthesis is necessary to produce tunnel-based nanostructures with various tunnel sizes, morphologies and atomic ordering. However, this process is not fully understood and requires fundamental understanding of the growth mechanisms on the nanoscale and even at the single-tunnel level.

Solution-based synthesis is often used to prepare tunnel-based materials, in the form of one-dimensional nanostructures.[15-23] The growth mechanism is generally believed to be an oriented attachment (OA) process where primary particles aggregate by sharing a common planar interface and form a secondary particle with a uniform orientation, allowing the rational design of hierarchical nanostructures for functional devices.[19,24-26] The driving force for the growth is thought to be the reduction of the surface energy when primary particles attach together.[27-29] The as-formed OA interface is usually imperfect,[30,31] because of the complex nature of different tunnel-tunnel intergrowths[32,33] as well as the strong interaction between tunnels and the inner stabilizers.[34,35] It is still unclear how primary tunnels grow to form secondary

---

nanowires with precise alignment of tunnels. Understanding the atomic structure of tunnel-based materials during growth is crucial for designing nanomaterials in which the tunneled structure can be tailored and controlled for desired applications.

α-MnO$_2$ represents an important family of tunnel-based structures with well-aligned 2×2 (4.6 Å × 4.6 Å) and 1×1 (1.9 Å × 1.9 Å) tunnels.[16] Polyhedral and atomic models of α-MnO$_2$ are illustrated in Figure 7.1. The larger 2×2 tunnels are generally stabilized by various cations, such as NH$_4^+$, Ba^{2+}, and K$^+$.[19] Here, K$^+$-stabilized α-MnO$_2$ nanowires were investigated to understand their tunnel-based structures during growth. For the first time, the morphology evolution of α-MnO$_2$ nanowires in aqueous solution environment was dynamically observed using liquid cell transmission electron microscopy (TEM), and sub-angstrom imaging of the tunneled interfaces was obtained using aberration-corrected scanning TEM (AC-STEM). The structural characterization was complemented by *ab initio* calculations to elucidate the surface energetics of K$^+$-stabilized α-MnO$_2$. It was found that primary α-MnO$_2$ nanowires prefer to attach together laterally along their {110} surfaces to form larger secondary nanowires facilitated by the reduction of their surface energy. In contrast to the conventional 1×1 and 2×2 tunnels, the {110} interfaces are composed of 2×3 tunnels parallel to the 1×1 and 2×2 tunnels. The formation of the 2×3 tunnel-based {110} interfaces during the growth process is driven by reduction of the surface energy and bonding of [MnO$_5$] units exposed at {110} surfaces with [MnO$_x$] radicals in solution. The importance of K$^+$ in forming the 2×3 tunnel-based interfaces during the oriented attachment growth is also demonstrated.
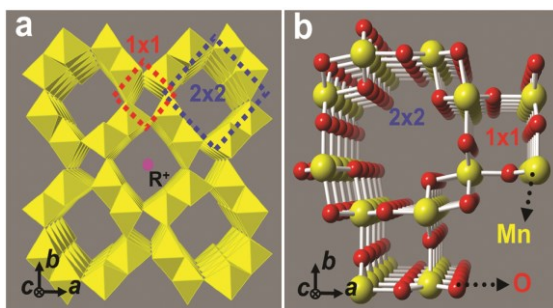
Figure 7.1. Crystal structures of α-MnO$_2$. (a) [MnO$_6$] octahedra model (b) atomic model viewed along [001] (*c*-axis). The 2×2 and 1×1 tunnels are indicated by blue

and red dashed squares, respectively, in (a); The typical definition of a tunnel is based on the number of [MnO_6] octahedra in each tunnel wall. R^+ indicates the position of 2×2 tunnel stabilizers such as NH_4^+, Ba^{2+}, and K^+.

7.2. Methods

The details for nanostructure synthesis, structural characterization and the DFT calculations are provided in Appendix D.

7.3. Results and discussion

7.3.1. Morphology and phase evolution

The morphology and phase evolution of MnO_2 nanowires under different reaction times were studied using X-ray diffraction (XRD) and transmission electron microscopy (TEM), and the results are presented in Figure 7.2. XRD results show that the characteristic peaks (red indices) of α-MnO_2 appear when the reaction time reaches 1.5 h. When the reaction time was increased from 1.5 to 9 h, the size and crystallinity of nanowires gradually improved, as indicated by the peak sharpening and intensity enhancing, respectively. From 9 to 12 h, the XRD peaks do not show any obvious difference, indicating stable and well-formed α-MnO_2. Layered δ-MnO_2, although not detected by XRD (probably on account of its low concentration and partial peak overlapping), was found by TEM to coexist with α-MnO_2 nanowires grown for less than 1.5 h. However, for longer reaction times, no evidence of δ-MnO_2 was found. This finding agrees well with previous reports stating that layered δ-MnO_2 functions as the precursor for tunnel-based α-MnO_2 nucleation and growth.[18] Figure 7.2 also shows that the primary α-MnO_2 nanowires gradually attached to each other and formed secondary α-MnO_2 nanowires with a larger diameter (marked as red dotted circles). This is indicative of a lateral OA mechanism operating during the growth of α-MnO_2.
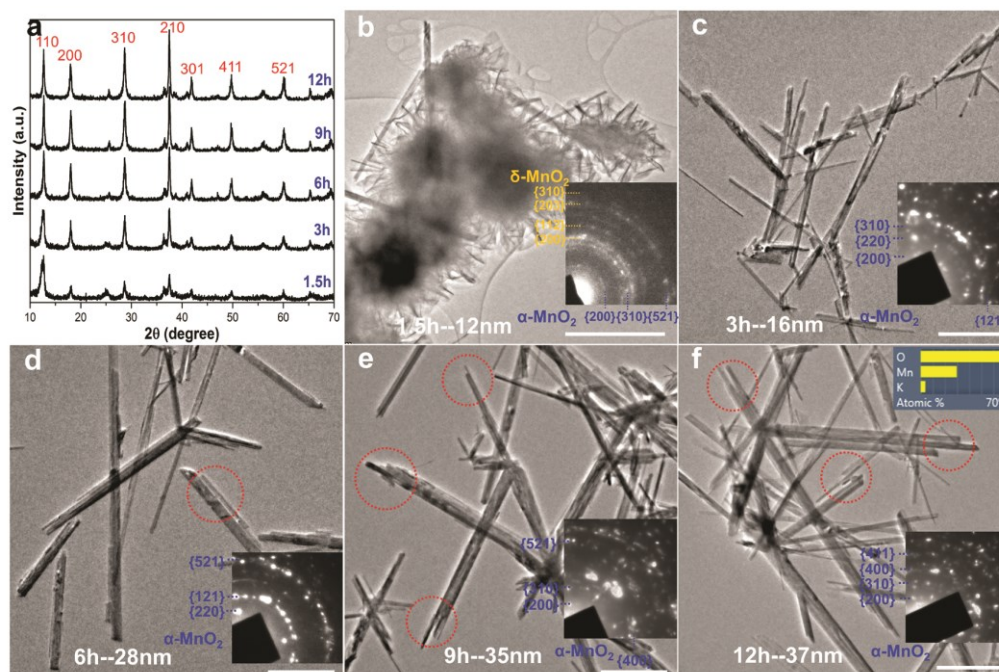
Figure 7.2. (a) XRD patterns for hydrothermally prepared α-MnO$_2$ nanowires for reaction times of 1.5, 3, 6, 9, and 12 hours; (b-f) TEM images and selected area electron diffraction patterns (insets) of the samples after different reaction times. The upper inset in (f) shows the EDS results confirming the presence of K$^+$. Scale bars are 100 nm.

The growth rate greatly decreased after 9 h, as confirmed by a slight change in the diameter of nanowires produced for reaction times between 9 and 12 h. The thickness contrast in each secondary nanowire is relatively uniform along the nanowire length. However, this is not the case radially. This indicates that primary nanowires share a common growth direction. The energy dispersive spectrometer (EDS) results in Figure 7.2f confirm the existence of a small concentration of potassium (K$^+$), consistent with use of a K$^+$-containing solution.

To confirm that the secondary nanowires are formed by the ordered alignment of several primary nanowires, we investigated secondary nanowires using *in situ* liquid cell TEM.[27,36-38] Interestingly, a high dose electron beam was sufficient to trigger the dissolution of secondary α-MnO$_2$ nanowires immersed in KCl solution and break

them down to the original building blocks. The corresponding movie illustrating this process is provided as Movie D1 (played in real time) in the Supporting Information, and Figure 7.3 shows *in situ* time-lapse TEM images of the morphology evolution of a secondary α-MnO$_2$ nanowire during this dissolution process. From 0 to 16 s, the secondary nanowire experienced isotropic dissolution both radially and axially in KCl solution. It is notable that the interface region (green arrows) was gradually etched during the dissolution process, which is demonstrated by the increase in brighter contrast. This finding indicates that the OA interface is metastable during the solution-based synthesis process. After 20 s, the interface was completely eliminated causing the detachment and misorientation of the two primary α-MnO$_2$ nanowires (the rotation directions are marked by the yellow arrows in figures 7.3f, g and h). To confirm that the electron beam is the driving force for the dissolution, we intentionally kept the secondary nanowire in the liquid environment for one hour before it was exposed to the electron beam for the *in situ* recording. Then the beam was turned on and the secondary nanowire was found in the well grown morphology with the OA interface clearly seen, indicating that no dissolution occurred when there was no electron beam. Hence, the dissolution of the oriented attachment interface can be attributed to the use of the electron beam.

We propose that the radiation chemistry plays a critical role in the dissolution and detachment of α-MnO$_2$ nanowires inside the TEM liquid cell. It has been reported that a water-based solution, when subjected to high dose electron beam, decomposes into excited and ionized species such as H$^+$, OH$^-$, H$_2$, and H$_2$O$_2$.[39] Due to the different reaction kinetics among these species, for an initially neutralized solution, the entire liquid cell will gradually exhibit an increased H$^+$ concentration and reduced pH.[40] The acid environment, according to *ex situ* solution synthesis experiments for α-MnO$_2$ nanostructures, is detrimental to the maintenance of larger tunnels such as 2×2 and 2×3 tunnels because the stabilizing effect of larger cations is weakened by H$^+$ in solution.[34] In the case of our KCl solution (with initial pH=7) that contains secondary α-MnO$_2$ nanowires, the solution environment would gradually become H$^+$ rich under

exposure to an electron beam. Such an acidic environment destabilizes the K^+ residing inside the 2×2 tunnels and facilitates the ion exchange process between K^+ and H^+. Due to the much weaker tunnel stabilizing effect of H^+ compared to K^+,[41] the 2×2 tunnel-based structure will not be stable any more resulting in its gradual dissolution. The interface region is therefore more vulnerable under electron beam radiation and the removal of K^+ stabilizers. This dynamic observation of the breakdown process directly confirms the existence of interfacial attachment that controls the growth process of α-MnO$_2$ nanostructures in solution environment.
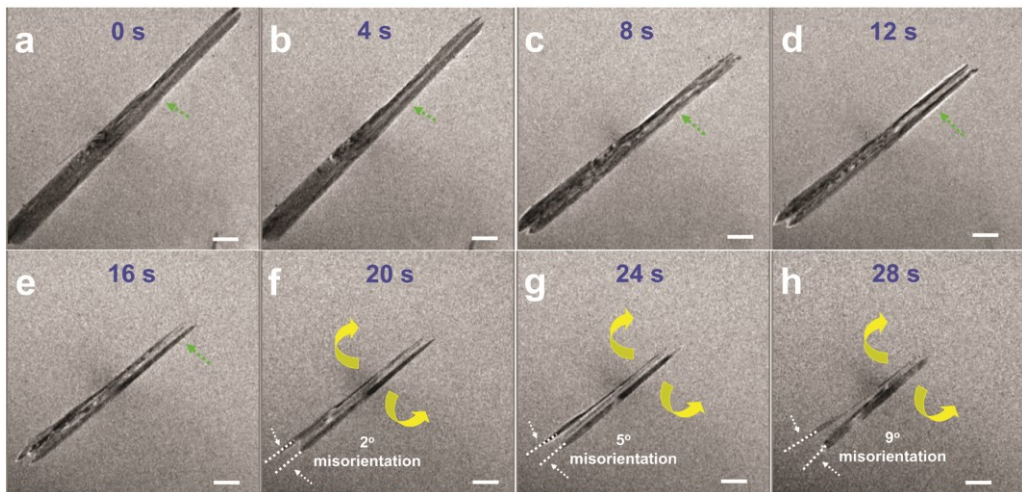
Figure 7.3. *In situ* time-lapse TEM images show the morphology evolution of a secondary α-MnO$_2$ nanowire in the liquid cell during its dissolution process driven by the incident electron beam. The green arrows in (a-e) indicate the OA interface region between two primary α-MnO$_2$ nanowires experiencing gradual dissolution, and the yellow curved arrows in (f, g, h) indicate the rotation direction (detachment) between the two primary nanowires. Scale bars in all: 150 nm.

7.3.2. Atomic structure of the oriented attachment-induced interface

Figure 7.4a shows a TEM image of one secondary α-MnO$_2$ nanowire viewed down [100]. The nanowire is composed of several well-aligned primary nanowires with diameters ranging from 10 to 20 nm. Despite the aggregation of multiple primary

nanowires, the secondary nanowire still appears to be monocrystalline, as confirmed by the corresponding selected area diffraction patterns (SAED), shown in Figure 7.4b. A high angular annular dark field (HAADF) image of one primary unit is shown in Figure 4c with the corresponding inverse fast Fourier transform (IFFT) given in the middle and the atomic model at the bottom. The 2×2 tunnel can be clearly seen to be surrounded by [MnO_6] octahedral units (yellow dots) and supported by K^+ atoms (pink dots) in their center, which agrees well with the atomic structure model. Results of the elemental analysis and the confirmation of the tunnel alignment along [001] are shown in Figure 7.6. Based on the SAED and HAADF results, the growth direction of α-MnO_2 nanowires is determined to be [001], which is parallel to the tunnel direction. Imaging down [100] did not reveal clearly any interfaces between primary nanowires, implying that this direction is not parallel to the OA interface.
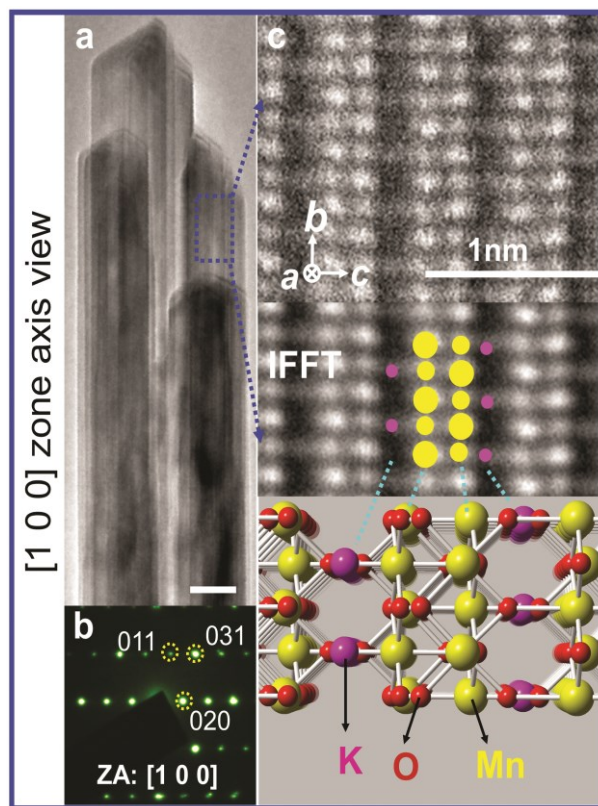
Figure 7.4. (a) A TEM image of secondary α-MnO_2 nanowires taken along [100]; (b) SAED pattern of the same region as (a); (c) A HAADF image of the blue-framed region of a primary nanowire in (a); the corresponding IFFT is given in the middle with the atomic model illustrated at the bottom, where yellow dots represent Mn, red

O and pink K^+; the signal of K^+ during HAADF imaging is weaker than that of Mn due to its smaller atomic weight. Scale bar in (a) is 10 nm.

Figure 7.5a is the [1 $\bar{1}$ 1] view of another secondary nanowire, which exhibits monocrystalline characteristics, as indicated by the SAED pattern in Figure 7.5b. The fact that secondary α-MnO$_2$ nanowires do not show multiple diffraction spots implies that the primary nanowires are precisely oriented with respect to each other. The interface is parallel to the electron beam when viewed down [1 $\bar{1}$ 1] and it clearly extends throughout the entire secondary nanowire. HRTEM images of the interface at different locations (marked by the blue dotted squares) are given in figures 7.5c and 7.5d. Within each individual primary nanowire, the $d_{\{110\}}$ spacing is 7 Å, while this value increases to 10 Å for the interfacial planes ($d_{interface}$). The HAADF imaging of the interface along [1 $\bar{1}$ 1] is given in Figure 7.5e with the corresponding atomic model shown at the bottom. According to this atomic image, the {110} alignment of the interfaces is associated with the ordering of Mn atomic columns. The larger $d_{interface}$ (10 Å) is a result of the addition of an extra row of Mn atoms in the center, which is probably introduced during the lateral OA growth. This result indicates that the α-MnO$_2$ {110} surface can act as the common surface across which the primary nanowires attach to each other. The finding that the {110} interface spacing is larger than that of α-MnO$_2$ {110} spacing also suggests that the growth of α-MnO$_2$ in solution is an "imperfect" OA process, as defined in other materials systems.[42]
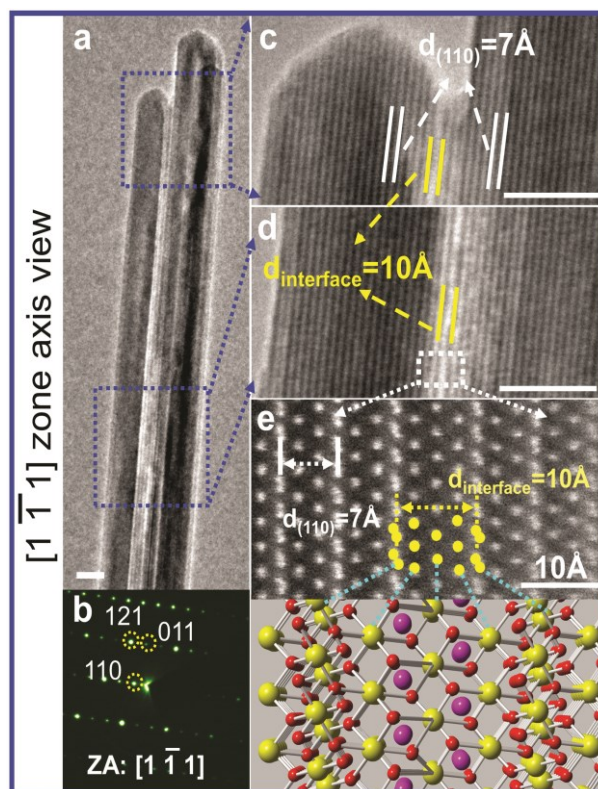
Figure 7.5. (a) A TEM image of one secondary α-MnO$_2$ nanowire taken along [1 $\bar{1}$ 1], where the {110} interface can be directly imaged; (b) SAED pattern of the same nanowire in (a); (c, d) HRTEM images of the OA-induced interface from the terminated and center parts of the nanowire, respectively; (e) A HAADF image of the white-framed interface region in (d); the corresponding atomic model is illustrated at the bottom, where yellow dots represent Mn, red O and pink K$^+$. Scale bars in (a) and (c, d) are 10 nm.

To efficiently explore the atomic arrangement of the OA interface, a secondary nanowire was examined parallel to the nanowire axis (Figure 7.6). The [001] ABF image in Figure 7.6a shows that the nanowire has a square-shaped cross section with four {100} lateral surfaces. The red dashed lines in Figure 7.6a also indicate several {110} dark stripes inside the nanowire, indicating heterogeneity in the structure. Close examination of several other cross-sectioned specimens perpendicular to the

140

nanowire axis indicates that most lateral surfaces of the nanowires correspond to {100} planes, and that the {110} stripes are always present (Figure D1 in Appendix D).

The bright central area in Figure 7.6a indicates that the secondary nanowire has a hollow section in the middle. Figure 7.6b is a HAADF image of the well-crystallized area where typical 1×1 and 2×2 tunnels of α-MnO_2 are clearly observed. Closer inspection reveals that 1×1 tunnels are empty while each 2×2 tunnel is occupied by a column of atoms in its center. These atoms were later confirmed to be K^+ (Figure 7.6e). The position of K^+ in the 2×2 tunnels was determined to be the Wyckoff 2a site (0, 0, 0) and the nanowire composition to be α-$K_{0.25}MnO_2$.

To assist in determining the atomic-scale structure, we also performed *ab initio* density functional theory (DFT) calculations on the α-$K_{0.25}MnO_2$ bulk system with K^+ ions on either the Wyckoff 2a (0, 0, 0) or 2b (0, 0, 1/2) sites, as illustrated in Figure D2. From these simulations the 2a site was found to be at least 300 meV lower in energy than the 2b site. This difference is significantly greater than the thermal energy at room temperature ($k_BT \sim 26$ meV), which suggests that the predicted position of K^+ ions in the central 2a site is in good agreement with the experimental observation.
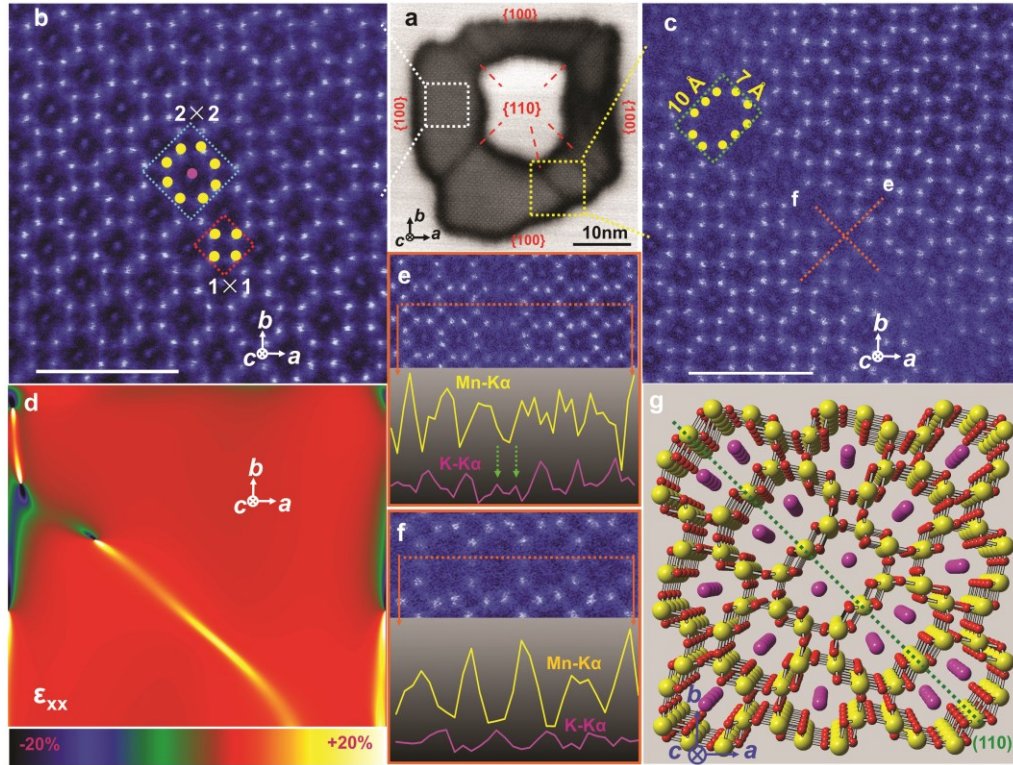
Figure 7.6. (a) An ABF image of an α-MnO$_2$ nanowire cross section viewed along the [001] zone axis; white and yellow squares indicate a perfect crystalline area and {110} defect-rich stripes, respectively; (b) False-colored HAADF image of the perfect crystalline area; blue and red squares indicate typical 2×2 and 1×1 tunnels of α-MnO$_2$, respectively, and yellow and pink dots indicate atomic columns of Mn and K$^+$, respectively; (c) False-colored HAADF image of the {110} defect-rich stripe revealing the 2×3 tunnels; (d) ε$_{xx}$ mapping near the 2×3 tunneled {110} interface; (e, f) EDS line scans across a 2×3 tunnel-based interface along the two vertical directions labeled "e" and "f" in (c); (g) The atomistic model illustrating the {110} interface structure, with yellow balls for Mn, red for O and pink for K$^+$. Scale bars in b and c are 2 nm.

The atomic-resolution HAADF image in Figure 6c obtained from one striped area shows that this stripe actually consists of 2×3 tunnels that are aligned parallel to the characteristic 1×1 and 2×2 tunnels of α-MnO$_2$. The width of 2×3 tunnels was measured to be 10 Å, which is consistent with the d$_{interface}$ spacing at the {110}

142

interface obtained from Figure 7.5c. This observation reveals that the 2×3 tunnel-based stripe is in fact the {110} interface *via* which primary α-MnO$_2$ nanowires laterally attach to each other. Figure 7.6d shows the ε_{xx} map around the {110} stripe, where a larger amount of strain is evident at the interface.

Atomic-resolution elemental analysis around 2×3 tunnels was performed by taking EDS line scans along two vertical directions marked "e" and "f" in Figure 7.6c; the results are plotted in figures 6e and f, respectively. The linear profile of Mn and K along direction e indicates that Mn is present in the 2×2 tunnel walls, with one K signal peak detected at the center of each 2×2 tunnel, and two K signal peaks (green arrows in Figure 7.6e) inside the 2×3 tunnel. The linear profile around the 2×3 tunnels along direction f reveals that the tunnel walls are still constructed from Mn, with one K signal peak detected at the tunnel center. Based on these results, the atomic configuration around a {110} interface region was constructed and shown in Figure 7.6g. The tunnel walls for both 2×2 and 2×3 tunnels are built from Mn atoms. Compared to the normal 2×2 tunnels stabilized by only one K$^+$ atom column, two K$^+$ columns exist inside the 2×3 tunnels. The presence of the extra K$^+$ column is found to stabilize the 2×3 tunnel-based OA interface of α-MnO$_2$, prevent structural collapse, and thus maintain the good crystallinity of solution-grown α-MnO$_2$ nanowires. This significant finding is in agreement with the conjecture that larger tunnels require more cation columns as tunnel stabilizers,[43] and implies the important role of excess solution cations during OA growth of tunneled structures.

The fact that tunnel-based interfaces are always parallel to {110} planes indicates that the solution-based OA growth of α-MnO$_2$ is a surface-controlled process. To examine this issue further, the energetics of a range of surfaces of α-MnO$_2$ in the presence of K$^+$ were explored by using well-established DFT methodology.[44-46] The wide range of surface planes were initially selected based on the low energy surfaces found from previous studies of pure α-MnO$_2$.[44] In Table 7.1 we list the calculated surface energies for α-K$_{0.25}$MnO$_2$. Such an analysis shows that the lowest energies correspond

to the (100) and (110) surfaces. Compared to other surfaces, the (211) surface also exhibits low energy, which was, however, not observed experimentally. Even if the (211) OA interface exists, the lateral surfaces of one secondary nanowire and its atomic arrangement along [001] would both be disrupted. The TEM observation indicates that the lateral surfaces of the nanowires are smooth and the atomic columns along [001] are well ordered (each column is clearly distinguishable with good contrast in the HAADF images in figures 7.6 and 7.7). These two facts indicate the low chances of (211) interface formation, which is thus not further explored in this work. Nevertheless, the DFT results clearly show that the (100) surface is considerably lower in energy than all other terminations, which is confirmed experimentally by Figure 7.6a (and Figure S1) showing the four lateral surfaces of α-MnO_2 nanowires to be parallel to {100} planes. The (110) surface is sufficiently favorable that we would expect it to dominate the morphology of the nanoparticles during the initial growth stages, in agreement with the experimental finding that interfaces are formed parallel to {110} planes.

Table 7.1. Calculated (DFT+U) surface energies for $K_{0.25}MnO_2$.

Miller Index	Surface Energy (Jm^{-2})
(100)	0.44
(110)	0.74
(211)	0.78
(210)	1.14
(001)	1.17
(101)	1.17
(201)	1.19
(111)	1.35

7.3.3. Atomistic mechanism for formation of 2×3 tunnel-based {110} interfaces

We now turn to the edge structure of the low energy surfaces {100} and {110}, in an attempt to understand how the fundamental characteristics of the exposed surfaces in solution drive the formation of 2×3 tunnel-based {110} interfaces. The structure of a (100) surface obtained from HAADF imaging is shown in Figure 7.7a, with the atomistic relaxed surface from DFT calculations given for comparison in Figure 7.7b. The (100) surface is essentially composed of a series of intact 2×2 tunnels with a bisected 2×2 tunnel sitting between the intact tunnels, agreeing well with the simulated structure. There is little calculated distortion between the unrelaxed and relaxed surface for this cleavage plane, as is typical for energetically favorable surfaces. In addition, Figure 7.7b shows that the Mn ions in the surface region remain well coordinated with 75% remaining in 6-fold coordination, identical to Mn ions in the bulk. The remaining 25% of Mn ions have 5-fold coordination and are unsaturated. Moreover, half of the surface K^+ ions reside within intact 2×2 tunnels in their preferred 8-fold coordination (as found in the bulk structure), with the other half maintaining a reduced 4-fold coordination. These structural features are likely to account for the low surface energies calculated for the {100} surfaces, and indicate that such {100} surfaces will be stable during the OA process. The fact that the {100} surface is covered by 2×2 tunnels instead of 1×1 tunnels is important for the improvement in performance of α-MnO$_2$ nanostructured materials. The direct exposure of large 2×2 tunnels is likely to reduce the distance and energy barrier for ion diffusion, improving the rate performance of α-MnO$_2$ in applications such as rechargeable battery electrodes,[47-50] supercapacitors[51-53] and Li-O$_2$ battery catalysts.[54-57] Indeed, future generations of these energy storage technologies will depend crucially on new nanostructured materials.
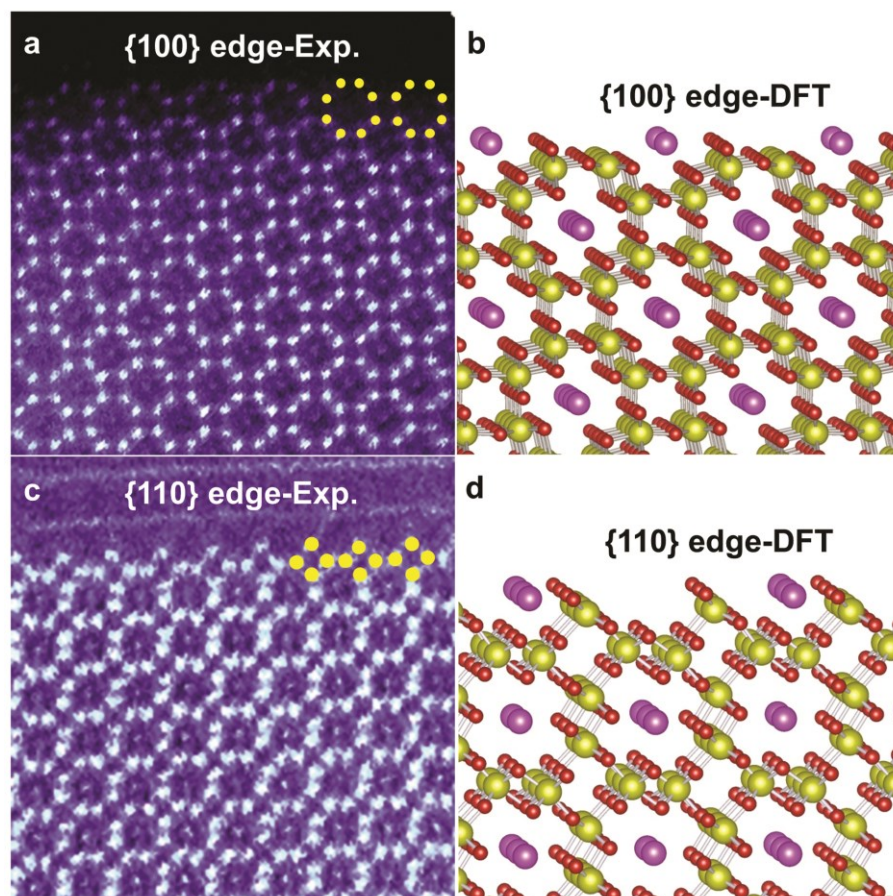
Figure 7.7. (a) Atomic-resolution HAADF image of a (100) edge in an α-$K_{0.25}MnO_2$ nanowire compared with (b) the calculated relaxed (100) surface structure of α-$K_{0.25}MnO_2$. (c) Atomic-resolution HAADF image of a (110) edge in an α-$K_{0.25}MnO_2$ nanowire compared with (d) the calculated relaxed (110) surface structure of α-$K_{0.25}MnO_2$. Yellow balls are Mn, red are O, and pink are K.

The structure of a (110) surface before the OA process begins can be seen in the HAADF image in Figure 7.7c. The simulated atomistic structure of the same surface is given in Figure 7.7d. The (110) surface forms a step-like edge that is covered by 1×1 tunnels, matching the theoretical model very well. Like the (100) surface, there is relatively little calculated distortion between the unrelaxed and simulated relaxed structures, indicating that this surface is relatively stable. The atomistic model also shows that the Mn ions at the (110) surface remain in a high coordination environment, with two thirds in 6-fold coordination sites. The remaining Mn ions,

corresponding to the most exposed ions, are in 5-fold coordination. Furthermore, the outermost K^+ ions are stabilized by a slight relaxation into the surface, which has the effect of increasing their coordination number from 4 to 5. The (110) surface has more unsaturated $[MnO_5]$ units than the (100) surface, a consequence of which is that the (110) surface is predicted to be less stable than (100). All the other surfaces have larger amounts of unsaturated $[MnO_5]$ units, with some even containing $[MnO_x]$ (x<5) units, making them unstable in solution.

Based on the sub-angstrom resolution image of the (110) edge structure in Figure 7.7, we propose an atomistic model to explain the formation of 2×3 tunnels at a {110} interface between two primary crystals (termed I_a and I_b). This process is illustrated in Figure 7.8 with perspective views, and is divided into three steps. At the beginning of the first step when I_a and I_b initially form in solution with random but close orientations, the dominant surfaces should be {100} and {110} as both types of surface possess lower surface energies than other crystal planes. Since {110} surfaces are less stable than {100}, there is a tendency among the primary crystals to attach to each other along their {110} surfaces to minimize the overall energy. Consequently, I_a and I_b approach each other through van der Waals forces, which has been widely reported for the OA growth of nanostructure,[27,28,58] and orient themselves parallel to their common {110} surfaces. In the second step, as I_a and I_b come into close proximity, the large repulsive force between exposed K ions on the {110} surfaces prevent them bonding. However, extra $[MnO_x]$ radicals in the surrounding solution are able to squeeze between the I_a and I_b crystals. In the third step, the extra $[MnO_x]$ radicals between the crystals bond with the dangling $[MnO_5]$ units from both {110} surfaces, resulting in the elimination of the two surfaces and formation of one 2×3 tunnel-based {110} interface. This process should be energetically favorable as the unsaturated $[MnO_5]$ units of the {110} surfaces become saturated, forming the more stable $[MnO_6]$ units. Following the similar steps, more primary α-MnO$_2$ nanowires can be gradually attached together across their exposed {110}, and the diameter of the

secondary nanowire could be gradually increased during the subsequent high order attachment in solution.

The lateral OA mechanism results in the aggregation of only a few primary nanowires instead of long-range ordered structures. This should be due to the gradual decrease of the OA driving force, namely the elimination of pairs of {110} surfaces. At the early stages when a substantial number of {110} surfaces exist in the solution, the lateral OA *via* {110} should occur in a large scale to eliminate the overall surface energy of the system by elimination of {110} surfaces. At later stages when a limited number of {110} surfaces remain and the secondary nanowires are well grown, the OA growth of α-MnO$_2$ nanowires is thus terminated. The effect of K$^+$ during the solution growth of α-MnO$_2$ nanostructures has been widely studied.[34,59-61] However, these reports have focused on the formation of α-MnO$_2$ phase instead of the defective interface. The conclusion has been that α-MnO$_2$ can only nucleate and grow when there are excess K$^+$ in solution because the large 2×2 tunnels need to be stabilized by certain cations such as K$^+$. Otherwise, other MnO$_2$ polymorphs (β-MnO$_2$ or γ-MnO$_2$) with smaller 1×1 and 1×2 tunnels will form when there are few or no K$^+$. Based on our work, we find that K$^+$ ions are important in the formation of the {110} OA interface because two K$^+$ atomic columns are present in one large 2×3 tunnel. It is reasonable to expect that the {110} interface, which is composed of even larger 2×3 tunnels, would not exist if there are no more K$^+$ in the solution during the lateral OA stage to support the large tunnels. The presence of [MnO$_x$] radicals in aqueous solution and the exact Mn oxidation state ("x" value) are difficult to be verified in the current experiment due to the strong effect from the liquid environment as well as various types of structural Mn-O bonds. Nevertheless, there might be other methods to confirm [MnO$_x$], such as *in situ* X-ray Absorption Spectroscopy (XAS) providing electronic structure information. Such an experiment requires a sealed liquid cell with an X-ray transparent window, X-ray with high penetration energy, and also proper data interpretation to get rid of the signals from other Mn-O bonds; this is clearly a topic for future work.
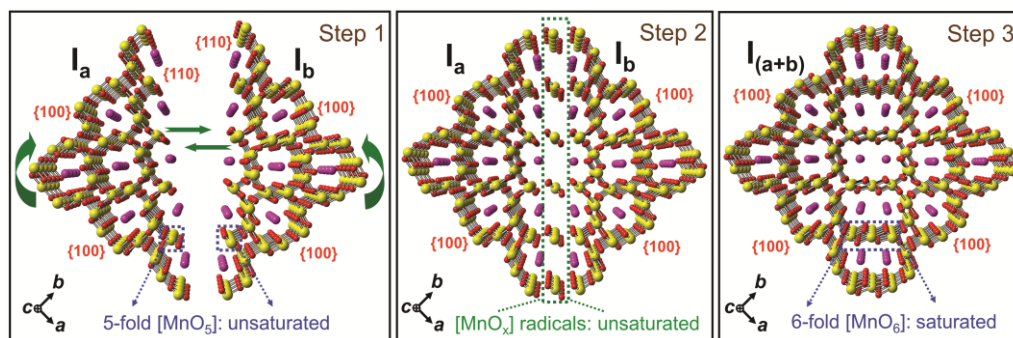
Figure 7.8. Schematic diagrams illustrating the formation of a 2×3 tunnel-based {110} interface during OA of two primary α-MnO$_2$ nanowires at the atomic level. The nanowires (I$_a$ and I$_b$) are orientated parallel to the *c* axis ([001]) with their stable {100} surfaces and metastable {110} surfaces exposed in solution. The curved and straight green arrows in Step 1 indicate the rotating and linear approaching movements of the primary nanowires, respectively. Surrounding the nanowires is the aqueous solution environment containing MnSO$_4$ and KMnO$_4$ in excess.

Although this study is not exhaustive, it does highlight an important area for further work on tunnel-based oxide nanostructures. Indeed, future studies could include rational design of various tunneled structures with ideal hierarchy, controllable dimension and morphology, and large-scale molecular dynamics simulations in solution-based systems.

7.4. Conclusion

K$^+$-stabilized α-MnO$_2$ nanowires were hydrothermally synthesized by an orientated attachment (OA) growth mechanism, and the structures of the nanowires and their interfaces were explored at the atomic scale. First, it was determined that primary α-MnO$_2$ nanowires prefer to combine laterally with each other by sharing their {110} surfaces to construct secondary α-MnO$_2$ nanowires. This OA process is driven by the reduction of the surface energy and the tendency of dangling [MnO$_5$] units at {110} surfaces to be saturated to form [MnO$_6$] by bonding with [MnO$_x$] radicals in solution. Second, the resulting {110} interfaces are defective and composed of 2×3 tunnels

supported by two K^+ columns rather than a normal 2×2 tunnel supported by one K^+ column. The presence of K^+ excess in solution plays an important role during the formation and stabilization of the OA interface.

This work provides greater fundamental understanding of the atomic structure at the surface and OA interface in one-dimensional tunneled α-MnO_2. A key example is the finding that the (100) surface is covered by 2×2 tunnels while (110) is covered by 1×1 tunnels; this suggests faster reaction at (100) surfaces than that at (110), since most reactions occur inside the large 2×2 tunnels. This understanding could guide selective surface engineering to synthesize α-MnO_2 nanostructures for improved functional performance. With the increasing interest in crystal facet engineering, the importance of surface chemistry demonstrated here could inspire related research on tunnel-based oxide nanostructures for potential applications in catalysis, sensors and energy storage.

7.5. References

1. Bursill, L. A.; Lodge, E. A.; Thomas, J. M. Zeolitic Structures as Revealed by High-Resolution Electron Microscopy. *Nature* **1980**, *286*, 111-113.

2. Tao, Y.; Kanoh, H.; Abrams, L.; Kaneko, K. Mesopore-Modified Zeolites: Preparation, Characterization, and Applications. *Chem. Rev.* **2006**, *106*, 896-910.

3. Behrens, E. A.; Clearfield, A. Titanium Silicates, $M_3HTi_4O_4(SiO_4)_3 \cdot 4H_2O$ (M=Na^+, K^+), with Three-Dimensional Tunnel Structures for the Selective Removal of Strontium and Cesium from Wastewater Solutions. *Microporous Mater.* **1997**, *11*, 65-75.

4. Kijima, N.; Sakao, M.; Tanuma, Y.; Kataoka, K.; Igarashi, K.; Akimoto, J. Synthesis, Crystal Structure, and Electrochemical Properties of Hollandite-Type $K_xTi_{1-y}Mn_yO_2$. *Solid State Ionics* **2014**, *262*, 14-17.

5. Zhang, H.; Banfield, J. F. Structural Characteristics and Mechanical and Thermodynamic Properties of Nanocrystalline TiO_2. *Chem. Rev.* **2014**, *114*, 9613-9644.

6. Yuan, J.; Li, W.; Gomez, S.; Suib, S. L. Shape-Controlled Synthesis of Manganese Oxide Octahedral Molecular Sieve Three-Dimensional Nanostructures. *J. Am. Chem. Soc.* **2005**, *127*, 14184-14185.

7. Chalmin, E.; Vignaud, C.; Menu, M. Palaeolithic Painting Matter: Natural or Heat-Treated Pigment? *Appl. Phys. A* **2004**, *79*, 187-191.

8. Zhang, K.; Han, X.; Hu, Z.; Zhang, X.; Tao, Z.; Chen, J. Nanostructured Mn-Based Oxides for Electrochemical Energy Storage and Conversion. *Chem. Soc. Rev.* **2015**, *44*, 699-728.

9. Chen, K.; Noh, Y. D.; Li, K.; Komarneni, S.; Xue, D. Microwave−Hydrothermal Crystallization of Polymorphic MnO_2 for Electrochemical Energy Storage. *J. Phys. Chem. C* **2013**, *117*, 10770-10779.

10. Suib, S. L. Structure, Porosity, and Redox in Porous Manganese Oxide Octahedral Layer and Molecular Sieve Materials. *J. Mater. Chem.* **2008**, *18*, 1623-1631.

11. Luo, J.; Zhang, Q.; Garcia-Martinez, J.; Suib, S. L. Adsorptive and Acidic Properties, Reversible Lattice Oxygen Evolution, and Catalytic Mechanism of Cryptomelane-Type Manganese Oxides as Oxidation Catalysts. *J. Am. Chem. Soc.* **2008**, *130*, 3198-3207.

12. Cao, Y.; Xiao, L.; Wang, W.; Choi, D.; Nie, Z.; Yu, J.; Saraf, L. V.; Yang, Z.; Liu, J. Reversible Sodium Ion Insertion in Single Crystalline Manganese Oxide Nanowires with Long Cycle Life. *Adv. Mater.* **2011**, *23*, 3155-3160.

13. Simon, P.; Gogotsi, Y. Materials for Electrochemical Capacitors. *Nat. Mater.* **2008**, *7*, 845-854.

14. Cai, J.; Liu, J.; Gao, Z.; Navrotsky, A.; Suib, S. L. Synthesis and Anion Exchange of Tunnel Structure Akaganeite. *Chem. Mater.* **2001**, *13*, 4595-4602.

15. Sui, N.; Duan, Y.; Jiao, X.; Chen, D. Large-Scale Preparation and Catalytic Properties of One-Dimensional α/β-MnO_2 Nanostructures. *J. Phys. Chem. C* **2009** *113*, 8560-8565.

16. Devaraj, S.; Munichandraiah, N. Effect of Crystallographic Structure of MnO_2 on Its Electrochemical Capacitance Properties. *J. Phys. Chem. C* **2008**, *112*, 4406-4417.

17. Wang, H.; Lu, Z.; Qian, D.; Li, Y.; Zhang, W. Single-Crystal α-MnO_2 Nanorods: Synthesis and Electrochemical Properties. *Nanotechnol.* **2007**, *18*, 115616-115620.

18. Zhang, X. ; Yang, W.; Yang, J. ; Evans, D. G. Synthesis and Characterization of α-MnO_2 Nanowires: Self-Assembly and Phase Transformation to β-MnO_2 Microcrystals. *J. Cryst. Growth* **2008**, *310*, 716-722.

19. Portehault, D.; Cassaignon, S.; Baudrin, E.; Jolivet, J. P. Morphology Control of Cryptomelane Type MnO_2 Nanowires by Soft Chemistry. Growth Mechanisms in Aqueous Medium. *Chem. Mater.* **2007**, *19*, 5410-5417.

20. Khan, M.; Yohannes, E.; Powell, D. Synthesis and Characterization of a New Mixed-Metal Oxide Framework Material Composed of Vanadium Oxide Clusters: X-Ray Crystal Structure of $(N_2H_5)_2[Zn_3V^{IV}_{12}V^{V}_6O_{42}(SO_4)(H_2O)_{12}]\cdot 24H_2$. *Chem. Commun.* 1999, *1*, 23-24.

21. Xu, M.; Kong, L.; Zhou, W.; Li, H. Hydrothermal Synthesis and Pseudocapacitance Properties of α-MnO_2 Hollow Spheres and Hollow Urchins. *J. Phys. Chem. C* **2007**, *111*, 19141-19147.

22. Santhanagopalan, S.; Balram, A.; Meng, D. D. Scalable High-Power Redox Capacitors with Aligned Nanoforests of Crystalline MnO_2 Nanorods by High Voltage Electrophoretic Deposition. *ACSNano* **2013**, *7*, 2114-2125.

23. Wang, X.; Li, Y. Selected-Control Hydrothermal Synthesis of α- and β-MnO_2 Single Crystal Nanowires. *J. Am. Chem. Soc.* **2002**, *124*, 2882-2883.

24. Li, W.; Yuan, J.; Shen, X.; Gomez-Mower, S.; Xu, L.; Sithambaram, S.; Aindow, M.; Suib, S. L. Hydrothermal Synthesis of Structure- and Shape-Controlled Manganese Oxide Octahedral Molecular Sieve Nanomaterials. *Adv. Funct. Mater.* **2006**, *16*, 1247-1253.

25. Galindo, H. M.; Carvajal, Y.; Njagi, E.; Ristau, R. A.; Suib, S. L. Facile One-Step Template-Free Synthesis of Uniform Hollow Microstructures of Cryptomelane-Type Manganese Oxide K-OMS-2. *Langmuir* **2010**, *26*, 13677-13683.

26. Lan, B.; Yu, L.; Lin, T.; Cheng, G.; Sun, M.; Ye, F.; Sun, Q.; He, J. Multifunctional Free-Standing Membrane from the Self-Assembly of Ultralong MnO_2 Nanowires. *ACS Appl. Mater. Interfaces* **2013**, *5*, 7458-7464.

27. Li, D.; Nielsen, M. H.; Lee, J. R. I.; Frandsen, C.; Banfield, J. F.; Yoreo, J. J. D. Direction-Specific Interactions Control Crystal Growth by Oriented Attachment. *Science* **2012**, *336*, 1014-1018.

28. Zhang, Q.; Liu, S. J.; Yu, S. H. Recent Advances in Oriented Attachment Growth and Synthesis of Functional Materials: Concept, Evidence, Mechanism, and Future. *J. Mater. Chem.* **2009**, *19*, 191-207.

29. Cho, K. S.; Talapin, D. V.; Gaschler, W.; Murray, C. B. Designing PbSe Nanowires and Nanorings through Oriented Attachment of Nanoparticles. *J. Am. Chem. Soc.* **2005**, *127*, 7140-7147.

30. Banfield, J. F.; Welch, S. A.; Zhang, H.; Ebert, T. T.; Penn, R. L. Aggregation-Based Crystal Growth and Microstructure Development in Natural Iron Oxyhydroxide Biomineralization Products. *Science* **2000**, *289*, 751-754.

31. Pacholski, C.; Kornowski, A.; Weller, H. Self-Assembly of ZnO: From Nanodots to Nanorods. *Angew. Chem. Int. Ed.* **2002**, *41*, 1188-1191.

32. Turner, S.; Buseck, P. R. Defects in Nsutite (γ-MnO_2) and Dry-Cell Efficiency. *Nature* **1983**, *304*, 143-146.

33. Turner, S.; Buseck, P. R. Manganese Oxide Tunnel Structures and Their Intergrowths. *Science* **1979**, *203*, 456-458.

34. Shen, X.; Ding, Y.; Liu, J.; Cai, J.; Laubernds, K.; Zerger, R. P.; Vasiliev, A.; Aindow, M.; Suib, S. L. Control of Nanometer-Scale Tunnel Sizes of Porous Manganese Oxide Octahedral Molecular Sieve Nanomaterials. *Adv. Mater.* **2005**, *17*, 805-809.

35. Leclaire, A.; Borel, M. M.; Grandin, A.; Raveau, B. Two Molybdenum Diphosphates with a Tunnel Structure Involving Mo(III): $KMoP_2O_7$ and $K_{0.17}MoP_2O_7$. *J. Solid State Chem.* **1989**, *78*, 220-226.

36. Williamson, M. J.; Tromp, R. M.; Vereecken, P. M.; Hull, R.; Ross, F. M. Dynamic Microscopy of Nanoscale Cluster Growth at the Solid–Liquid Interface. *Nat. Mater.* **2003**, *2*, 532-536.

37. Zheng, H.; Smith, R. K.; Jun, Y.; Kisielowski, C.; Dahmen, U.; Alivisatos, A. P. Observation of Single Colloidal Platinum Nanocrystal Growth Trajectories. *Science* **2009**, *324*, 1309-1312.

38. Smeets, P. J. M.; Cho, K. R.; Kempen, R. G. E.; Sommerdijk, N. A. J. M.; Yoreo, J. J. D. Calcium Carbonate Nucleation Driven by Ion Binding in a Biomimetic Matrix Revealed by *in situ* Electron Microscopy. *Nat. Mater.* **2015**, *14*, 394-399.

39. Grogan, J. M.; Schneider, N. M.; Ross, F. M.; Bau, H. H. Bubble and Pattern Formation in Liquid Induced by an Electron Beam. *Nano Lett.* **2014**, *14*, 359-364.

40. Schneider, N. M.; Norton, M. M.; Mendel, B. J.; Grogan, J. M.; Ross, F. M.; Bau, H. H. Electron−Water Interactions and Implications for Liquid Cell Electron Microscopy. *J. Phys. Chem. C* **2014**, *118*, 22373-22382.

41. Liu, J.; Makwana, V.; Cai, J.; Suib, S. L.; Aindow, M. Effects of Alkali Metal and Ammonium Cation Templates on Nanofibrous Cryptomelane-Type Manganese Oxide Octahedral Molecular Sieves (OMS-2). *J. Phys. Chem. B* **2003**, *107*, 9185-9194.

42. Penn, R. L.; Banfield, J. F. Imperfect Oriented Attachment: Dislocation Generation in Defect-Free Nanocrystals. *Science* **1998**, *281*, 969-971.

43. Shen, X.; Ding, Y.; Liu, J.; Laubernds, K.; Zerger, R. P.; Polverejan, M.; Son, Y. C.; Aindow, M.; Suib, S. L. Synthesis, Characterization, and Catalytic Applications of Manganese Oxide Octahedral Molecular Sieve (OMS) Nanowires with a 2×3 Tunnel Structure. *Chem. Mater.* **2004**, *16*, 5327-5335.

44. Tompsett, D. A.; Parker, S. C.; Islam, M. S. Surface Properties of α-MnO_2: Relevance to Catalytic and Supercapacitor Behaviour. *J. Mater. Chem. A* **2014**, *2*, 15509-15518.

45. Tompsett, D. A.; Islam, M. S. Electrochemistry of Hollandite α-MnO_2: Li-Ion and Na-Ion Insertion and Li_2O Incorporation. *Chem. Mater.* **2013**, *25*, 2515-2526.

46. Islam, M. S.; Fisher, C. A. Lithium and Sodium Battery Cathode Materials: Computational Insights into Voltage, Diffusion and Nanostructural Properties. *Chem. Soc. Rev.* **2014**, *43*, 185-204.

47. Arthur, T. S.; Zhang, R.; Ling, C.; Glans, P. A.; Fan, X.; Guo, J.; Mizuno, F. Understanding the Electrochemical Mechanism of K-αMnO$_2$ for Magnesium Battery Cathodes. *ACS Appl. Mater. Interfaces* **2014**, *6*, 7004-7008.

48. Li, W.; Cui, X.; Zeng, R.; Du, G.; Sun, Z.; Zheng, R.; Ringer, S. P.; Dou, S. Performance Modulation of α-MnO$_2$ Nanowires by Crystal Facet Engineering. *Sci. Rep.* **2015**, *5*, 8987.

49. Li, L.; Nan, C.; Lu, J.; Peng, Q.; Li, Y. α-MnO$_2$ Nanotubes: High Surface Area and Enhanced Lithium Battery Properties. *Chem. Commun.* **2012**, *48*, 6945-6947.

50. Yuan, Y.; Nie, A.; Odegard, G. M.; Xu, R.; Zhou, D.; Santhanagopalan, S.; He, K.; Asayesh-Ardakani, H.; Meng, D. D.; Klie, R. F. *et al.* Asynchronous Crystal Cell Expansion during Lithiation of K$^+$−Stabilized α-MnO$_2$. *Nano Lett.* **2015**, *15*, 2998-3007.

51. Yang, P.; Ding, Y.; Lin, Z.; Chen, Z.; Li, Y.; Qiang, P.; Ebrahimi, M.; Mai, W.; Wong, C. P.; Wang, Z. L. Low-Cost High-Performance Solid-State Asymmetric Supercapacitors Based on MnO$_2$ Nanowires and Fe$_2$O$_3$ Nanotubes. *Nano Lett.* **2014**, *14*, 731-736.

52. Zhai, D.; Li, B.; Xu, C.; Du, H.; He, Y.; Wei, C.; Kang, F. A Study on Charge Storage Mechanism of α-MnO$_2$ by Occupying Tunnels with Metal Cations (Ba^{2+}, K$^+$). *J. Power Sources* **2011**, *196*, 7860-7867.

53. Xiao, W.; Xia, H.; Fuh, J. Y. H.; Lu, J. Growth of Single-Crystal α-MnO$_2$ Nanotubes Prepared by a Hydrothermal Route and Their Electrochemical Properties. *J. Power Sources* **2009**, *193*, 935-938.

54. Qin, Y.; Lu, J.; Du, P.; Chen, Z.; Ren, Y.; Wu, T.; Miller, J. T.; Wen, J.; Miller, D. J.; Zhang, Z. *et al. In Situ* Fabrication of Porous-Carbon-Supported α-MnO$_2$ Nanorods at Room Temperature: Application for Rechargeable Li-O$_2$ Batteries. *Energy Environ. Sci.* **2013**, *6*, 519-531.

55. Hutchings, G. S.; Rosen, J.; Smiley, D.; Goward, G. R.; Bruce, P. G.; Jiao, F. Environmental *In Situ* X-Ray Absorption Spectroscopy Evaluation of Electrode Materials for Rechargeable Lithium-Oxygen Batteries. *J. Phys. Chem. C* **2014**, *118*, 12617-12624.

56. Truong, T. T.; Liu, Y.; Ren, Y.; Trahey, L.; Sun, Y. Morphological and Crystalline Evolution of Nanostructured MnO_2 and Its Application in Lithium–Air Batteries. *ACS Nano* **2012**, *6*, 8067-8077.

57. Débart, A.; Paterson, A. J.; Bao, J.; Bruce, P. G. α-MnO_2 Nanowires: A Catalyst for the O_2 Electrode in Rechargeable Lithium Batteries. *Angew. Chem.* **2008**, *120*, 4597-4600.

58. Du, N.; Zhang, H.; Chen, B.; Ma, X.; Yang, D. Ligand-Free Self-Assembly of Ceria Nanocrystals into Nanorods by Oriented Attachment at Low Temperature. *J. Phys. Chem. C* **2007**, *111*, 12677-12680.

59. Wang, X.; Li, Y. Synthesis and Formation Mechanism of Manganese Dioxide Nanowires/Nanorods. *Chem. Eur. J.* **2003**, *9*, 300-306.

60. Portehault, D.; Cassaignon, S.; Baudrinc, E.; Jolivet, J. P. Structural and Morphological Control of Manganese Oxide Nanoparticles upon Soft Aqueous Precipitation through MnO_4^-/Mn^{2+} Reaction. *J. Mater. Chem.* **2009**, *19*, 2407–2416.

61. Ding, Y.; Shen, X.; Sithambaram, S.; Gomez, S.; Kumar, R.; Crisostomo, V. M. B.; Suib, S. L.; Aindow, M. Synthesis and Catalytic Activity of Cryptomelane-Type Manganese Dioxide Nanomaterials Produced by a Novel Solvent-Free Method. *Chem. Mater.* **2005**, *17*, 5382-5389.

Chapter 8. Conclusion

This PhD project first covers the application of *in situ* TEM technique in studying and solving the material problems in rechargeable ion batteries with details literature review. The atomic mechanisms of tunnel-directed natural behaviors of α-MnO$_2$ nanostructures are then dynamically studied using *in situ* TEM. Four topics are covered including (1) the tunnel-driven Li$^+$ transport in α-MnO$_2$ nanowire, (2) tunnel-driven Na$^+$ transport and its comparison with Li$^+$ transport, (3) the effect of large cations (K$^+$) on the tunnel-driven Li$^+$ transport property, and (4) the atomistic exploration of oriented attachment growth of α-MnO$_2$ nanostructures.

The *in situ* TEM of Li$^+$ insertion in 2×2 tunnels of α-MnO$_2$ nanowires reveals a novel asynchronous lattice expansion along *a* and *b* directions, which is originated from the sequential Jahn-Teller distortion of [Mn^{3+}O$_6$] caused by Li$^+$ insertion. The microscopic asynchronous expansion leads to crystalline symmetry degradation from tetragonal to orthorhombic, generating undesired anisotropic volume change of α-MnO$_2$ nanostructures during lithiation. This fundamental discovery helps to explain the commonly observed poor cycling performance of α-MnO$_2$ as a cathode material for rechargeable lithium ion battery, and provides insights towards efficient improvement of such cathode materials.

The *in situ* TEM of reversible Na$^+$ insertion/extraction in 2×2 tunnels of α-MnO$_2$ nanowires reveals an intermediate stage where tunneled structure evolves into spinel Na$_{0.5}$MnO$_2$ before it is totally reduced to Mn$_2$O$_3$. The comparison with Li$^+$ insertion shows that the tunnels are more vulnerable during Na$^+$ insertion, which is ascribed to the fact that the Na+ interacts with the tunnel walls much stronger than Li$^+$ does. A voltage control (cycling between 4 -1.5 V in a Na/MnO$_2$ battery) is thus designed and shown to be effective in maintaining the tunnel stability without significant capacity loss.

The presence of large K^+ in 2×2 tunnels of α-MnO₂ is demonstrated to be positive in improving both the electrical conductivity and the Li^+ diffusivity. K^+ in 2×2 tunnels expands the tunnel cavity across *a-b* plane, and thus allows more free space for Li^+ diffusion through the off-centered 8h sites in the tunnels. With K^+ doping, Mn^{4+} are partially reduced to Mn^{3+}, and the generated Mn^{4+}/Mn^{3+} couples function as the path ways for electron hoping, resulting in the improvement of e- conductivity. These two positive factors lead to an improved rate performance of α-MnO₂ as a cathode of rechargeable lithium ion battery.

The growth of α-MnO₂ nanostructures during hydrothermal synthesis is confirmed to be an oriented attachment mechanism, where nanowires laterally attach with each other sharing their common {110} surfaces with only {100} exposed as the surfaces finally. This is driven by the surface energy reduction of the system with {110} predicted to possess higher surface energy than the most stable {100} surface. The formed {110} interface is essentially composed of well aligned 2×3 tunnels with each supported by two K^+ atomic columns, indicating the important role of surface tunnel alignment in directing the oriented attachment growth in atomic level.

Chapter 9. Future Work

The PhD projects shown here clearly illustrate the atomic structure of tunneled transitional metal oxides as well as their critical roles in energy storage and selective surface engineering. In addition, these studies demonstrate the powerfulness of aberration corrected electron microscopy in resolving atomic level reactions, and pave the way toward atomistic understanding of the multi-functionality of α-MnO$_2$ in various applications. Therefore, several future directions are proposed and discussed below.

9.1. *In situ* TEM study of multivalent cation insertion in α-MnO$_2$

The urgent demand for rechargeable batteries with high energy density for electric vehicle application has necessitated the research beyond lithium ion battery to other systems, such as Li-O$_2$, Li-S and multivalent batteries.[1] Due to the relatively large size of the 2×2 tunnels, α-MnO$_2$ nanostructure has been widely studied as a host for reversible insertion of Mg^{2+},[2] Zn^{2+},[3] and Ni^{3+}[4]. The interaction between these cations and the tunneled structures is expected to be more complicated than Li$^+$ (Na$^+$) insertion due to their higher electrostatic polarization and the difference ionic sizes and electronegativities. Table 9.1 lists the ionic radii[5] and electronegativities[6] for several commonly used charge carriers. It is generally accepted that multivalent cations are more difficult to be inserted due to a high redox polarization effect caused by sluggish insertion/extraction kinetics.[7] The higher charge of these cations polarize the host electrode during their intercalation and thus decrease the mobility and rate capability as the battery goes under cycling.[8]

Table 9.1. The ionic radii and electronegativities for Li, Na, Mg, Zn and Ca.

	Li^+	Na^+	Mg^{2+}	Zn^{2+}	Ca^{2+}
Ionic radius (in nm)[5]	0.68	0.97	0.66	0.74	0.99
electronegativity[6]	0.95	0.90	1.2	1.5	1.0

Up to now, there are hardly any *in situ* TEM reports realizing the insertion of multivalent cations into electrode materials. As far as the author is concerned, only Ca^{2+} was reported to be inserted into WO_3 as a conversion-based electrode inside the TEM chamber, where a Ca^{2+} intercalation step prior to conversion is explicitly revealed at atomic scale for the first time.[9] Mg^{2+} and Al^{3+} were also tried for the insertion into Co_3O_4 nanocubes in TEM, where no obvious ion insertion phenomena except sluggish reaction kinetics were observed.[10] The possible insertion of Mg^{2+}, Zn^{2+} and Ca^{2+}, in 2×2 tunnels has been theoretically predicted based on comparison between the ionic sizes and the free open space inside one 2×2 tunnel, where maximum passable ionic radius calculated to be 1.30 Å.[11] In addition, *ex situ* battery work has demonstrated the possibility for reversible insertion of Zn^{2+} and Mg^{2+} in α-MnO_2.[12,13] Yet, there are no successful *in situ* TEM reports. Therefore, many scientific questions remain unexplored. For example, Zn^{2+} insertion into α-MnO_2 has been explained by several different mechanisms, such as two-phase intercalation and conversion reaction involving H^+ participation. Even within the intercalation mechanism, different insertion products are reported, such as spinel $ZnMnO_2$[14] and tunneled Zn_xMnO_2[15]. For Mg^{2+} insertion, either reversible tunnel-driven intercalation[2] or conversion reaction mechanism[13] has been proposed by *ex situ* characterization. It is apparent that an insightful dynamic understanding regarding the multivalent cation insertion mechanisms in tunneled nanostructures is necessary.

The similar *in situ* TEM setup discussed previously in the dissertation could be used to explore the insertion mechanisms of multivalent cations in α-MnO_2. However, some practical hurdles should be overcome before this "open cell" system can be used for the study of multivalent batteries. According to previous theoretical

calculations, the activation energy for Li^+ migration in Li_2O is in the range of 0.27-0.33 eV,[16] while this value for Mg^{2+} migration in MgO is as high as 1.4 eV.[17] Therefore, it might not be plausible by simply applying Mg/MgO (Zn/ZnO) as the counter electrode, as done for the Li^+ and Na^+ system *via in situ* TEM. In Li/Li_2O and Na/Na_2O system, a large overpotential is required to electrochemically insert Li^+ and Na^+ into the α-MnO_2 working electrode, whereas it is possible that an even larger overpotential is required for Zn^{2+} and Mg^{2+} insertion, making the practical operation difficult. This problem is likely to be solved by applying nanosized oxide electrodes, considering the fact that many ions could diffuse with low energy barrier when the materials go into nanoscale.[18],[19] One method is thus proposed here using Mg nanowire as the counter electrode with its surface intentionally oxidized to act as the solid electrolyte. Figure 9.1 shows such a design.
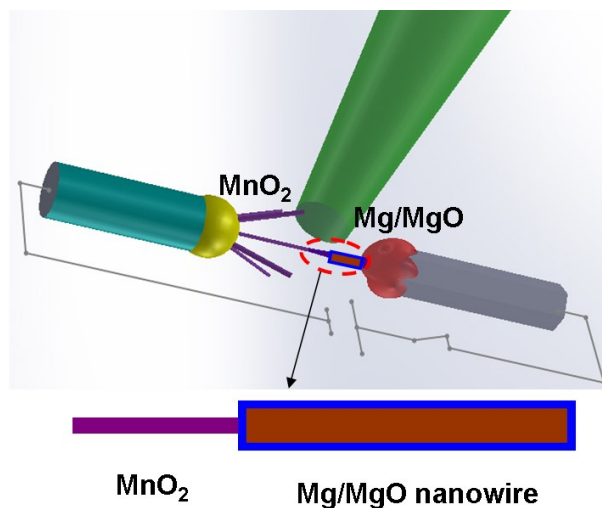
Figure 9.1. Schematic showing the open cell design using in situ TEM for Mg/MgO/α-MnO_2 battery system. The Mg nanowire is pre-oxidized with a thin MgO layer on the surface.

Specifically, the following task is proposed for the future work:

Task: In situ TEM study of Mg^{2+} (Zn^{2+}) insertion/extraction in α-MnO_2 nanowires. The objective is to understand the complete Mg^{2+} (Zn^{2+})-tunnel interaction. Since both pure Mg^{2+} (Zn^{2+}) intercalation and conversion reaction mechanisms are reported in literature, this work here aims to clarify how these mechanisms compete with each

other. The hypothesis is that, the competing mechanisms between intercalation and phase transition are highly dependent on the discharge rate: a low rate favors intercalation mechanism while a high rate favors phase transition to spinel phase. The experimental setup will follow Figure 9.1. The information to be captured and measured includes the phase evolution during Mg^{2+} (Zn^{2+}) insertion/extraction (by SAED), the tunnel expansion (HRTEM) and any localized inhomogeneity (EELS and EDS), which are also compared at different current densities. Previous studies have also shown that the size,[20] surface structure[21] and morphology[22] of α-MnO_2 affect its performance in the fields of lithium ion battery and catalysis. For example, Li *et al*. have demonstrated that α-MnO_2 nanowires exhibit a better capacity retention upon cycling when their lateral surfaces are {210}compared to {110}, which was attributed to the higher exposure rate of 2×2 tunnels to the electrolyte when {210} are the surfaces.[21] Taking these into consideration, the effect of material size, surface structure and morphology will also be studied to see whether they affect the insertion mechanisms of multivalent cations.

9.2. *In situ* liquid TEM studying the catalytic mechanism of α-MnO_2 in Li-O_2 battery

As mentioned earlier, Li-O_2 battery offers a much higher energy density and energy power than lithium ion battery and thus has a promising application in the fields of electric vehicles.[23] The working process and discharge/charge reactions in a typical Li-O_2 battery are illustrated in Figure 9.2a, where a metallic lithium anode, a porous air cathode and aprotic electrolyte are shown.[23] During discharge, Li^+ diffuse through the electrolyte from the metallic lithium anode into the porous cathode, where they meet oxygen and form various lithium oxides (Li_2O_2 for most of the cases). In charge, lithium oxides will decompose to Li^+ and oxygen with Li^+ diffusing back to the anode while O_2 released to the outside.
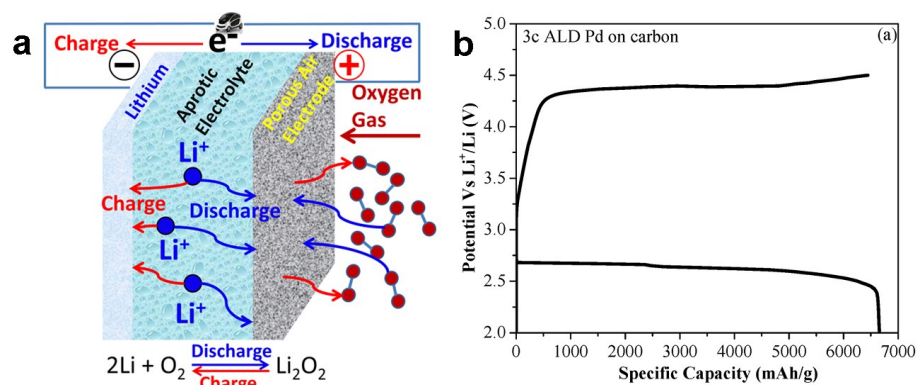
Figure 9.2. (a) Schematic showing the working mechanisms of a Li-O₂ battery as well as the reversible discharge and charge reactions.[23] (b) a typical discharge−charge profile of an aprotic Li−O₂ battery showing the large polarization.[24]

One critical problem existing in Li-O₂ system is the large overpotential during discharge and charge process, which is caused by sluggish reaction kinetics and reduces the energy efficiency and battery life, as shown in Figure 9.2b.[24] To address this issue, people have developed various catalysts into the system to reduce the overpotentials and improve the reaction kinetics.[25] Among these various catalysts, nanostructured α-MnO₂ is widely used and shows outstanding catalysis performance by improving the kinetics of both discharge and charge processes.[20] Figure 9.3a shows an example of utilizing α-MnO₂ to improve the reaction kinetics of Li-O₂ battery during the discharge process (oxygen reduction reaction, i.e. ORR).[26] It shows that under the same potential, the carbon cathode with MnO₂ shows much higher ORR current than pure carbon cathode or the one with Ni doping. However, the catalysis mechanism of α-MnO₂ in Li-O₂ system is not well understood currently due to the lack of an efficient characterization method doing real time study. Questions such as whether 2×2 tunnels of α-MnO₂ take part in the oxygen evolution reaction and oxygen reduction reaction, which surface of α-MnO₂ has the best catalytic property, and why different MnO₂ morphologies have distinct catalytic properties are thus difficult to answer.[27] Figure 9.3(b-e) shows the morphology of discharged products without MnO₂ (b) and with various phases and morphologies of MnO₂,

where α-MnO$_2$ nanotubes show obviously the formation of individual discharged microparticles.[28]
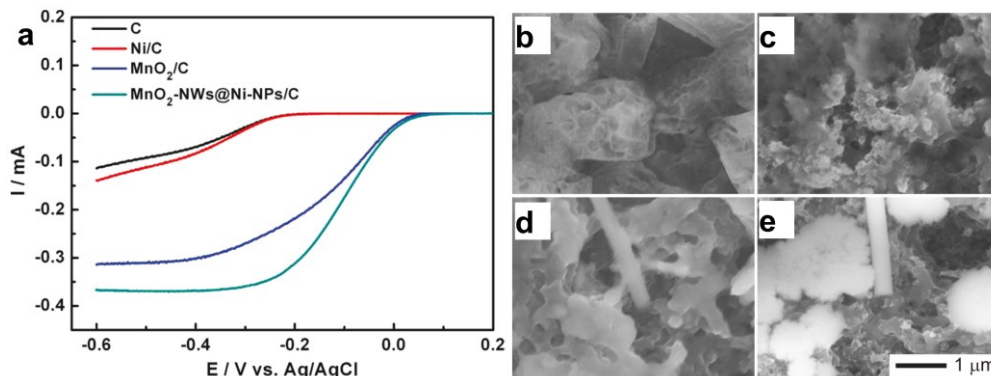
Figure 9.3. (a) The linear scanning voltammograms (LSV) curves of C, Ni/C, α-MnO$_2$/C, and α-MnO$_2$-NWs@Ni-NPs/C obtained at a rotation speed of 900 rpm and a potential scan rate of 1 mV/s.[26] (b) SEM images of porous carbon cathode after 30 cycles at a completely discharged state. The electrode shown in (b) did not include MnO$_2$ nanostructures, while the electrodes in (c-e) include δ-MnO$_2$ nanosheets, α-MnO$_2$ nanowires, and α-MnO$_2$ nanotubes, respectively.[28]

Here the dynamic study of catalytic mechanisms of α-MnO$_2$ in a working Li-O$_2$ system is proposed based on the well developed liquid cell for *in situ* TEM study. The experimental design is shown in Figure 9.4. The design of the *in situ* liquid cell has been well explained in Chapter 3. To achieve a typical Li-O$_2$ battery setup, LiCoO$_2$ cathode is pre-deposited onto the counter electrode, and built-in glassy carbon electrode is directly used as the cathode material to absorb O$_2$. Single α-MnO$_2$ nanoparticle can be then implanted onto the carbon electrode *via* focus ion beam operation with Pt welding. The introduction of O$_2$ into the system is achieved by utilizing an O$_2$-rich liquid electrolyte obtained *via* flowing pure O$_2$ through electrolyte for hours, which has been demonstrated to be effective in the liquid cell holder in TEM.[29] The discharge and charge processes can be controlled by alternating the biasing applied to the counter electrode and the working electrode. Any particle deposition during discharge and dissolution during charge can be dynamically recorded and the reaction kinetics can thus be explored in real time. It has been

reported that the particle size and morphology affect the electrocatalytic activity of α-MnO$_2$ towards oxygen evolution reaction and oxygen reduction reaction, and the mechanism is, however, not clearly understood.[22] As such, by varying the particle size and morphology of welded MnO$_2$ nanostructures (particle, nanorod, nanotube, *etc*.), the difference in catalytic kinetics can also be studied.
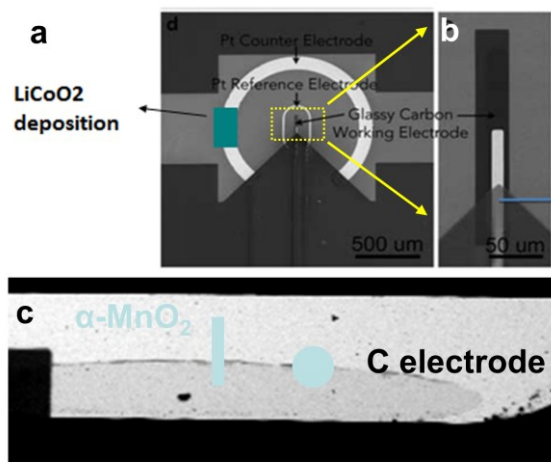
Figure 9.4. (a) Schematic showing the configuration of the liquid cell capable of biasing. The glassy carbon (yellow frame) is the working electrode, and the outer circular ring is the Pt reference electrode with LiCoO$_2$ nanoparticles pre-deposited. (b) Enlarged view of the carbon working electrode. (c) Schematic showing the deposition of α-MnO$_2$ particles with various morphologies as the catalyst on carbon electrode.

Specifically, the task is described as follow:

Task: In situ liquid TEM study of catalytic ability for different facets of α-MnO$_2$. The hypothesis is that when α-MnO$_2$ is in the shape of one-dimensional wires, the catalytic effect of Li-O$_2$ reaction is better compared to the cases where α-MnO$_2$ is in spherical shape. To do the experiment, α-MnO$_2$ particles with various morphologies, such as wires and spheres will be first prepared and attached on to the working electrode of the liquid TEM chip as shown in Figure 9.4. The difference in catalytic ability of various particles can be understood based on the order and quantity that the discharge products precipitate on each α-MnO$_2$ particle. The particle first exhibiting

165

the formation of Li_2O_2 as well as the largest amount of formation on its surface has the best catalytic property.

9.3. Layer-to-tunnel growth mechanism study of MnO_2 nanostructures

It is well accepted that all MnO_2 phases with tunneled structures are generated form the layered MnO_2 phase as the precursor, especially during the hydrothermal synthesis.[30] For example, it has been widely reported that birnessite MnO_2 (δ-MnO_2) with a 7 Å interlayer spacing is the precursor for α-, β-, γ-MnO_2 possessing different tunneled structures, while buserite MnO_2 with a 10 Å interlayer spacing is the precursor for todorokite MnO_2 (T-MnO_2) with a 3×3 tunneled structure.[31,32] Figure 9.5 shows the *ex situ* SEM study of such a layer-to-tunnel transition.[32] Currently, it is not clear how the layered structure transitions into the tunneled structure stably in the hydrothermal conditions and what is the atomic mechanism directing this long-range ordered phase transition. The concentration of large cations (Ba^{2+}, K^+ and Ag^+) are also shown to affect the morphology and structure o the final products, which is however, poorly understood. For any controllable synthesis with desired tunnel size and dimension, it is critical to understand the atomic phase transition mechanism.
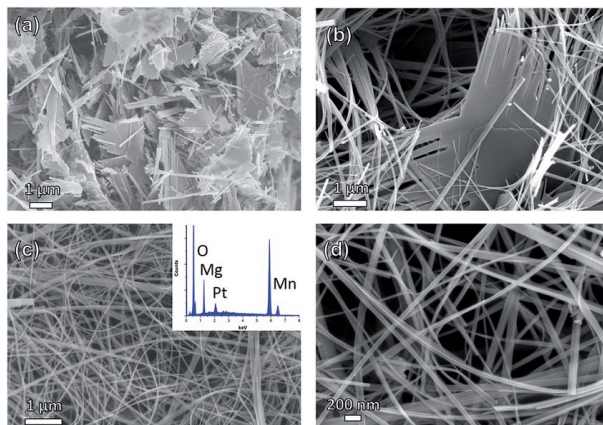
Figure 9.5. SEM images of (a) todorokite plates and nanowires after 24-hour hydrothermal synthesis, (b) todorokite plates splitting into nanowires after 48-hour hydrothermal synthesis at 220 ºC, and (c) low and (d) high magnification SEM

images of todorokite nanowires after hydrothermal synthesis at 220 °C for 4 days. Note in (b) that there is a geometrical relationship (120°) between the layered parent phase and the split nanowires.[32]

A recent paper has pioneered the atomic scale exploration of layer-to-tunnel transition by simulating all possible atomic paths during this process. A layer shear-distortion mechanism is predicted as shown in Figure 9.6.[33] However, there is currently no experimental exploration regarding the atomic level transition mechanism, and any simulation work is too early to be testified at this early stage. It is thus necessary to conduct experimental analysis to explore this mechanism in details.
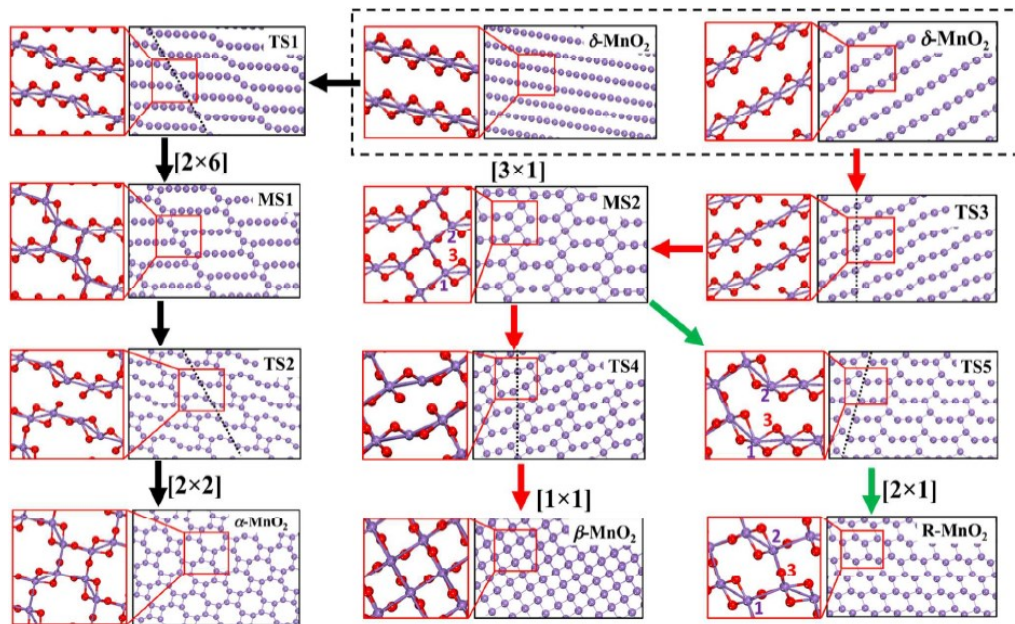
Figure 9.6. The intermediate stages during the phase transition from layered δ-MnO$_2$ to tunneled MnO$_2$ (α-MnO$_2$ on the left), (β-MnO$_2$ in the middle) and (R-MnO$_2$ on the right).[33]

The future task is described as follow:

Task: Exploration of atomistic mechanisms accounting for the layer-tunnel transition. The objective is to understand the atomistic mechanism accounting for the layer-tunnel transition. Our hypothesis is that the driving force for layer-tunnel transition is the reduction of the strain energy of each precursor layer caused by nonuniform Jahn-

Teller distortion of [$Mn^{3+}O_6$]. To test the hypothesis, it is first required to obtain MnO_2 layers/nanowires grown at different stages to differentiate the growth process. Atomic imaging of the cross sectional structures will be then performed to understand the gradual layer-tunnel transition process. EELS will be performed at both the layer region and the tunnel wall region to quantify the Mn valence. It is expected that the Mn valence at the tunnel wall should be close to 3+, while is it close to 4+ inside the layer region.

9.4. References

1. Thackeray MM, Wolverton C, Isaacs ED. Electrical energy storage for transportation—approaching the limits of, and going beyond, lithium-ion batteries. *Energy & Environmental Science* **5**, 7854-7863 (2012).

2. Zhang R, *et al.* α-MnO 2 as a cathode material for rechargeable Mg batteries. *Electrochemistry Communications* **23**, 110-113 (2012).

3. Lee B, Yoon CS, Lee HR, Chung KY, Cho BW, Oh SH. Electrochemically-induced reversible transition from the tunneled to layered polymorphs of manganese dioxide. *Scientific reports* **4**, (2014).

4. Xu C, Chen Y, Shi S, Li J, Kang F, Su D. Secondary batteries with multivalent ions for energy storage. *Scientific reports* **5**, (2015).

5. Ahrens LH. The use of ionization potentials Part 1. Ionic radii of the elements. *Geochimica et cosmochimica Acta* **2**, 155-169 (1952).

6. Gordy W, Thomas WO. Electronegativities of the elements. *The Journal of Chemical Physics* **24**, 439-444 (1956).

7. Kim YJ, Wu W, Chun SE, Whitacre JF, Bettinger CJ. Catechol‐Mediated Reversible Binding of Multivalent Cations in Eumelanin Half‐Cells. *Advanced Materials* **26**, 6572-6579 (2014).

8. Rong Z, *et al.* Materials Design Rules for Multivalent Ion Mobility in Intercalation Structures. *Chemistry of Materials* **27**, 6016-6021 (2015).

9. He Y, *et al.* Atomistic Conversion Reaction Mechanism of WO3 in Secondary Ion Batteries of Li, Na, and Ca. *Angewandte Chemie International Edition* **55**, 6244-6247 (2016).

10. Luo L, *et al.* Reactions of graphene supported Co3O4 nanocubes with lithium and magnesium studied by in situ transmission electron microscopy. *Nanotechnology* **27**, 085402 (2016).

11. Young MJ, Holder AM, George SM, Musgrave CB. Charge Storage in Cation Incorporated α-MnO2. *Chemistry of Materials* **27**, 1172-1180 (2015).

12. Alfaruqi MH, *et al.* A high surface area tunnel-type α-MnO 2 nanorod cathode by a simple solvent-free synthesis for rechargeable aqueous zinc-ion batteries. *Chemical Physics Letters* **650**, 64-68 (2016).

13. Arthur TS, *et al.* Understanding the Electrochemical Mechanism of K-αMnO2 for Magnesium Battery Cathodes. *ACS applied materials & interfaces* **6**, 7004-7008 (2014).

14. Xu C, Li B, Du H, Kang F. Energetic zinc ion chemistry: The rechargeable zinc ion battery. *Angewandte Chemie International Edition* **51**, 933-935 (2012).

15. Alfaruqi MH, *et al.* Electrochemically induced structural transformation in a γ-MnO2 cathode of a high capacity zinc-Ion battery system. *Chemistry of Materials* **27**, 3609-3620 (2015).

16. Islam MM, Bredow T, Minot C. Theoretical analysis of structural, energetic, electronic, and defect properties of Li2O. *The Journal of Physical Chemistry B* **110**, 9413-9420 (2006).

17. Mortlock A. Divalent cation impurity diffusion in MgO. *Mass Transport in Oxides US Government Printing Office, Washington, DC*, 85-87 (1968).

18. Malik R, Burch D, Bazant M, Ceder G. Particle size dependence of the ionic diffusivity. *Nano letters* **10**, 4123-4127 (2010).

19. Kosacki I, Rouleau CM, Becher PF, Bentley J, Lowndes DH. Nanoscale effects on the ionic conductivity in highly textured YSZ thin films. *Solid State Ionics* **176**, 1319-1326 (2005).

20. Débart A, Paterson AJ, Bao J, Bruce PG. α‑MnO2 Nanowires: A Catalyst for the O2 Electrode in Rechargeable Lithium Batteries. *Angewandte Chemie International Edition* **47**, 4521-4524 (2008).

21. Li W*, et al.* Performance modulation of α-MnO2 nanowires by crystal facet engineering. *Scientific reports* **5**, (2015).

22. Selvakumar K, Kumar SS, Thangamuthu R, Kruthika G, Murugan P. Development of shape-engineered α-MnO 2 materials as bi-functional catalysts for oxygen evolution reaction and oxygen reduction reaction in alkaline medium. *International Journal of Hydrogen Energy* **39**, 21024-21036 (2014).

23. Lu J, Li L, Park J-B, Sun Y-K, Wu F, Amine K. Aprotic and aqueous Li–O2 batteries. *Chemical reviews* **114**, 5611-5640 (2014).

24. Lei Y*, et al.* Synthesis of porous carbon supported palladium nanoparticle catalysts by atomic layer deposition: application for rechargeable lithium–O2 battery. *Nano letters* **13**, 4182-4189 (2013).

25. Bruce PG, Freunberger SA, Hardwick LJ, Tarascon J-M. Li-O2 and Li-S batteries with high energy storage. *Nature materials* **11**, 19-29 (2012).

26. Cheng F, Su Y, Liang J, Tao Z, Chen J. MnO2-based nanostructures as catalysts for electrochemical oxygen reduction in alkaline media†. *Chemistry of Materials* **22**, 898-905 (2009).

27. Trahey L*, et al.* Synthesis, Characterization, and Structural Modeling of High‑Capacity, Dual Functioning MnO2 Electrode/Electrocatalysts for Li‑O2 Cells. *Advanced Energy Materials* **3**, 75-84 (2013).

28. Truong TT, Liu Y, Ren Y, Trahey L, Sun Y. Morphological and crystalline evolution of nanostructured MnO2 and its application in lithium–air batteries. *ACS nano* **6**, 8067-8077 (2012).

29. Kushima A, Koido T, Fujiwara Y, Kuriyama N, Kusumi N, Li J. Charging/Discharging Nanomorphology Asymmetry and Rate-Dependent Capacity Degradation in Li–Oxygen Battery. *Nano letters* **15**, 8260-8265 (2015).

30. Shen XF, *et al.* Control of Nanometer‐Scale Tunnel Sizes of Porous Manganese Oxide Octahedral Molecular Sieve Nanomaterials. *Advanced Materials* **17**, 805-809 (2005).

31. Wang X, Li Y. Synthesis and formation mechanism of manganese dioxide nanowires/nanorods. *Chemistry–A European Journal* **9**, 300-306 (2003).

32. Byles B, West P, Cullen D, More K, Pomerantseva E. Todorokite-type manganese oxide nanowires as an intercalation cathode for Li-ion and Na-ion batteries. *RSC Advances* **5**, 106265-106271 (2015).

33. Li Y-F, Zhu S-C, Liu Z-P. Reaction Network of Layer-to-tunnel Transition of MnO2. *Journal of the American Chemical Society*, (2016).

Appendix A. Supporting Information for Chapter 4®

A.1. Experimental details

α-MnO₂ nanowires are prepared via a low-cost, scalable hydrothermal synthesis method using KMnO₄ and MnSO₄ as reactants.[1] For the cross section slices preparation, the nanowires are first fixed using Epofix embedding resin and Epofix hardener mixture; the sample is then placed under an Edge Craft™ diamond knife mounted in Ultramicrotome (Leica UCT) and is cut to slices at a feeding step size of 500 nm. The slices are directly moved to copper grid and dried at 50ºC for 24 hours before TEM characterization.

The experiments were carried out inside an aberration-corrected JEOL JEM-ARM 200CF STEM equipped with a 200 keV Schottky cold-field emission gun, a HAADF detector, and a postcolumn Gatan Enfina EELS spectrometer. 22 mrad probe convergence angle was used for all the images and spectra. The HAADF images were acquired using a 90 mrad inner-detector angle, and the EELS spectra were obtained with a 45 mrad collection angle.

The in-situ setup is similar to the method used by others.[2] The nanoscale electrochemical open cell used for in-situ observation is schematically illustrated in Figure S1a. Single α-MnO₂ nanowire is attached by conductive epoxy to a gold wire to be the working electrode, and Li metal is attached to a tungsten tip and functions as the counter electrode. This step is finished inside a glove box filled with Ar. Transportation of the sample from glove box to TEM will result in a naturally grown Li₂O layer on the surface of Li metal, and this layer can function as a solid-state electrolyte to facilitate the diffusion of Li⁺ from Li metal to α-MnO₂. In-situ operation

---

is achieved via a Nanofactory TEM-scanning tunneling microscope holder. Lithiation is initiated when a constant potential of -2 V is applied to MnO_2 against Li counter electrode.

Here it is worth to mention some practical facts about TEM operation. In our present situation, we cannot tilt the same nanowire 90° and change views between [010] and [100], although such method is the most efficient way to prove the proposed theory. Also, when using the in-situ holder, the highly sensitive device will be subjected to any vibration or noise, not to mention a purposed holder tilting, which will easily destroy the in-situ setup and the targeted nanowire will drop or move out of view.

Electrode composed of 80 wt% of α-MnO_2 nanowires, 10 wt% super P carbon and 10 wt% of PVDF binder were well mixed in *N*-methyl-pyrrolidinone (NMP) to get a homogenous slurry. The obtained slurry was casted onto an Al foil to make electrode. The electrode was dried at 75 °C for 4 hours, and followed by being thoroughly dried at 75 °C overnight under vacuum. Electrochemical measurement was carried out on the CR2032 coin cell with Li metal as counter electrode, CELGARD 2325 membrane as the separator and 1.2 M $LiPF_6$ in EC/EMC (3:7 by weight) as the electrolyte. Cyclic voltammetric (CV) curve of α-MnO_2 in the coin cell was performed at a scanning rate of 0.05 mV s^{-1} in a voltage range of 1.5 V- 4 V using a multislit Solartron system. In-situ Synchrotron XRD (λ=0.118 Å) was performed at Beamline 11-ID-C located in Advanced Photon Sources of Argonne National Laboratory. The slurry was made from the same components and ratios as mentioned above but with much higher loading amount on Al foil. The test coin cell was assembled using pre-punctured spacer and electrode caps for better X-ray penetration, and was cycled at a 0.05C rate between 1.5 V-4 V.

A.2. Simulation details

Spin-polarized DFT simulations were conducted to determine the most favorable Li^+ insertion sites in the $K_{0.25}MnO_2$ crystal. For these simulations, version 5.2.12 of the

Vienna Ab Initio Simulation Package[3,4,5]. The DFT+U method was used for these simulations, as implemented in VASP using the rotationally invariant approach of Liechtenstein et al.[6]. For the transition metal Mn, it was assumed that U = 6.2 eV and J = 1.0 eV, based on the results of previous work[7]. The Perdew-Burke-Ernzerhof exchange-correlation functional was used[8,9] with an optimized cut-off energy of 550 eV. For Li atoms, the 1s and 2s states were treated as valence states. For the K atoms, the 3s, 3p, and 4s states were treated as valence states. For Mn, the 3s, 3p, 3d, and 4s states were treated as valence states. For O, the 2s and 2p states were treated as valence states. For all DFT simulations, relaxations were simulated for ionic positions, unit cell shape, and unit cell size.

The $K_{0.25}MnO_2$ crystal was simulated first, followed by simulations of Li^+ insertion into the Wychoff 2b, 4c,4d, 4e, 8f, 8g, 8h, and 16i sites; starting with a single Li^+ atom and ending with Li^+ saturation, as shown in Figure 6. Γ-centered Monkhorst-Pack grids[10] were generated for each of the systems with an optimized k-point grid spacing of 5×5×17. As can be seen in Figure 6, the unit cell consists of a 2×2 tunnel at the middle, partial 1×1 tunnels on each edge, and partial 2×2 tunnels at the corners. Therefore, given the periodic boundaries, a total of two 2×2 tunnels are simulated in the unit cell.

The energies of formation for each level of Li^+ insertion were calculated using

$$E_f = E_x - (8x)E_{Li} - E_{K2Mn8O16}$$

where E_x is the electronic energy for the $Li_x K_{0.25}MnO_8$ unit cell (x defined as the number of inserted Li atoms/8), E_{Li} is the energy for an Li solid in its ground state[11] (per Li atom), and $E_{K2Mn8O16}$ is the energy associated with the unlithiated unit cell. The corresponding values of E_f are plotted in Figure 6. It is clear from this data that the 8h and 16i insertion sites have the overall lowest energies, and the 8h site is energetically most favorable at $x = 1$.

Because the 8h site shows the overall lowest energies, the Convex Hull method was used to investigate the reaction path for Li intercalation in the 8h site, similar to Ling and Mizuno[12]. The energy of formation is given by

$$E_f = E_x - x E_{LiK0.25MnO2} - (1-x) E_{K0.25MnO2}$$

where E_x, $E_{LiK0.25MnO2}$, and $E_{K0.25MnO2}$ are the total energies of $Li_xK_{0.25}MnO_2$, $LiK_{0.25}MnO_2$ and $K_{0.25}MnO_2$, respectively. The lowest energies for each value of x corresponded to the most likely Li intercalation sites, and the lattice parameters reported in Figure 7 corresponded to these structures.

A.3. Supporting figures
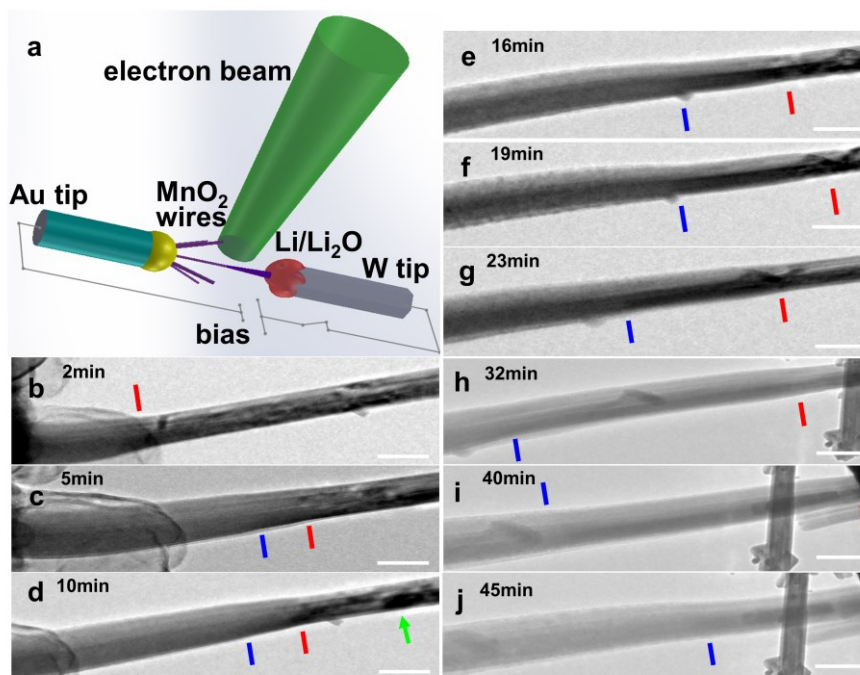
Figure A1 a: Schematic of in-situ setup; b-j: Time sequence of TEM images of single MnO_2 nanowire during lithiation (from left to right). The scale bar is 100 nm in each image; red bar indicates the first reaction front and blue bar indicates the second front. Bias: +2 V on Li side. View projection: [010]
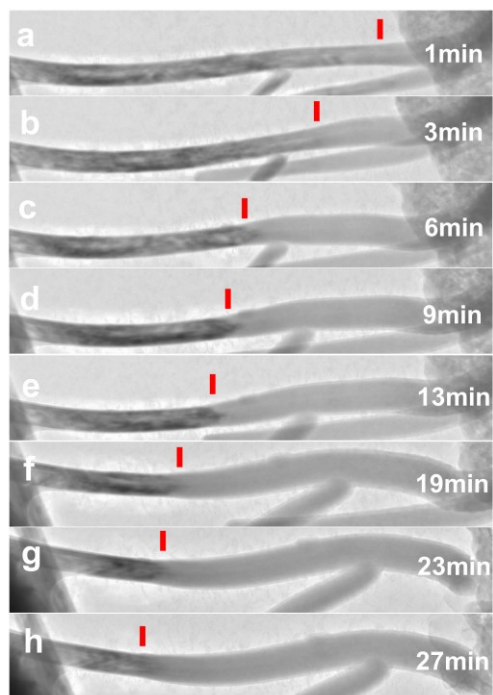
Figure A2 Time sequence of TEM images of single α-MnO$_2$ nanowire during lithiation (from right to left). The red bar indicates the single lithiation front. Bias: +2 V on Li side. View projection: [100]
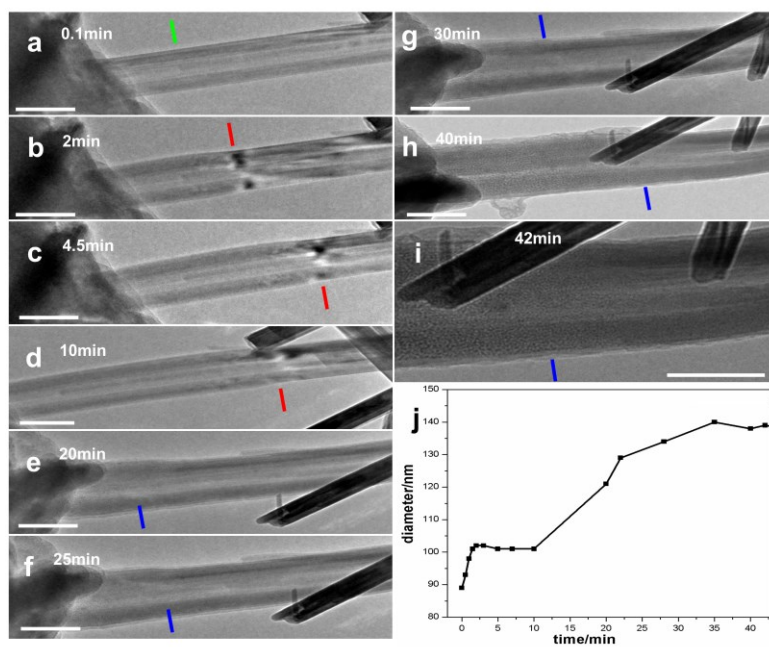
Figure A3 a-h: Time sequence of TEM images of single α-MnO$_2$ nanowire during lithiation (from left to right); i: High-mag TEM showing the second reaction front with sharply different contrast change. The first front is beyond view due to its fast moving. The white scale bar is 100 nm in each image; red bar indicates the first front, blue bar for the second front and green bar is where the projected diameter is measured to construct Figure S2j. Bias: +2 V on Li side. View projection: [010]
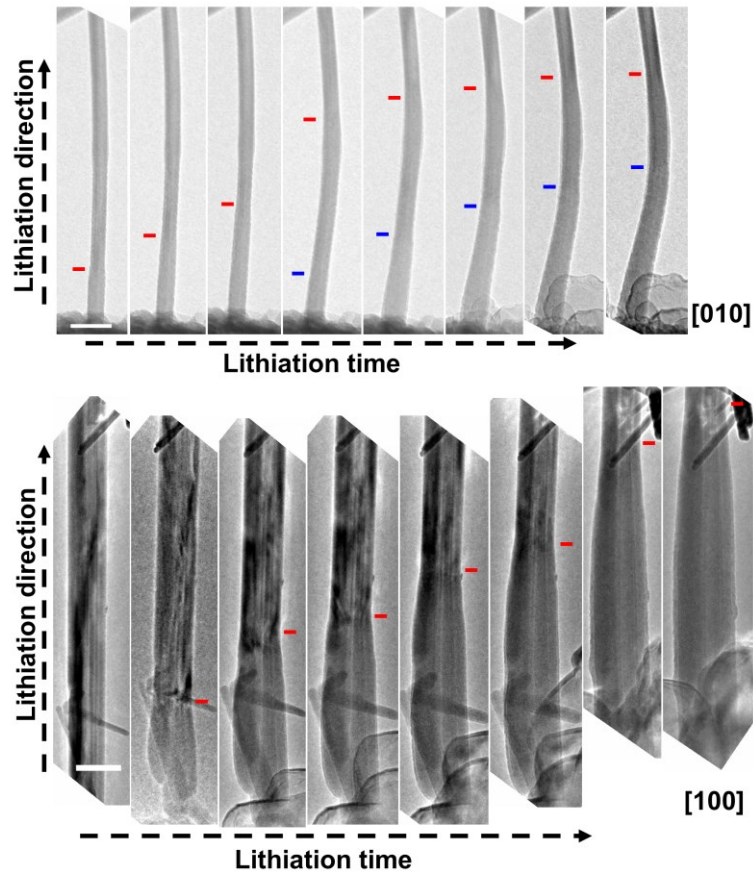
Figure A4 Two nanowires being lithiated and viewed under [010] (top) and [100] (bottom) zone axes. The top nanowire is pristine with no "bundling" phenomenon, and two-front expansion (red for the first front and blue for the second front) features its lithiation. The bottom one is featured by striped contrast, indicating the existence of "bundling", and single expansion front (red) features its lithiation. The images are aligned so that the nanowires are placed at the same level for better observation. Scale bars in all images: 100 nm.
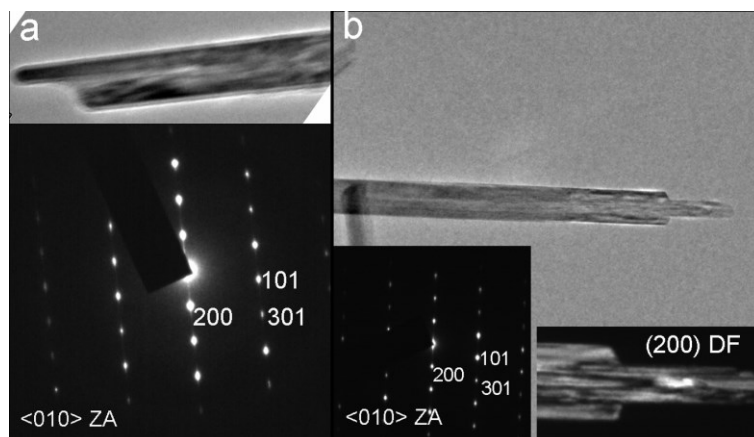
Figure A5 a: one α-MnO$_2$ nanowire showing "bundling" phenomenon with its SAED shown in the bottom; b: another α-MnO$_2$ nanowire showing "bundling" phenomenon with its SAED and (200) dark field image shown in the bottom. It shows that both nanowires are essentially single crystalline, indicating a lateral oriented attachment mechanism to direct their solution growth process.
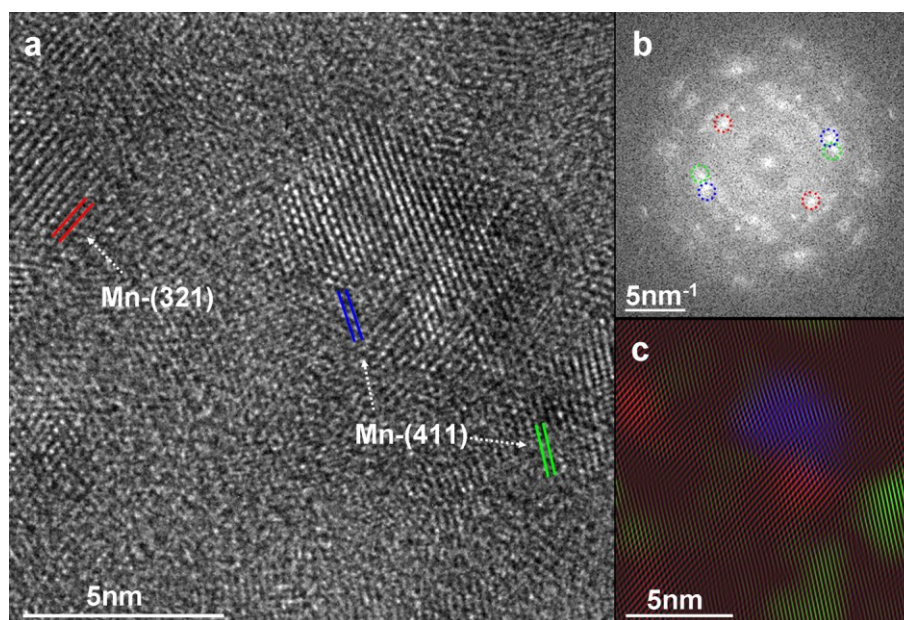
Figure A6 a: HRTEM of Zone D$_{[010]}$ (D$_{[100]}$) showing nanograins embedded in Li$_2$O matrix; b: FFT of the same area proving these nanograins to be Mn; c: Constructed RGB image showing Mn nanograins with different crystallographic orientations (the color of each grain helps to identify which specific reciprocal spot it contributes to).
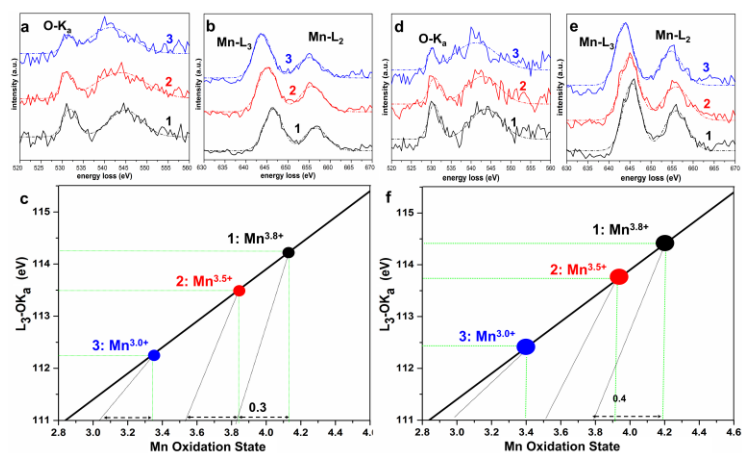
Figure A7 (a, d): Fitted oxygen K-edge spectrum with prepeak O-Kα indicated; (b, e): Fitted Mn-$L_{2,3}$ white lines; (c, f): Mn valence identification based on ΔE (Mn L_3-O Kα) fingerprints. The black, red and blue dots correspond to locations (curves) 1, 2 and 3, respectively; location 1 with known $Mn^{3.8+}$ valence is used to slightly offset the horizontal coordinate value for more precise valence identification of locations 2 and 3. (a-c) are analyses for the nanowire under [010] TEM projection; (d-f) are for the nanowire under [100] projection. Note that among all the different fitting functions (Gauss, Gaussin, Voigt) used, Gaussian function gives the smallest fitting error for calculating the energy difference between the energy loss peaks. Using Gaussian function, the standard error is 0.14 eV for Curve 1, 0.15 eV for Curve 2 and 0.2 eV for Curve 3.

The oxygen K-edge prepeak (O-Kα) around 530 eV in Figures 5b (e) and Figure S6a (d) is due to transition from $1s$ core states to $2p$ states hybridized with Mn $3d$ orbitals, and the second peak around 545 eV is linked with the projected unoccupied oxygen p states mixed with Mn $4sp$ band at higher energy above the Fermi level. The intensity of O-Kα decreases as more Li^+ are inserted, indicating less chance of electron transfer to d_z^2 orbital due to increasing electron occupancy at d_z^2 orbital when Mn is continuously reduced during lithiation. Manganese L_3 and L_2 white lines located between 640 eV and 660 eV correspond to electron transitions from $2p_{3/2}$ and $2p_{1/2}$ core states to unoccupied $3d$ states localized on the excited Mn ions and are separated

by spin-orbit splitting $\Delta E(L_2-L_3)$. Upon lithiation, both L_3 and L_2 peaks shift toward lower energy side with L_3 showing a larger shifting trend, indicating that the valence of Mn decreases during lithiation, which is already proved by previous work.
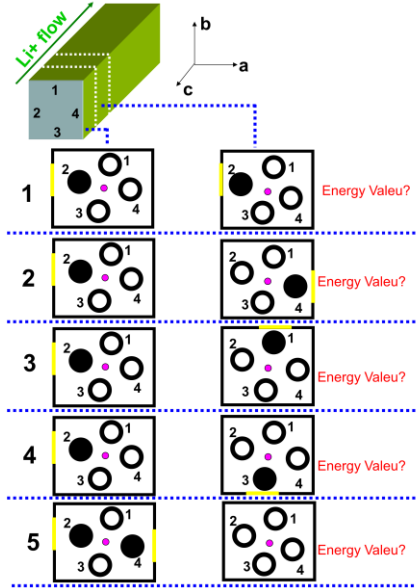
Figure A8. Simulated Li^+ occupancy sequence at 8h sites along [001] direction. Two 2×2 tunnels along c-axis were built to simulate the formation and growth of a lithiation front. Five situations were simulated to determine the preferred 8h Li intercalation sites along the c-direction. The corresponding electronic energies are shown. These simulations were conducted using the same simulation parameters and methods described above.
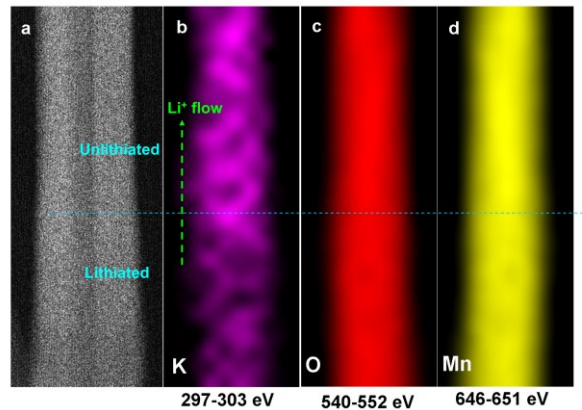
Figure A9 a: HAADF image of a partially lithiated nanowire with upper section unlithiated and lower section lithiated. b-d: EELS mapping for K,O and Mn elements.

Partial removal of K in the lithiated section is confirmed by the weaker K signal than that in the unlithiated section.
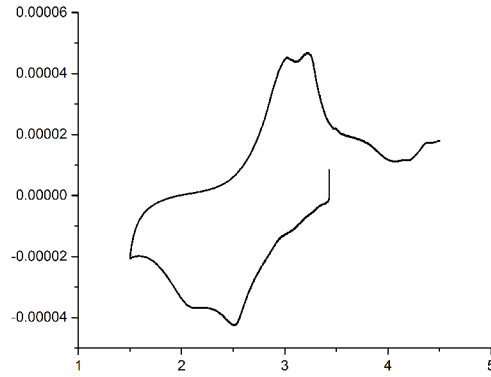
Figure A10. CV curve of α-K$_{0.25}$MnO$_2$ nanowire electrode (coin cell) at a scanning rate of 0.05 mV s^{-1} over voltage range of 1.5 V-4 V. Two cathodic peaks appear at 2.5 V and 2.1 V, which likely corresponds to the Tetragonal-Orthorhombic transition and Orthorhombic-Tetragonal transition, respectively. In the following charge process, two anodic peaks appear at 2.9 V and 3.2 V, confirming the reversible lithiation/delithiation cycling in α-K$_{0.25}$MnO$_2$ nanowires.
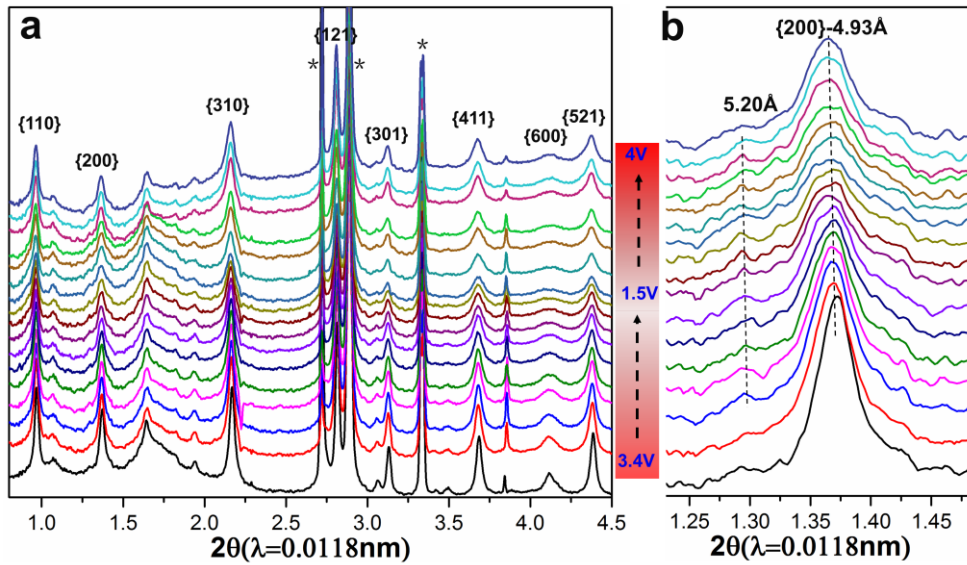
Figure A11. a: In-situ synchrotron XRD showing the structural evolution of a Li/α-K$_{0.25}$MnO$_2$ coin cell during its first discharge-charge cycle. The strong star peaks correspond to the metallic background signals; b: Enlarged {200} peak region

showing that the main peak is broadened during lithiation with gradual appearance of a small peak to its left side.

It is notable that the small peak to the left of {200} is equal to 5.20 Å spacing, which is close to the fully expanded {200} spacing from TEM observation. The coexistence of two peaks (5.20 Å and 4.93 Å) should correspond to the intermediate discharge state when a fully expanded and b is not expanded, i.e. at the end of Zone B (orthorhombic phase). Theoretically, the 4.93 Å peak should disappear when it reaches the end of discharge (around 1.5 V) and then appear again during charge. Actually, however, it is always shown in the pattern with only broadening behavior. This can be explained by the incomplete electrochemical reaction inside a large coin cell, where not all nanowires take part in the (de)lithiation. Vice verse, the fully lithiated nanowires cannot be thoroughly delithiated, so the 5.20 Å peak is always shown in the pattern since its first appearance during lithiation.

Movie A1. Lithiation process of α-$K_{0.25}MnO_2$ nanowire under [010] TEM zone axis. Video is at ×8 rate.

Movie A2. Lithiation process of α-$K_{0.25}MnO_2$ nanowire under [100] TEM zone axis. Video is at ×8 rate.

A.4. References

1. Santhanagopalan, S.; Balram, A.; Meng, D. D. *ACS Nano* **2013,** 7, 2114-2125.

2. Ghassemi, H.; Au, M.; Chen, N.; Heiden, P.A.; Yassar, R.S. *ACS Nano* **2011,** *5*, 7805-7811.

3. Kresse, G.; Furthmuller, J. *Phys. Rev. B* **1996,** *54*, 11169-11186.

4. Kresse, G.; Furthmuller, J. *Comput. Mater. Sci.* **1996,** *6*, 15-50.

5. Kresse, G.; Hafner, J. *Phys. Rev. B* **1994,** *49*, 14251-14269.

6. Liechtenstein, A. I.; Zaanen, J. *Phys. Rev. B* **1995,** *52*, R5467-R5470.

7. Tompsett, D. A.; Islam, M. S. *Chem. Mater.* **2013,** *25*, 2515-2526.

8. Perdew, J.P.; Burke, K.; Ernzerhof, M. *Phys. Rev. Lett.* **1996,** *77*, 3865-3868.

9. Kresse, G.; Joubert, D. *Phys. Rev. B* **1999,** *59*, 1758-1775.

10. Monkhorst, H. J.; Pack, J. D. *Phys. Rev. B* **1976,** *13*, 5188-5192.

11. Lejaeghere, K.; Van Speybroeck, V.; Van Oost, G.; Cottenier, S. *Crit. Rev. Solid State Mater. Sci.* **2014,** *39*, 1-24.

12. Ling, C.; Mizuno, F. *Chem. Mater.* **2012,** *24*, 3943-3951.

Appendix B. Supporting Figures for Chapter 5[⑦]
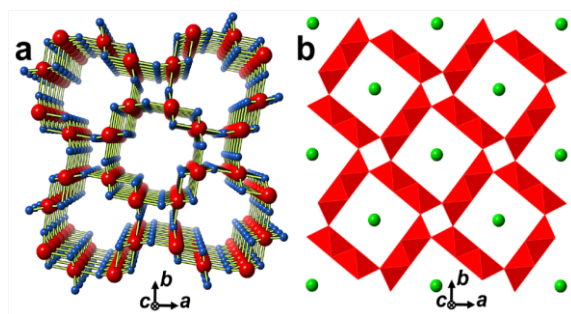
Figure B1. (a) Atomic model of α-MnO$_2$ with a space group of I4/m and the tetragonal symmetry; red is for Mn and blue for O. (b) [MnO$_6$] octahedral model of K$^+$-α-MnO$_2$ where the green atoms are K$^+$.
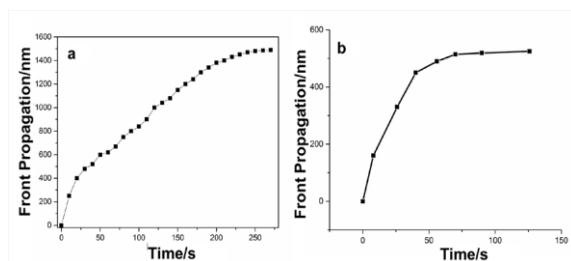
Figure B2. The measured relationship between the sodiation front position and the sodiation time for two α-MnO$_2$ nanowires as shown in the Movie B1 and Movie B2.
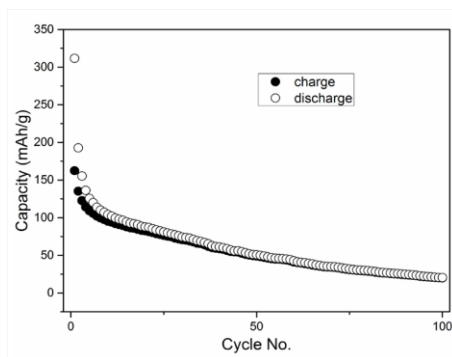
Figure B3. The cycling performance of Na/α-MnO₂ battery at a current of 0.1 C.
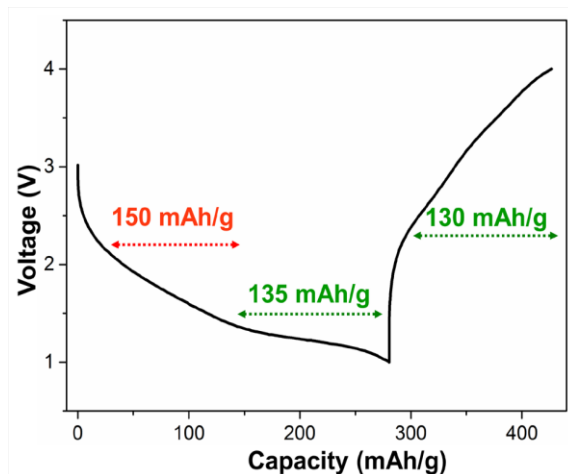
Figure B4. The voltage profile during the first discharge/charge cycle between 4-1 V at a current rate of 0.1 C.

Movies B1 (X8): One α-MnO₂ nanowire being sodiated using the *in situ* open cell design inside TEM chamber.

Movies B2 (X4): One α-MnO₂ nanowire being sodiated using the *in situ* open cell design inside TEM chamber.

Movie B3 (X64): One α-MnO₂ nanowire being sodiated and desodiated for several cycles using the *in situ* open cell design inside TEM chamber.

Appendix C. Supporting Information for Chapter 6[®]

C.1. Supporting figures
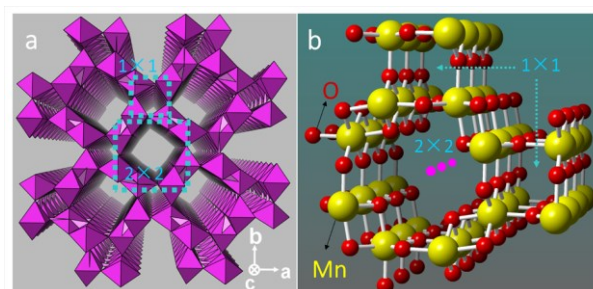
Figure C1. (a): Polyhedral model of α-MnO_2 along [001] zone axis with 1×1 and 2×2 tunnels indicated by the blue squares; (b): Atomic model showing one 2×2 tunnel and two adjacent 1×1 tunnels. The pink spheres refer to 2×2 tunnel stabilizers such as K^+, Ba^{2+} and NH_4^+.
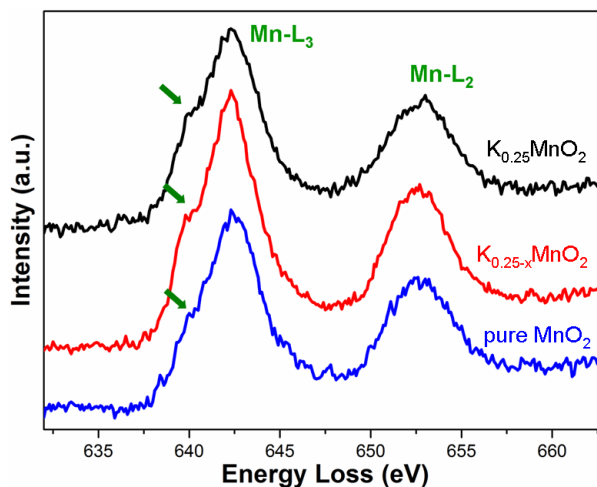
	$K_{0.25}MnO_2$	$K_{0.25-x}MnO_2$	pure MnO_2
L_2-L_3 (eV)	10.648 ± 0.024	10.596 ± 0.025	10.476 ± 0.033
Mn valence	3.46	3.58	3.85
L_3/L_2	2.092 ± 0.023	1.980 ± 0.035	1.837 ± 0.039
Mn valence	3.72	3.84	3.97

Figure C2. Top: The EELS results for three groups of nanowires ($K_{0.25}MnO_2$, $K_{0.25-x}MnO_2$, pure MnO_2). The green arrows indicate the existence of Mn^{3+}. Bottom: The quantification of Mn valence evolution during acid treatment using two methods, (L_2-L_3) and (L_2/L_3).

According to the literature, there are two competing mechanisms explaining the removal of K^+ from the 2×2 tunnels of MnO_2 in an acid solution. One is K^+-H^+ exchange mechanism, and the other one is the redox mechanism. The detailed reaction paths for these two mechanisms were proposed by Feng et al.,[1] where the reactions are given as:

$$\{K_2\}[\square_{0.5}Mn^{IV}_{7.5}]O_{16}+2H^+ = \{H_2\}[\square_{0.5}Mn^{IV}_{7.5}]O_{16}+2K^+$$

for K^+-H^+ exchange, and

$$8\{K_2\}[Mn^{III}_2Mn^{IV}_6]O_{16}+32H^+ = 7\{\}[Mn^{IV}_8]O_{16}+16K^++8Mn^{2+}+16H_2O$$
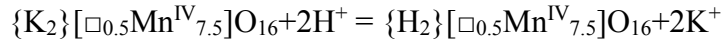
for redox mechanism, where {}, [], and □ denote the (2×2) tunnel sites, octahedral sites for Mn, and octahedral vacant sites, respectively. The critical difference between these two mechanisms is whether Mn valence of the oxide is increased or not, which is however, not fully explored by the authors. Many groups also report the K^+ removal results are explained by either the K^+-H^+ exchange[2,3] or the redox mechanism[4,5]. Yet, there is no overall consensus as to which one is dominant due to the lack of a systematic study.

Our conclusion from the present study is that the K^+ removal from the 2×2 tunnels of MnO_2 is dominated by the redox mechanism, i.e. the Mn valence is gradually increased to Mn^{4+} with the removal of K^+. We systematically studied the Mn valence evolution for nanowires before HNO_3 treatment, after 1-day treatment, and after 4-day treatment using two different methods: electron energy loss spectroscopy (EELS) and X-ray photoelectron spectroscopy (XPS). If K^+ removal was controlled by the K^+-H^+ exchange mechanism, then the Mn valence would have been unchanged. The results of XPS and EELS both confirmed that there is an obvious trend of Mn oxidation (up to Mn^{4+}) with the gradual removal of K^+ from the tunnels, which is a

solid proof that the K^+ removal is dominated by direct Mn oxidation instead of the K^+-H^+ exchange mechanism.

Fig. C2 shows the EELS data of the three groups of nanowires (top) with the quantification of Mn valence shown in the table (bottom). Three different signatures are used here to characterize the change of Mn valence. The green arrows indicate the existence of Mn^{3+} shoulder peak on the left side of the Mn^{4+} peak, which has been used as a signature of the Mn valence change.[6] The gradual decrease of the shoulder peak intensity during the acid treatment confirms the gradual oxidation of Mn^{3+} to Mn^{4+} accompanying the removal of K^+ form the tunnels. Another signature is the energy difference between Mn white lines (L_2-L_3), which is known to be sensitive to the change of Mn valence.[6-8] The decrease of (L_2-L_3) value (shown in the bottom table of Fig. C2) during the treatment also confirms the oxidation of Mn. The third signature is the peak intensity ratio of L_3/L_2, which is also sensitive to Mn oxidation state.[9] The decrease of the L_3/L_2 ratio (shown in the bottom table of Fig. C2) during the treatment further confirms the oxidation of Mn. The quantification details are given in the table with reference to reported standard values[7].

Fig. C3 gives the XPS data of the three groups of nanowires with both the original curves and the fitted curves. Fig. C3a confirms the gradual removal of K^+ as evidenced by the decrease of K 2p signal during the treatment. Fig. C3b-d compare Mn 2p peaks for three groups of nanowires with emphasis on the quantification of Mn^{4+}/Mn^{3+} intensity ratio. After fitting the curves, the ratio of the integrated intensity of Mn^{4+} and Mn^{3+} peaks is (i) 1:1 for the nanowires without treatment, (ii) 2.5:1 for the nanowires after 1-day treatment, and (iii) 5: 1 for the nanowires after 4-day treatment. This indicates the Mn valence in K_xMnO_2 nanowires being increased from $Mn^{3.5+}$ (no treatment), to $Mn^{3.71+}$ (1-day treatment) and to $Mn^{3.83+}$ (4-day treatment). Note that XPS of the 4-day treated nanowires still shows a residual Mn^{3+} signal, which is probably due to the unsaturated Mn on the surface with 3+ valence states, which has been suggested by our recent work.[10]
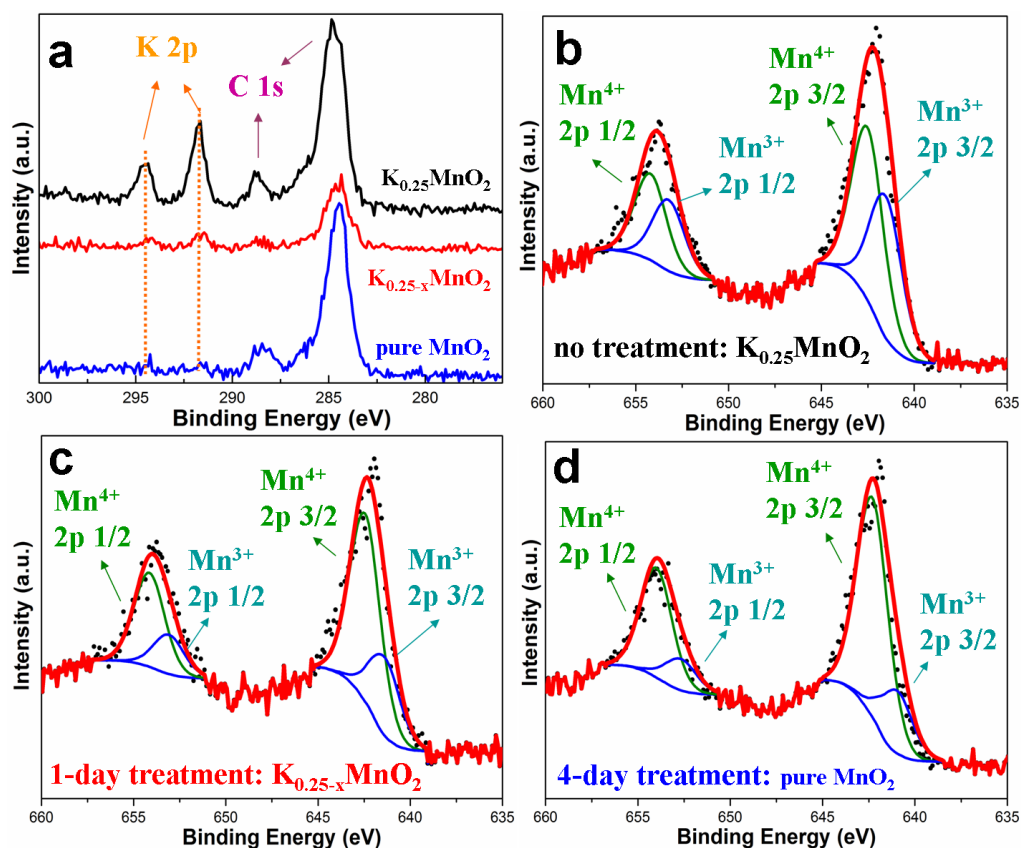
Figure C3. a: The XPS survey curves for three groups of nanowires (black for no treatment, red for 1-day treatment, blue for 4-day treatment). b-d: The XPS results around Mn 2p peaks for three groups of nanowires.

In short, our XPS and EELS results on the Mn valence analysis are consistent with each other, leading to the conclusion that the K^+ removal process is dominated by the Mn oxidation mechanism rather than the K^+-H^+ exchange mechanism. So the possibility of H^+ presence in the tunnels is minimized.

We have considered the possibility of H^+ residing inside the 2×2 tunnels as a result of the K^+-H^+ exchange mechanism.[11] Due to the challenge in H^+ detection, we can not completely exclude the existence of trace amount of H^+ in the tunnels. However, if we assume that one K^+ removal is compensated by one H^+ insertion into the tunnels, there should be no Mn oxidation. Our detailed Mn valence analysis clearly indicates

189

Mn oxidation, and we therefore conclude that Mn oxidation is the dominant mechanism.
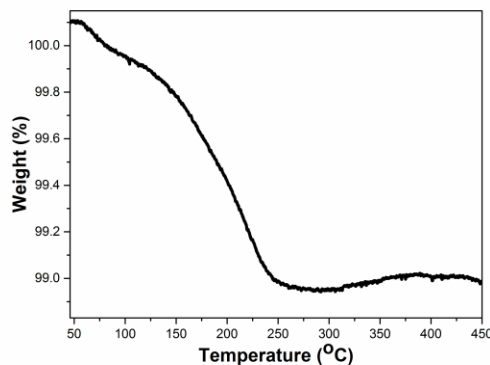
Figure C4. TGA curve of the nanowires (pure MnO_2) after 4-day acid treatment.

We have excluded the possibility of residual water inside the tunnels by heating the nanowires at 280 °C in dry air (right after acid treatment) to remove any absorbed water. According to previous studies, 280 °C is high enough to remove any tunnel water.[12,13] To confirm the removal of water as well as the thermal stability of the nanowires after K^+ removal, we also carried out Thermogravimetric Analysis (TGA) on the nanowires after 4-day treatment, with the results shown in Fig. C4. It shows one weight loss trend (0.2%) from 60 °C to 130 °C,due to the evaporation of surface absorbed water from the nanowires. The second loss starts from 150 °C to 250 °C owing to the removal of tunnel water (1%). Above 250 °C, the nanowires maintain structural stability without any weight loss (O release, *etc.*) up to 450 °C.

The *in situ* heating experiment was performed on a TEM heating stage, and the results are shown in Fig. C5. This real time study focused on tens of nanowires with one single nanowire targeted for the high-mag TEM imaging and diffraction. The selective area electron diffraction (SAED) pattern from these nanowires confirms that the tetragonal α-MnO_2 phase is stable when heated to 280 °C based on indexing the polycrystalline pattern to be α-MnO_2. The unchanged morphology of the nanowires (and the targeted single nanowire) also confirms the thermal stability at 280 °C. When

190

it is heated above 350 °C (to 450 °C), the SAED pattern of these nanowires is still indexed to be tetragonal α-MnO$_2$ phase, but the polycrystalline pattern becomes ring-like. In addition, the dynamic observation of one single nanowire shows that the nanowire's single crystalline diffraction pattern also generates some new diffraction spots after 350 °C. Both signatures indicate the gradual polycrystallization of individual nanowire above 350 °C, although the tetragonal phase is maintained. The morphology evolution of the single nanowire further confirms the polycrystallization behavior, which starts with the surface pulverization around 350-400 °C and extends into the inner parts of the nanowire at 450 °C. The thermal-induced polycrystallization of α-MnO$_2$ nanowires is probably driven by the formation of crystal interfaces and twin boundaries that are fast developing at high temperature.
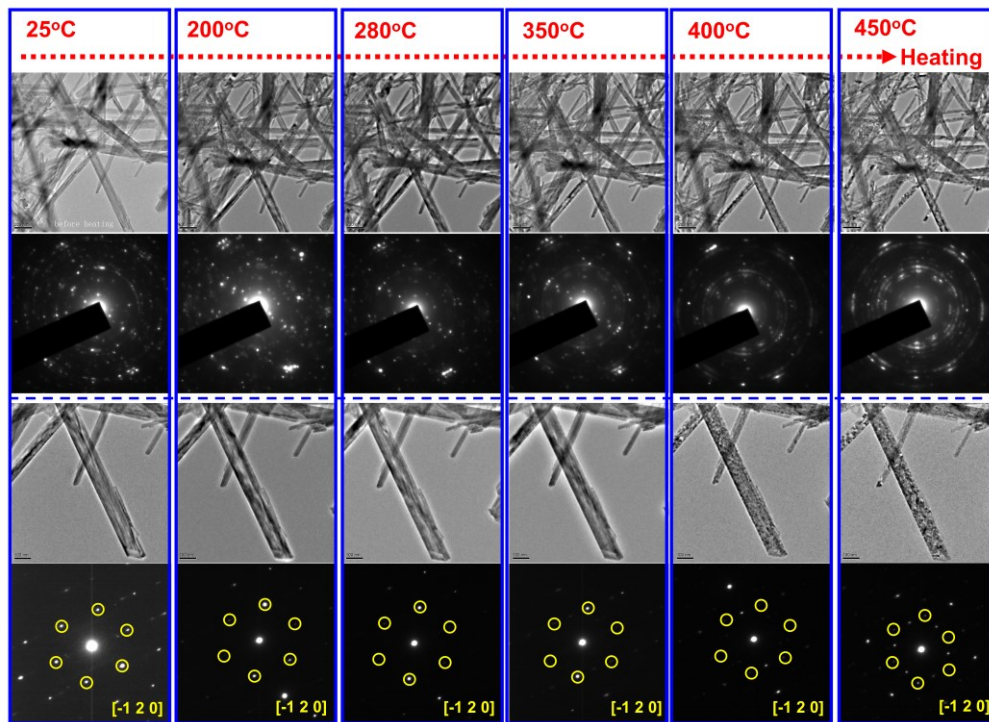
Figure C5. (Top two rows) *In situ* heating of several nanowires with their SAED recorded. (Bottom two rows) One nanowire is magnified for detailed phase and morphology analysis.

Both TGA and *in situ* heating inside TEM confirm that the nanowires are thermally stable at 280 ºC. Note that the thermal stability of the nanowires above 350 ºC is characterized to be different in TGA and the in situ heating. This is understandable considering that the oxides are easier to release O under a TEM vacuum environment than in the N_2-filled TGA atmosphere.
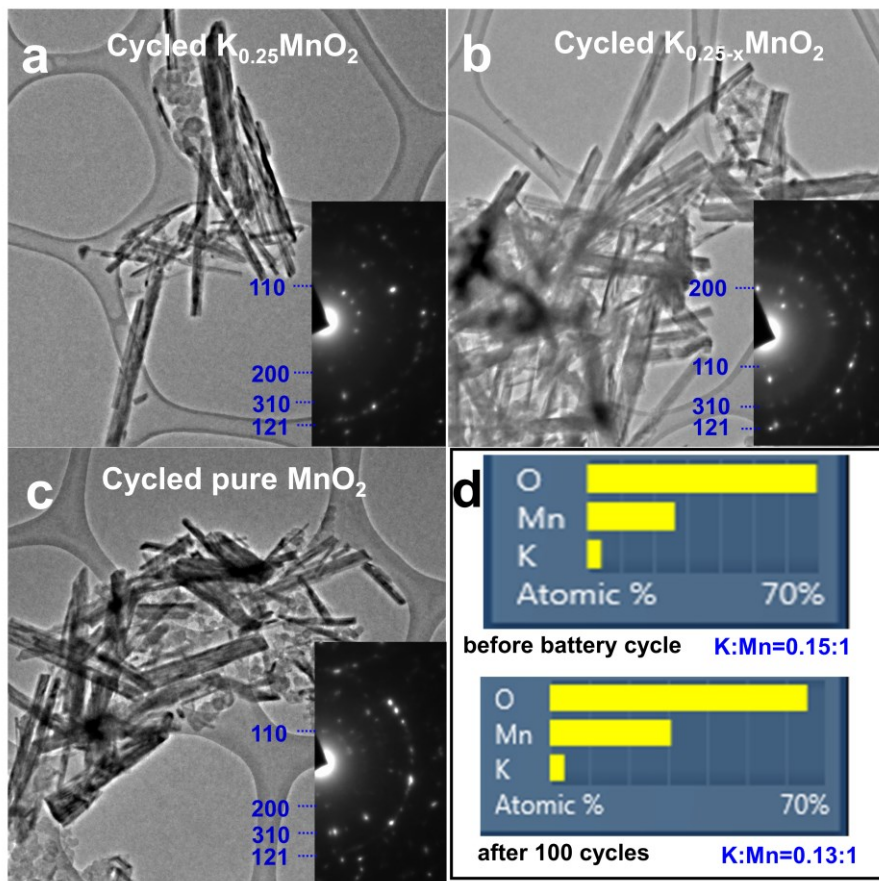
Figure C6. (a-c): TEM images and the corresponding SAED patterns for the nanowires after 100 cycles as lithium-ion battery cathodes. Indexing of the diffraction rings indicates that the nanowires consist of tetragonal α-MnO_2 and the tunnel structures are thus well maintained. (d): EDS analysis of the nanowires ($K_{0.25}MnO_2$ nanowires without acid treatment) before and after 100 battery cycles at 0.1 C. K^+ concentration in the nanowires is slightly affected by the battery cycling while the majority of K^+ are still within the nanowires. It shows that K^+ concentration in the tunnels is only slightly affected by the cycling, and a small amount of K^+ might be

probably lost into the electrolyte while the majority of K^+ remains inside the nanowires.
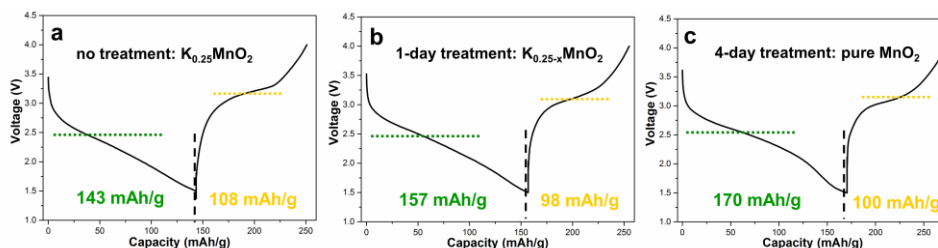
Figure C7. The first discharge/charge profile for three groups of nanowires as lithium battery cathodes. The green line indicates the discharge reaction happening around 2.5 V for all three cells, while the yellow one indicates the charge reaction around 3.2 V for all three cells.

To investigate the effect of K^+ concentration during the first cycle, the galvanostatic discharge/charge curves for the three groups of nanowires are shown in Figure C7. While all three groups exhibit a discharge voltage around 2.5 V (*vs* Li/Li+), the variation in the first discharge capacity is observed among three groups of nanowires. The nanowires after 4-day acid treatment have a capacity of 170 mAh/g, compared to the capacity of 143 mAh/g for the nanowires without acid treatment, which can be ascribed to the addition of K^+ that increases the inactive mass of the material. We have measured several cells and found that the discharge capacity for the nanowires without treatment is in the range of 130-143 mAh/g, so 130 mA/g is used as the practical 1 C rate. Upon charge, however, we observed the opposite trend. The capacity of the 4-day treated nanowires is lower than the nanowires without treatment.

Figure C8 gives the rate performance of the three groups of nanowires during cycling. The discharge capacity of each cycle has been normalized to the capacity measured at 0.1 C. While the capacity retention is similar for the three groups at lower current, it indeed shows higher capacity retention at higher current (2 C and 5 C) for the nanowires with the highest K^+ concentration.
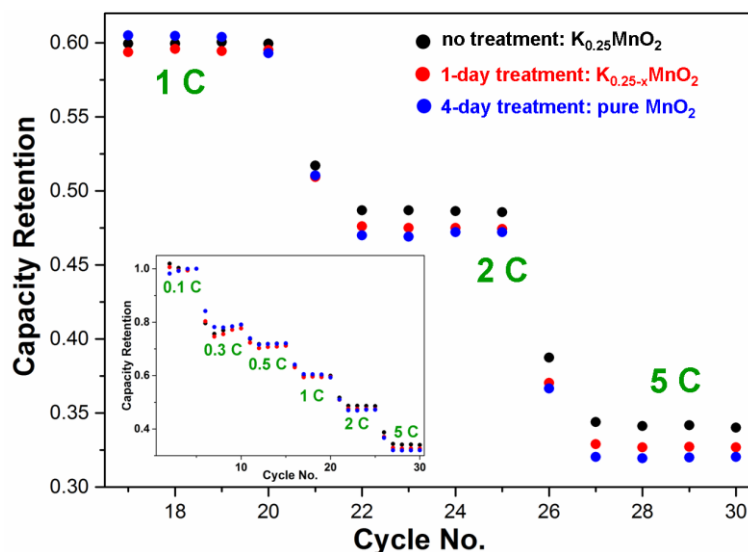
Figure C8. Cycling-rate performance of the three groups of nanowires ($K_{0.25}MnO_2$, $K_{0.25-x}MnO_2$, pure MnO_2) as lithium battery cathodes at 1, 2 and 5 C. Each cycle is normalized to the discharge capacity at 0.1 C as shown in the inset.

It is worth mentioning that the rate testing for all three groups of nanowires is 1 C=130 mA/g (Note that the practical discharge capacity for nanowires without acid treatment is in the range of 130 mAh/g-143 mAh/g based on several experiments in our case). The actual capacity for 1-day (157 mAh/g) and 4-day (170 mAh/g) treated nanowires are higher than 130 mAh/g. In addition, due to the accumulation of many other factors (such as irreversible (de)lithiation), the effect of K^+ concentration on the rate performance should gradually fade with increasing cycling times. Considering these effects, it is reasonable to expect a much better rate performance of K^+-doped nanowires than that of the nanowires with K^+ removed.

194
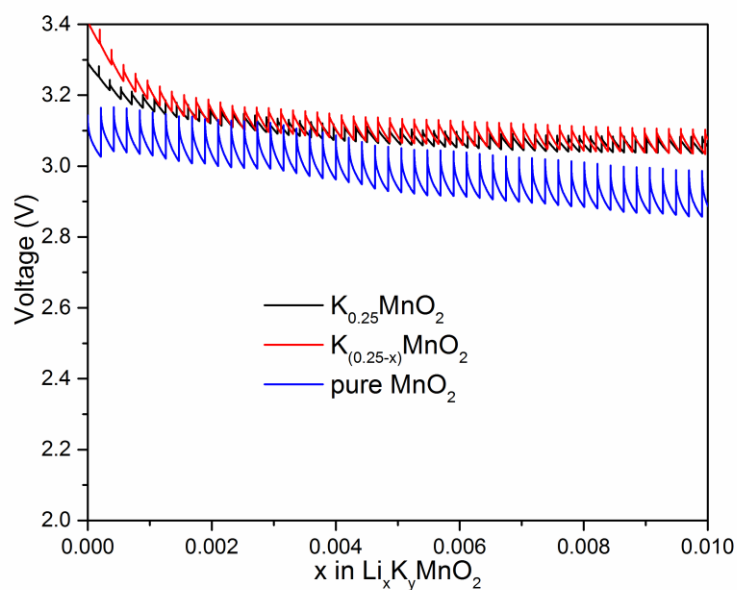
Figure C9. GITT curves for the three groups of nanowires, where dE/dX is measured.

Table C1. BET surface area for the three groups of nanowires ($K_{0.25}MnO_2$, $K_{0.25-x}MnO_2$, pure MnO_2) (N_2 isotherm).

	$K_{0.25}MnO_2$	$K_{0.25-x}MnO_2$	pure MnO_2
surface area (m^2/g)	28.2	26.8	26.7

Table C2. Calculated conductance values for α-MnO_2 nanowires (at T = 25 °C) stabilized by different concentrations of K^+. The conductance values and error bars are for the linear fitting of all the curves in the region ranging from +8 V to +10 V.

Composition	Conductance (i.e. slope) (µS)	Error
$K_{0.25}MnO_2$	0.15253	0.00244
	0.16195	0.00303
	0.18614	0.00382
$K_{(0.25-x)}MnO_2$	0.03445	0.00112
	0.02485	0.00069
	0.03156	0.00041
K_0MnO_2	0.00496	0.00013
	0.00111	0.00003
	0.00122	0.00003

Table C3. Calculated (DFT +U) and experimental lattice parameters of $K_{0.25}MnO_2$.

Lattice Parameter	Experimental value (Å)	Calculated value (Å)
a	9.94	10.03
b	9.94	9.74
c	2.857	2.88

C.2. Calculation of the Li^+, K^+ and O^{2-} arrangement in one 2×2 tunnel

We set r_{Li+}=0.59 Å, r_{K+}=1.37 Å, r_{O2-}=1.21 Å following Young's paper[11] and establish the atomic model with $a=b$=9.82308 Å and c=2.85443 Å based on our XRD Rietveld refinement in Figure 6.2. Then the D_{O-O} (the shortest distance of two O atoms surrounding one 8h site) is calculated to be 3.66 Å, D_{K-O}=(the shortest distance of one K and one O surrounding one 8h site) is 4.64 Å. So the O-O distance allows a

maximum free spherical space with $r_{max} = (3.66 - 2 \times 1.21)/2 = 0.62$ Å, while the K-O distance allows a maximum free spherical space of $r_{max} = (4.64 - 1.37 - 1.21)/2 = 1.03$ Å. So the theoretical maximum sphere that can be inserted around one 8h site is limited by D_{O-O} and the resulted r_{max} is 0.62 Å, which is larger than that of Li^+ (0.59 Å). This is an indication that Li^+ can be inserted at 8h sites when K^+ already occupy the 2a sites.

C.3. References

1. Feng, Q. *et al*. *J. Mater. Chem.* **9**, 319-333 (1999).

2. Tanaka, Y. *et al*. *Phys. Chem. Chem. Phys.* **2**, 1473-1479 (2000).

3. Kijima, N. *et al*. *J. Solid State Chem.* **177**, 1258-1267 (2004).

4. Kijima, N. *et al*. *Solid State Ionics* **262**, 14-17 (2014).

5. Feng, Q. et *al*. *Chem. Mater.* **7**, 148-153 (1995).

6. Schmid, H.K. *et al*. *Micron* **37**, 426-432 (2006).

7. Zhang, S. *et al*. *Am. Mineral.* **95**, 1741-1746 (2010).

8. Yuan, Y. *et al*. *Nano Lett.* **15**, 2998-3007 (2015).

9. Wang, Z.L. *et al*. *J. Phys. Chem. B* **103**, 751-753 (1999).

10. Yuan, Y. *et al*. *ACS Nano* **10**, 539-548 (2016).

11. Young, M.J. *et al*. *Chem. Mater.* **27**, 1172-1180 (2015).

12. Johnson, C.S. *J. Power Sources* **165**, 559-565 (2007).

13. Espinal, L. *et al*. *J. Am. Chem. Soc.* **134**, 7944-7951 (2012).

Appendix D. Supporting Information for Chapter 7[⑨]

D.1. Methods

D.1.1. Sample peparation

α-MnO$_2$ nanowires were produced by a hydrothermal process using KMnO$_4$ and MnSO$_4$ as the reactants. The reaction was carried out in a Teflon-lined stainless steel autoclave at 160ºC for 1.5, 3, 6, 9 and 12 h to obtain α-MnO$_2$ nanowires at different stages of growth. To prepare electron-transparent slices of the nanowire cross sections, the nanowires were first mixed with cold mounting epoxy resin (EPOFIX, Electron Microscopy Sciences) under 10 min supersonic vibrations. Hardener (EPOFIX, Triethylenetetramine, Electron Microscopy Sciences) was then added into the solution to facilitate the solidification process in atmosphere at 60ºC for 24 hours. After that, the solid solution was fixed on the sample stage of a Leica Ultracut UCT ultramicrotome equipped with a diamond knife. The nanowires were mechanically cut into slices at a feeding step size of 500 nm.

D.1.2. Sample characterization

Phase analysis was performed using powdered X-ray diffraction (XRD). The representative diameter of each sample was obtained statistically by averaging the diameters of tens of nanowires from different sample areas under low-magnification TEM. The atomic structure was analyzed using a spherical aberration-corrected JEOL JEM-ARM200CF scanning transmission electron microscope (STEM) equipped with a 200 kV cold-field emission gun, annular bright field (ABF) and high angle annular dark field (HAADF) detectors, and an energy dispersive spectrometer (EDS). A 22-mrad-probe convergence angle was used for all STEM images. The HAADF images were captured using a 90-mrad inner-detector angle.

The *in situ* liquid cell TEM experiment was carried out using a commercialized liquid holder (Protochips. Poseidon 500) inside the JEOL JEM-ARM200CF STEM at an acceleration voltage of 200 kV. Two chips made of Si substrates with 50 nm thick Si_3N_4 layers were used to construct the liquid cell with the inner space of 150 nm, enabling good electron transparence. Since the Si_3N_4 was the working surface that directly contacted the aqueous solution, before assembling the liquid cell, the Si_3N_4 surfaces were washed with methanol and then plasma cleaned for 1 min to remove contaminants and make the surface hydrophilic. The size of each Si_3N_4 window (where Si substrate was etched beforehand) was 550 μm × 20 μm. The two windows were aligned in parallel so that the imaging area was maximized. The flow of liquid into the cell was using a coaxial PEEK^{TM} tubing with an inner diameter of 100 μm and the tubing was connected with a syringe, which contained 0.5 ml KCl solution. The concentration of K^+ was kept at 0.03 mol/L, the same as it was in the actual solution during the hydrothermal synthesis. The electron dose rate was maintained approximately at 5.5 (± 0.5) × 10^3 e/(nm^2·s).

D.1.3. *Ab initio* computer modeling

Surface calculations were performed using density functional theory (DFT) with PAW potentials, as implemented in the VASP code.[1] The generalized gradient approximation (GGA) of Perdew-Burke-Ernzerhof (PBE)[2] was applied with a Hubbard U correction, as this has been demonstrated to give a good description of the ion insertion, surface energies and electronic structure of α-MnO_2,[3,4] and other transition metal oxides.[5] A planewave basis set cutoff energy of 520 eV and a minimum grid of 3×3×7 k-points was used in the Brillouin zone for bulk calculations. The calculated lattice parameters for $K_{0.25}MnO_2$ agree well with experiment, as shown in Supporting Information Table S1, although the common tendency for PBE+U to slightly overestimate the unit cell volume is apparent. Surface energies were calculated based upon slabs with a minimum thickness of 20 Å, with surface energy converged against slab thickness. Full geometrical relaxation of the ionic positions was performed to incorporate surface relaxation effects.

D.2. Supporting figures and tables.

Table D1. Calculated (DFT +U) and experimental lattice parameters of $K_{0.25}MnO_2$.

Lattice Parameter	Expt Å	Calc Å
a	9.866	9.990
b	9.866	9.955
c	2.857	3.022
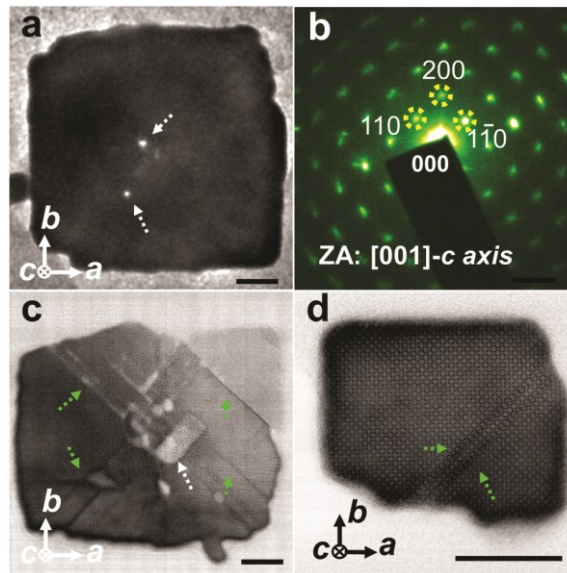
Figure D1. (a): [001] TEM image of an α-MnO$_2$ slice after cross sectioning; b: SAED of the same slice in a; (c,d): [001] ABF images of two α-MnO$_2$ slices vaguely showing closely packed 2×2 tunnels and {110} stripes (green dashed arrows). The white dashed arrows in (a) and (c) indicate inner holes and cracks. Scale bars: 10 nm.

Figure D1 shows low magnification (S)TEM images of cross-sectioned α-MnO$_2$ slices along the [001] zone axis. The specimens generally have a square-shaped cross section under this projection. However, some exhibited inner cracks and holes (white dashed arrows in (a) and (c)) that are probably caused by incomplete attachment of the primary nanowires. The lateral surfaces are characterized as parallel to {100} planes based on the corresponding SAED, indicating that the {100} surface is the

most stable in α-MnO$_2$ during solution synthesis. It is notable in figures D1c and d that the slices feature many dark stripes embedded within them. Interestingly, all the stripes are orientated parallel to {110} planes and are essentially tunnel-based structures (Figure D1d). According to the typical OA mechanism where defective interfaces usually form between two attached primary units,[6,7] these stripes should be an indication of interfaces (Figure 7.4d) that are introduced during the lateral OA process of primary α-MnO$_2$ nanowires.
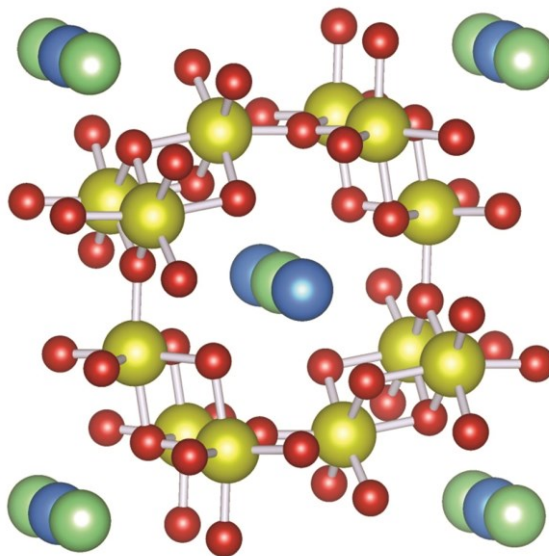
Figure D2. Structure of K$_{0.25}$MnO$_2$ with Mn in yellow and O in red. The Wyckoff 2a sites are shown in green, and the 2b sites in blue.

D.3. References

1. Kresse, G.; Furthmuller, J. Efficient Iterative Schemes for *ab initio* Total-Energy Calculations using a Plane-Wave Basis Set. *Phys. Rev. B: Condens. Matter Mater. Phys.* **1996**, *54*, 11169-11186.

2. Perdew, J.P.; Burke, K. Generalized Gradient Approximation Made Simple. *Phys. Rev. Lett.* **1996**, *77*, 3865-3868.

3. Tompsett, D. A.; Parker, S. C.; Islam, M. S. Surface Properties of α-MnO_2: Relevance to Catalytic and Supercapacitor Behaviour. *J. Mater. Chem. A* **2014**, *2*, 15509-15518.

4. Tompsett, D. A.; Islam, M. S. Electrochemistry of Hollandite α-MnO_2: Li-Ion and Na-Ion Insertion and Li_2O Incorporation. *Chem. Mater.* **2013**, *25*, 2515-2526.

5. Armstrong, A. R.; Lyness, C.; Panchmatia, P. M.; Islam, M. S.; Bruce, P. G. The Lithium Intercalation Process in the Low Voltage Lithium Battery Anode $Li_{1+x}V_{1-x}O_2$. *Nat. Mater*. **2011**, *10*, 223-229.

6. Zhang, J.; Huang, F.; Lin, Z. Progress of Nanocrystalline Growth Kinetics Based on Oriented Attachment. *Nanoscale* **2010**, *2*, 18-34.

7. Huang, F.; Zhang, H.; Banfield, J.F. Two-Stage Crystal-Growth Kinetics Observed during Hydrothermal Coarsening of Nanocrystalline ZnS. *Nano Lett.* **2003**, *3*, 373-378.